Three Dimensional Finite-Element Numerical Modeling of Geophysical Electromagnetic Problems Using Tetrahedral Unstructured Grids

by

©Seyedmasoud Ansari

A Thesis submitted to the School of Graduate Studies in partial fulfillment of the requirements for the degree of

Doctor of Philosophy

Department of Earth Sciences

Memorial University of Newfoundland

December 2014

St. John's Newfoundland and Labrador

Abstract

Finite-element solutions to the three-dimensional geophysical electromagnetic forward modeling problem in the frequency domain are presented. The method is firstly examined for the solution to the E-field Helmholtz equation. Edge-element basis functions are used for the electric field. An alternative method is also used which is based on decomposing the electric field into vector and scalar potentials in the Helmholtz equation and in the equation of conservation of charge. Edge element and nodal element basis functions are used respectively for the vector and scalar potentials. This decomposition is performed with the intention of satisfying the continuity of the tangential component of the electric field and the normal component of the current density across the inter-element boundaries, therefore finding an efficient solution to the problem. The computational domain is subdivided into unstructured tetrahedral elements. The system of equations is discretized using the Galerkin variant of the weighted residuals method, with the approximated vector and scalar potentials as the unknowns of a sparse linear system. Both iterative and direct solvers are used for the solutions to the E-field and decomposed systems. A generalized minimum residual solver with an incomplete LU preconditioner is used to iteratively solve the system. The direct solver, MUMPS, is used to provide the direct solution to the system of equations. The forward modeling methods are validated using a number of examples. The fields generated by small dipoles on the surface of a homogeneous half-space are

compared against their corresponding analytic solutions. The next example provides a comparison with the results from an integral equation method for a long grounded wire source on a model with a conductive block buried in a less conductive half-space. The decomposed method is also verified for a large conductivity contrast model where a magnetic dipole transmitter-receiver pair moves over a graphite cube immersed in brine. Solutions from the numerical approach are in good agreement with the data from physical scale modeling of this scenario. Another example verifies the solution for a resistive disk model buried in marine conductive sediments. For all examples, convergence of the solution that used potentials was significantly quicker than that using the electric field. The inductive and galvanic components of the electromagnetic response are also investigated for the above examples. Furthermore a detailed investigation of these effects are presented for models with varying conductivity contrasts. The characteristics of the solutions in terms of implicitly and explicitly enforcing the Coulomb gauge condition are investigated for the decomposed system. Numerical computations show that for the above-mentioned grounded wire example the electromagnetic response is significantly affected by the contribution from the galvanic part. By contrast for the example where a magnetic dipole excites a graphite cube immersed in brine solutions, the inductive scenario dominantly contributes to the model's electromagnetic response.

Acknowledgements

I would like to first and foremost thank my supervisor, Dr. Colin Farquharson, for his lasting patience and support during my PhD studies. I would also thank him for allocating exclusive times for scientifically discussing the numerical modeling challenges of this work. I would also like to thank Dr. Peter Lelièvre for providing auxiliary meshing subroutines and also for his assistance in dealing with the difficulties of working with unstructured meshes. I also thank my committee members Dr. Charles Hurich and Dr. Jeremy Hall for their constructive and positive criticism regarding the completion of this project. I would like to also thank Dr. Gordon West for specifically discussing the issues regarding the numerical simulation of thin rectangular plates. Dr. Chester Weiss is also appreciated for providing numerical data for the marine disk model. I would also appreciate the School of Graduate Studies for providing part of the financial support for this project.

Table of Contents

List of Tables

List of Figures

Chapter 1

Introduction

Geophysical electromagnetic (EM) methods, in the form of profiling and sounding techniques, have been used to remotely map the variations in the electrical conductivity of the Earth either laterally or with depth. In the context of mineral exploration these methods continue to be important in the search for and characterization of conductive ore deposits, e.g., volcanogenic massive sulfides, uranium deposits, and kimberlite pipes (Frischknecht et al., 1991). Both airborne and ground-based EM methods have been used for these types of explorations (see e.g., reviews by Palacky and West, 1991, and Vallée et al., 2011). The strength of the EM response is a function of the electrical conductivity of the rock forming minerals. In particular, individual conducting minerals, such as pyrite and pyrrhottite in the case of massive sulfide deposits, and how well the grains are electrically connected forms the bulk conductivity of the ore deposit (Frischknecht et al., 1991). As a sounding EM technique, the controlled-source electromagnetic method (CSEM) is also used for mineral exploration scenarios (see Zonge and Hughes, 1987, and references therein). This method uses an artificial signal source, for instance, a grounded electric line source or a horizontal loop of current, to energize the conducting Earth. For hydrocarbon

exploration scenarios, CSEM has been used to map the structure of the thin resistive layers thought to contain hydrocarbons prior to drilling (see e.g., Constable and Weiss, 2006; and Weiss and Constable, 2006), and also as a reconnaissance method before resolving the detailed structure with reflection seismics (Zonge and Hughes, 1987). The rationale for using CSEM in this field emerges from the fact that electrical conductivity provides insights on porosity of geologic structures (Constable and Weiss, 2006). In fact the relative conductivity of porous rocks decreases significantly if saturated with hydrocarbon materials.

The complexity of realistic geological models demands powerful, flexible modelling methods. It is now widely accepted that complicated geological structures, i.e., contacts between rock units and topography features, can be recovered efficiently using wireframes of connected triangles (Lelièvre et al., 2012). Traditional rectilinear meshing techniques produce a pixellated representation of the curvilinear Earth models that can give rise to calculating an inadequate three-dimensional geophysical response. In order to avoid this concern unstructured tetrahedral meshes can be used to construct the arbitrarily complex geological Earth models.

In terms of the physical justification for the mechanism of remote sensing EM methods Maxwell's equations can be employed. As a consequence of the temporally varying electromagnetic fields generated by EM sources mentioned above electric currents can be induced in the subsurface. Depending on the conductivity of the Earth, secondary magnetic and electric fields are generated by the induced eddy currents and measured on the surface. In order to extract information about the electrical conductivity of the structures in the subsurface a calculation of these induced fields is necessary. For a given geological model if a good agreement between the calculated and observed fields is seen, the real structure of the subsurface could be non-uniquely conjectured.

In order to quantitavely model the subsurface resistivity distribution and extract as much information as possible from survey data numerical solution methods for computing synthetic data are required.

To genuinely model an arbitrary 3D object in the ground, a quantitative understanding of how the EM response is affected by inductive and galvanic parts is necessary. Despite the long history of EM methods in geophysical exploration, there has not yet been a thorough investigation of these effects. The induction portrays the distortion of the electric field by a time-varying magnetic field generated, for example, by a closed-loop current as the signal source. By contrast, a synopsis of the galvanic process would be the direct flow of the current to and from the grounded source similar to what is observed in direct-current (DC) resistivity methods. In fact, channelling of the electric current at the regions of conductivity gradient characterizes the galvanic response (West and Macnae, 1991). In order to explore the relative contributions from inductive and galvanic parts and the interplay between them an $\mathbf{A}-\phi$ decomposition of the electric field is studied in this thesis where $\mathbf{A}$ and ϕ are the magnetic vector potential and scalar electric potential respectively.

Difficulties in analytically solving Maxwell's equations for irregular and complex-shaped geometries in the Earth give rise to three dimensional (3D) numerical modeling solutions. Despite involving large numbers of unknowns and computational difficulties, 3D modeling of geophysical electromagnetic problems has been practiced and improved since the 1970s. For the earliest studies see for example Jones and Pascoe, 1972; Raiche, 1974; Hohmann, 1975; Weidelt, 1975. Three methods have been used: the integral-equation (IE), finite-difference (FD) and finite-element (FE) methods. The IE method was firstly favored wherein the scattering current was considered only inside the localized inhomogeneity and the total electric field was calculated using the

sum of primary and scattered fields (Hohmann, 1975; Raiche, 1974; Weidelt, 1975). Here, due to the discretization of only the anomalous region rather than the whole subsurface, a small system of equations is involved. Considering the limited computer memory at the time, the IE method was the first to receive most attention. However, if the discretized region was enlarged the memory required by the dense system of equations increases dramatically. This severely restricts the size of discretized region that could be considered.

With an increase in memory and computer processing speed, an easy-to-implement differential equation method, that is finite difference, became more popular (e.g., Dey and Morrison, 1979; Wang and Hohmann, 1993; Newman and Alumbaugh, 1995; Smith, 1996; Smith, 1996). Using the FD method the entire Earth was typically subdivided into staggered rectangular grids (Yee, 1966). Although the large system of equations formed using FD was to occupy a large space in terms of the computer's memory, more general geometries of the subsurface structures could be investigated. Also, using the FD method an entire image of the computational domain was reproduced while the IE method only concerned modelling a localized conductive anomaly in an otherwise simple background.

The finite-element method was successfully used to solve Maxwell's equations in an electrically conducting medium space (see for example Coggon, 1971, for an early study) and has attracted more attention in recent years (e.g., Badea et al., 2001; Mitsuhata and Uchida, 2004; Börner et al., 2008; Um et al., 2010; Farquharson and Miensopust, 2011). The solution to the FE problem is given either by weighting the residual of the differential equation or by minimizing a functional with respect to the solution vector and finally integrating over the entire computational domain (Jin, 2002). The unknown fields in the differential equations are approximated using ap-

propriate basis functions. The FE method has been favored over the FD method as it can be readily applied to unstructured meshes. These meshes, e.g. the unstructured tetrahedrons used in this study, are more suitable to model the curves of complex-shaped volumes and irregular geometries in the realistic Earth. Furthermore, the ability to locally refine the mesh at the regions of interest and coarsen it near the domain boundaries enables a complicated domain to be discretized efficiently.

Coggon (1971) presented a detailed formulation of the FE method, using the principle of energy minimization, for geophysical EM problems. Based on this approach, the controlled-source EM problem is solved by Pridmore et al. (1981) for only the electric field and by Livelybrooks (1993) for both electric and magnetic fields. Both Pridmore et al. (1981) and Livelybrooks (1993) expanded the EM fields using nodal-element (scalar) basis functions on structured rectangular grids. The scalar basis functions were defined at the vertices (nodes) of each element and the fields were interpolated by a linear combination of these functions in each rectangle. The continuity of such a scalar basis function expansion from one element to the next is guaranteed because each basis function vanishes linearly away from a particular node towards all neighboring nodes in the grid. This results in the tangential component of the electric field being continuous across interfaces of distinct conductivities. However, it violates the discontinuity condition for the normal component of the electric field across conductivity contrasts. Moreover, in opposition to what is required, the approximated electric field does not necessarily meet the requirement on the true field of being divergence-free in a source-free or a charge-free cell. In order to address these deficiencies, edge-element (vector) basis functions were introduced by Nédélec (1980) and have since been applied to geophysical EM modeling by Sugeng (1998), Nam et al. (2007), Börner et al. (2008), Liu et al. (2008), Schwarzbach (2009), Um et al. (2010), and Farquharson and Miensopust (2011). In all of these applications the electric

field is approximated using vector basis functions which are defined along the edges within the mesh. This guarantees the continuity of the tangential component of the approximated electric field, while allowing its normal component to jump across the inter-element boundaries. Also, as a significant property and by construction, the divergence of the vector basis function is zero within each cell.

As far as the stability of the solution is concerned, the vector Helmholtz equation, expressed solely in terms of the electric or magnetic field, is a partial differential equation (PDE) of second order. Solving this PDE for a situation where the EM fields are discretized using the FE method, and where very low frequencies are employed, is not efficient. A number of studies using potentials in three-dimensional forward modelling of geophysical EM problems have been carried out either for the finite-difference and finite-volume methods (e.g., Haber et al., 2000; Aruliah et al., 2001; Weiss, 2013) or for the finite-element method (e.g., Everett and Schultz, 1996; Biro, 1999; Badea et al., 2001; Mitsuhata and Uchida, 2004; Franke et al., 2007; Börner et al., 2008; Schwarzbach, 2009; Farquharson and Miensopust, 2011; Franke-Börner et al., 2012; Puzyrev et al., 2013). Furthermore, the potential field finite-element approximation for wave and eddy current problems in electrical engineering applications has also been used (e.g., Fujiwara et al., 1996; Dyczij-Edlinger et al., 1998). By decomposing the electric field into magnetic vector ($\mathbf{A}$) and electric scalar (ϕ) potentials, Haber et al. (2000) present a FD solution for a rectangular grid. In conjunction with the Coulomb gauge condition, that is enforced to uniquely define the potenial fields, Haber et al. (2000) performed an $\mathbf{A} - \phi$ decomposition of the electric field to derive a strongly decoupled system of differential equations. However, Haber et al. (2000) do not study how the two potentials, in isolation or in combination, contribute to the total electric field. Biro (1999) reviewd all formulations of eddy current problems for the vector and scalar potentials with respect to the finite-element discretization. Again using the

$\mathbf{A} - \phi$ decomposition but for primary and secondary potentials, Badea et al. (2001), Stalanker (2004) and Puzyrev et al. (2013) presented a FE solution to the EM induction problem. In spite of using tetrahedral elements for discretization, they only used nodal basis functions for both vector and scalar potentials. For the same type of basis functions used for the potentials Everett and Schultz (1996) modelled the decomposed problem for the total fields. By using nodal basis functions for three components of the vector potential normal and tangential continuity conditions were ensured therein. This approach however violates the necessity, from the Coulomb gauge condition, of the vector potential being divergenceless in a source-free element. Fujiwara et al. (1996) and Dyczij-Edlinger et al. (1998) investigated the superior convergence of the ungauged $\mathbf{A} - \phi$ method for the high frequencies (i.e. in the range of GHz) of engineering modeling scenarios. For unstructured meshes Franke et al. (2007) solved the potential formulation of the induction equation, for the secondary vector potential. Franke et al. (2007) used quadratic edge elements for the finite-element expansion of the vector potentials. In a recent study Weiss (2013) developed a finite-volume forward solver based on the Lorentz-gauged $\mathbf{A} - \phi$ decomposition of the electric field. Weiss (2013) also used the total field formulation of the vector and scalar potentials and discretized those fields on structured rectangular grids. Mitsuhata and Uchida (2004) decomposed the magnetic field into vector and scalar potentials and expanded each using edge- and nodal-element basis functions respectively. Farquharson and Miensopust (2011) also used edge-elements to directly approximate the electric field and employed nodal elements to approximate a divergence correction potential. The FE implementations of Mitsuhata and Uchida (2004) and Farquharson and Miensopust (2011) were performed for the magnetotelluric (MT) problem and for structured rectangular meshes. By using unstructured meshes Schwarzbach (2009) presented a mixed $\mathbf{E} - V$ formulation of the Helmholtz equation and used nodal-elements for the

scalar potential (V) and edge elements for the electric field (**E**). By adding the scalar term to the electric field Schwarzbach (2009) was aiming to precondition the problem and thus increase the rate of convergence for low frequencies. In a convergence study Franke-Börner et al. (2012) solved the three-dimensional $\mathbf{A} - \phi$ system for the magnetotelluric boundary value problem. The discretized system of equations therein was assembled using the simulation software COMSOL Multiphysics, and solved using the PARDISO library.

In terms of the characteristics of the finite-element discretization for 3D EM problems the condition number for the system of equations strongly depends on the mesh geometry, e.g., largest to smallest cell size, elongation of cells and more specifically the dihedral angles in the case of unstructured tetrahedral grids (Du et al., 2009). For comparable hexahedral meshes Schwarzbach et al. (2010) showed that FE and FD discretizations to the stabilized $\mathbf{E} - V$ formulation result in similar condition numbers for the system of equations. Schwarzbach et al. (2010) used a direct matrix equation solver and a primary-secondary field formulation. Schwarzbach et al. (2011) used a combination of iterative and direct routines to solve the E-field system for a primary-secondary field formulation and for unstructured meshes. Grayver and Streich (2012) solved the stand-alone Helmholtz equation using an iterative solver for low frequencies greater than 2 Hz. However Grayver and Streich (2012) again formulated the problem in terms of the secondary electric field and implemented the finite-difference method on staggered grids. Finite-element solution of the stabilized formulation by a preconditioned iterative method was found to be discouraging as it resulted in poorer convergence in comparison to the corresponding finite-difference solutions (Schwarzbach, 2009).

A number of studies for the investigation of inductive and galvanic components, in

isolation or in combination, while developing 3D numerical modeling schemes has been performed. Lamontage and West (1971) formulated the EM equations in terms of a divergence-free vector potential (solely inductive component) and presented a finite-difference solution for the classic scenario of an inductively thin plate embedded in free-space. Again for models consisting of a finite, thin, conductive plate but surrounded by a conductive host Lajoie and West (1976) solved the electromagnetic problem using the integral-equation method. However, because of the mixed interaction between inductive and galvanic fields in the presence of a relatively resistive host Lajoie and West (1976) encountered erroneous secondary fields when solving the conventional scattered electric field formulation. In order to counteract this problem the electric field therein was formulated in terms of divergence-free and curl-free scalar potentials, i.e., induction and conduction potentials.

This thesis concerns the development of the three-dimensional forward modeling of CSEM problems based on the finite-element method for unstructured meshes. There are many purposes for the work presented here. Firstly, the problem is solved for unstructured grids, which provide more flexibility in generating general geometries of the Earth. As for the main focus of this work, decomposing the electric field into potentials and discretizing the problem using both vector and scalar basis functions leads to an efficient solution to the system of equations. Moreover the specific inductive and galvanic contributions to the electric field can be investigated for a range of Earth models, transmitters, and frequencies. Also from the practical standpoint the computer code written during the course of this thesis research is applicable to general types of transmitters for example an electric dipole, a loop of current and a long grounded wire of finite length. I begin in Chapter 2 by introducing the total electric field (E-field) Helmholtz partial differential equation with the relevant boundary and interface conditions. The minimization of the E-field system using the method

of weighted residuals is performed. The vectorial finite-element method is then introduced for discretization of the system. The iterative and direct solutions to the E-field system are carried out for a number of preliminary models. Chapter 2 is ended by a discussion of the weakness and inefficiency of the total field solution of the E-field system for unstructured meshes. In order to remedy these difficulties Chapter 3 presents a solution to the electromagnetic vector-scalar potential formulation. In this chapter the EM diffusion problem is formulated in terms of the vector and scalar potentials of the electric field. Similar to the preceding chapter the $\mathbf{A} - \phi$ decomposed system of equations is minimized using the method of weighted residuals followed by a discretization using the finite-element method. The system of equations is solved using the appropriate iterative method. Chapter 3 is ended by showing the accuracy and efficiency of the potential solutions for the comparable examples presented in Chapter 2. Chapter 4 begins by introducing and displaying the inductive and galvanic nature of the electromagnetic diffusion phenomena. Also in Chapter 4, further verification of the $\mathbf{A} - \phi$ decomposition method is presented for a variety of examples from previous classic geophysical studies. The inductive and galvanic contributions to the total electric field is also simulated for the examples presented therein. Forward modeling scenarios wherein the total field is dominated by only the inductive effect, only the galvanic effect, and a mixture of these two are presented.

Finally a detailed investigation of the electromagnetic response and also inductive and galvanic components in terms of different conductivity contrasts between the conductive target and the surrounding host is presented in Chapter 5. The explicit Coulomb gauged formulation of the decomposed system with the calculated fields and currents is also presented in this chapter. Chapter 5 is ended by demonstrating the continuity of the fields and currents at the conductivity inerfaces.

In summary, as a new study for the geophysical EM exploration scenarios, a finite-

element $\mathbf{A} - \phi$ approach using the edge and nodal elements for the respective vector and scalar potentials, and for the total field formulation is developed. Also, a proper investigation of the inductive and galvanic parts and the interplay between them has been conducted for various geophysical examples. Unlike using the black-box engineering finite-element packages and libraries, the entire FE discretization including the evaluation of inner-product integrals is performed and analyzed on a paper and pencil work. After deriving the finite-element formulas the whole numerical aspects of the work are coded in the Fortran programming language.

Chapter 2

Frequency Domain Finite-Element Electromagnetic Boundary Value Problems

Geophysical electromagnetic boundary value problems concern solving the frequency-domain Maxwell's equations within the Earth. The main EM property considered is the spatial conductivity distribution of the medium in three dimensions: $\sigma(\mathbf{r})$ with the $\mathbf{r}$ being the position vector. The solution to the Helmholtz equations provides a 3D ground image of the electric field, $\mathbf{E}(\mathbf{r}, \omega)$, and the magnetic field, $\mathbf{H}(\mathbf{r}, \omega)$, where ω is the angular frequency. In this chapter, after introducing Maxwell's equations, the Helmholtz equation for the electric field is derived. The finite-element method for tetrahedral unstructured meshes is then applied to this equation and next the system of equations is solved.

2.1 E-field Equation

With a time dependence of $e^{i\omega t}$ in the quasi-static regime Faraday's law and Ampere's law in a region containing electric or magnetic sources are written as:

$$\nabla \times \mathbf{E} + i\omega\mathbf{B} = -\mathbf{J}^{\mathbf{s}}_{\mathbf{m}} \tag{2.1}$$

and

$$\nabla \times \mathbf{H} - \sigma\mathbf{E} = \mathbf{J}^{\mathbf{s}}_{\mathbf{e}}, \tag{2.2}$$

where μ_0 is the magnetic permeability of free space; $\mathbf{J}^{\mathbf{s}}_{\mathbf{m}}$ and $\mathbf{J}^{\mathbf{s}}_{\mathbf{e}}$ are the magnetic current density and the electric current density of the EM source (Ward and Hohmann, 1988). Also $\mathbf{B}$ is the magnetic flux density and is connected to the magnetic field through the constitutive relation of $\mathbf{B} = \mu_0\mathbf{H}$ (Ward and Hohmann, 1988). These equations are first-order linear differential equations and referred to as a coupled set to join vector quantities $\mathbf{E}$ and $\mathbf{H}$ (Sadiku, 2001). A simpler equation which gives rise to a tractable numerical solution approach is obtained if either of the electric field or the magnetic field is eliminated from the system of equations. This is done by taking the curl of equation 2.1 and using equation 2.2 to derive the following second-order partial differential equation (PDE) for the electric field:

$$\nabla \times \nabla \times \mathbf{E} + i\omega\mu_0\sigma\mathbf{E} = -i\omega\mu_0\mathbf{J}^{\mathbf{s}}_{\mathbf{e}} - \nabla \times \mathbf{J}^{\mathbf{s}}_{\mathbf{m}}, \tag{2.3}$$

which is the general form for the decoupled Helmholtz equation and is called the E-field equation here. Also in terms of solving for the fields analytically, the solution to the E-field equation is more apparent (for example for a simple 1-D case and for a whole space scenario) rather for the case where equations 2.1 and 2.2 are simultaneously solved. However, because of the difficulty in finding the analytical solution to such an equation

(equation 2.3) for general 3D Earth models a numerical modeling solution is needed. In brief, numerical solutions are obtained by approximating the partial differential equation subject to the relevant boundary conditions and solving a linearized matrix equation. However for the problem presented here equation 2.3 does not completely describe the behavior of electromagnetic fields at boundaries between two regions with different physical properties. Also, to find a unique solution to the partial differential equation appropriate boundary conditions need to be considered on the boundaries of the domain.

2.2 Field continuity and boundary conditions

2.2.1 Interface conditions

The behavior of the EM fields at interfaces between two media with different conductivities is given by considering the integral form of Maxwell's equations. To show this behavior on the boundary surface S (see Figure 2.1) a small pillbox with its upper and lower surfaces situated in mediums 1 and 2 respectively is constructed. The area for each of these surfaces is Δs and the total thickness of the pillbox is Δt. Considering the closed surface S here the integral form of the divergence law for the magnetic flux density, $\nabla \cdot \mathbf{B} = 0$, is given as:

$$\oint_S \mathbf{B} \cdot d\mathbf{a} = 0 \tag{2.4}$$

(Griffiths, 1999). For the situation in which the thickness of the pillbox is infinity small ($\Delta t \to 0$) the normal component of the magnetic intensity will be continuous across the interface: $\mathbf{n} \cdot (\mathbf{B}_2 - \mathbf{B}_1) = 0$. Also by integrating Faraday's law (equation 2.1) over the boundary surface and using Stokes' theorem the following equation is given

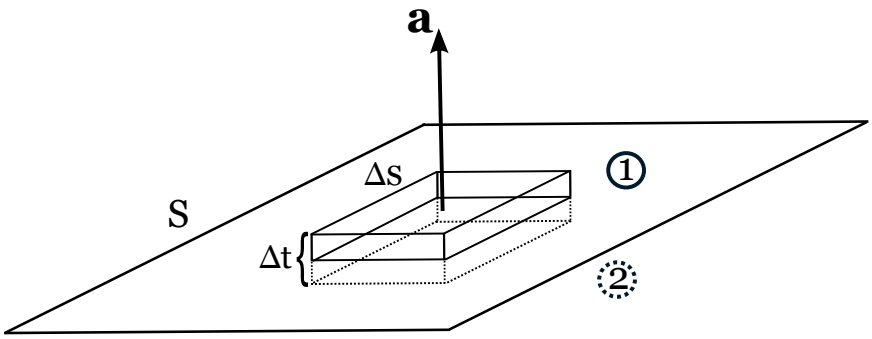

Figure 2.1: A rectangular pillbox enclosing two media with different electrical properties. The vector **a** is the outward normal for the top surface of the pillbox located in medium 1.

for the thin Amperian loop shown in Figure 2.2

$$\mathbf{E}_2 \cdot \Delta\mathbf{l} - \mathbf{E}_1 \cdot \Delta\mathbf{l} = -i\omega \oint_{S'} \mathbf{B} \cdot d\mathbf{a} \tag{2.5}$$

where $\mathbf{E}_1$ and $\mathbf{E}_2$ are the electric fields along the large sides of the loop for two media in contact. Assuming that the parameter $\mathbf{B}$ is finite on the surface, for the situation in which the height of the contour loop (Δh in Figure 2.2) is small, equation 2.4 forces the integral on the right hand side of the above equation to become zero. Therefore, the electric field parallel to the boundary will be the same on either side. In fact, the tangential component of the electric field becomes continuous across the interface:

$$\mathbf{n} \times \mathbf{E} = 0, \tag{2.6}$$

where $\mathbf{E} = \mathbf{E}_1 - \mathbf{E}_2$. The behavior of the normal component of the electric field is given by the electric Gauss law, $\nabla \cdot (\epsilon_0 \mathbf{E}) = \rho$, where ϵ_0 is the electric permittivity of free space and ρ is the density due to free charges. For a volume element around the surface S (see Figure 2.1) the divergence theorem can be used to derive the following

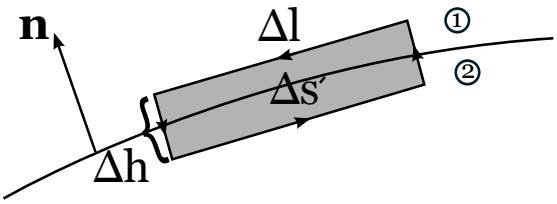

Figure 2.2: An Amperian loop straddling the interface boundary between two media. The normal vector $\mathbf{n}$, the thickness (height) of the loop element Δh and its length Δl are also shown. The area of the loop is also $\Delta s^{'}$ (Ward and Hohmann, 1988).

equation in integral form:

$$\oint_S \epsilon_0 \mathbf{E} \cdot d\mathbf{a} = \int_\Omega \rho \; dv \tag{2.7}$$

where Ω is the volume enclosed by S. For a tiny volume element the right hand side of the above equation is equal to $\rho \Delta s \Delta t$ and therefore,

$$\mathbf{n} \cdot (\mathbf{E}_1 - \mathbf{E}_2) = \frac{\rho_s}{\epsilon_0} \tag{2.8}$$

where $\rho_s = \rho \; \Delta t$ is the surface charge density. The above equation indicates that due to charge accumulation the normal component of the electric field can be discontinuous at the interface.

In order to quantify the discontinuity in the electric field across the interface between two media of different conductivities, σ_1 and σ_2, an understanding of the interface condition of the current density is required. Considering the quasi-static phenomena, the divergence of the current density is zero in a source free medium:

$$\nabla \cdot \mathbf{J} = 0. \tag{2.9}$$

This indicates that the normal component of the current density must be continuous across the conductivity gradients. Considering the pillbox in Figure 2.1 the normal component of the current crossing the interface is given with $\mathbf{J}_i \cdot \mathbf{n} \Delta s$, where $i = 1, 2$

and Δs is the area for either upper and lower faces. Here $\mathbf{J}_1$ and $\mathbf{J}_2$ are the current densities in mediums 1 and 2. The continuity in the normal current dictates,

$$\mathbf{n} \cdot (\mathbf{J}_1 - \mathbf{J}_2) = 0. \tag{2.10}$$

Using Ohm's law the above equation changes to

$$\mathbf{n} \cdot (\sigma_1 \mathbf{E}_1 - \sigma_2 \mathbf{E}_2) = 0 \tag{2.11}$$

which indicates that the discontinuity in the normal component of the electric field across the interface depends on the conductivities of the neighboring mediums.

2.2.2 Boundary Conditions

In order to obtain a unique solution to the EM partial differential equation, imposition of boundary conditions at the outer (truncation) boundaries of the physical domain is required. The Sommerfeld condition of radiation (Sommerfeld, 1949) is used here. This condition states that the radiation from the electromagnetic source scatters such that at the infinite boundary no energy reflects back into the conductive medium. Therefore the EM energy must vanish on the boundaries of the problem. According to Poynting's theorem the EM energy on the boundary surface, Γ, is a function of both electric and magnetic fields, and of the current density:

$$\oint_{\Gamma} (\mathbf{E} \times \mathbf{H}) \cdot d\mathbf{a} \;=\; \mathcal{F}(\mathbf{E}, \mathbf{H}, \mathbf{J}), \tag{2.12}$$

where the parameter $\mathcal{F}$ is a generic function. A similar equation can be derived when proving the uniqueness theorem for the boundary value problem (Subbaro, 2011):

$$\oint_{\Gamma}(\Delta\mathbf{E}\times\Delta\mathbf{H})\cdot d\mathbf{S}=\mathcal{I}(\epsilon_0\Delta\mathbf{E},\mu_0\Delta\mathbf{H})+\mathcal{G}(\sigma\Delta\mathbf{E}) \tag{2.13}$$

where $\mathcal{I}$ and $\mathcal{G}$ are again some generic functions, $\Delta\mathbf{E}=\mathbf{E}_2-\mathbf{E}_1$ and $\Delta\mathbf{H}=\mathbf{H}_2-\mathbf{H}_1$ with $\mathbf{E}_1$, $\mathbf{E}_2$, $\mathbf{H}_1$, and $\mathbf{H}_2$ as two pairs of different solutions for the electric and magnetic fields. Here only tangential components of $\Delta\mathbf{E}$ and $\Delta\mathbf{H}$ contribute to a nonzero integral term on the left hand side of the above equation. Hence the tangential component of $\Delta\mathbf{E}$ vanishes only if the tangential $\mathbf{E}_1$ and $\mathbf{E}_2$ are equal on the surface (similarly for $\mathbf{H}$) and the surface energy integral in the above equation vanishes. This guarantees a unique solution for the electric field, $\mathbf{E}_1=\mathbf{E}_2$ (and the magnetic field, $\mathbf{H}_1=\mathbf{H}_2$). As a result, considering a truncation boundary sufficiently far from the EM source, the tangential component of the electric field is set to zero for the boundary condition in equation 2.3 (Coggon, 1971; Pridmore et al., 1981; Livelybrooks, 1993):

$$(\mathbf{n}\times\mathbf{E})_{\,\Gamma}=0. \tag{2.14}$$

2.3 The Finite-Element Method

A complete description of the FE solution of numerically solving the EM boundary value problem is given in Jin (2002), Sadiku (2001) and Monk (2003). In this section a summary of the various steps through the method is explained for solving the E-field Helmholtz equation.

2.3.1 The minimization problem

The solution of PDE boundary value problems using the finite-element method is based on the variational principle or the method of weighted residuals. In both of these methods, the problem of solving the differential equation is replaced by that of solving the differential equation in an average sense, i.e. its weak form, over the whole domain. In particular, the problem of integrating the differential equation is equivalently replaced by a new equation consisting of the inner-product integrals of some vector functions. The general form of the derived equation is given by the following equation,

$$\mathcal{L}\mathcal{X} = \mathcal{F} \tag{2.15}$$

and its relevant boundary condition on the boundaries of the domain. In equation 2.15 the parameter $\mathcal{F}$ is known and $\mathcal{X}$ is the unknown vector to be determined. The parameter $\mathcal{L}$ is also a differential operator which includes the inner-product integrals. The solution to the above equation is a function (e.g. the electric field in equation 2.3) which provides a minimum to all inner-product terms in the discretized equation. Either the Rayleigh-Ritz method, as a variational method, or the Galerkin method, which is referred to as a method of weighted residuals, are conventionally used for discretizing EM diffusion equations, i.e. equation 2.3 (Coggon, 1971; Hohmann, 1987; Jin, 2002). The first step in using the Rayleigh-Ritz method is forming a functional whose minimum is the relevant differential equation (e.g. equation 2.3 here). The argument or input variable of the functional is itself a function which can be for example the electric field or potentials in this context. After approximating the input variable using the appropriate elemental functions the approximated functional is formed. The new functional is then minimized with respect to its unknown coefficients. This procedure leads to a linear equation in the form of equation 2.15. The unknown

parameter $\mathcal{X}$ is eventually obtained by solving the derived equation. In this thesis however, I used the method of weighted residuals to solve the EM equations. As an advantage over the variational methods, the method of weighted residuals does not concern the construction of the appropriate functional in its implementation process, therefore, enabling a wider use in general EM problems. A complete description of the method of weighted residuals through its application to equation 2.3 is presented in the following section.

2.3.2 The method of weighted residuals

The method of weighted residuals approximates the solution (e.g. $\mathcal{X}$ in equation 2.15) to the differential equation (Hohmann, 1987). The residual arises if the true solution in the differential equation is replaced with an approximate, i.e., numerical solution. Here, I aim to cast the Helmholtz equation (eq. 2.3) into the linear form seen in equation 2.15. The unknown parameter in the Helmholtz equation is the electric field, $\mathbf{E}$, vector. Assuming an approximate solution for the electric field, $\tilde{\mathbf{E}}$, the residual of equation 2.3 is written as follows,

$$\mathbf{r} = \nabla \times \nabla \times \tilde{\mathbf{E}} + i\omega\mu_0\sigma\tilde{\mathbf{E}} + i\omega\mu_0\mathbf{J_e^s} + \nabla \times \mathbf{J_m^s}, \tag{2.16}$$

where the parameter $\tilde{\mathbf{E}}$ is the approximated electric field. The weighted residuals method finds the best approximation for $\tilde{\mathbf{E}}$ by reducing the residual to its minimum value. In fact, it forces the inner-product statement, consisting of the inner product of the weight function, $\mathbf{W}$, and the residual to zero over the domain of the problem, Ω:

$$\int_\Omega \mathbf{W} \cdot \mathbf{r} \; d\Omega = \mathbf{0}. \tag{2.17}$$

Here the weighting function $\mathbf{W}$ is such that if the residual can be made to be orthogonal to $\mathbf{W}$ a good solution is obtained. Replacing the approximated residual in the above equations gives:

$$\begin{aligned}\int_{\Omega} \mathbf{W} \cdot (\nabla \times \nabla \times \tilde{\mathbf{E}})\, d\Omega \;+\; i\omega\mu_0 \int_{\Omega} \sigma \mathbf{W} \cdot \tilde{\mathbf{E}}\, d\Omega \;+ \\ i\omega\mu_0 \int_{\Omega} \mathbf{W} \cdot \mathbf{J^s_e}\, d\Omega \;+\; \int_{\Omega} \mathbf{W} \cdot \nabla \times \mathbf{J^s_m}\, d\Omega \;=\; \mathbf{0}.\end{aligned} \tag{2.18}$$

To extract the portion of the electric field due to the boundary effects the first integral in the left hand side of the above equation is integrated by parts:

$$\int_{\Omega} (\mathbf{W} \cdot \nabla \times \nabla \times \tilde{\mathbf{E}})\, d\Omega \;=\; \int_{\Omega} (\nabla \times \mathbf{W}) \cdot (\nabla \times \tilde{\mathbf{E}})\, d\Omega \;-\; \int_{\gamma+\Gamma} \mathbf{W} \times (\nabla \times \tilde{\mathbf{E}}) \cdot \mathbf{n}\, dS. \tag{2.19}$$

The surface integral here shows the behavior of the approximated electric field at the inner, γ, and outer, Γ, boundaries of the mesh. Here the behavior of the integrals at internal boundaries is of particular attention as the total conductivity model $\sigma(\mathbf{r})$ will break into cells of constant conductivities, therefore, many of these internal interfaces need to be considered. As explained later in this chapter, in order to satisfy the continuity of the tangential component of the electric field across the internal boundaries, edge-element basis functions are used. For the situation where the weight function is normal to the interface, the integrand $\mathbf{W} \times (\nabla \times \tilde{\mathbf{E}})$ is purely tangential to the face and therefore there would be no contribution from the surface integral term. In contrast, for a situation where the weight function is tangential to the face, the integrand $\nabla \times \tilde{\mathbf{E}}$ will have a normal and a tangential component to the face. Here by considering the true electric field instead of $\tilde{\mathbf{E}}$ and also using Faraday's law (e.g., equation 2.1 for a source free case) and the constitutive relation for the magnetic field, the integrand of the surface integral term would alter to $-i\mu_0\omega(\mathbf{W} \times \mathbf{H}) \cdot \mathbf{n}$. This integrand concerns the behavior of the vector $\mathbf{W} \times \mathbf{H}$ normal to the face. Through selection of an appro-

priate expression for the weight function (i.e. the edge-element basis function here) the vector $\mathbf{W}$ would also be continuous across the interface by construction. The vector $\mathbf{W} \times \mathbf{H}$ is normal to the face if the tangential component of $\mathbf{H}$ is considered. From the physical standpoint the tangential component of $\mathbf{H}$ is continuous across the faces shared between neighboring cells. Therefore the vector $\mathbf{W} \times \mathbf{H}$, which is normal to the face, would also be continuous. This indicates that, for a shared face, the contribution from the surface integral term from a particular cell would be cancelled by the corresponding surface integral term from the neighboring cell. According to the above argument the surface integral term in equation 2.19 is ignored and only the volume integral term resulting from the integration by parts $\int_\Omega (\nabla \times \mathbf{W}) \cdot (\nabla \times \tilde{\mathbf{E}})\ d\Omega$ is used. The outer boundary Γ is chosen to be sufficiently far from the source of excitation. This satisfies the Sommerfeld boundary condition (Sommerfeld, 1949) such that no energy reflects back into the conductive medium at the infinite boundary. This condition is further guaranteed by enforcing the surface integral term to zero at the outer boundaries of the mesh. Considering the above discussion, equation 2.18 changes to:

$$\begin{aligned} \int_\Omega (\nabla \times \mathbf{W}) \cdot (\nabla \times \tilde{\mathbf{E}})\ d\Omega \ + \ i\omega\mu_0 \int_\Omega \sigma \mathbf{W} \cdot \tilde{\mathbf{E}}\ d\Omega \ + \\ i\omega\mu_0 \int_\Omega \mathbf{W} \cdot \mathbf{J_e^s}\ d\Omega \ + \ \int_\Omega \mathbf{W} \cdot \nabla \times \mathbf{J_m^s}\ d\Omega \ = \ \mathbf{0}. \end{aligned} \tag{2.20}$$

It is equation 2.20 that is discretized using the finite-element method.

2.3.3 Elemental basis functions in tetrahedral elements

The initial step in the numerical solution of equation 2.20 calls for the subdivision of the solution space into finite elements. Because of the reasons mentioned in Chapter 1, the computational domain is subdivided into unstructured tetrahedral elements.

Choosing an appropriate space of functions for the geometric subdomains is the second step in using the finite-element method. The usual choice for such spaces is piecewise polynomials, which are convenient to employ. The approximated electric field is expressed in terms of a series of polynomials, namely the basis functions, in each element:

$$\tilde{\mathbf{E}}(\mathbf{r}) = \sum_{j=1}^{n} \mathbf{N}_j(\mathbf{r})\ E_j \tag{2.21}$$

where $\mathbf{N}_j$ is the basis function; the expansion coefficients E_j are the unknown functionals or degrees of freedom (Monk, 2003; Ciarlet, 1978). Also, the parameter n is the number of edges in each tetrahedron for which the approximations are performed i.e., the number of basis functions. Substituting the above equation into equation 2.20 gives:

$$\begin{aligned} \sum_{j=1}^{n}\ E_j \int_{\Omega} (\nabla \times \mathbf{W}) \cdot (\nabla \times \mathbf{N}_j)\ d\Omega\ +\ i\omega\mu_0 \sum_{j=1}^{n} E_j \int_{\Omega} \sigma \mathbf{W} \cdot \mathbf{N}_j\ d\Omega\ = \\ -\ i\omega\mu_0 \int_{\Omega} \mathbf{W} \cdot \mathbf{J}^{\mathbf{s}}_{\mathbf{e}}\ d\Omega\ -\ \int_{\Omega} \mathbf{W} \cdot \nabla \times \mathbf{J}^{\mathbf{s}}_{\mathbf{m}}\ d\Omega \end{aligned} \tag{2.22}$$

In the above equation the coefficients E_j are the parameters to be determined. Using equation 2.21 the FE method formulates each of the integral terms in equation 2.20 using piecewise polynomial functions in each cell, Ω (Monk, 2003). For the inner-product terms in equation 2.22 to be integrable or well-defined an appropriate choice for the basis and weight functions are required. Here, the basis function is assumed to vary linearly in each element. Also among different methods of choosing the weighting function, $\mathbf{W}$, the Galerkin method is used for which the weighting function is equated to the basis function:

$$\mathbf{W} = \mathbf{N}. \tag{2.23}$$

Before solving equation 2.22 using the finite-element method, an introduction to the construction of basis functions is necessary. Two types including scalar and vector basis functions and their properties are discussed below.

2.3.3.1 Scalar basis functions

An arbitrary function, $E(\mathbf{r})$, in each tetrahedral element can be approximated using first-order (linear) polynomials:

$$E^e(x, y, z) = a^e + b^e x + c^e y + d^e z, \tag{2.24}$$

where the superscript e indicates the relevant element considered here. The coefficients a, b, c, and d are parameterized by enforcing the equation 2.24 at the four vertices (nodes) of a tetrahedral element and solving the system of equations for the coefficients. For example, the expression obtained for the coefficient a^e is shown below,

$$a^e = \frac{1}{6V^e} \begin{vmatrix} \phi_1^e & \phi_2^e & \phi_3^e & \phi_4^e \\ x_1 & x_2 & x_3 & x_4 \\ y_1 & y_2 & y_3 & y_4 \\ z_1 & z_2 & z_3 & z_4 \end{vmatrix} \tag{2.25}$$

where V^e is the volume of each tetrahedral element. Expressions for three other coefficients are also derived. (A complete description can be found in Appendix A.) By substituting equation 2.25 and the similar expressions given for the coefficients b^e, c^e, and d^e into equation 2.24 the following equation is obtained,

$$E^e(\mathbf{r}) = \sum_{k=1}^{4} N_k^e(\mathbf{r})\ E_k, \tag{2.26}$$

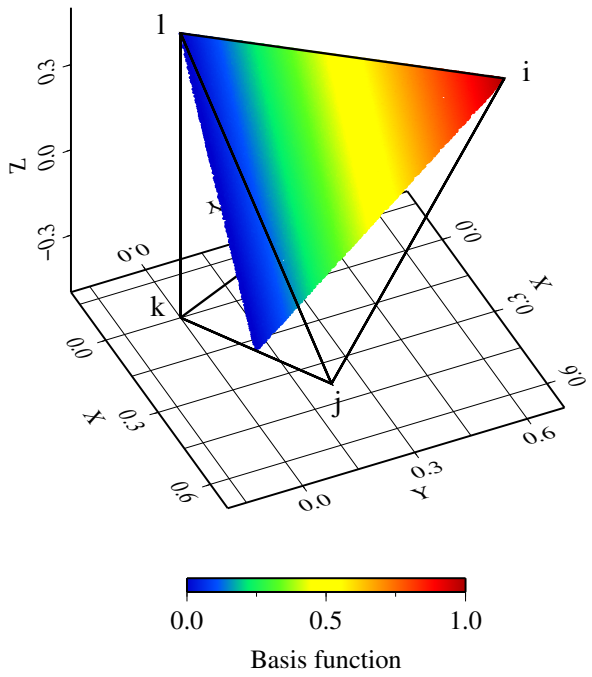

Figure 2.3: Scalar plots of three-dimensional scalar basis function for the i^{th} node, i.e., N_i^e, over an arbitrary plane inside the tetrahedron.

where N_k is the value of the basis function associated with the kth node (vertex) in an arbitrary location in the element:

$$N_k^e(x, y, z) = \frac{1}{6V^e}(a_k^e + b_k^e x + c_k^e y + d_k^e z) \tag{2.27}$$

(see Appendix A for the parameterized expressions of a_k^e, b_k^e, c_k^e, and d_k^e). Figure 2.3 shows the variation of the scalar basis function for the node i, i.e., N_i^e over a plane inside a typical tetrahedral element. It can be seen that N_i^e has a maximum value of 1 at the location of the i^{th} node and linearly reduces towards the other nodes (j, k, and l) in the tetrahedron. In fact, the arbitrary function E^e in equation 2.24 approaches its nodal value, E_i at node i. Also the basis function N_i^e vanishes to zero at the face $[j, k, l]$ opposite to the i^{th} node. Figure 2.4 shows the scalar basis function for a node located on an inter-element face shared by two adjacent cells. Here, the basis

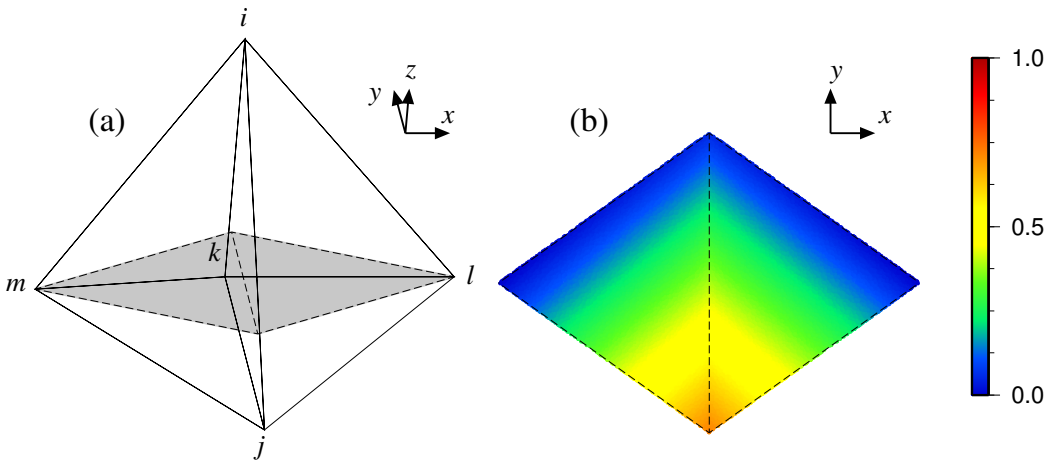

Figure 2.4: Scalar plot of the basis function for the j^{th} node shared by two neighbor tetrahedrons ($[i, j, k, l]$ and $[i, j, k, m]$).

function is calculated on the gray-shaded plane shown in panel (a). For this plane the continuity of the nodal basis function, N_j, from the left to the right cell is indicated in panel (b). It is seen here that the basis function reduces in magnitude away from the j^{th} node in all directions.

2.3.3.2 Vector basis functions

The vector basis functions (edge elements) assign the degrees of freedom to the edges of a particular tetrahedron. These functions were first introduced in Whitney (1957), and further discussed in Nédéléc (1980) for their application to tetrahedral elements. By using edge elements the basis functions are purely constrained along the edges of a particular element. Considering a particular edge j with length ℓ_j and with two nodes ($j1$ and $j2$) at either ends, the lowest-order edge elements are used here:

$$\mathbf{N}_j = \ell_j(N^e_{j1}\nabla N^e_{j2} - N^e_{j2}\nabla N^e_{j1}), \tag{2.28}$$

where N_{j1} and N_{j2} are the scalar basis functions for the $j1$ and $j2$ nodes respectively. Figure 2.5 shows the vector basis function related to two neighboring identical cells.

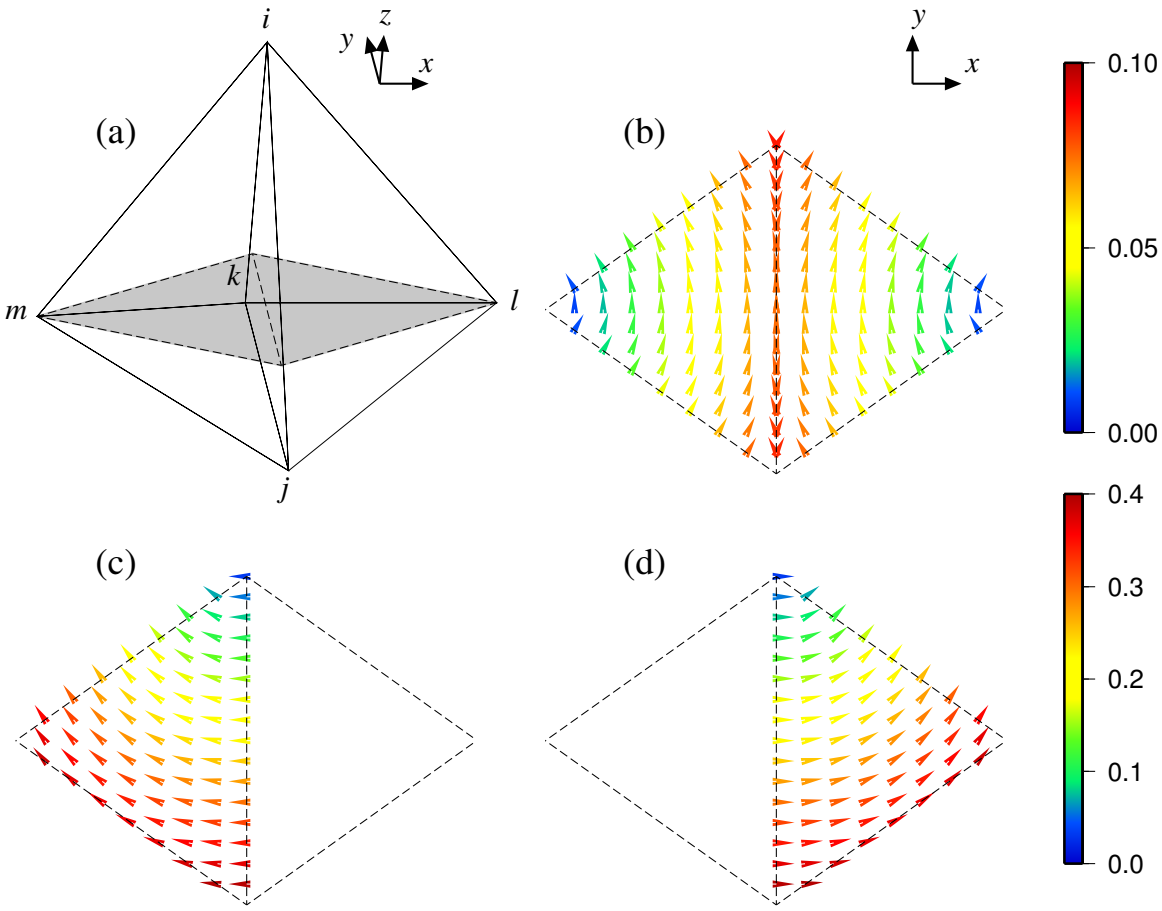

Figure 2.5: Vector plots for the basis functions for two identical neighbors: left (i, j, k, m) and right (i, j, k, l) cells. The plots are for the gray colored plane shown in panel (a). Panel (b) shows the projection of $\mathbf{N}_{ji}$ onto the gray plane for two cells. Panels (c) and (d) respectively show the projection of the vector basis functions $\mathbf{N}_{jm}$ and $\mathbf{N}_{jl}$ onto the gray plane.

Here, panel (b) shows the projection of the vector basis function $\mathbf{N}_{ji}$ on the gray-shaded plane in panel (a). Arrows are colored in terms of the magnitude of the basis function. It is seen here that the intensity of the basis function reduces linearly away from the central shared face. Also the vector $\mathbf{N}_{ji}$ is purely tangential to the dashed line at the center, i.e., the shared face, and its tangential component is continuous across the entire interface. However this vector begins to obtain a small normal component away from the center of the shared interface. Moreover, panels (c) and (d) respectively

show the behavior of the vector basis functions from edges jm and jl in the dashed plane. It is seen that these edge elements only posses normal components across the shared interface.

2.3.3.3 Discussion on scalar and vector basis functions

In order to satisfy the interface conditions within the finite-element solution of the Helmholtz equation, it is important that a proper choice for the basis functions is made. As illustrated above the scalar basis function is continuous across the interface shared by two neighboring cells. Therefore, choosing scalar basis functions to express each of the components of the approximate electric field in equation 2.26 results in the continuity of both tangential and normal components of the approximate electric field on the interface. When considering different conductivities for adjacent cells, the interface discontinuity condition for the normal component of the approximate electric field is then violated. Also, as a result of $\nabla \cdot N \neq 0$, nodal elements used for approximating the components of the electric field fail to satisfy the divergence condition of $\nabla \cdot \mathbf{E} = 0$ in a source free cell. Therefore if each component of the electric field is expressed as equation 2.26, then the divergence of the electric field is not necessarily zero within a tetrahedron. As a type of basis functions that is aligned with the edges, edge elements satisfy the continuity of the tangential component of the electric field while allowing the normal component to jump across the inter-element boundaries between cells with different electrical conductivities. Also, as a significant property, the divergence of the vector basis function is zero within each cell, $\nabla \cdot \mathbf{N} = 0$, which satisfies the condition that the approximate electric field should also be divergence free. In the following section by replacing edge elements for both the weight and basis functions in equation 2.22 the system of equations is discretized.

2.3.4 Discretization

Replacing the vector basis function for the weight functions in equation 2.22 and expanding the equation over the entire tetrahedralized mesh gives,

$$\sum_{j=1}^{N_{edges}} E_j \int_\Omega (\nabla \times \mathbf{N}_i) \cdot (\nabla \times \mathbf{N}_j)\ d\Omega \ + \ i\omega\mu_0 \sum_{j=1}^{N_{edges}} E_j \int_\Omega \sigma \mathbf{N}_i \cdot \mathbf{N}_j\ d\Omega \ = \\ - \ i\omega\mu_0 \int_\Omega \mathbf{N}_i \cdot \mathbf{J^s_e}\ d\Omega \ - \int_\Omega \mathbf{N}_i \cdot \nabla \times \mathbf{J^s_m}\ d\Omega. \tag{2.29}$$

Each of the inner product integrals in the above equation is calculated using the expression given in equation 2.28 for the basis functions. Depending on the approach considered for constructing the EM excitation sources, only one of the terms on the right hand side of the above equation need be used. Here, for the situations where current lines are utilized to construct electric sources (e.g. an electric dipole and a line of current) and magnetic sources (e.g. small and large rectangular loops), only the first term on the right-hand side exists in the system. The second term however vanishes as no point source is used. In contrast, for the case where a point magnetic source represents a hypothetical magnetic dipole, only the second term on the right-hand side remains while the first term vanishes. After splitting the unknown coefficient, E_j, into real and imaginary parts the following system is obtained in the form shown in equation 2.15:

$$\begin{pmatrix} \mathbf{C} & -\omega\mu_0\mathbf{D} \\ \omega\mu_0\mathbf{D} & \mathbf{C} \end{pmatrix} \begin{pmatrix} \tilde{E}^R \\ \tilde{E}^I \end{pmatrix} = \begin{pmatrix} S_1 \\ -\omega\mu_0 S_2 \end{pmatrix} \tag{2.30}$$

where $C_{ij} = \int_\Omega (\nabla \times \mathbf{N}_i) \cdot (\nabla \times \mathbf{N}_j)\ d\Omega$ and $D_{ij} = \int_\Omega \sigma\ \mathbf{N}_i \cdot \mathbf{N}_j\ d\Omega$ are the interactions between the vector basis functions. Also, $S_1 = \int_\Omega \mathbf{N}_i \cdot \nabla \times \mathbf{J^s_m}\ d\Omega$ and $S_2 = \int_\Omega \mathbf{N}_i \cdot \mathbf{J^s_e}\ d\Omega$ are the interactions between the vector basis functions and the source functions. $\tilde{E}^R$

and $\tilde{E}^I$ are the real and imaginary parts of the approximate electric field. Given the particular choice for the edge elements closed-form formulae for these integrals are derived (see Appendix B).

In preparation for solving the above system, the Dirichlet boundary condition for the electric field is implemented on the outer boundaries of the mesh. On the boundary, Γ, equation 2.14 changes to $\mathbf{n} \times \mathbf{E} = E_j$. Here the subscript j is associated with a particular edge on the outer boundary of the mesh. In order to force this coefficient to its theoretical zero value on the outer boundary, the particular element on the row of the coefficient matrix that corresponds to that edge located on the truncation boundary of the mesh is set to zero except for the diagonal element (Jin, 2002). Also the element in the corresponding row of the source vector on the right-hand side of equation 2.30 is set to zero. However the elimination of these rows and their corresponding coefficients in the vector of unknowns was not found to be necessary.

2.3.5 Solution of the discretized system

Although the coefficient matrix on the left hand side of equation 2.30 is sparse it nevertheless occupies large memory space in the computer for typical number of edges. Hence it is computationally expensive to solve the system using a direct solver. In order to avoid this problem, the system is solved using an iterative solver. GMRES (Generalized minimum residual) from SPARSKIT (Saad, 1990) is used here. The iterative solver BCGSTAB (Bi-conjugate gradient stabilized) (Saad, 1990) was also tried as the iterative solution. It however failed to solve the system for the variety of modeling problems considered in this thesis. The preconditioner to the linear system is an incomplete LU decomposition of the coefficient matrix (e.g., $\mathcal{L}$ in equation 2.15). The maximum number of non-zero elements in each row of both the triangular L and

U matrices is given using the fill-in parameter.

In the following sections equation 2.30 will be solved for different examples where electric and magnetic sources are used.

2.4 Examples

2.4.1 Conductive whole-space problem

For the simplest example the problem of a harmonic magnetic dipole located at the origin of a conductive whole space is considered here. The magnetic dipole is constructed firstly using a point source and secondly using a small loop of current.

2.4.1.1 A magnetic point source

In the following example the problem of an infinitesimal magnetic dipole, which is represented by a point source, located at the center of a conductive whole-space is considered. The magnetization vector due to a vertical magnetic dipole with a dipole moment of m and located at (x_0, y_0, z_0) is given by the following expression,

$$\mathbf{M} = m\ \delta(x - x_0)\delta(y - y_0)\delta(z - z_0)\ \hat{\mathbf{z}}, \tag{2.31}$$

where the parameter δ represents the delta function. This equation can be connected to the magnetic source current density, $\mathbf{J}_m^s$, through the following equation (Ward and Hohmann, 1988),

$$\mathbf{J}_m^s = i\omega\mu_0\ \mathbf{M}. \tag{2.32}$$

Substituting equations 2.31 and 2.32 into the source term S_1 gives,

$$S_1 = -i\omega\mu_0 \int_\Omega \mathbf{N}_i \cdot \nabla \times \mathbf{M}\, d\Omega. \tag{2.33}$$

To counteract the difficulty of calculating the curl of the delta function here, the First Vector Green's Theorem is used to modify the above integral into the combination of a surface and a volume integral:

$$S_1 = i\omega\mu_0 \Big(\int_S \mathbf{N}_i \times \mathbf{M} \cdot \mathbf{n}\, dS \; - \; \int_\Omega \mathbf{M} \cdot \nabla \times \mathbf{N}_i \, d\Omega \Big). \tag{2.34}$$

Because the source point is taken here to be located inside a particular tetrahedron, the surface integral term in the above equation is cancelled to zero. The closed-form formula for S_1 is presented in Appendix B. Also, the parameter S_1 in equation 2.34 is purely imaginary; therefore, for this example equation 2.30 changes to:

$$\begin{pmatrix} \mathbf{C} & -\omega\mu_0\mathbf{D} \\ \omega\mu_0\mathbf{D} & \mathbf{C} \end{pmatrix} \begin{pmatrix} \tilde{E}^R \\ \tilde{E}^I \end{pmatrix} = \begin{pmatrix} 0 \\ S_1 \end{pmatrix}. \tag{2.35}$$

Once the above system has been solved for the real and imaginary parts of the electric field, the magnetic field is obtained using equation 2.1. In particular, the magnetic field is calculated by taking the curl of the electric field and using the edge-element basis functions:

$$\mathbf{H} = \frac{-1}{i\omega\mu_0} \sum_{j=1}^{N_{edges}} \tilde{E}_j \nabla \times \mathbf{N_j}. \tag{2.36}$$

The problem presented here concerns the behavior of the magnetic field due to an infinitesimal magnetic dipole. Figure 2.6 shows the geometry of the problem in which a source point is located at the origin of a conductive whole-space of 0.01 S/m. The

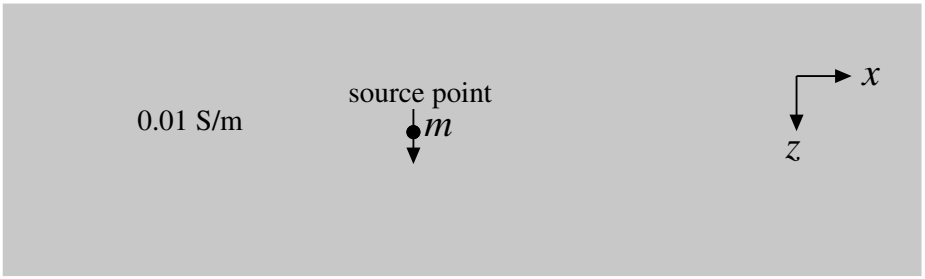

Figure 2.6: The geometry of the conductive whole-space for the first example. A small magnetic dipole with a moment m is located at the origin. Observation points are along the x-axis.

magnetization vector due to the point source is positive in the z-direction with a dipole moment equal to unity. The computational domain is meshed into Delaunay tetrahedral elements using the TetGen library (Si, 2007) (for a full description of the unstructured mesh generation see Appendix C). The quality of the generated mesh is guaranteed by carefully choosing a reasonable maximum (e.g., 1.414 here) for the radius-edge (aspect) ratio and dihedral angles (Si, 2007). Figure 2.7 shows a view of the entire meshed domain. It is seen here that the tetrahedral elements are small at the central part and gradually increase in size towards the truncation boundaries of the mesh. Also, as illustrated in Figure 2.8, in order to accurately compute the behavior of the EM fields the mesh is locally refined about the source and observation locations. For this refinement the source point lies inside an individual tetrahedron at the center of the mesh. The volume of this tetrahedron is 1.121×10^{-5} m^3. Also, the average size of edges for this cell is 0.05761 m. The dimension of the whole mesh is 50 km $\times$ 50 km $\times$ 50 km. To maintain a balance between the number of elements and the accuracy of the solution an aspect ratio of 1.414 with a reasonable dihedral angle (i.e., 16 degrees here with the maximum quality dihedral angle as 18 degrees) is chosen. The number of cells, nodes and edges for the generated mesh are 661613, 108298 and 770305 respectively which results in 1757206 unknowns in the system of

equations. In particular, the total number of unknowns is twice (e.g., because of real and imaginary parts) the total number of edges and nodes combined. A Krylov subspace of 200 for the GMRES solver and a fill-in factor of $lfil = 3$ (Saad, 2003) for the ILUT preconditioner were used.

Figure 2.9 shows the z-component of the total magnetic field at locations along the x-axis for frequencies of 3 and 300 Hz. The data shown by the circles are the fields produced using the E-field finite-element approach mentioned above. The curves shown in red are calculated using the analytic formula of Ward and Hohmann (1988). For the frequency of 3 Hz the mesh shown in Figure 2.7 is used. The mesh used for the frequency of 300 Hz consists of 660491 cells, 107922 nodes, and 768795 edges. It is seen here that the data calculated from the E-field approach does not agree well with the analytic solutions for both frequencies of 3 and 300 Hz. The erroneous behavior of the magnetic field especially for the imaginary parts is due to the slow convergence of the E-field solution. The preconditioned residual norms of the iterative solver for these runs are shown in Figure 2.10. According to Saad (2003) the GMRES approximation is a vector that minimizes the function $||Ax - b||$. The preconditioned residual norm is intrinsically provided during the iterative procedure by SPARSKIT solvers. In particular GMRES provides the current (absolute) residual norm once the iterative process is terminated. Here despite a rapid reduction of the residual norm for the first 500 iterations it struggles to decrease for higher iterations of the iterative solver. In fact, residual norms of approximately 10^{-12} and 10^{-8} for, respectively, frequencies of 3 and 300 Hz are not adequate for the iterative solution process to have converged to the correct solution of the system of equations. The computations were done on a HP workstation with 2.8GHz 6-core Intel processors and 24GB of memory The computation time for solving the system of equations was roughly an hour for

10000 iterations of the iterative solver. The results shown here are the best obtained after investigating a variety of meshes and solver parameters.

2.4.1.2 A small loop of current

An infinitesimal magnetic dipole can also be represented by a small loop of current. For this scenario the excitation source can be constructed using a rectangular wire. Here the current source is used, therefore, only the source term S_2 has to be considered in equation 2.39 and the contribution from the source term S_1 vanishes. For a particular element of the current line (which passes through a particular cell in the mesh in a specific orientation) the current density, $\mathbf{J}_e^s$, is expressed using a combination of the Heaviside and delta functions. For a current element for example in the x-direction:

$$\mathbf{J}_e^s = I\Big(\mathcal{H}(x_{i+1}) - \mathcal{H}(x_i)\Big)\ \delta(y-y_0)\delta(z-z_0)\ \hat{\mathbf{x}}, \tag{2.37}$$

where I is the scalar current running in the wire. The operator $\mathcal{H}$ represents the Heaviside function, and x_i and x_{i+1} are x coordinates for the endpoints of the wire segment. Also, because there is no current running in the y- and z-directions perpendicular to the current line the delta function is used here. Using the above expression the source term in the ith element of S_2 is formulated as:

$$(S_2)_i = I\ \int_\Omega \mathbf{N}_i \cdot \Big(\mathcal{H}(x_{i+1}) - \mathcal{H}(x_i)\Big)\ \delta(y)\delta(z)\ \hat{\mathbf{x}}\ d\Omega, \tag{2.38}$$

(for the closed-form expression see Appendix B) and the discretized form of the system of equations is formed:

$$\begin{pmatrix} \mathbf{C} & -\omega\mu_0\mathbf{D} \\ \omega\mu_0\mathbf{D} & \mathbf{C} \end{pmatrix} \begin{pmatrix} \tilde{E^R} \\ \tilde{E^I} \end{pmatrix} = \begin{pmatrix} 0 \\ -\omega\mu_0 S_2 \end{pmatrix}. \tag{2.39}$$

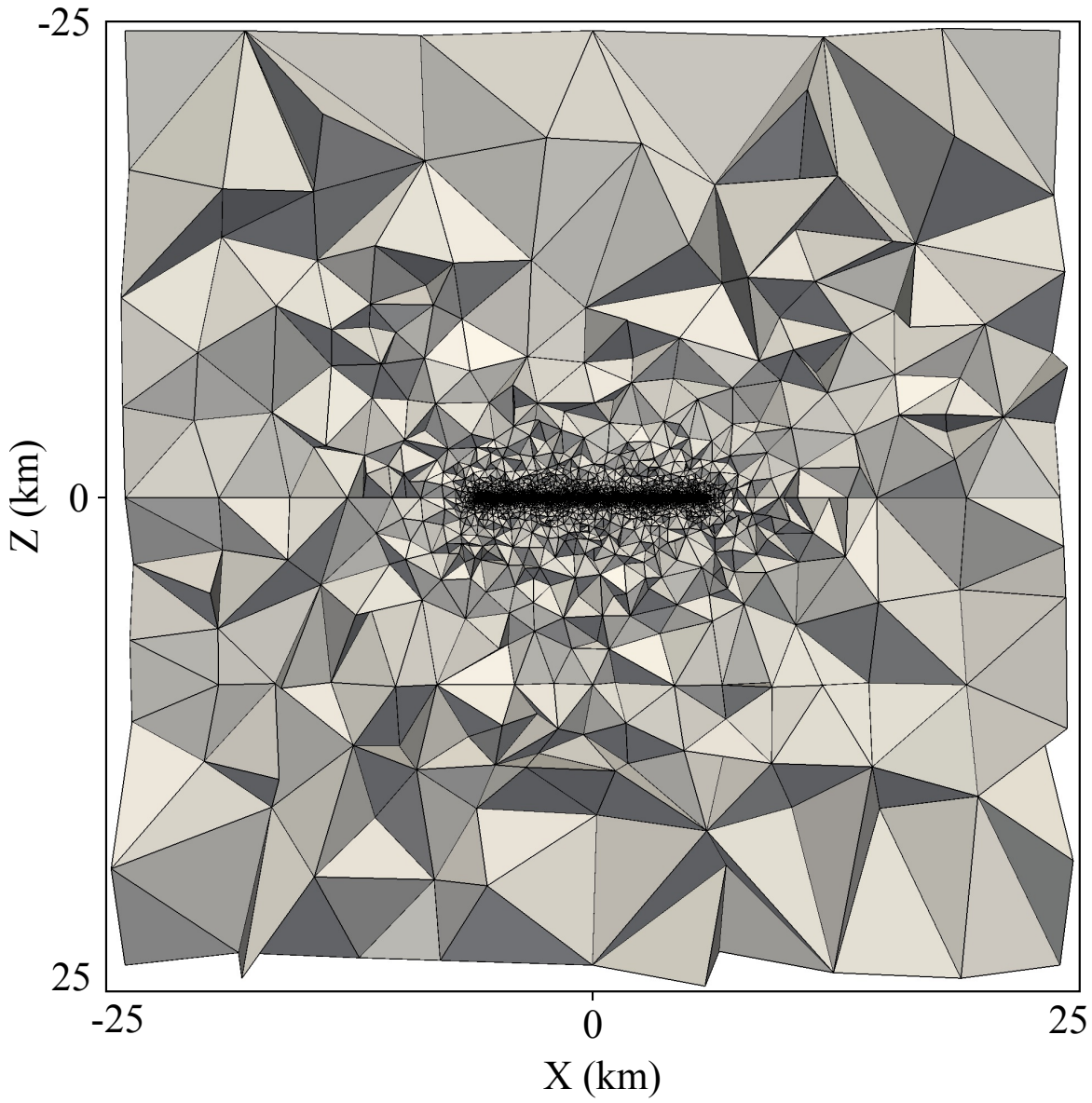

Figure 2.7: The entire xz-section through the center of the tetrahedral mesh used for the conductive whole-space model.

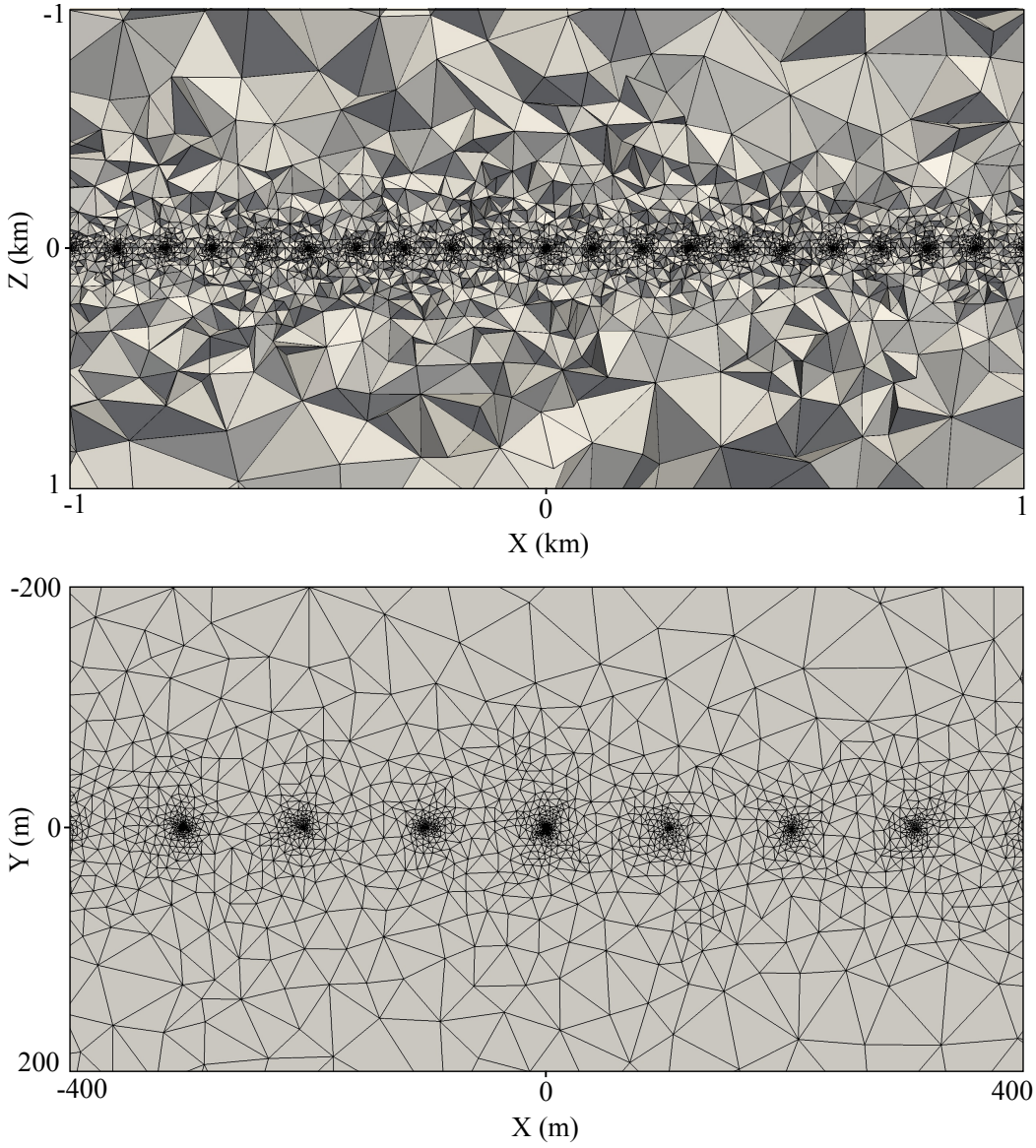

Figure 2.8: An enlarged xz (top) and xy (bottom) view of the central part of the tetrahedral mesh used for the conductive whole-space model. The mesh is refined about the source point at the origin and around observation locations

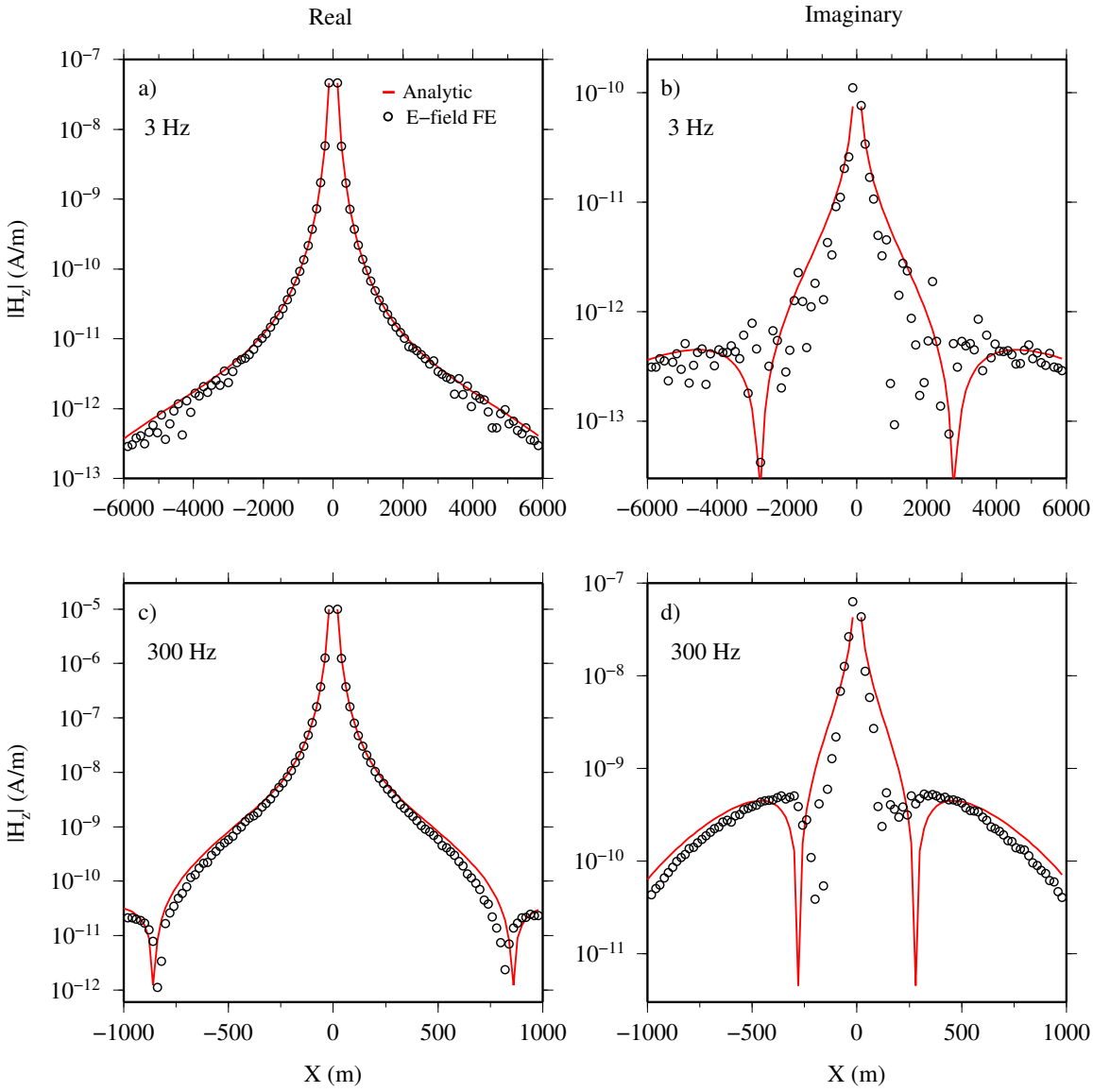

Figure 2.9: The real and imaginary parts of the z-component of the magnetic field, H_z, for two frequencies for the whole-space model of 0.01 S/m using a point magnetic dipole source. Circles and solid lines in each panel are magnetic fields calculated using the E-field finite-element method and the analytic formula of Ward and Hohmann (1988) respectively.

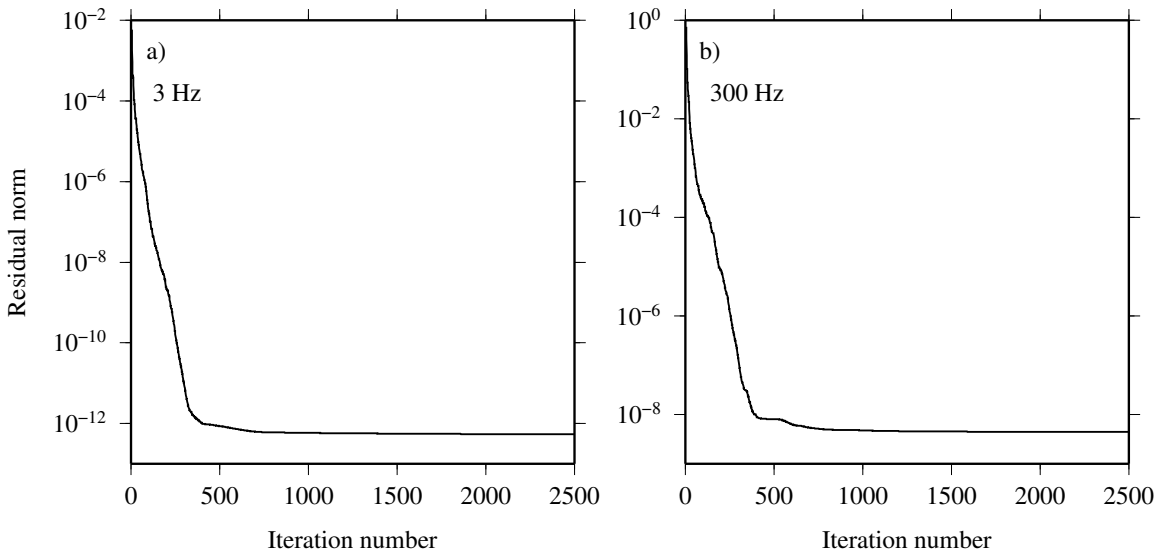

Figure 2.10: The convergence curves for the E-field solutions for frequencies of 3 and 300 Hz for the conductive whole-space model of 0.01 S/m. Data are the residual norms provided by the GMRES solver that was used.

The above equation is again solved for the real and imaginary parts of the electric field.

For the same mesh and the same frequencies and parameters for the iterative solver as used in the previous example, the above system of equations is solved. Here the loop source with a positive magnetic moment is placed at the origin. The size of the rectangular loop is $10^{-6} \times 10^{-6}$ m in the x- and y-directions. The source is enclosed by a particular cell at the center. Figure 2.11 shows the z-component of the total magnetic field. Again the data shown using circles are the finite-element E-field solutions at the observation locations along the x-axis. Figure 2.12 shows the preconditioned residual norm of the iterative solver for these runs. Here the poor convergence of the iterative solver for both frequencies of 3 and 300 Hz causes erroneous magnetic fields and a poor match with the analytic solutions as observed in Figure 2.11.

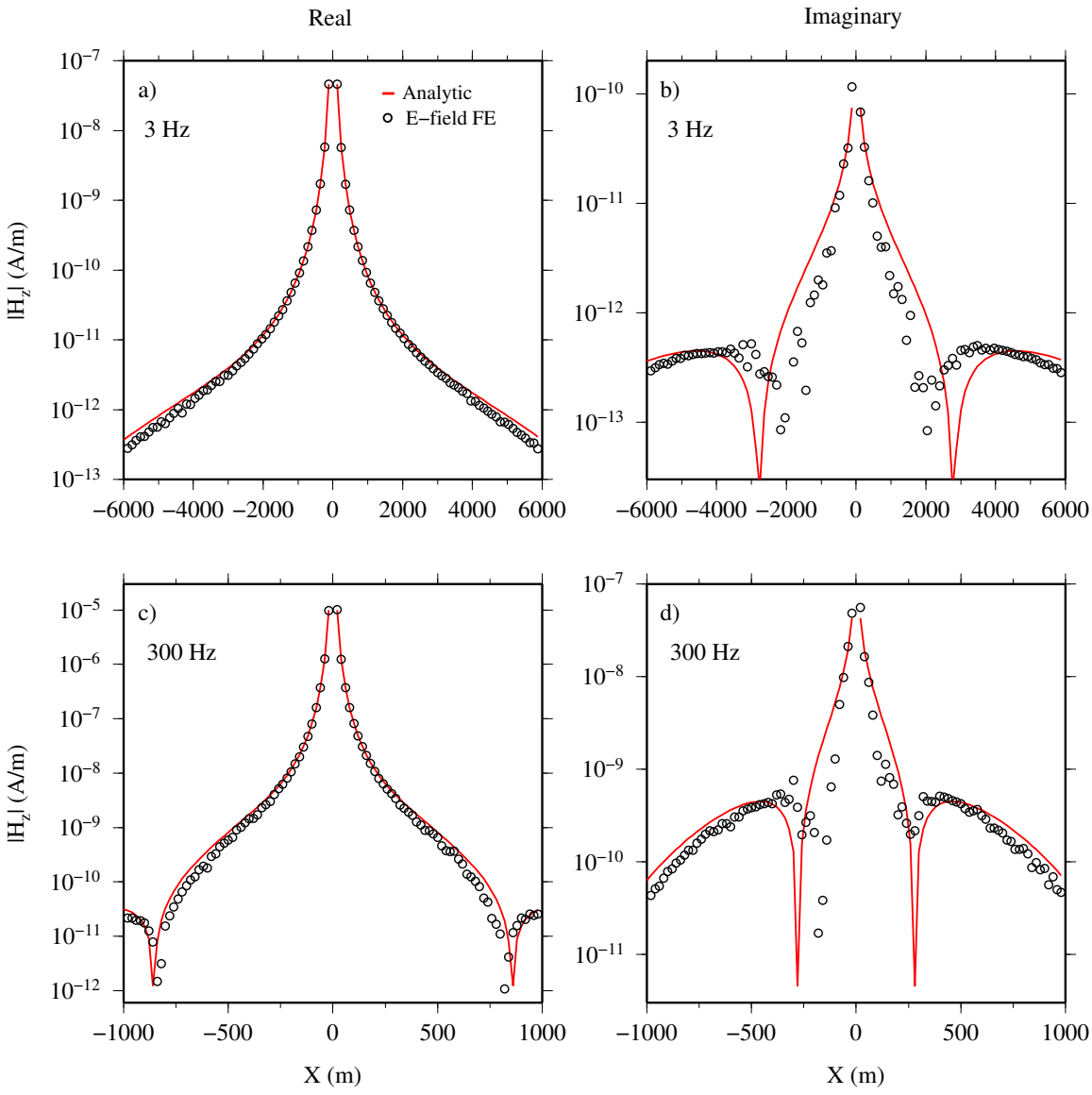

Figure 2.11: The real and imaginary parts of the z-component of the magnetic field, H_z, for two frequencies for the whole-space model of 0.01 S/m using a small loop as the magnetic dipole source.

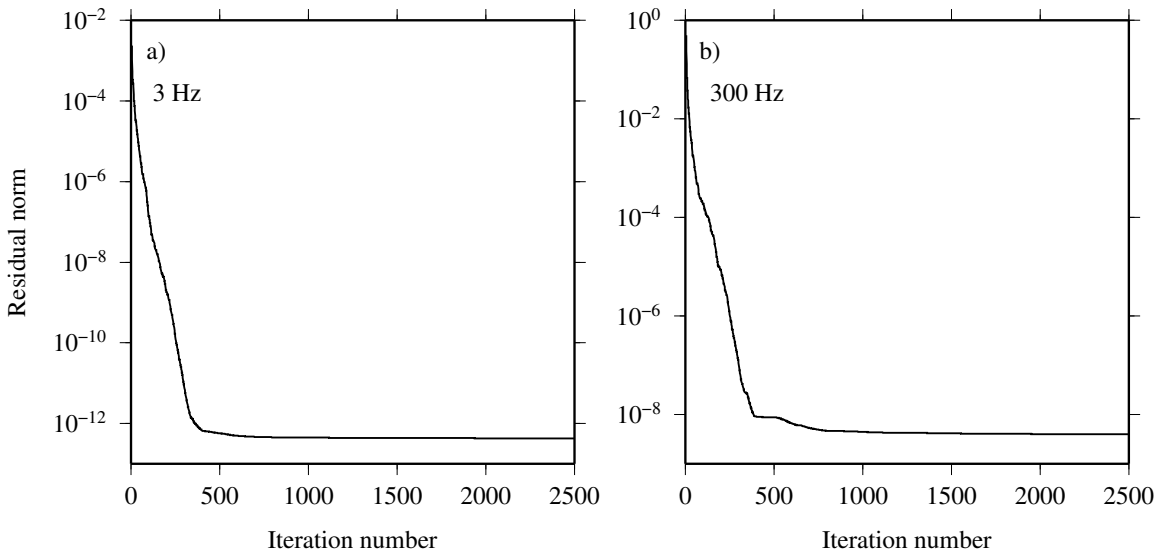

Figure 2.12: The convergence curves for the E-field solutions for frequencies of 3 and 300 Hz for the conductive whole-space model of 0.01 S/m.

2.4.2 Conductive half-space problem

In a realistic geophysical scenario the air layer needs to be considered in the model. Here, for the analogous examples presented in the previous section but with both the resistive air and the conductive Earth considered, the solution to the E-field equation is investigated.

For the mesh shown in Figure 2.7 but with the air layer for $z < 0$ the E-field equation is solved for a magnetic dipole point source. The conductivity of the air is 10^{-8} S/m. Again the iterative solver GMRES with a dimension of 200 for the Krylov subspace along with the ILUT preconditioner is used. Figures 2.13 and 2.14 show the magnetic field due to a source point and a small loop respectively. Again it is seen here that the finite-element E-field approach gives a poor match between the numerical and analytic solutions for the half-space problems.

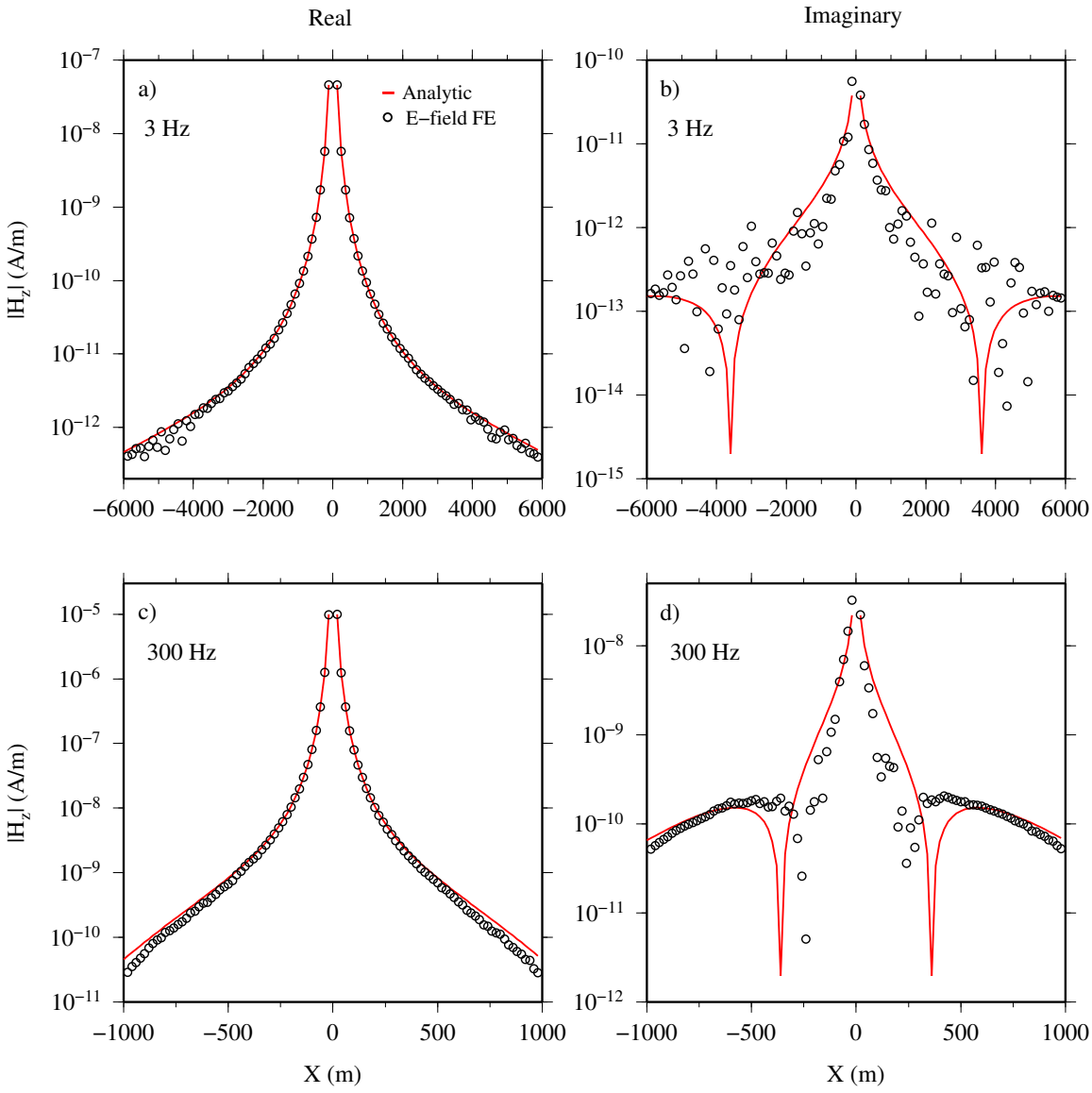

Figure 2.13: The real and imaginary parts of the z-component of the magnetic field, H_z, for the point source for two frequencies for the half-space model of 0.01 S/m.

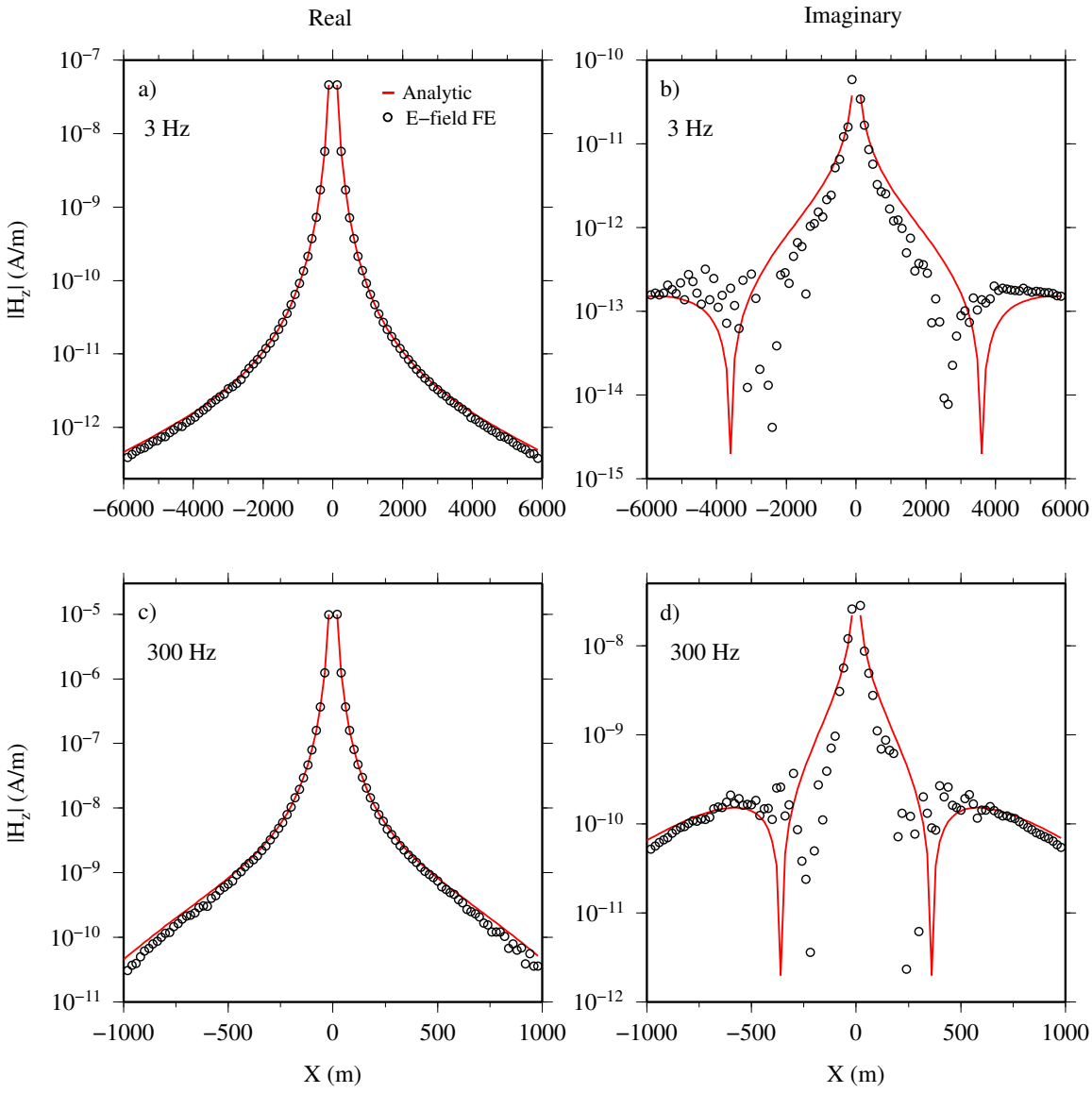

Figure 2.14: The real and imaginary parts of the z-component of the magnetic field, H_z, for the small loop source for two frequencies for the half-space model of 0.01 S/m.

2.5 The weakness of the E-field system and direct solution

As demonstrated in the above examples the finite-element iterative solution to the stand-alone total E-field system for low frequencies and for unstructured meshes does not necessarily simulate an adequate response for the electric field in a conductive medium. In particular, because of the small ω that is the consequence of the low frequencies used by EM exploration methods in geophysics, the coupling between $\mathbf{E}$ and $\mathbf{H}$ reduces in the two curl Maxwell's equations (equations 2.1 and 2.2). For these circumstances, electric charges become more important in distorting the electric field in the conductive medium as frequency decreases (West and Macnae, 1991). In this situation the electric field is maintained by the equation of conservation of charge:

$$\nabla \cdot \mathbf{J} = \begin{cases} -\nabla \cdot \mathbf{J}^s & \text{at the source location,} \\ 0 & \text{otherwise,} \end{cases} \tag{2.40}$$

where $\mathbf{J}(\mathbf{r}, \omega)$ is the current density and is connected to the electric field by Ohm's law: $\mathbf{J} = \sigma\mathbf{E}$. Here, from the physical standpoint, the electric field in equation 2.3 is anticipated to implicitly fulfill the above-mentioned divergence equation. In fact equation 2.40, scaled by the angular frequency ω, can be produced by taking the divergence of the E-field equation:

$$i\omega\mu_0 \ \nabla \cdot (\sigma\mathbf{E}) = -i\omega\mu_0 \ \nabla \cdot \mathbf{J}_e^s. \tag{2.41}$$

As a difficulty for an absolute frequency of zero (which causes $\omega = 0$) equation 2.41 is of no use. Also for a zero frequency the E-field equation alters to $\nabla \times \nabla \times \mathbf{E} = 0$, which results in a non-unique solution for the electric field. Therefore there is a unique

solution for the electric field only for non-zero frequencies ($\omega \neq 0$). The instability of the E-field equation (see equation 2.3) to give an adequate solution for the low frequencies (near to the geophysical zero limit) of 3 and 300 Hz used in the examples in Section 2.4 is analogous because of the vanishing conductivity term $\omega\mu_0\sigma\mathbf{E}$.

The difficulties mentioned above can be rectified by solving the E-field equation in conjunction with the divergence equation (equation 2.40). The E-field Helmholtz equation is discretized using an edge-element expansion because of reasons given in Section 2.3.3.3. As a difficulty here FE solution of $\nabla \cdot \mathbf{J} = 0$ is not feasible using edge elements but requires nodal-element expansion of $\mathbf{E}$. These solution difficulties observed in this section can be mitigated using direct solvers to solve the E-field Helmholtz equation as explained in the next section.

2.5.1 Direct solution

Direct solvers can be used as a quick remedy for correctly solving the E-field Helmholtz equation. Here I used the public domain sparse direct solver library, MUMPS, Multifrontal Massively Parallel Solver (Amestoy et al., 2001; Amestoy et al., 2006). MUMPS is a solver package that can be used for solving sparse systems of the form seen in equation 2.15 in a memory efficient manner. Based on a multifrontal approach MUMPS uses a direct method and depending on the characteristics of the sparse system performs either a LU or a LDL^T factorization. Here I used MUMPS in the double precision arithmetic configuration and in sequential mode.

The problem of poor results for the magnetic dipole (e.g., a point source) in a conductive half-space presented in Section 2.5.1 is resolved using MUMPS. Figure 2.15 shows a comparison of the solutions obtained using the direct and iterative solvers.

Here in contrast to the incorrect iterative solutions (shown in black circles), the direct solver provides correct estimations (shown in blue triangles) of the magnetic fields for both frequencies of 3 and 300 Hz. The computation times for these runs were 490 and 536 seconds for frequencies of 3 and 300 Hz respectively. Despite the correct answer obtained here the direct solver uses a significant amount of memory space in the computer. For the meshes used here (see Section 2.4.1.1) the memory usage was 18.5 and 19.5 Gbytes for 3 and 300 Hz respectively.

With the intention of obtaining the correct EM response using an iterative solver, allowing larger Earth models to be considered, the electromagnetic field is treated indirectly by using the vector-scalar potential field formulation instead of the direct electric or magnetic fields. The formulation of this approach will be discussed in Chapter 3.

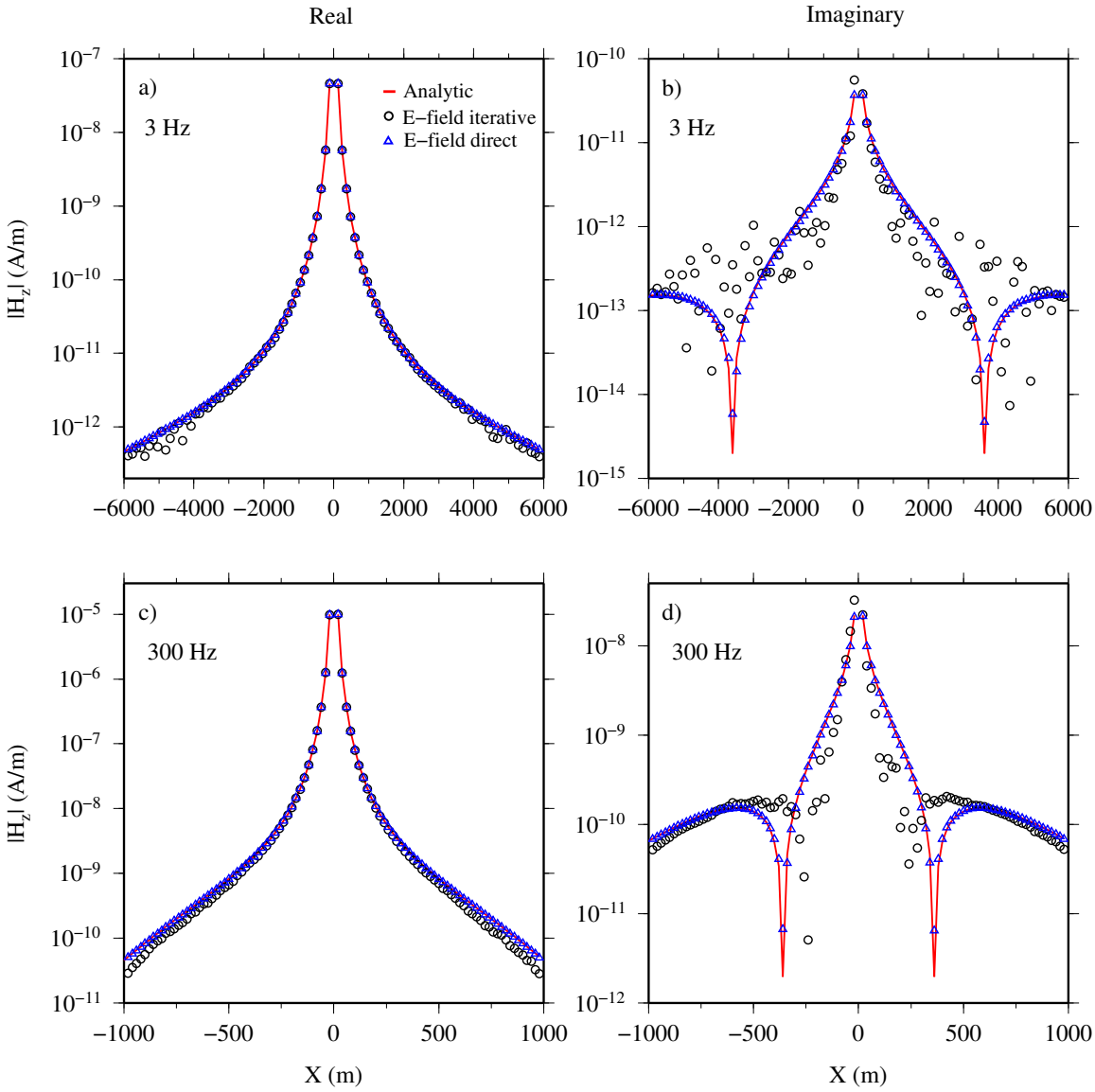

Figure 2.15: The real and imaginary parts of the z-component of the magnetic field, H_z, for the point source for two frequencies for the half-space model of 0.01 S/m. Circles and triangles in each panel are magnetic fields calculated using the iterative and direct solvers respectively.

Chapter 3

Solution to the Geophysical Electromagnetic Vector-Scalar Potentials Formulation

Formulating the EM boundary value problem directly based on the electric or magnetic field allows the simulation of the fields as a physical quantity. However as discussed in Chapter 2, the total E-field equation struggles to converge to an adequate solution for the range of frequencies and scale of problem considered in exploration geophysics. In order to overcome this difficulty I formulated the problem in terms of vector and scalar potentials, which are mathematical in nature but which correspond directly to contrasting physical behaviors in the geophysical EM context.

3.1 Vector-scalar potential formulation

The E-field partial differential equation (equation 2.3) and the equation of conservation of charge (equation 2.40) were introduced in Chapter 2. According to the

Helmholtz theorem each vector field can be determined by the sum of a solenoidal (divergence-free) field and an irrotational (curl-free) field. The basic tool for introducing these quantities in electromagnetics is Gauss's law of magnetism:

$$\nabla \cdot \mathbf{B} = 0. \tag{3.1}$$

Here, because the magnetic flux $\mathbf{B}$ is divergence-free, it can be expressed as the curl of a vector potential $\mathbf{A}$:

$$\mathbf{B} = \nabla \times \mathbf{A} \tag{3.2}$$

Substituting the above equation into equation 2.1 gives:

$$\nabla \times (\mathbf{E} + i\omega\mathbf{A}) = 0. \tag{3.3}$$

Because the curl of the vector $(\mathbf{E} + i\omega\mathbf{A})$ is zero, it can be equated to the negative gradient of a scalar potential, $-\nabla\phi$, and the following equation is obtained:

$$\mathbf{E} = -i\omega\mathbf{A} - \nabla\phi, \tag{3.4}$$

where the parameter ϕ is the scalar potential (Ward and Hohmann, 1988). This decomposition however suffers from the non-uniqueness problem of the potentials. The vector potential in equation 3.2 has an intrinsic ambiguity as does any function with vanishing curl i.e., the gradient of any scalar function, added to $\mathbf{A}$ would have no effect on $\mathbf{B}$. Also any function whose gradient is zero can be added to the scalar potential in equation 3.4 with no effect on $\mathbf{E}$. Extra conditions can be applied on potentials to remedy these non-uniqueness problems, with the condition wherein the principal quantities $\mathbf{E}$ and $\mathbf{B}$ remain invariant. To suppress the freedom of vector

potential the Coulomb gauge condition is often used:

$$\nabla \cdot \mathbf{A} = 0. \tag{3.5}$$

Using equation 3.4 to replace $\mathbf{E}$ with potentials in equation 2.3 gives:

$$\nabla \times \nabla \times \mathbf{A} + i\omega\mu_0\sigma\mathbf{A} + \mu_0\sigma\nabla\phi = \mu_0\mathbf{J_e^s} - \frac{i}{\omega}\nabla \times \mathbf{J_m^s}. \tag{3.6}$$

Here $\mathbf{A}$ and ϕ are complex-valued functions of both position and frequency. To solve the above equation for both the vector and scalar potentials an extra equation is required. Here the equation of conservation of charge (equation 2.40) is used. Using Ohm's law and substituting equation 3.4 into equation 2.40 gives,

$$-i\omega\nabla \cdot (\sigma\mathbf{A}) - \nabla \cdot (\sigma\nabla\phi) = -\nabla \cdot \mathbf{J_e^s}. \tag{3.7}$$

The resulting joint system consisting of equations 3.6 and 3.7 is of square form and diagonally dominated by the terms from both vector and scalar potentials.

In order to solve the system of equations consisting of equations 3.6 and 3.7 the natural boundary conditions on both $\mathbf{A}$ and ϕ are used Jin (2002). Considering the Dirichlet boundary condition and introducing Ω for the entire domain of the physical problem with Γ as its outer boundary the following boundary conditions are applied,

$$(\mathbf{n} \times \mathbf{A})_\Gamma = 0, \tag{3.8}$$

$$\phi_\Gamma = 0, \tag{3.9}$$

where $\mathbf{n}$ is the normal vector for the boundary surfaces of the domain. These boundary

conditions are essentially equivalent to those applied to **E** when solving the E-field Helmholtz equation in Chapter 2. The system of equations given by equations 3.6 and 3.7 is the system that is discretized here using the finite-element approach.

3.2 Construction of the weak form equations

Similar to the approach used for constructing the E-field system in Chapter 2, here again the method of weighted residuals is used as it does not require construction of initial functionals before the minimization process. In order to apply this method a vector residual is firstly formed from equation 3.6:

$$\mathbf{r} = \nabla \times \nabla \times \tilde{\mathbf{A}} + i\omega\mu_0\sigma\tilde{\mathbf{A}} + \mu_0\sigma\nabla\tilde{\phi} - \mu_0\mathbf{J_e^s} + \frac{i}{\omega}\nabla \times \mathbf{J_e^m}. \tag{3.10}$$

where $\tilde{\mathbf{A}}$ and $\tilde{\phi}$ are the approximated vector and scalar potentials respectively. The inner product of the vector residual in equation 3.10 with a vector weight function, **W**, is then equated to zero:

$$R = \int_\Omega \mathbf{W} \cdot \mathbf{r}\ d\Omega\ =\ 0. \tag{3.11}$$

Here the weighting function **W** is such that if the residual can be made to be orthogonal to **W** a good solution is obtained. Substituting equation 3.10 into equation 3.11 and integrating the first term, which involves $\mathbf{W} \cdot \nabla \times \nabla \times \tilde{\mathbf{A}}$, by parts gives:

$$\begin{aligned} \int_\Omega (\nabla \times \mathbf{W}) \cdot (\nabla \times \tilde{\mathbf{A}})\ d\Omega\ -\ \int_{\gamma+\Gamma} \mathbf{W} \times (\nabla \times \tilde{\mathbf{A}}) \cdot \mathbf{n}\ dS\ + \\ i\omega\mu_0 \int_\Omega \sigma\ \mathbf{W} \cdot \tilde{\mathbf{A}}\ d\Omega\ +\ \mu_0 \int_\Omega \sigma\ \mathbf{W} \cdot \nabla\tilde{\phi}\ d\Omega\ = \\ \mu_0 \int_\Omega \mathbf{W} \cdot \mathbf{J^s}\ d\Omega - \frac{i}{\omega} \int_\Omega \mathbf{W} \cdot \nabla \times \mathbf{J}_e^m\ d\Omega. \end{aligned} \tag{3.12}$$

By replacing the magnetic current $\mathbf{J}_e^m$ with the magnetization vector in equation 2.32 the above equation is modified to:

$$\begin{aligned}\int_\Omega (\nabla \times \mathbf{W}) \cdot (\nabla \times \tilde{\mathbf{A}})\ d\Omega\ -\ \int_{\gamma+\Gamma} \mathbf{W} \times (\nabla \times \tilde{\mathbf{A}}) \cdot \mathbf{n}\ dS\ + \\ i\omega\mu_0 \int_\Omega \sigma\ \mathbf{W} \cdot \tilde{\mathbf{A}}\ d\Omega\ +\ \mu_0 \int_\Omega \sigma\ \mathbf{W} \cdot \nabla\tilde{\phi}\ d\Omega\ = \\ \mu_0 \int_\Omega \mathbf{W} \cdot \mathbf{J^s}\ d\Omega + \mu_0 \int_\Omega \mathbf{W} \cdot \nabla \times \mathbf{M}\ d\Omega.\end{aligned} \tag{3.13}$$

The surface integral term in the above equation expresses the behavior of the approximated vector potential at the inner, γ, and outer, Γ, boundaries of the mesh.

An inner product of the scalar residual, r, of equation 3.7 with a scalar weight function, v, is also constructed and then equated to zero:

$$\rho = \int_\Omega\ v\ r\ d\Omega\ =\ 0, \tag{3.14}$$

where

$$r = -i\omega\nabla \cdot (\sigma\tilde{\mathbf{A}})\ -\ \nabla \cdot (\sigma\nabla\tilde{\phi})\ + \nabla \cdot \mathbf{J^s}. \tag{3.15}$$

By substituting this residual term into equation 3.14 and applying integration by parts to the volume integrals involving both potentials, the following equation is derived:

$$\begin{aligned} i\omega \int_\Omega \nabla v \cdot \sigma\tilde{\mathbf{A}}\ d\Omega\ -\ i\omega \int_{\gamma+\Gamma} v\ \sigma\tilde{\mathbf{A}} \cdot \mathbf{n}\ dS\ + \\ \int_\Omega \nabla v \cdot \sigma\nabla\tilde{\phi}\ d\Omega\ -\ \int_{\gamma+\Gamma} v\ \sigma\nabla\tilde{\phi} \cdot \mathbf{n}\ dS\ =\ -\int_\Omega v\ \nabla \cdot \mathbf{J^s}\ d\Omega. \end{aligned} \tag{3.16}$$

The surface integral terms in equations 3.13 and 3.16 involve the behavior of the normal current density from the $\mathbf{A}$ and $\nabla\phi$ components of the approximate electric field at the boundaries of the mesh, which will be discussed later in this chapter.

3.2.1 Application of the finite-element method

To solve the system of equations 3.13 and 3.16 using the finite-element method the computational domain is again subdivided into a grid of unstructured tetrahedral elements. Also similar to the electric-field case described in Chapter 2, the approximated vector and scalar potentials are expressed in terms of a series of basis functions:

$$\tilde{\mathbf{A}} = \sum_{j=1}^{n_A} \tilde{A}_j \ \mathbf{N}_j, \tag{3.17}$$

$$\tilde{\phi} = \sum_{k=1}^{n_\phi} \tilde{\phi}_k \ N_k, \tag{3.18}$$

where $\mathbf{N}_j$ and N_k are vector and scalar basis functions respectively, and the parameters $\tilde{A}_j$ and $\tilde{\phi}_k$ are the unknown coefficients to be determined. Here piecewise linear polynomials are used for basis functions in each computational domain, in particular, the nodal-element basis functions described in section 2.3.3.1 are used for the scalar potential and the edge-element basis functions described in section 2.3.3.2 are used for the vector potential (e.g., Whitney, 1957; Silvester and Ferrari, 1983; Jin, 2002 and Monk, 2003). Also in equations 3.17 and 3.18, n_A and n_ϕ are the number of edges and nodes in each tetrahedron respectively. Because of using linear basis functions here $n_A = 6$ and $n_\phi = 4$ which are respectively the number of edges and nodes in each tetrahedral element. One reason for choosing these elemental functions is to best satisfy the behavior of the electric field at the inter-element boundaries between tetrahedral cells in the meshed domain. Another reason is linear edge-elements are simpler than higher-order basis functions. In order to justify these choices the interface conditions for the scalar and vector potentials are firstly described in the following section.

3.2.2 Interface Conditions for the potentials

For the vector potential the magnetostatic boundary condition can be applied. Considering the rectangular pillbox and the Amperian loop shown respectively in Figures 2.1 and 2.2, and $\mathbf{B} = \nabla \times \mathbf{A}$, the divergence law of $\nabla \cdot \mathbf{B} = 0$ alters to the following equation in integral form

$$\oint \mathbf{B} \cdot d\mathbf{a} = \int \mathbf{A} \cdot d\mathbf{l} = 0. \tag{3.19}$$

This means that for the shrinking sizes of the pillbox and the Amperian loop on the interface the tangential component of the vector potential is continuous. The condition $\nabla \cdot \mathbf{A} = 0$ justifies the continuity of the normal component of the vector potential across the interface. Therefore similar to the scalar potential the vector potential would be also continuous across an interface:

$$\mathbf{A}_2 = \mathbf{A}_1. \tag{3.20}$$

Similar to the interface conditions for the current density in Chapter 2, the normal component of the current density needs to be continuous here. The normal current density as constructed here deals with the continuity in the combination of the normal components of the vector and scalar potentials rather than directly the electric field:

$$\mathbf{J} \cdot \mathbf{n} = \sigma(-i\omega\mathbf{A} - \nabla\phi) \cdot \mathbf{n}. \tag{3.21}$$

Here because of unawareness in what portion of $\mathbf{A}$ and ϕ is contributing to the continuity and discontinuity conditions there is an ambiguity in what exactly the interface conditions can be. For the special DC resistivity case, i.e., when a frequency of zero is used, the interface condition follows the conditions for the scalar potential (e.g.,

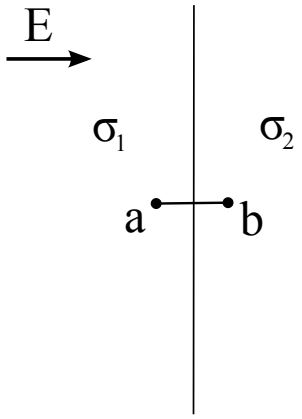

Figure 3.1: The boundary between two media of different conductivities. **E** is the external electric field applied (modified from Ward and Hohmann, 1988).

its gradient here) as used for the static case. The interface conditions for the scalar potential itself follows from the boundary conditions in electrostatics. Considering a plane boundary shared between two adjacent media of different conductivities (see Figure 3.1), the following equation holds for the scalar potential and the electric field (Griffiths, 1999),

$$\phi_2 - \phi_1 = -\int_a^b \mathbf{E} \cdot d\mathbf{l}, \tag{3.22}$$

where a and b are two individual points with epsilon distance from the interface on either sides of the boundary. As the path $a-b$ shrinks to zero (only on the boundary) the above integral on the right hand side reduces to zero and as a result the scalar potential turns to be continuous across the interface:

$$\phi_2 = \phi_1. \tag{3.23}$$

Considering the above argument the finite-element basis function for the scalar potential needs to be chosen so as to be continuous across the inter-element boundaries.

The interface conditions for $\mathbf{A}$ and ϕ described here will be revisited and investigated in Chapter 5.

Similar to the case for the electric field in Chapter 2, vector basis functions are used for the vector potential here. This explicitly satisfies the Coulomb gauge condition of $\nabla \cdot \mathbf{A} = 0$ within a source-free cell and the tangential component of the vector potential is continuous between cells. However, it is not necessarily true to claim that the normal component of the vector potential is continuous. Here the nodal-element basis functions are used for the scalar potentials, which means that ϕ is continuous between cells. Figure 3.2 shows the behavior in two neighboring tetrahedral cells of the gradient of the scalar basis function for the shared node j (see Figure 2.3 for the behavior of ϕ itself). In panel (a) the gray-shaded plane is shared by two adjacent tetrahedrons that share the face (i, j, k). The direction and the magnitude of the gradient of the scalar basis function for the corresponding node is illustrated in panel (b). In particular, the different orientations of the arrows at the shared boundary indicate that the normal component of ∇N_j is discontinuous across the interface. Here the continuity of the tangential components of ∇N_j and $\mathbf{N}_{ji}$ (see Figure 2.5, panel b) guarantee the continuity of the tangential component of the electric field across the interface. The discontinuity of the normal component of ∇N_j can account for the discontinuity of the normal component of the electric field across interfaces between distinct conductivities, removing this responsibility from the vector basis functions (which they are not good at, Farquharson and Miensopust, 2011).

3.2.3 The discretization problem

Here the finite-element basis functions and the interface conditions are applied to equations 3.13 and 3.16. The surface integral terms in these equations again need to

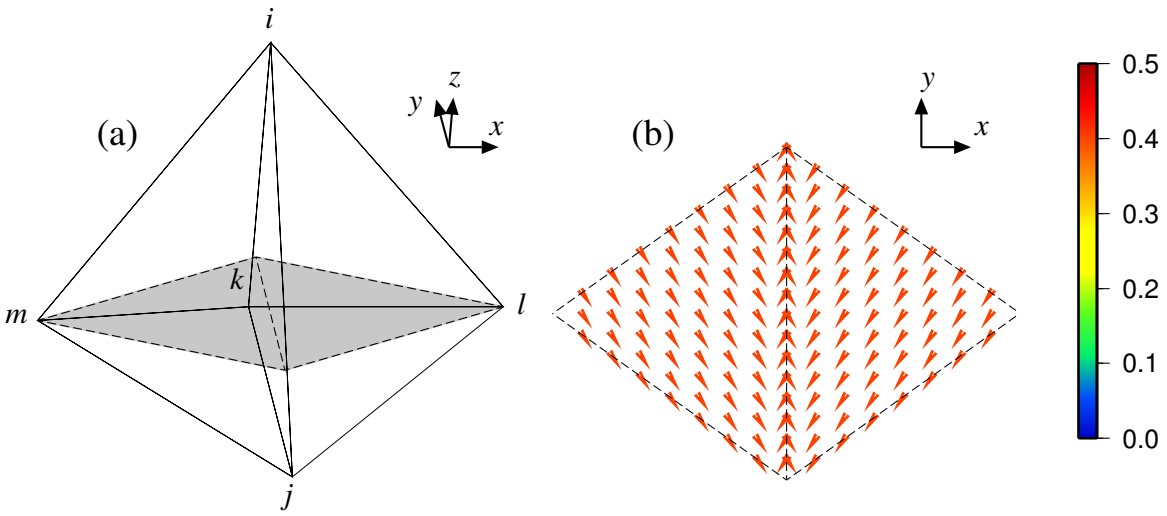

Figure 3.2: Vector plots for the gradient of the scalar basis function for the j^{th} node shared by two neighbor tetrahedrons ($[i, j, k, l]$ and $[i, j, k, m]$).

be analyzed. The surface integral term $\int_{\gamma+\Gamma} \mathbf{W} \times (\nabla \times \tilde{\mathbf{A}}) \cdot \mathbf{n}\, dS$ in equation 3.13 is firstly investigated, considering that edge-elements basis functions are used for the vector potential. The analysis presented here is similar to that for the electric field in Chapter 2. For the situation where the weight function is normal to the inter-element face, the integrand $\mathbf{W} \times (\nabla \times \tilde{\mathbf{A}})$ is purely tangential to the face and, therefore, there would be no contribution from the surface integral term. In contrast, if the weight function is tangential to the shared face, the integrand $\mathbf{W} \times \nabla \times \tilde{\mathbf{A}}$ will have a normal and a tangential component to the face. Here again by considering the true vector potential instead of $\tilde{\mathbf{A}}$ and also using the constitutive relation $\mathbf{H} = \frac{1}{\mu_0}\mathbf{B} = \frac{1}{\mu_0}\nabla \times \mathbf{A}$, the integrand of the surface integral term would change to $\mu_0(\mathbf{W} \times \mathbf{H}) \cdot \mathbf{n}$. This expression deals with the behavior of the vector $\mathbf{W} \times \mathbf{H}$ normal to the face. By choosing an appropriate expression for the weight function (i.e. the edge-element basis functions as in Chapter 2) the tangential component of vector $\mathbf{W}$ would be continuous across the interface by construction. The vector $\mathbf{W} \times \mathbf{H}$ is normal to the face for the tangential component of $\mathbf{H}$. Again as discussed in Chapter 2, as a result of the tangential $\mathbf{H}$ being continuous across the interface, the vector $\mathbf{W} \times \mathbf{H}$, which is

normal to the face, would also be continuous. This indicates that, for a shared face, the contribution from the surface integral term from a particular cell would be cancelled by the corresponding surface integral term from the neighboring cell. According to the above argument the surface integral term in equation 3.13 is ignored and only the volume integral term resulting from the integration by parts $\int_\Omega (\nabla \times \mathbf{W}) \cdot (\nabla \times \tilde{\mathbf{A}})\, d\Omega$ is used. The Sommerfeld boundary conditions are also satisfied by considering the outer boundary Γ to be sufficiently far from the EM source.

The surface integral terms in equation 3.16 involve the behavior of the normal current density from the $\mathbf{A}$ and $\nabla\phi$ components of the approximate electric field at the external and internal boundaries of the mesh. By combining the surface integral terms the integrand of the new surface term involves $v\ \tilde{\mathbf{J}} \cdot \mathbf{n}$ where $\tilde{\mathbf{J}} = \sigma\tilde{\mathbf{E}}$ is the approximate current density. Suppose it were the true rather than the approximate current density. The normal component of the true current density is continuous across the interfaces (γ here) between neighboring cells of distinct conductivities. Therefore with an appropriate choice for the scalar weight function, v, the contribution to the combination of the surface integral terms in equation 3.16 from a particular face in volume Ω would be cancelled by the contribution from the same face in the neighboring volume. Also considering that the outer boundaries (Γ here) of the physical domain are sufficiently far from the source of excitation the Sommerfeld boundary condition is guaranteed by enforcing the above surface integral term to zero.

The Galerkin version of the method of weighted residuals, in which the weighting function is chosen to be equal to the basis function, that is $\mathbf{W} = \mathbf{N}$ for the vector and $v = N$ for the scalar weight functions, is used here. Considering this and substituting equations 3.17 and 3.18 into equations 3.13 and 3.16 the following discretized forms

for the relevant equations are derived:

$$\sum_{j=1}^{N_{edges}} \tilde{A}_j \int_\Omega (\nabla \times \mathbf{N}_i) \cdot (\nabla \times \mathbf{N}_j)\ d\Omega\ + i\omega\mu_0 \sum_{j=1}^{N_{edges}} \tilde{A}_j \int_\Omega \sigma\ \mathbf{N}_i \cdot \mathbf{N}_j\ d\Omega\ + \mu_0 \sum_{k=1}^{N_{nodes}} \phi_k \int_\Omega \sigma\ \mathbf{N}_i \cdot \nabla N_k\ d\Omega\ =\ \mu_0 (\int_\Omega \mathbf{N}_i \cdot \mathbf{J^s}\ d\Omega\ + \int_\Omega \mathbf{N}_i \cdot \nabla \times \mathbf{M}\ d\Omega), \tag{3.24}$$

$$i\omega \sum_{j=1}^{N_{edges}} \tilde{A}_j\ \int_\Omega \nabla N_l \cdot (\sigma\ \mathbf{N}_j)\ d\Omega\ +\ \sum_{k=1}^{N_{nodes}} \tilde{\phi_k}\ \int_\Omega \nabla N_l \cdot (\sigma\ \nabla N_k)\ d\Omega\ = -\ \int_\Omega N_l\ \nabla \cdot \mathbf{J^s}\ d\Omega, \tag{3.25}$$

where $i = 1, \cdots, N_{edges}$ and $l = 1, \cdots, N_{nodes}$, and N_{edges} and N_{nodes} are the total numbers of edges and nodes, respectively, in the mesh. Equations 3.24 and 3.25 are solved for the coefficients, $\tilde{\phi_k}$, of the approximate scalar potential and the coefficients, $\tilde{A}_j$, of the approximate vector potential.

3.2.4 Solution of the discrete system

The integrals on the left-hand side of equations 3.24 and 3.25 involve the interactions between the edge-element basis functions themselves (as discussed in Chapter 2), between the nodal-element basis functions and between the edge- and nodal-element basis functions (see Appendix B for the closed-form formulae). Also, the interactions between the source term and the basis functions are given by the integral terms on the right-hand side of these equations. The matrix form of the system of equations is:

$$\begin{pmatrix} \mathbf{C} + i\omega\mu_0\mathbf{D} & \mu_0\mathbf{F} \\ i\omega\mathbf{G} & \mathbf{H} \end{pmatrix} \begin{pmatrix} \tilde{A} \\ \tilde{\phi} \end{pmatrix} = \begin{pmatrix} \mu_0(S_1 + S_2) \\ S_3 \end{pmatrix}. \tag{3.26}$$

By separating the approximate potentials into their real and imaginary parts, a real-valued matrix form for the system of equations is built. Preconditioned iterative

methods are used in a number of studies (e.g., Axelsson and Kucherov, 2000; and Axelsson et al., 2013) for the solution to the real-valued variants of the original complex systems. The decomposed system hence reads,

$$\begin{pmatrix} \mathbf{C} & -\omega\mu_0\mathbf{D} & \mu_0\mathbf{F} & 0 \\ \omega\mu_0\mathbf{D} & \mathbf{C} & 0 & \mu_0\mathbf{F} \\ 0 & -\omega\mathbf{G} & \mathbf{H} & 0 \\ \omega\mathbf{G} & 0 & 0 & \mathbf{H} \end{pmatrix} \begin{pmatrix} \tilde{A^R} \\ \tilde{A^I} \\ \tilde{\phi^R} \\ \tilde{\phi^I} \end{pmatrix} = \begin{pmatrix} \mu_0(S_1 + S_2) \\ 0 \\ S_3 \\ 0 \end{pmatrix} \tag{3.27}$$

where $C_{ij} = \int_\Omega (\nabla \times \mathbf{N}_i) \cdot (\nabla \times \mathbf{N}_j)\ d\Omega$; $D_{ij} = \int_\Omega \sigma\ \mathbf{N}_i \cdot \mathbf{N}_j\ d\Omega$; $F_{il} = \int_\Omega \nabla N_l \cdot (\sigma\ \mathbf{N}_j)\ d\Omega$; $\mathbf{G}$ is the transpose of the matrix $\mathbf{F}$; $H_{lk} = \int_\Omega \nabla N_l \cdot (\sigma\ \nabla N_k)\ d\Omega$; $i, j = 1, \cdots, N_{edges}$ and $l, k = 1, \cdots, N_{nodes}$. Also, $S_1 = \int_\Omega \mathbf{N}_i \cdot \mathbf{J^s}\ d\Omega$, $S_2 = \int_\Omega \mathbf{N}_i \cdot \nabla \times \mathbf{M}\ d\Omega$ and $S_3 = -\int_\Omega N_l\ \nabla \cdot \mathbf{J^s}\ d\Omega$ are the contributions from the source terms, and $\tilde{A^R}$, $\tilde{A^I}$, $\tilde{\phi^R}$, and $\tilde{\phi^I}$ are the real and imaginary parts of the coefficients for the approximate vector and scalar potentials respectively. The dimension of the above system is twice the sum of the number of edges and nodes in the mesh.

Axelsson and Kucherov (2000) investigated the real-valued solution of systems in the complex form of $(\mathbf{L} + i\omega\mathbf{I})\mathbf{u} = \mathbf{f}$ where $\mathbf{L}$ is the coefficient matrix, $\mathbf{I}$ is the identity matrix and $\mathbf{u}$ is the solution vector. In fact as discussed therein, because of the limited choices for suitably preconditioning the complex systems, I used an efficient combination of preconditioning and iterative solver for the real-valued form of the problem.

In preparation for solving the system of equations Dirichlet boundary conditions for the vector and scalar potentials are implemented on the outer boundaries of the mesh. On the boundary Γ, equations 3.8 and 3.9 change to $\mathbf{n} \times \mathbf{A} = A_j$ and $\phi = \phi_k$ respectively. Here subscripts j and k are respectively associated with edges and nodes on the

outer boundaries of the mesh. In order to force those coefficients to their theoretical zero value on the outer boundaries those elements on the rows of the coefficient matrix (see equation 3.27) that correspond to the edges and nodes located on the truncation boundaries of the mesh are set to zero except for the diagonal element Jin (2002). Also, the element in the corresponding row of the source vector on the right-hand side of equation 3.27 is set to zero.

Similar to the situation with the E-field solution in Chapter 2 the resulting system of equations is solved using the iterative solver GMRES from SPARSKIT (Saad, 1990). Also the system is preconditioned using an incomplete LU decomposition approach (Saad, 2003). Once the system has been solved for the real and imaginary parts of the vector and scalar potentials the electric field is obtained using equation 3.4. The magnetic field is calculated by taking the curl of the vector potential and using the edge-element basis functions:

$$\mathbf{H} = \frac{1}{\mu_0} \sum_{j=1}^{N_{edges}} \tilde{A}_j \, \nabla \times \mathbf{N}_j. \tag{3.28}$$

3.3 Verification Examples

The performance of the method presented above is illustrated for the same examples presented for the E-field solution in Chapter 2. Again a total-field solution is being considered, and examples for the homogeneous whole-space and half-space Earth models are included. The results are compared against the analytic solutions.

3.3.1 Magnetic dipole problem

3.3.1.1 Conductive whole-space and magnetic point source

Similar to the example in Section 2.4.1.1 the problem of an infinitesimal magnetic dipole is also considered here. For this type of source the only non-zero term on the right-hand side of equation 3.27 emerges from the term S_2 while the contributions from both S_1 and S_3 disappear. The approach to evaluate S_2 has already been described in Chapter 2 and its closed-form formulation is presented in Appendix B. Therefore, the matrix form of the system of equations in complex form is,

$$\begin{pmatrix} \mathbf{C} + i\omega\mu_0\mathbf{D} & \mu_0\mathbf{F} \\ i\omega\mathbf{G} & \mathbf{H} \end{pmatrix} \begin{pmatrix} \tilde{A} \\ \tilde{\phi} \end{pmatrix} = \begin{pmatrix} \mu_0 S_2 \\ 0 \end{pmatrix}. \tag{3.29}$$

The real-valued $\mathbf{A} - \phi$ system is formed by splitting the potentials into their real and imaginary parts. For the same whole-space model used in section 2.4.1.1, including the same mesh, the decomposed system of equations is solved. Figure 3.3 shows the z-component of the total magnetic field at observation locations along the x-axis for frequencies of 3 and 300 Hz. Circles and solid lines shown in each panel therein are data calculated using the $\mathbf{A} - \phi$ finite-element approach and the analytical formula of Ward and Hohmann (1988) respectively. It is seen here that the solution gives a good match with the analytic response. For the solution here again a Krylov subspace of 200 for the GMRES solver and a fill-in factor of $lfil = 3$ for the truncated ILU preconditioner are used. In fact, these are exactly the same solver parameters used for the corresponding E-field example. Choosing larger values of fill-in did not improve the convergence of the iterative solver. Figure 3.4 shows the preconditioned residual norm of the iterative solver during these runs. Here the decomposed system reaches a residual norm of approximately 10^{-18} for 3 Hz in panel (a) and 10^{-15} for 300 Hz in

panel (b). These residual norms are considerably smaller than those obtained for the E-field solution for exactly the same example.

3.3.1.2 Conductive whole-space and small loop of current

As shown in Chapter 2 a small loop of current can be used as an alternative for the magnetic source point. As the rationale for this choice, for the sake of generality and to obviate the need for forcing the edges of some tetrahedrons to coincide with the source line of current, the source is arbitrarily positioned in the mesh. In contrast to the previous example where a magnetic source point is used, the non-zero contributions to the source vector on the right-hand side of equation 3.26 now emerges from the terms S_1 and S_3. Here the parameter S_2 is zero as the magnetic dipole source is constructed using four individual wires not a point source. Also in accordance with the characteristics of a magnetic dipole source, the term S_2 turns out to be zero after the assembly process. Equation 3.26 then changes to the following form:

$$\begin{pmatrix} \mathbf{C} + i\omega\mu_0\mathbf{D} & \mu_0\mathbf{F} \\ i\omega\mathbf{G} & \mathbf{H} \end{pmatrix} \begin{pmatrix} \tilde{A} \\ \tilde{\phi} \end{pmatrix} = \begin{pmatrix} \mu_0 S_1 \\ 0 \end{pmatrix}. \tag{3.30}$$

The closed-form formula for the source term is given by equation B.48 presented in Appendix B. Here the parameters of the source including the magnetic moment, current, and size are identical to those used in Section 2.4.1.2. The same tetrahedral grids are also used for the individual frequencies of 3 and 300 Hz. Again for the same solver parameters, including a Krylov subspace of 200 for GMRES and $lfil = 3$ for the ILU preconditioner, the decomposed system shown in equation 3.30 is solved. The total magnetic field response for the z-component and the corresponding residual norms are shown in Figures 3.5 and 3.6 respectively. Here also the $\mathbf{A} - \phi$ decomposed solution coincides with the analytic curves as presented in Figure 3.5. For the number

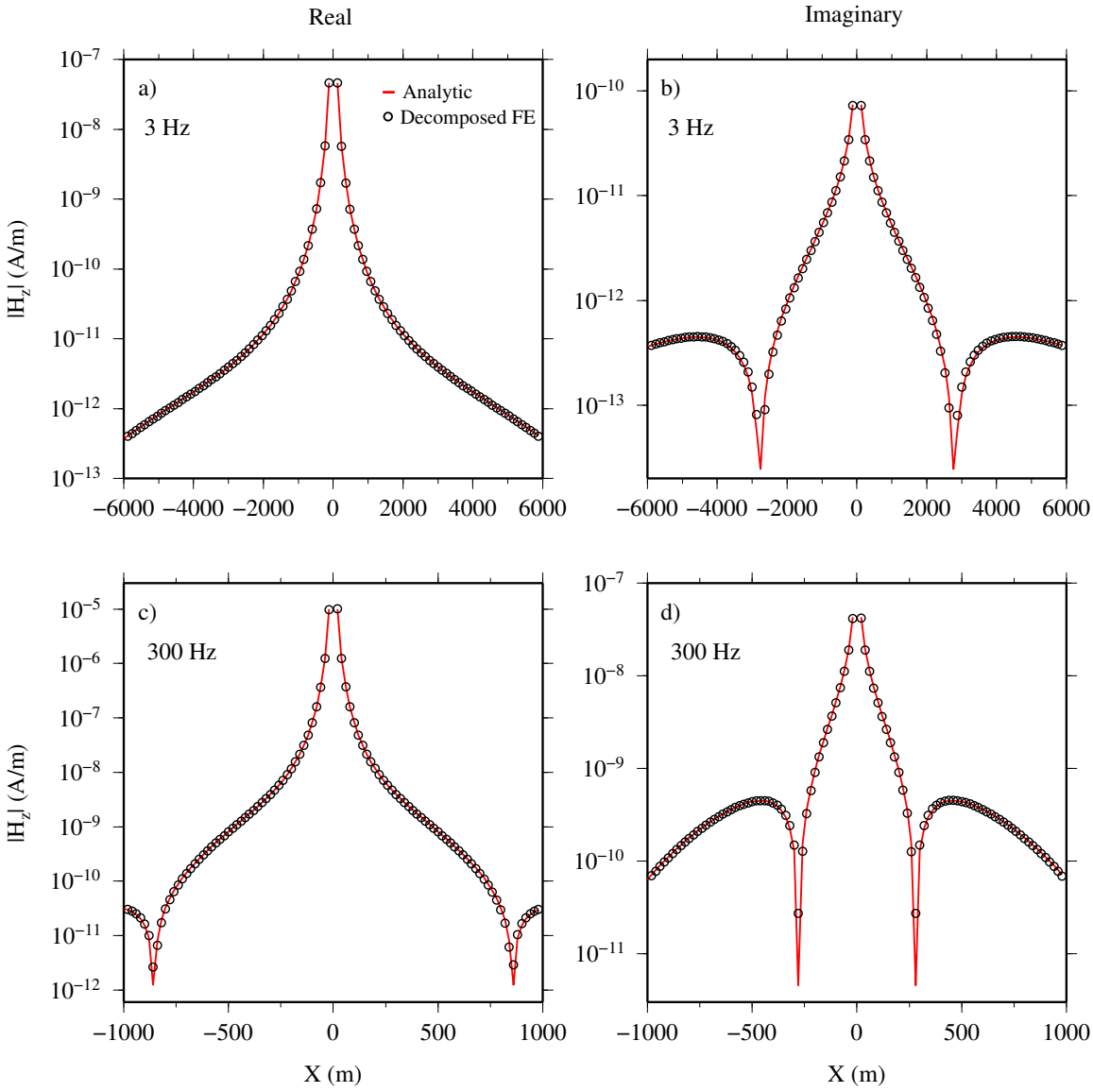

Figure 3.3: A comparison of the z-components of the real and imaginary parts of the magnetic field observed along the x-axis for the whole-space and point source example. Data are synthesized using the analytic formula (red solid line) and $\mathbf{A} - \phi$ decomposed FE (circles). Panels (a) and (b) are for a frequency of 3 Hz; panels (c) and (d) are for a frequency of 300 Hz.

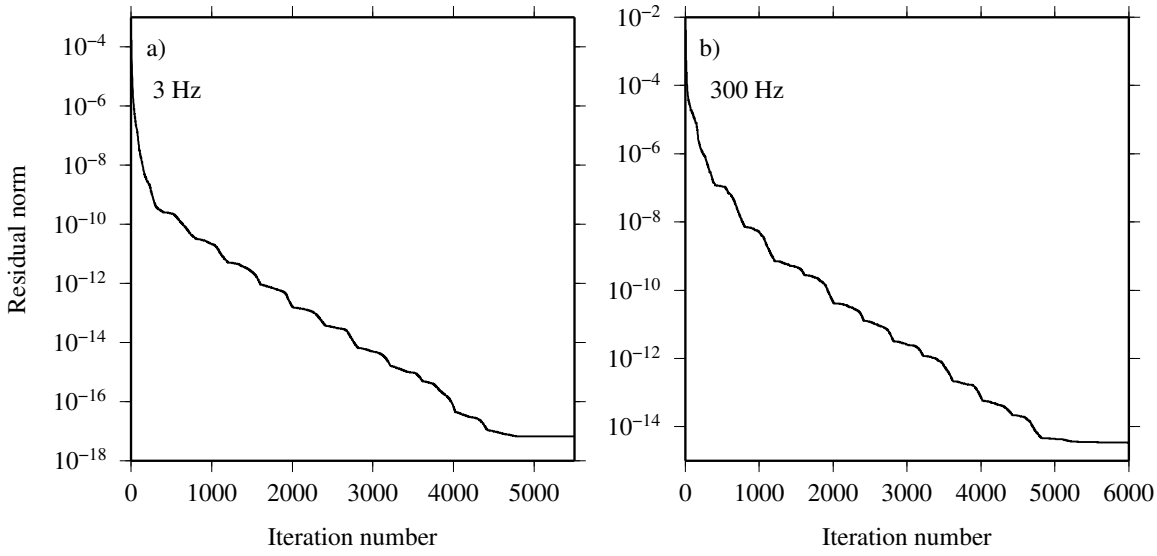

Figure 3.4: The convergence curves for the decomposed solutions for frequencies of 3 and 300 Hz for the conductive whole-space model of 0.01 S/m. The data in Figure 3.3 are for the residual norms of the iterative solver after 6000 iterations.

of iterations shown in Figure 3.6 the approximate computation times were 45 minutes for the frequency of 3 Hz and 65 minutes for the frequency of 300 Hz.

3.3.1.3 Conductive half-space and a magnetic point source

The identical mesh presented in Section 3.3.1.1 is used to solve the half-space problem with a central magnetic source point located on the surface. The system to solve is again equation 3.29. Here the conductivity for the air is considered to be 10^{-8} S/m. Also, the same parameters for the iterative solver as used in Section 3.3.1.1 are again used for this example. Figure 3.7 shows the H_z response at the observation locations along the x-axis. It is also seen here that the numerical solutions are coincident with the analytic solutions. The convergence curves for the calculated fields are shown in Figure 3.8. The computation times for solving the system of equations for frequencies of 3 and 300 Hz were 40 and 48 minutes respectively.

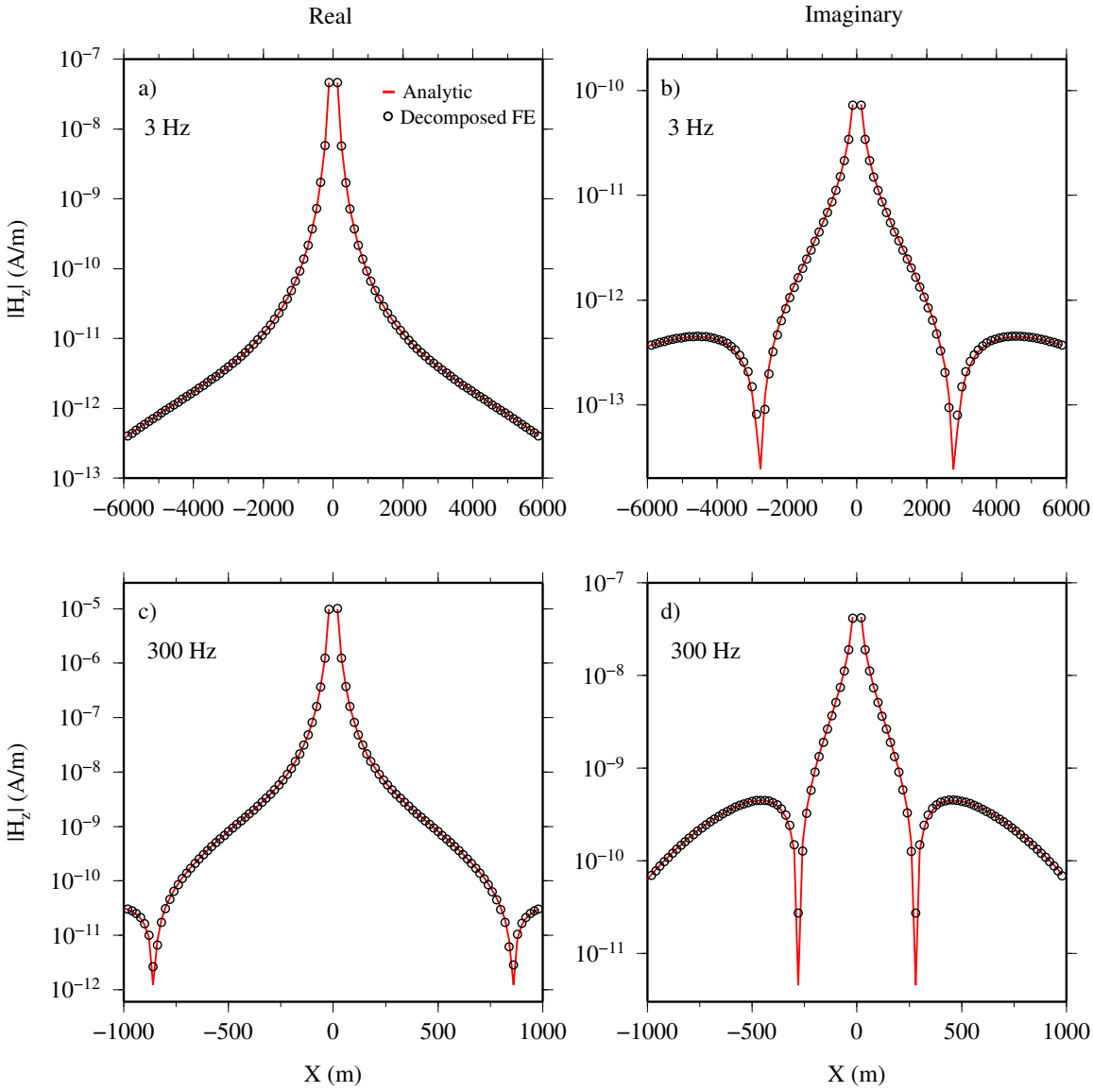

Figure 3.5: A comparison of the z-components of the real and imaginary parts of the magnetic field observed along the x-axis for the whole-space and loop example.

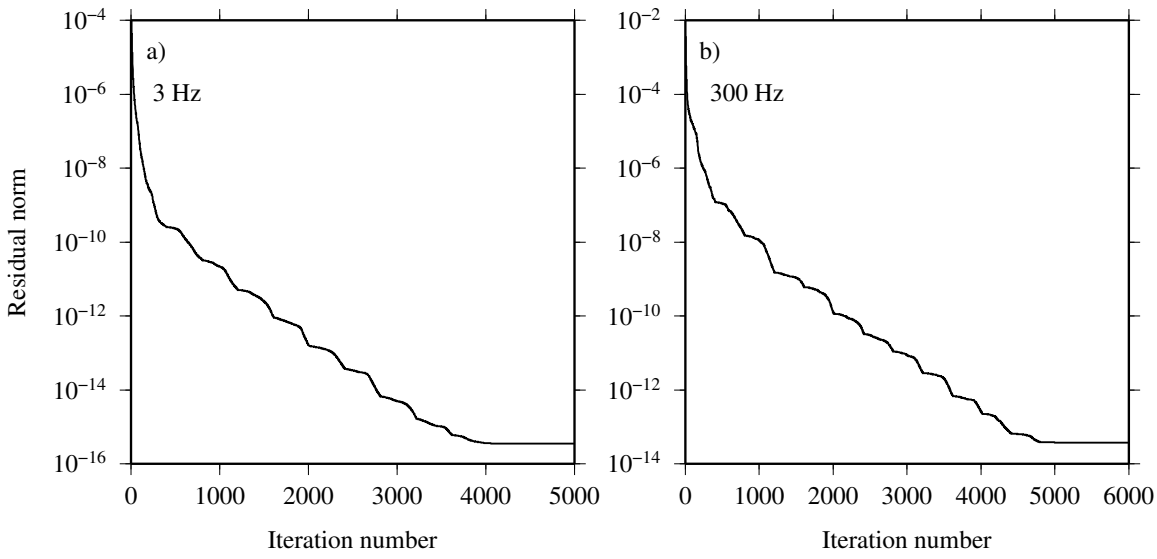

Figure 3.6: The convergence curves for the decomposed solution for frequencies of 3 and 300 Hz for the conductive whole-space model of 0.01 S/m. The data in Figure 3.5 are for the residual norms of the iterative solver after 5000 iterations for 3 Hz and 6000 iterations for 300 Hz.

3.3.1.4 Conductive half-space and a loop of current

The model presented in Section 3.3.1.2 but for a half-space problem is also solved. An identical loop of current is located at the origin on the Earth's surface. The conductivity of the air is also 10^{-8} S/m. The same frequencies and parameters of the iterative solver used in Section 3.3.1.2 are used here. Figure 3.9 is the total magnetic field response H_z for the two frequencies and for observation locations along the x-axis. Figure 3.10 shows the corresponding residual norm of the iterative solver for these runs. Here the small residual norms reached for both frequencies give satisfactory numerical solutions which agree well with the solutions calculated using the analytic formula. Computation times for frequencies of 3 and 300 Hz for the number of iterations shown in Figure 3.10 are 38 and 49 minutes respectively.

With the intention of providing an insight into the efficiency of the decomposed total

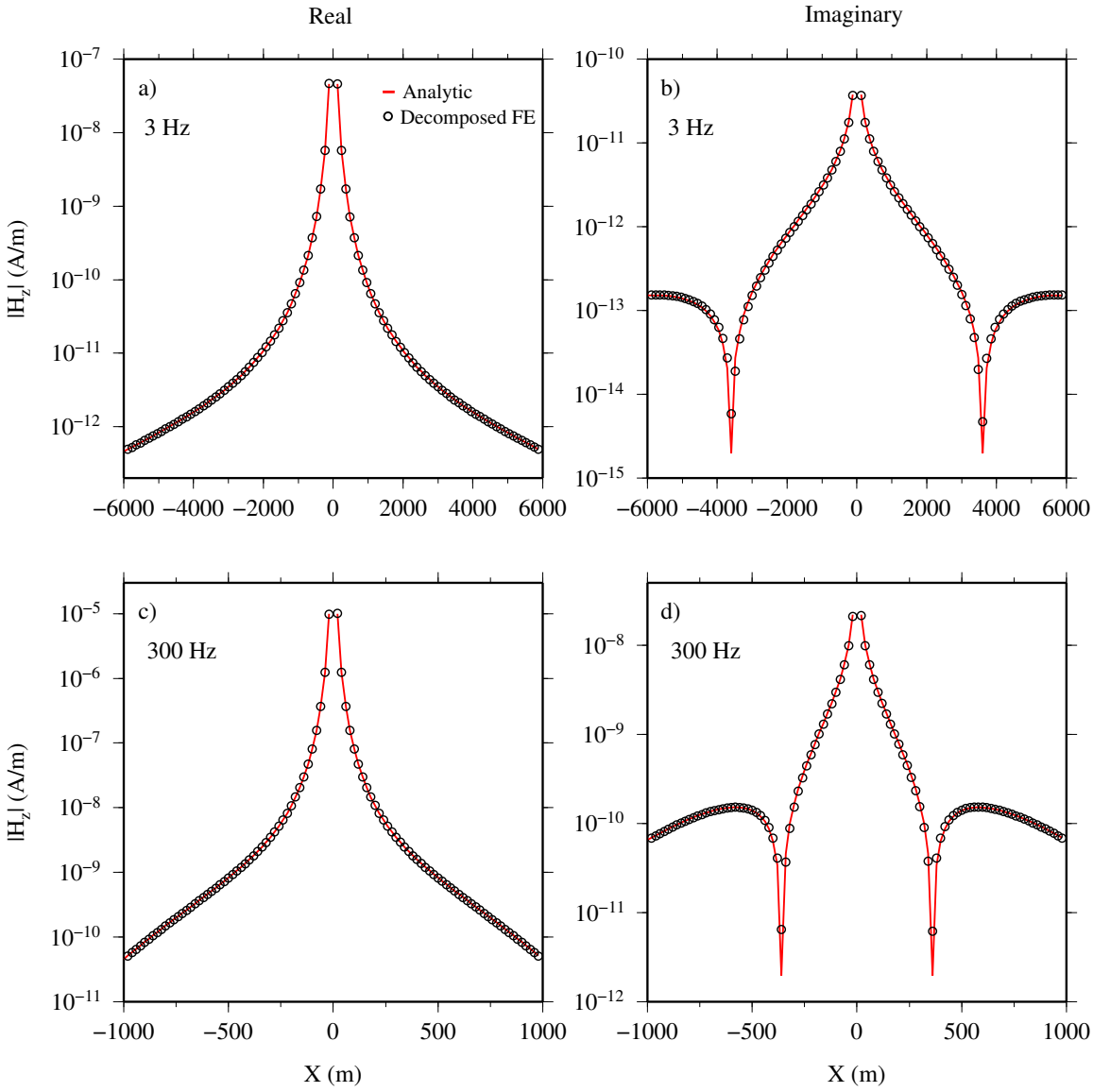

Figure 3.7: A comparison of the z-components of the real and imaginary parts of the magnetic field observed along the x-axis for the half-space and point source example.

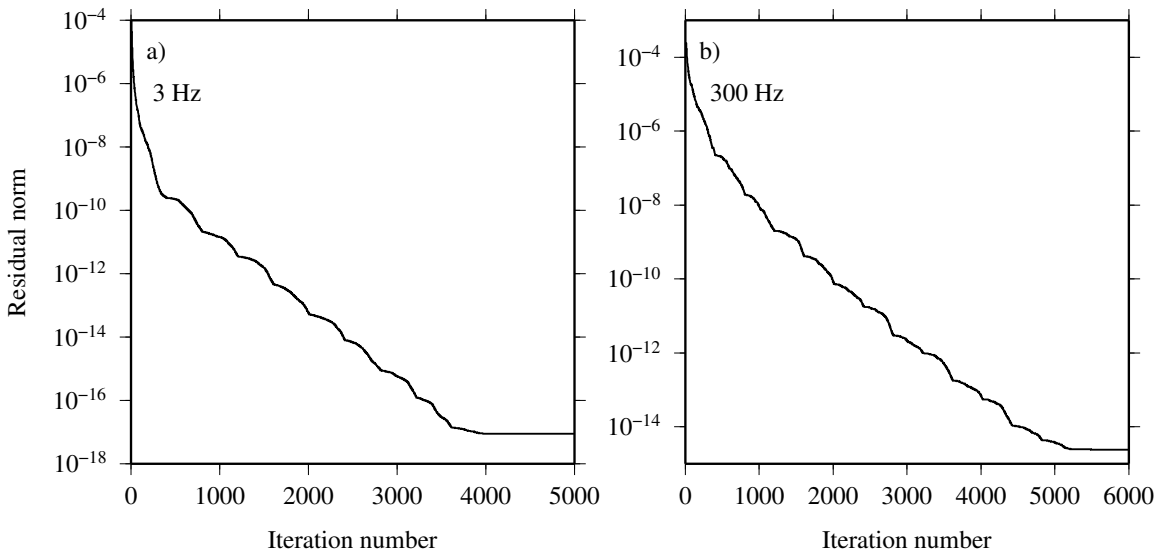

Figure 3.8: The convergence curves for the decomposed solutions for frequencies of 3 and 300 Hz for the conductive half-space model of 0.01 S/m and the point magnetic source.

field solutions on unstructured meshes the data calculated in the above examples can be compared to those of the E-field solutions presented in Chapter 2. It was observed in Chapter 2 that the data calculated using the finite-element E-field approach does not agree well with the analytic solutions. In contrast, the solution using the decomposed potentials gives a good match, e.g. only 1.6 percent difference on average for the 3 Hz example in Section 3.3.1.4, with the analytic response. The relative residual norm (e.g., $\frac{||Ax-b||}{||b||}$) is also calculated for a number of examples presented above. For the relevant number of iterations, for the loop of current and half-space example, the relative residual norms for a frequency of 3 Hz were 6.73×10^{-11} and 1.21×10^{-7} for the final $\mathbf{A} - \phi$ and E-field solutions respectively. The corresponding residuals for the frequency of 300 Hz were 5.02×10^{-10} for the decomposed system and 7.96×10^{-5} for the total E-field system. Clearly the iterative solver has been able to converge to a significantly more accurate solution for the $\mathbf{A} - \phi$ system than for the E-field system.

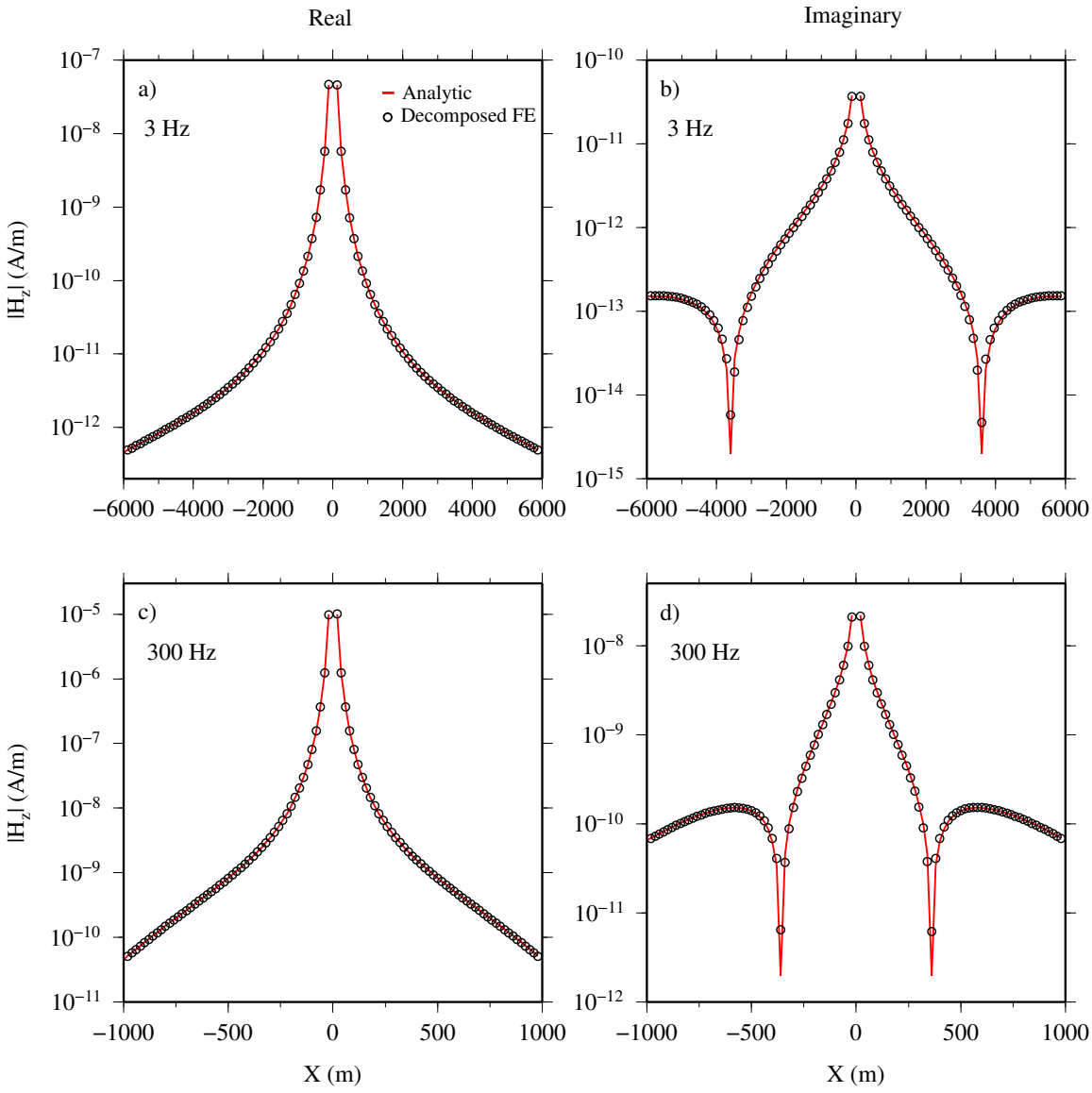

Figure 3.9: The real and imaginary parts of the z-component of the magnetic field, H_z, for two frequencies, the loop of current, and the half-space model of 0.01 S/m.

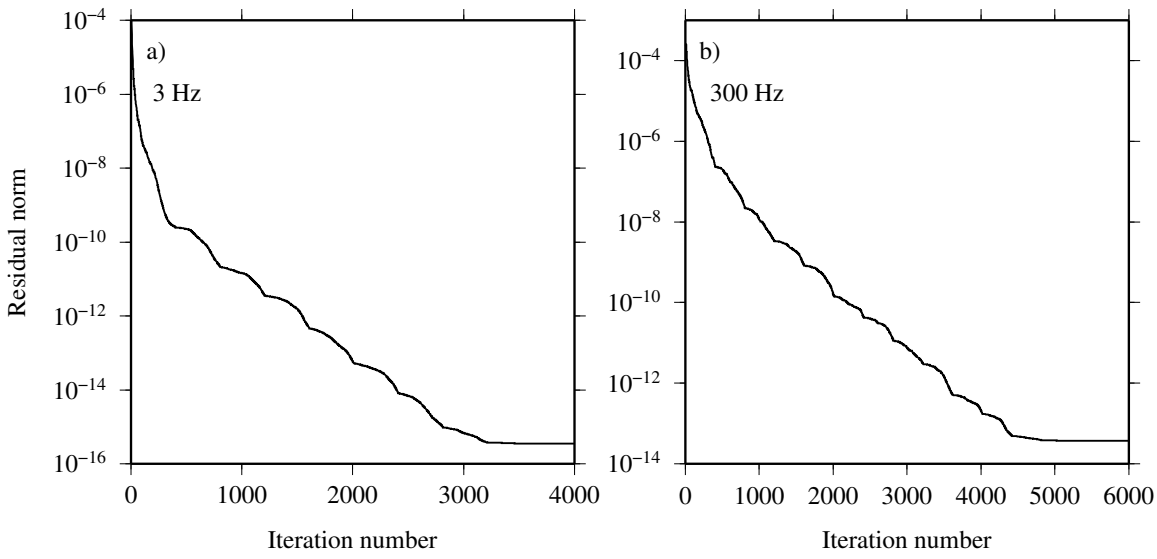

Figure 3.10: The convergence curves for the decomposed solution for frequencies of 3 and 300 Hz for the conductive half-space model of 0.01 S/m and the loop magnetic source. The data in Figure 3.9 are for the residual norms of the iterative solver after 4000 iterations for 3 Hz and 6000 iterations for 300 Hz.

For the example presented in Section 3.3.1.4 I also considered calculating the fields for longer source-receiver distances for a lower frequency of 0.1 Hz. For this purpose the mesh is refined along 24 km of observation locations (12 km on each side of the dipole source) on the surface. The new mesh consists of 708769 cells, 116058 nodes, and 825232 edges. Again as shown in Figure 3.11 the results from the $\mathbf{A} - \phi$ finite-element approximation agree with the analytic solution (average difference of 1.5 percent) for both real and imaginary parts of the magnetic field.

3.3.2 Electric dipole problem

3.3.2.1 Conductive half-space and electric dipole source

This example considers the problem of a conductive half-space excited by a small electric dipole located on the Earth's surface. For the situation where an electric dipole of a single wire is used as the source of excitation the matrix-form for the

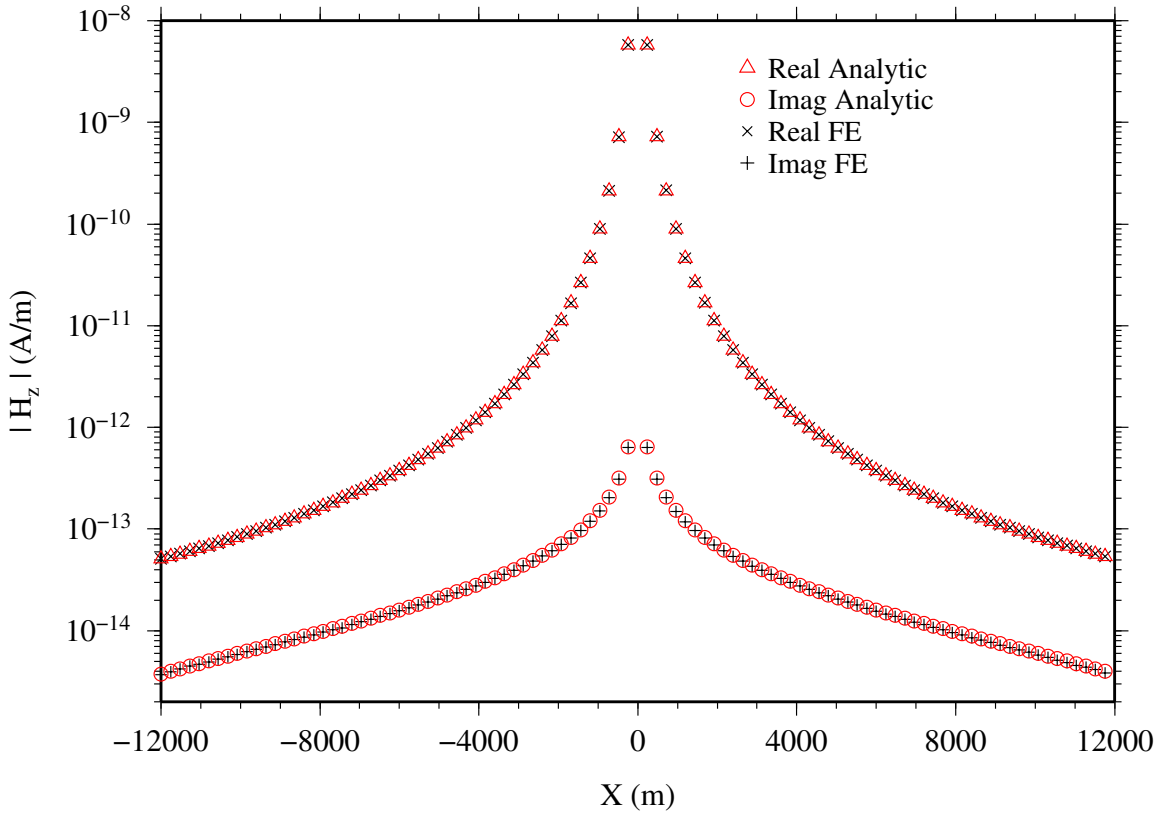

Figure 3.11: The real and imaginary parts of the z-component of the total magnetic field, H_z, on the Earth's surface for a frequency of 0.1 Hz for the homogeneous half-space model. A comparison of the real and imaginary parts obtained using the FE method (shown respectively with crosses and pluses) and the analytic formula (shown respectively in triangles and circles) is presented.

discretized system of equations 2.30 and 3.26 are as follows,

$$\left(\mathbf{C} + i\omega\mu_0\mathbf{D}\right)\tilde{E} = -i\omega\mu_0 S_1, \tag{3.31}$$

for the E-field system and

$$\begin{pmatrix} \mathbf{C} + i\omega\mu_0\mathbf{D} & \mu_0\mathbf{F} \\ i\omega\mathbf{G} & \mathbf{H} \end{pmatrix} \begin{pmatrix} \tilde{A} \\ \tilde{\phi} \end{pmatrix} = \begin{pmatrix} \mu_0 S_1 \\ S_3 \end{pmatrix}. \tag{3.32}$$

for the $\mathbf{A} - \phi$ decomposed system. Here because a physical current of I flows in the electric dipole source, the source terms that exist are those constructed using the relevant current density of $\mathbf{J}_e^s$ and the contribution from the source term that includes the magnetic current $\mathbf{J}_m^s$, namely $\int_\Omega \mathbf{N}_i \cdot \nabla \times \mathbf{M}\, d\Omega$, would be zero. Source terms in equation 3.31 and 3.32 are the same as those seen in equation 3.27. The closed-form formula for these source terms are presented in Appendix B.

Similar to the examples presented in Section 3.3.1 the model here comprises a homogeneous half-space of 0.01 S/m with an overlaying air layer of 10^{-8} S/m. A current of 1 A runs through the dipole which extends from 0.5 to 0.5 m in the x-direction on the Earth's surface. Figure 3.12 shows the tetrahedral mesh used for this example. Here, in order to accurately calculate the behavior of the EM field, the mesh is locally refined about the source and line of observation locations (see Figure 3.12). For this refinement the source passes through a total of 52 cells. Also, the cell dimensions gradually increase in size away from the refined regions. The dimension of the whole mesh is 300 km $\times$ 300 km $\times$ 300 km. The number of cells, nodes, and edges for this mesh are 708796, 116058 and 825232, which results in 1650464 unknowns in the E-field and 1882580 unknowns in the $\mathbf{A} - \phi$ systems of equations. In addition, the

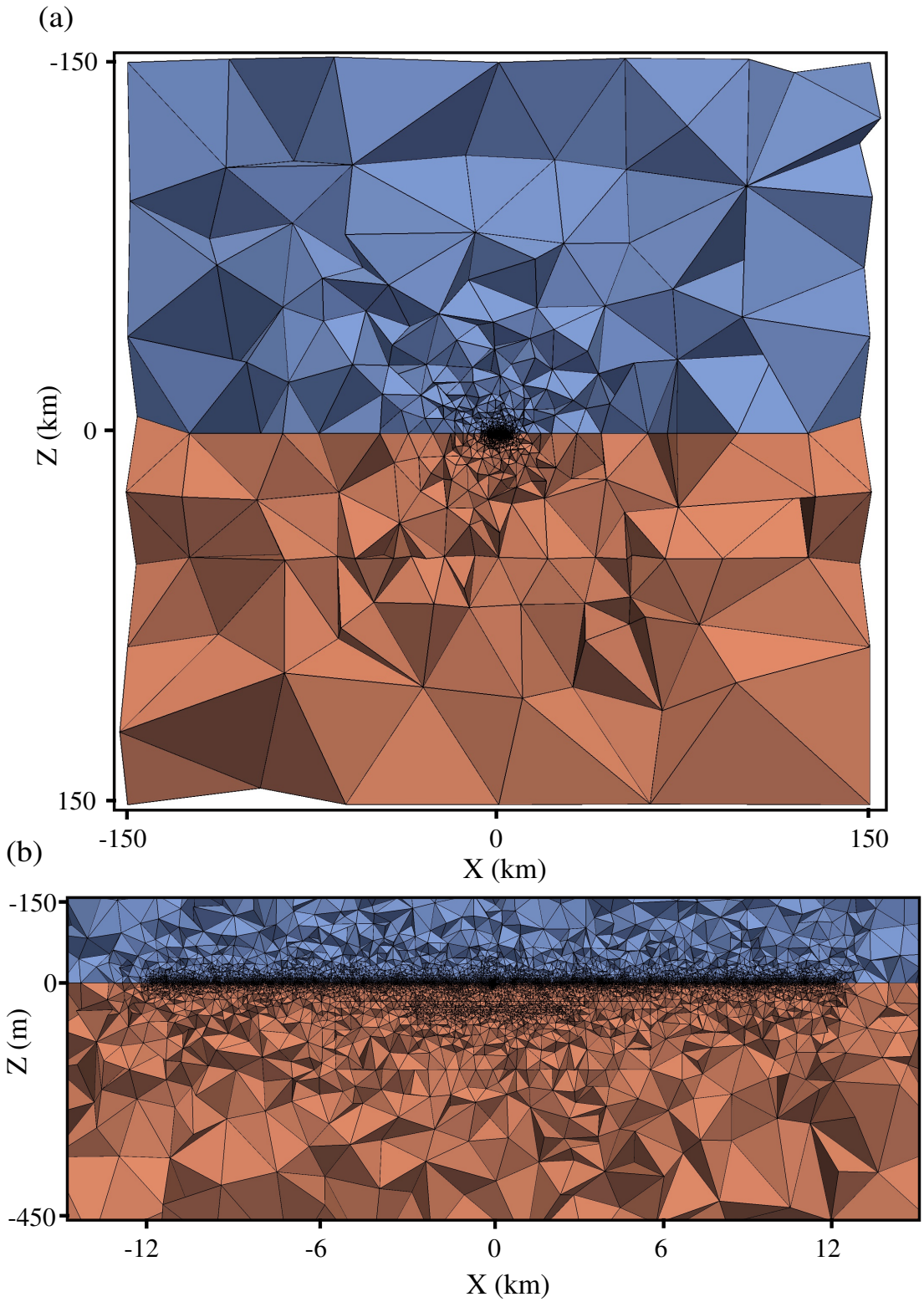

Figure 3.12: (a) The entire view and (b) the enlarged cross-section of the central part of the tetrahedral mesh used for the homogeneous half-space and electric dipole source example model. The conductive ground and the resistive air are shown in orange and blue respectively. The Earth surface is flat, and the mesh is refined about the dipole source at the origin and along 24 km of observation locations.

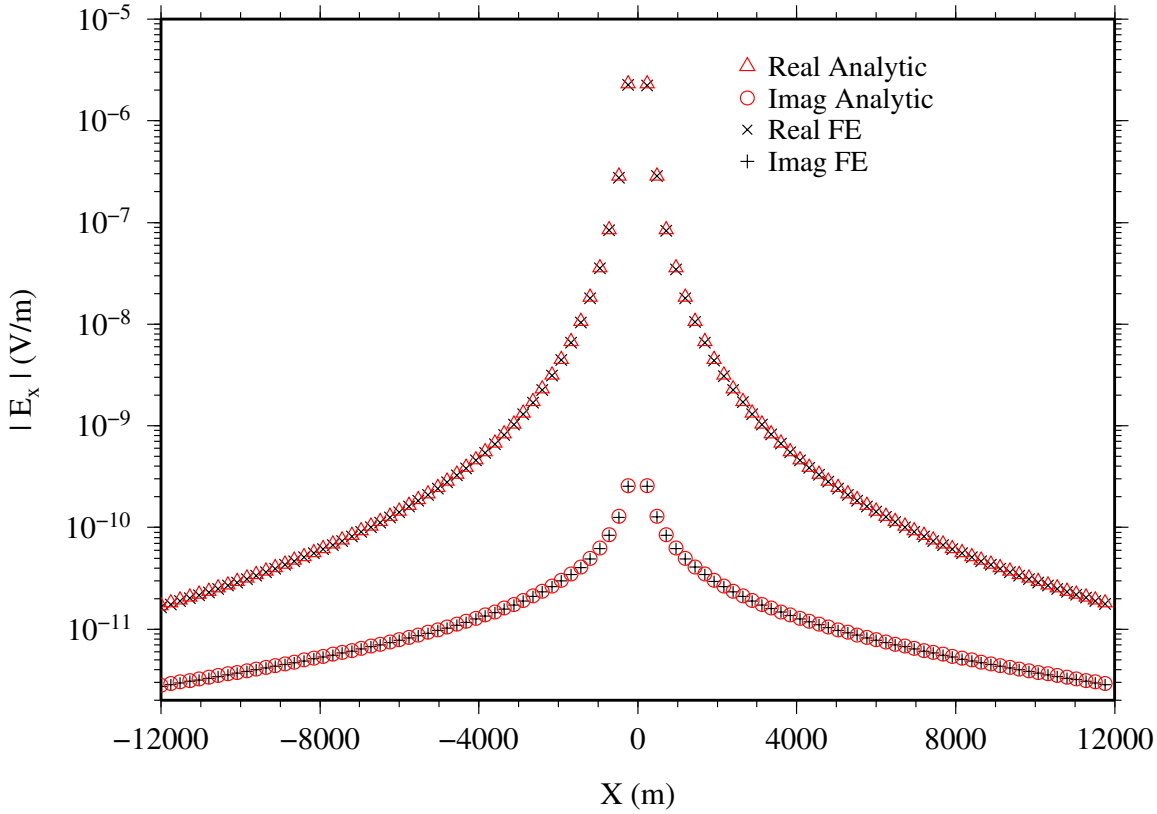

Figure 3.13: The magnitude of the x-component of the electric field, E_x, for a frequency of 0.1 Hz for the homogeneous half-space model. The cross and plus symbols are the real and imaginary parts respectively of the electric field calculated using the $\mathbf{A} - \phi$ finite-element method presented here. The triangles and circles are the real and imaginary parts of the electric field calculated using the analytic formula.

number of edges and nodes on the outer boundary of the mesh are 381 and 1706 respectively.

Figure 3.13 shows the values of the x-component of the electric field at locations along the x-axis for a frequency of 0.1 Hz. Cross and plus symbols indicate the values of the real and imaginary parts of the electric field calculated using the $\mathbf{A} - \phi$ approach presented here, triangles and circles are the corresponding analytic solutions of Ward and Hohmann (1988). A good agreement between the finite-element results and the analytic results is clear as the FE data on average match within 98.5 percent of the

analytic data. For this example the truncated ILU preconditioner (Saad, 1990) was applied to the coefficient matrices in equations 3.31 and 3.32. Again a value of 3 for the fill-in parameter is selected. Figure 3.14 shows the preconditioned residual norm which is supplied by the SPARSKIT solvers during the iterative process. Here the GMRES solver with a dimension of 200 for the Krylov subspace is again used. The blue curve in Figure 3.14 indicates the behavior of the convergence of the solution during the solution process for the $\mathbf{A} - \phi$ decomposition. As shown in Figure 3.14 after almost 4000 iterations a residual norm of approximately 10^{-12} was reached. The relative residual norm here was 2.95×10^{-10} for the final solution. As for the convergence criterion here the iterative solver was terminated once the residual norm stopped decreasing. The computation time for this run was roughly 35 minutes and the total memory usage was 8 Gbytes. The curve shown in black in Figure 3.14 is the residual norm when attempting to solve the non-decomposed E-field equation (see equation 3.31) using the same solver parameters as for the $\mathbf{A} - \phi$ system (preconditioner, dimension of the Krylov subspace, and the total number of iterations). The residual norm of the non-decomposed system does not decrease by more than half an order of magnitude compared to the decrease of 14 orders of magnitude achieved by the $\mathbf{A} - \phi$ solution.

3.4 Discussion on the convergence of the E-field and $\mathbf{A} - \phi$ solutions

For comparable examples presented here and in Chapter 2 it is demonstrated that unlike the E-field system the decomposed system presented in this chapter gives a faster convergence of the iterative solver and subsequently provides the correct solution to the EM modeling problem. The superior convergence of the $\mathbf{A} - \phi$ formulation rela-

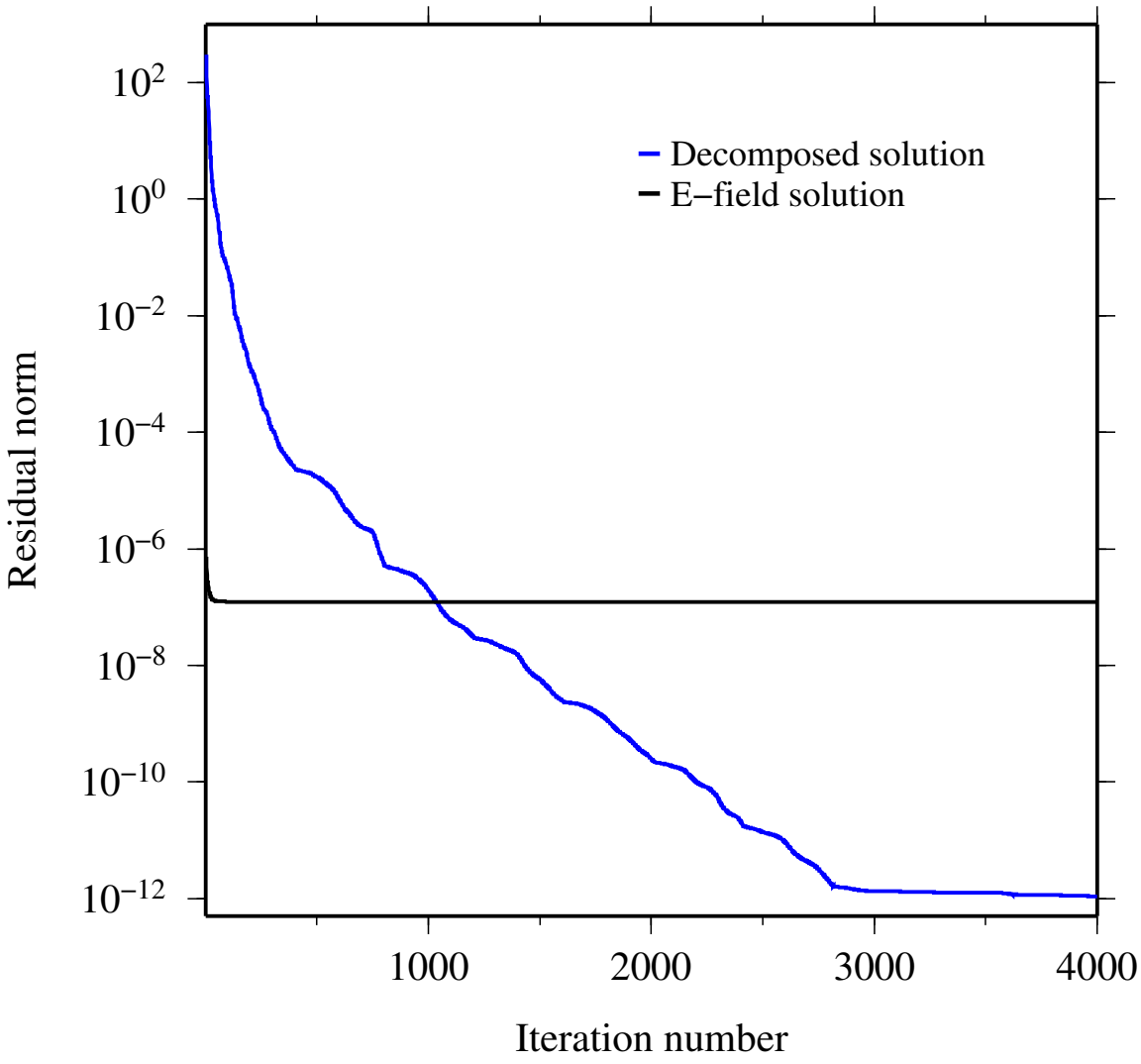

Figure 3.14: The convergence curves for the E-field solution (black) and $\mathbf{A}-\phi$ solution for a frequency of 0.1 Hz for the first half-space and electric dipole example.

tive to that for the E-field formulation is because the conductivity term in the E-field equation (equation 2.3) almost disappears whereas in the decomposed system (consisting of equations 3.6 and 3.7) two terms, $i\omega\nabla\cdot(\sigma\mathbf{A})$ and $\sigma\cdot(\nabla\phi)$, are sufficiently large to maintain the influence of the conductivity in the system of equations.

To further illustrate this fact, both E-field and $\mathbf{A}-\phi$ systems were re-run for two individual frequencies of 0.1 and 100 Hz for the model presented in the previous section for the electric dipole example. The values shown in Table 3.1 are the elements of the coefficient matrix for this example at three different locations. These three points correspond to the coordinates of the center of the three selected edges in the mesh. Three edges were chosen with sizes ranging from small to large. The volumes of the cells associated with these edges also vary from small to large. The first edge (region 1 in Table 3.1) with a length of 0.12 m belongs to a tetrahedral cell near the origin immediately below the surface with the source line passing through it. The average volume of the elements surrounding this edge is 10^{-4} m^3. The small magnitudes for the size of the edges and volume of the cells is a result of refinement at region 1. The second point (region 2 in Table 3.1) is considered at $(x, y, z) = (280, 40, 500)$ m. The center of the edge associated with this point is located in the main area of consideration 500 m in the ground. The length of the size of this edge is 225.39 m and the average volume of the surrounding cells is 6×10^6 m^3. The third point is chosen far away from the source in the deeper parts of the mesh where the dimensions of cells begin to get large. The coordinate of the third point is $(x, y, z) = (5600, 30, 1400)$ m with a length of 790 m for the considered edge and an average volume of 2×10^8 m^3 for the surrounding cells.

For each frequency, and for the specific row of the coefficient matrix that corresponds

to each of the edges chosen above, the maximum values of C_{ij} and $\omega\mu_0 D_{ij}$ (which are their diagonal elements C_{ii} and $\omega\mu_0 D_{ii}$) are shown. Also, the maximum value of the term, $\mu_0 F_{il}$, where l is the specific column of the coefficient matrix that corresponds to the above node, is indicated. For this node, the maximum-valued element from the term ωG_{lj} and H_{ll} (which again is the diagonal element of $\mathbf{H}$) are also shown. As illustrated in Table 3.1, small sizes of the edges and subsequently small volumes of the cells in region 1 cause relatively small matrix entries. Although by decreasing the frequency from 100 to 0.1 Hz the magnitude of the conductivity terms $\omega\mu_0 D_{ij}$ and ωG_{lj} decrease in each region, the entries C_{ii} and H_{ll} remain constant and preserve the diagonal structure of the coefficient matrix. However, because of the large volume of the cells, the term ωG_{lj} increases significantly in the second and third regions especially for the higher frequency of 100 Hz. For the edges located along the refined line of observations the term H_{ll} is comparable to or larger than that of ωG_{lj} for lower frequencies (e.g., see the values in Table 3.1 for 0.1 Hz in region 1). Because of the vanishing conductivity term, $\omega\mu_0 D_{ij}$, the E-field system, which only comprises $\mathbf{C}$ and $\omega\mu_0\mathbf{D}$, looses its conductivity information and struggles to converge. However, in the decomposed system, the conductivity information is present additionally in the term $\mathbf{H}$ which maintains its influence as the frequency decreases. Hence, the system can be solved efficiently using iterative methods.

For the edge and its corresponding node in region 1 the magnitude of the source terms $\mu_0 S_1$ and S_3 are 2.61×10^{-8} and 0.366 respectively. This comparison also holds for the average values of these two terms. This results in larger values of the scalar potentials. This is a situation for which the galvanic component coming from the equation of conservation of charge dominates the induction component. This is confirmed in Figure 3.15 which shows the galvanic part ($-\nabla\phi$), inductive part ($i\omega\mathbf{A}$),

Table 3.1: A sample of the entries of the coefficient matrix (see equation 3.27) for the model used in Section 3.3.2 for frequencies of 100 and 0.1 Hz. The numbers correspond to particular edges and nodes in six different regions in the conductive half-space (see text for details).

Elements of the coefficient matrix							
region	freq (Hz)	C_{ij}	$\omega\mu_0 D_{ij}$	$\mu_0 F_{il}$	ωG_{lj}	H_{ll}	$\ell(m)$
1	100.	0.6800	5.05×10^{-3}	8.26×10^{-13}	4.13×10^{-4}	3.52×10^{-3}	0.12
2	100.	1400.5	11.2	1.42×10^{-4}	71082	7.722	225.39
3	100.	4615.5	425	1.23×10^{-3}	617682	30.51	789.37
1	0.1	0.6800	5.05×10^{-6}	8.26×10^{-13}	4.13×10^{-7}	3.52×10^{-3}	0.12
2	0.1	1400.5	1.12×10^{-2}	1.42×10^{-4}	71.082	7.722	225.93
3	0.1	4615.5	0.425	1.23×10^{-3}	617.682	30.51	789.37

and total electric field. The horizontal component of the fields on a horizontal plane at a depth of 50 m in the ground is shown. It is clear that the inductive part is negligible and that the electric field is dominated by the contribution from the scalar potential. Detailed investigation of the inductive and galvanic parts of the electric field for different examples and formulations are presented in the following chapters.

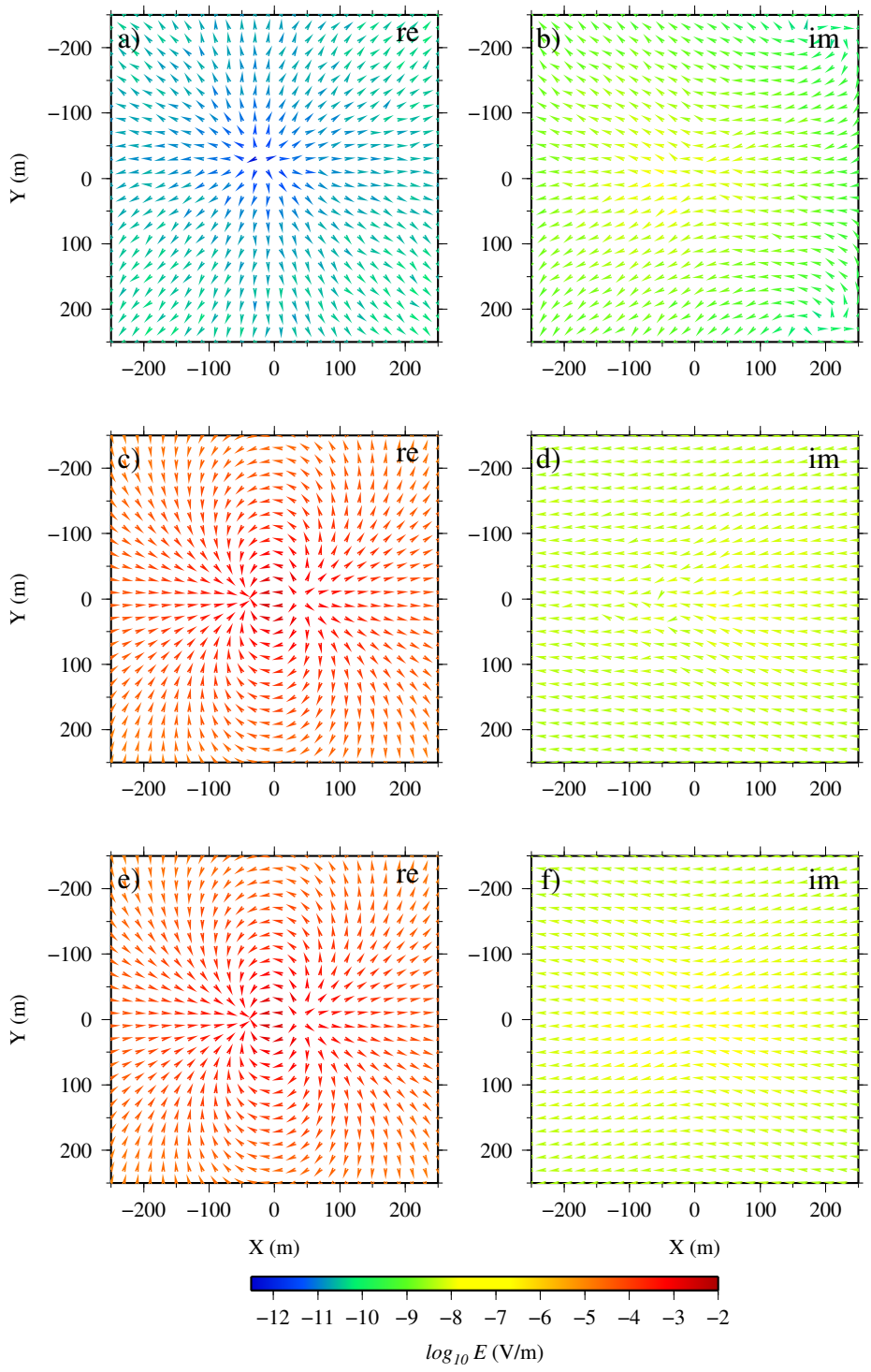

Figure 3.15: The inductive part (a and b), galvanic part (c and d) and total electric field (e and f) for the first half-space example for a frequency of 0.1 Hz. All six panels show the horizontal component of the field at a depth of 50 m in the ground. Direction and strength of the fields are respectively shown using the arrows and their colors. Panels (a), (c) and (e) show the real parts. Panels (b), (d) and (f) show the imaginary parts.

Chapter 4

Inductive and Galvanic Components of the Electromagnetic Response

4.1 Introduction to inductive and galvanic fields

In this chapter the numerical modeling code for the $\mathbf{A} - \phi$ decomposition approach is further verified for a number of models presented in geophysical literature. As discussed in Chapter 1 a revealing description of the geophysical electromagnetic distortion can be given in terms of the inductive and galvanic effects. In theory both of these effects are present in the entire frequency range. However depending on the frequency applied, and the type of EM excitation source and its position relative to the underground anomaly, the contributions from the inductive and galvanic fields vary (Menvielle, 1988). For the $\mathbf{A} - \phi$ method using the formulation presented in Chapter 3, an investigation of the inductive and galvanic components of the EM field is presented here.

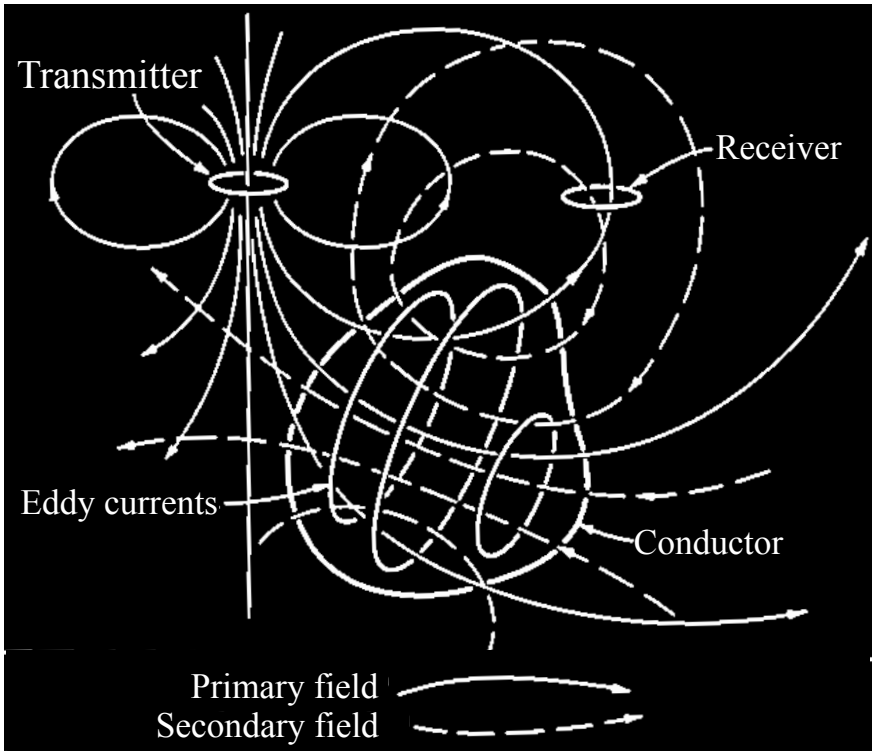

Figure 4.1: A general picture of the electromagnetic induction phenomena (modified from Grant and West, 1965)

The inductive field and current, by definition, arises via the time derivative of the magnetic flux, **B**, in Faraday's law of induction (see equation 2.1) (West and Macnae, 1991). The inductive electromagnetic response is a function of electrical properties (i.e., conductivity here) and geometry in addition to being an explicit function of frequency (Jiracek, 1990). Closed vortex type of field and current circulations are induced in a situation where a conductive target is isolated by free-space or a significantly resistive host. Figure 4.1 shows the generalized concept of the EM induction phenomena. Here the subsequent primary field, established using an alternating current through the transmitter coil, induces eddy current fields in the underground electrical conductor (Grant and West, 1965). Circulation of currents in the conductive structure generates a secondary magnetic field that is measured in the receiver coil.

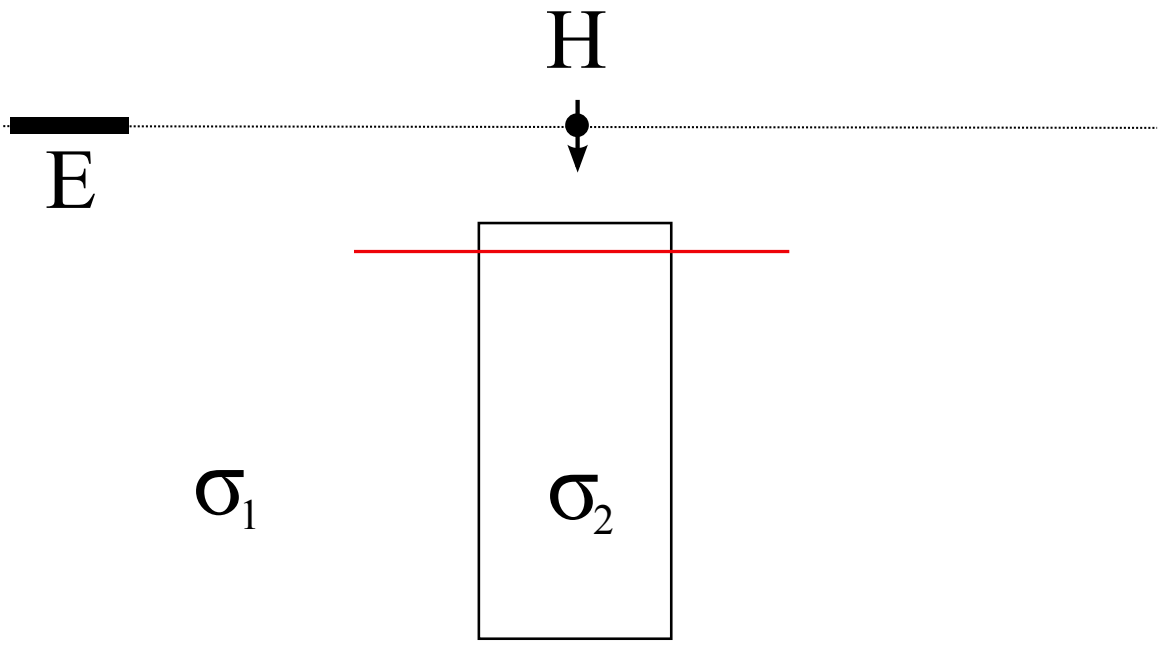

Figure 4.2: The geometry of the model considered for conceptual illustration of the inductive and galvanic effects. For the inductive effect shown in Figure 4.3 the magnetic dipole source located above the prism is used. For the galvanic effects shown in Figure 4.8 the electric dipole source located on the side to the rectangular body is used.

A typical representation of the inductive effect is shown in Figure 4.3 where the arrows of electric field, current density, and magnetic field are shown for an infinitesimal magnetic dipole source. Here, the model (see Figure 4.2) consists of a rectangular conductive body of $\sigma_2 = 1$ S/m with dimensions of 100 m $\times$ 100 m $\times$ 400 m in the x-, y-, and z-directions. Also, the background medium is considered as a resistive host, i.e. $\sigma_1 = 10^{-4}$ S/m. A vertical magnetic dipole is also located at the origin 100 m above the center of the conductive rectangle. A frequency of 10 Hz is considered for this example. The arrows plotted in Figure 4.3 are the horizontal component of the total fields in a horizontal plane (shown in red in Figure 4.2) which passes through the conductive target. The moment of the magnetic dipole is perpendicular to the horizontal plane and induces vortex electric fields and the resulting current densities in the horizontal plane. As illustrated in panel (b) in Figure 4.3 the induction process

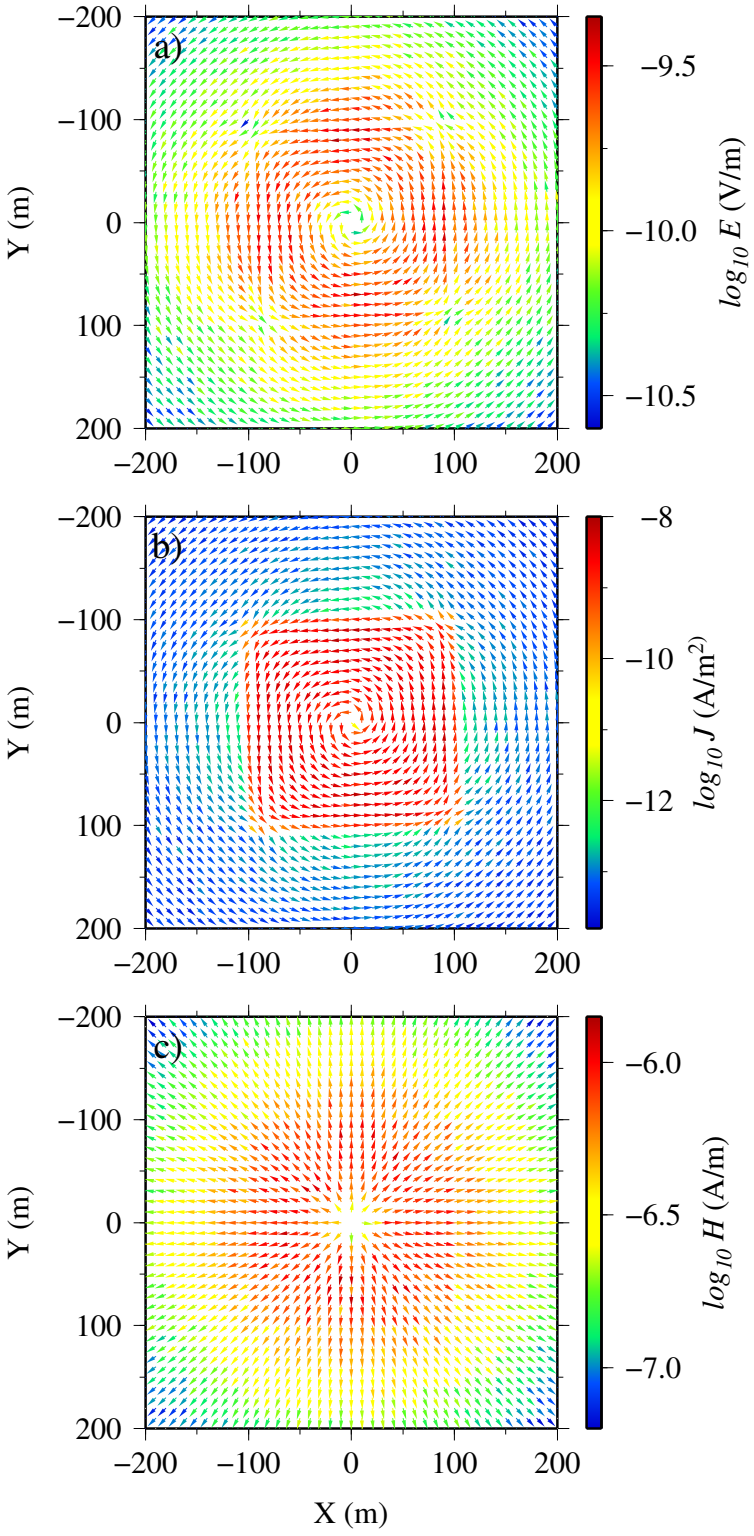

Figure 4.3: Arrows of the total a) electric field, b) current density, and c) magnetic field for a vertical magnetic dipole source and a rectangular conductive body situated in free-space (see Figure 4.2). The conductivity of the target is 1 S/m.

is significant in the conductive target and negligible in the resistive host. Figure 4.4 also shows the magnetic field arrows in the xz-plane at $y = 0$. The coupling between the source and the conductive body is seen here as the magnetic field cuts nicely through the conductive body.

The galvanic phenomena emerges from the principles of the DC resistivity method. For a homogeneous Earth, Figure 4.5 shows the current flow from two current electrodes (Dohr, 1981). These physical flow of current can be seen in the EM exploration scenario if, for example, a grounded wire is used as the source of excitation. Figure 4.6 shows the produced total electric field and the relevant current density for a conductive half-space of 0.01 S/m. Here a 200 m wire which is located on the surface at the origin and oscillates with a frequency of 1 Hz is chosen as the source of excitation. However, for the situation where there is an inhomogeneity in the subsurface, i.e. the sphere of different conductivity in Figure 4.7, the charge build up alters the field around the anomaly and subsequently deflects the current lines (Li and Oldenburg, 1991). In order to demonstrate this effect a conductive object of conductivity σ_2 which is surrounded by or in touch with an otherwise conductive host of conductivity σ_1 (see Figure 4.2) is considered. Depending on the relative magnitude of these conductivities the galvanic effect occurs in the form of current channelling into the conductive regions and current deflection around the resistive zones (Jiracek, 1990). An illustration of this effect is shown in Figures 4.8 and 4.9 where the horizontal components of the electric field and current density are shown respectively for the same geometry described above (see Figure 4.2). Here the conductive body is excited from the side (i.e., the left side here) by a horizontal wire source of 200 m as shown in Figure 4.2. The electric source oscillates with a frequency of 1 Hz and is located far enough (e.g., approximately 1 km) that incident fields are perpendicular to the vertical sides of the

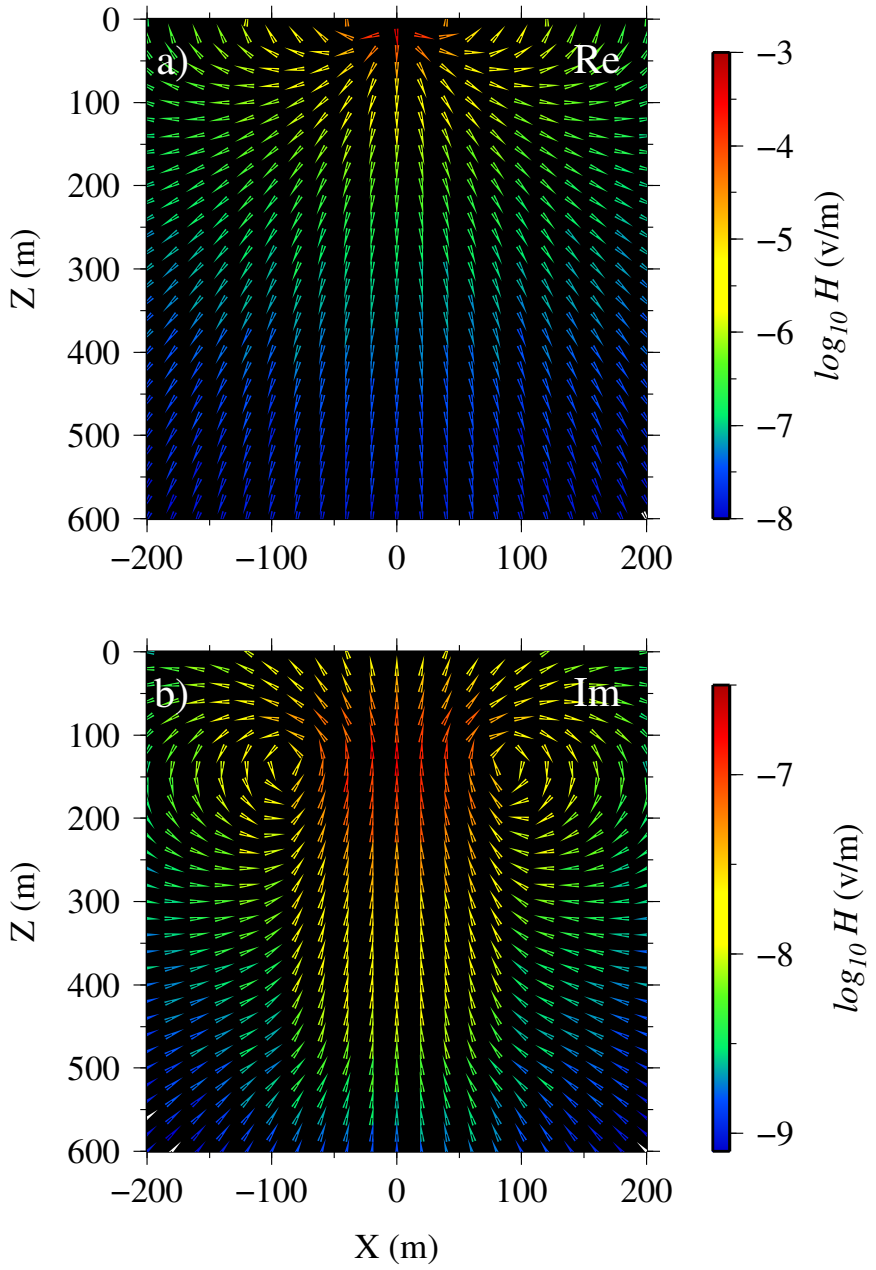

Figure 4.4: Arrows of the total magnetic field for the a) real and b) imaginary components in the xz-plane cutting vertically through the rectangular body.

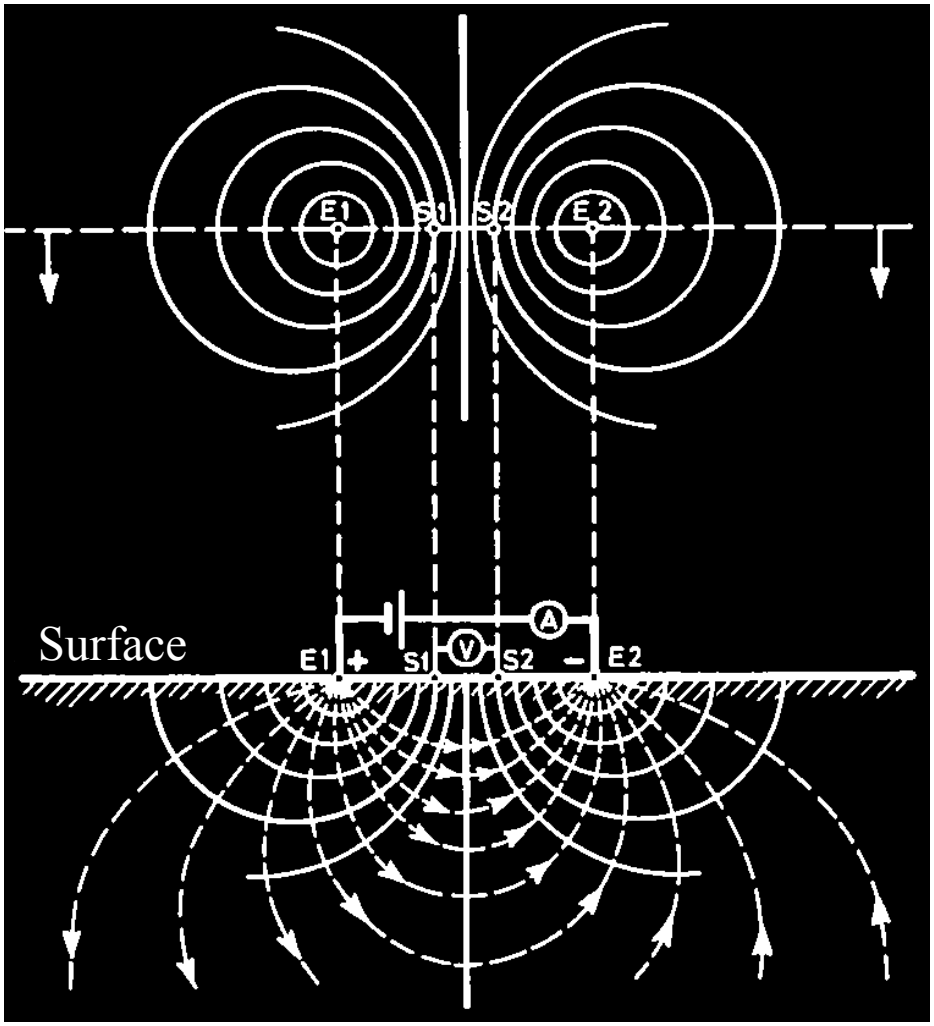

Figure 4.5: An illustration for the distribution of the DC-resistivity current and potential in a homogeneous Earth model. E_1 and E_2 are the current electrodes, and S_1 and S_2 are the potential electrodes. The top panel shows the line of equal potentials at the horizontal Earth surface. The bottom panel shows the current lines (dotted) and the potential lines (solid) in a vertical section (modified from Dohr, 1981).

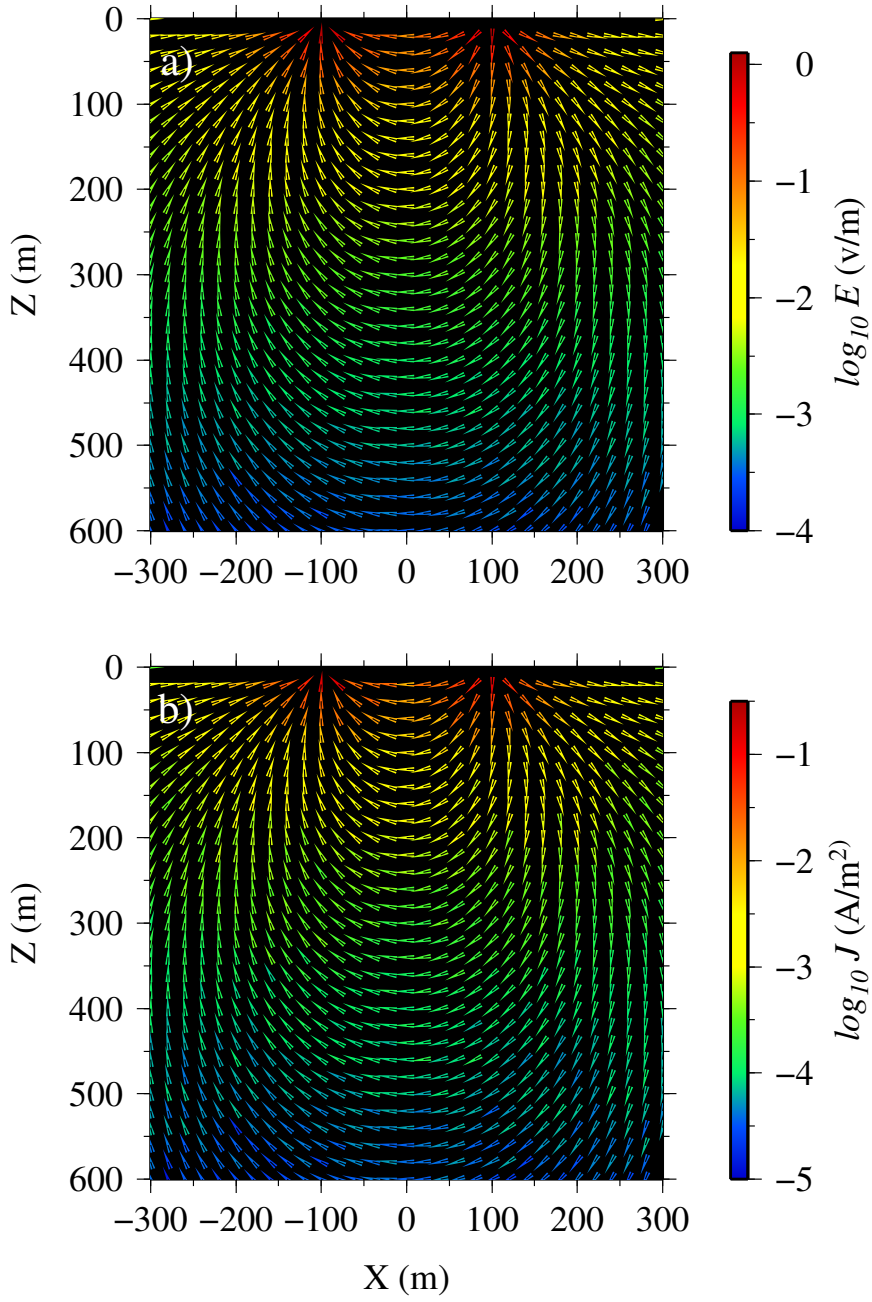

Figure 4.6: Arrows of the real component of the total a) electric field and b) current density for a wire source of 200 m and a frequency of 1 Hz.

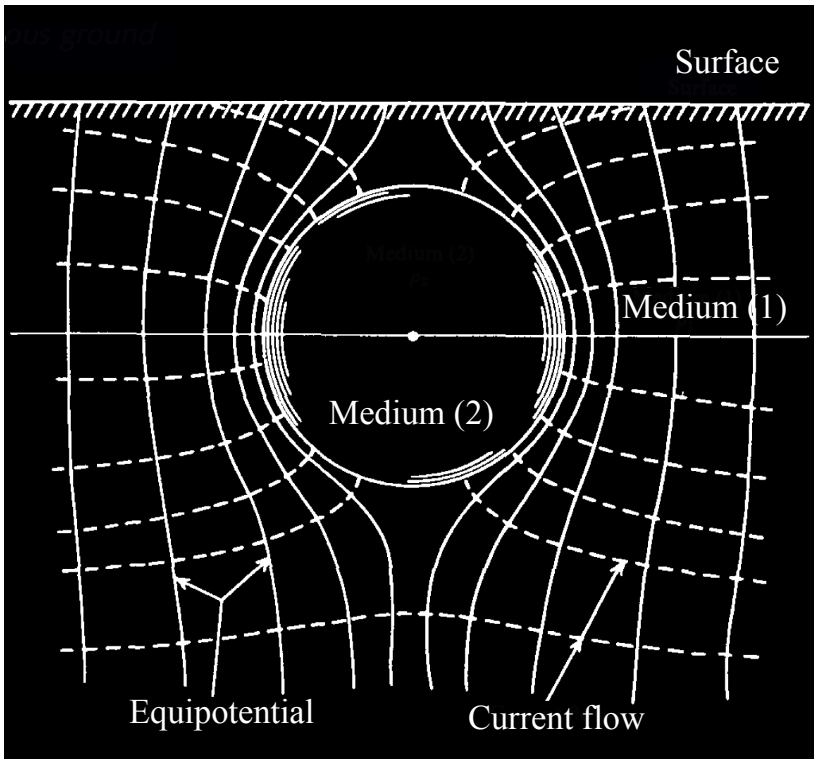

Figure 4.7: A schematic picture of current flow (dotted) and equipotantial (solid) lines for a conductive sphere buried in a background of distinct conductivity. The external electric field is directed horizontally from the left to the right (modified from Telford et al., 1990).

body. The resulting fields and currents shown in panels (a) of Figures 4.8 and 4.9 are for a model which consists of a conductive block of $\sigma_2 = 0.1$ S/m located in a resistive host with a conductivity of $\sigma_1 = 0.01$ S/m. It is seen that because of the greater conductivity of the target relative to the surrounding host the electric field (in panel a of Figure 4.8) and the current density (in panel a of Figure 4.9) tend to be drawn in by and channel through the conductive target. In contrast, the fields and the corresponding currents shown in panels (b) of Figures 4.8 and 4.9 are for a model in which the conductivity of the target is less than that of the surrounding host ($\sigma_2 = 0.01$ S/m and $\sigma_1 = 0.1$ S/m). In contrast to the current channelling effects seen for the model containing the conductive target, the electric field and the current density avoid entering the resistive target and tend to flow around it in the conductive host. The behaviors of the fields and currents seen here correspond to a purely galvanic case that is seen for the DC resistivity scenarios.

4.2 Examples

In this section the numerical modeling code developed in this thesis is tested and verified for a variety of examples which have been published in the literature. The examples presented in the following sections are for different configurations in geophysical modeling scenarios. The first example investigates the field from a grounded horizontal electric wire that is used as the most common type of source in the low-frequency land-based CSEM surveys (see e.g., Zonge and Hughes, 1987). The second model of conductivity (the graphite cube in brine example) considered here contains large conductivity contrasts that mimic the classical geophysical EM modeling scenarios of a highly conductive metalliferous body residing in resistive shield rocks (see e.g., Frischknecht et al., 1991). This ivolves a common profiling EM survey method

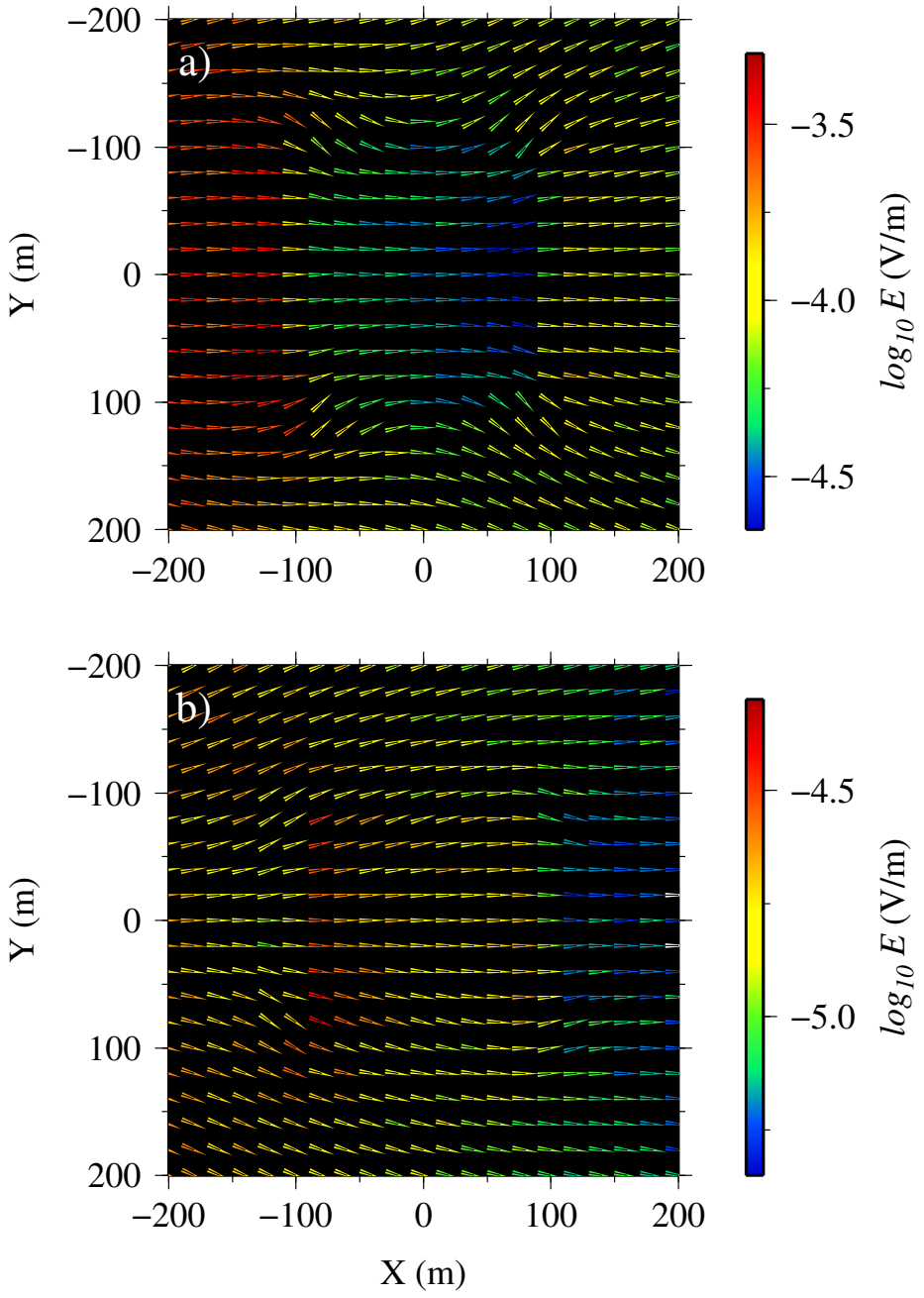

Figure 4.8: Arrows of the horizontal component of the total electric field for an electric wire source and a rectangular body. The geometry of source and rectangular body is shown in Figure 4.2. In panel (a) the conductive target of 0.1 S/m is surrounded by a less conductive host with a conductivity of 0.01 S/m. In panel (b) the conductive host with a conductivity of 0.1 S/m surrounds a less conductive target of 0.01 S/m.

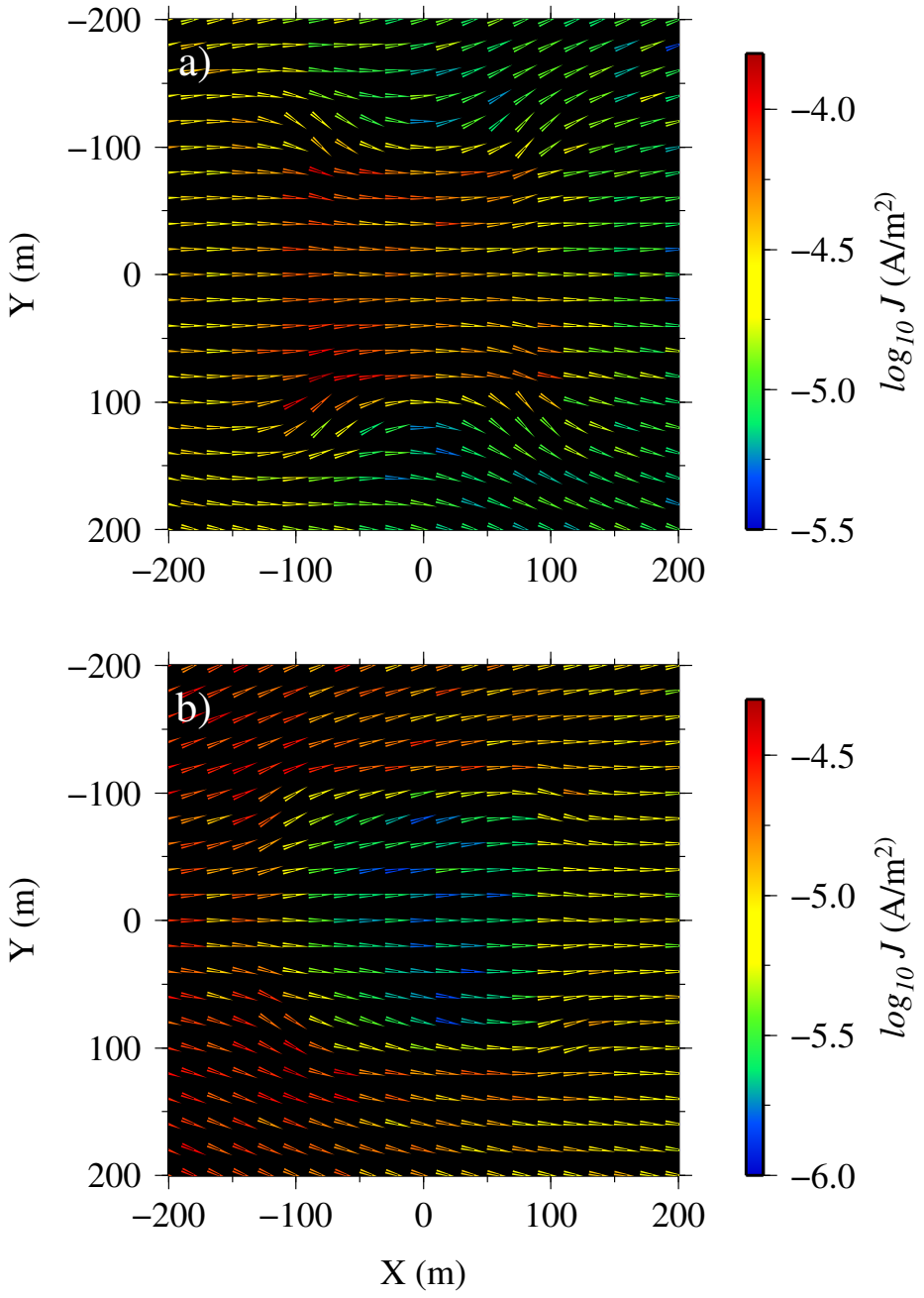

Figure 4.9: Arrows of the horizontal component of the current density for an electric dipole source and a rectangular body. In panel (a) the conductive target of 0.1 S/m is surrounded by a less conductive host with a conductivity of 0.01 S/m. In panel (b) the conductive host with a conductivity of 0.1 S/m surrounds a less conductive target of 0.01 S/m.

that uses a moving dipolar source-receiver configuration. Such profiling configurations are used in both airborne (e.g., Helicopter EM surveys; Miensopust et al., 2013) and land-based (e.g., Geonics EM-34 ground conductivity meter) exploration scenarios. The third example, which investigates a resistive canonical disk model, is the subject of recent modeling problems for hydrocarbon exploration in marine environments. Similar to the first example, this problem consists of a wire source (conventionally named a finite dipole) that has inductive interaction with the Earth due to its insulated length and also galvanic coupling because of its bare end-points. For all examples presented here the inductive and galvanic components of the resulting electromagnetic responses, and the interplay between them, are investigated.

4.2.1 Prism-in-a-half-space and electric line source

The first example presented here is for a conductive prism in a homogeneous half-space background model and for an electric line source. Figure 4.10 shows a vertical cross-section of the 3D model. The model consists of a vertical prism with a conductivity of 0.2 S/m buried in a homogeneous half-space of 0.02 S/m. The grounded wire source extends from the origin to 100 metres in the x-direction. The center of the conductive prism is 1000 metres away from the origin. The current is set to 1 A and a frequency of 3 Hz is chosen. This model and the relevant frequency is presented in Farquharson and Oldenburg (2002). The entire computational domain of 35 km $\times$ 35 km $\times$ 35 km is subdivided into tetrahedral elements. Figure 4.11 shows a meshed view of the main area of the mesh consisting of the source, the line of observation locations and the conductive prism. By imposing a minimum quality factor of 1.414 for the radius-edge ratio and a minimum dihedral angle of 16 degrees in the meshing program (TetGen) the number of generated tetrahedrons is 613300. Also the total number of edges and nodes in the mesh are 713542 and 99855 respectively. The mesh is locally refined

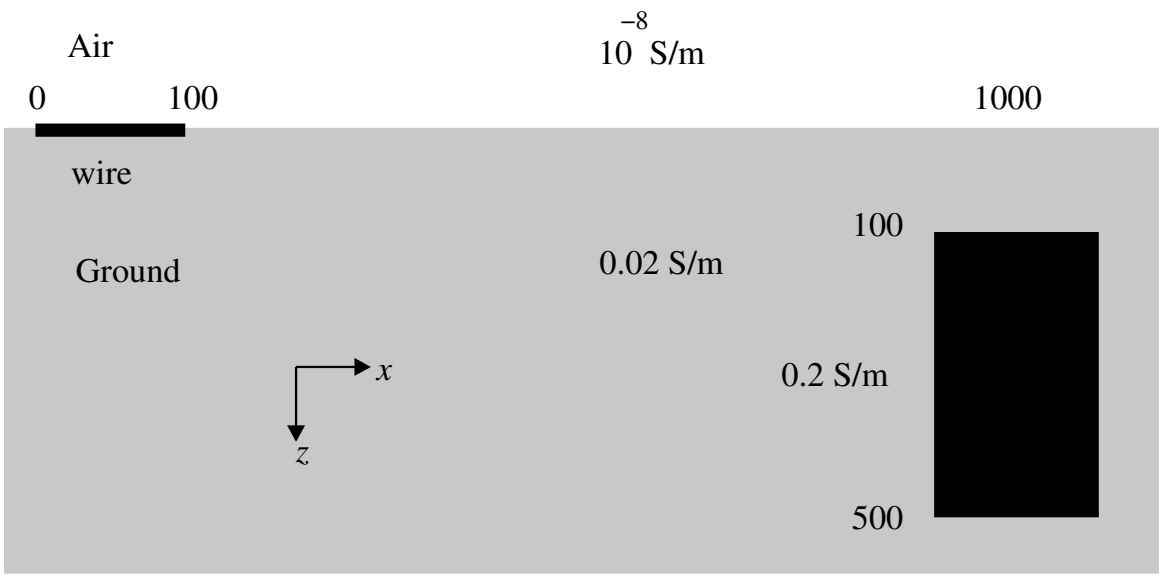

Figure 4.10: The geometry for the prism and electric line source example. The 100 m grounded wire is located on the air-ground interface. The dimensions of the conductive prism are 120 m $\times$ 200 m $\times$ 400 m in the x-, y- and z-directions.

about the source, the line of observation locations and in the conductive prism.

For this mesh Figure 4.12 shows the behavior of the total electric field at observation points along the profile over the center of the prism. The respective cross and plus symbols are the real and imaginary parts of the electric field calculated using the $\mathbf{A} - \phi$ decomposed FE approach. The results are verified through comparison with those from the integral-equation (IE) solution of Farquharson and Oldenburg (2002), and those from the DC resistivity modeling program of Li et al. (1999), DCIP3D. DC resistivity data were only available for 9 locations over the prism and for the real component of the electric field. It can be seen in Figure 4.12 that the results calculated using these three approaches are alike for the total electric field. Here for the integral-equation solution of Farquharson and Oldenburg (2002) the conductive prism is subdivided into $8 \times 8 \times 8$ cells in the x-, y- and z- directions. Also, the agreement between the responses is quantified by averaging the corresponding data

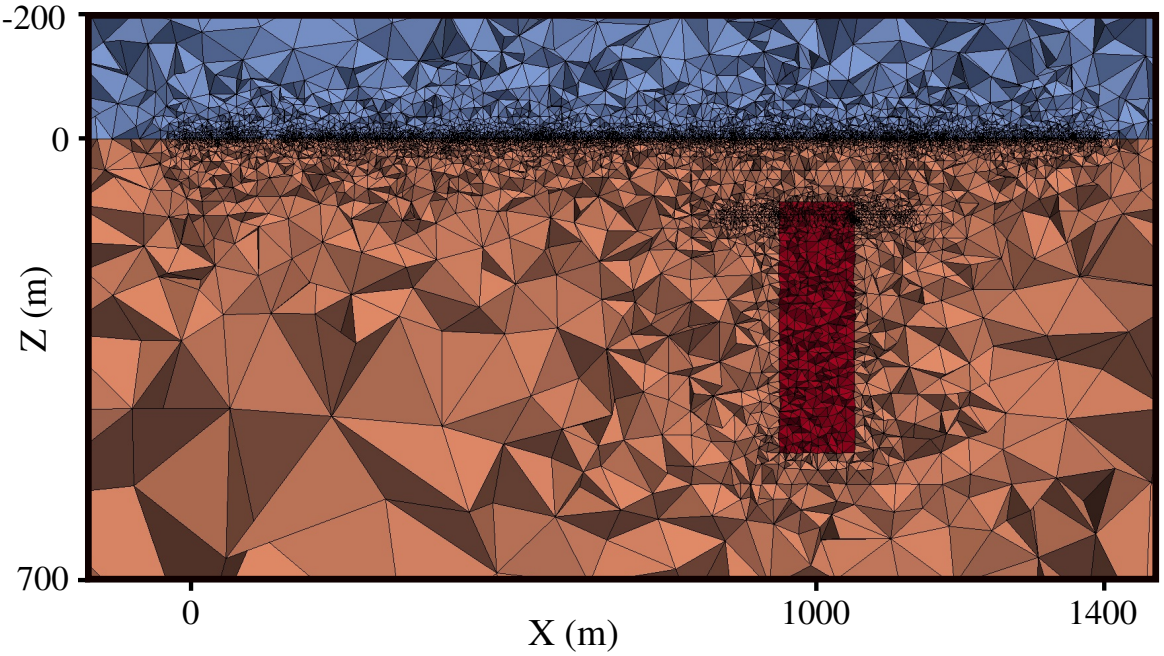

Figure 4.11: An enlarged xz cross-section of the central part of the tetrahedral mesh used for the prism and electric line source example. The conductive ground and the resistive air are shown in light brown and blue respectively. The conductive prism is shown in red. The Earth's surface is flat and the mesh is refined about the grounded wire source, along 1000 metres of observation locations, and around the conductive prism.

differences at each observation location (e.g., $(\sum_{i=1}^{n_{obs}} \frac{|\mathbf{E}_2 - \mathbf{E}_1|}{max(\mathbf{E}_2, \mathbf{E}_1)})/n_{obs}$). In particular for a frequency of 3 Hz, the average mismatch in the total field between the FE and IE results is only 1.35 percent for the real part and 2.25 percent for the imaginary part. In order to compare with the DC resistivity data (see squares symbols in Figure 4.12), the finite-element EM solution is implemented for an absolute frequency of zero (see blue circles in Figure 4.12). As a good agreement for the points shown here these electric fields are different by only 1.39 percent in average. The effect of the conductive prism on the data is apparent in the small reduction of the electric field around $x = 1000$ m.

The secondary electric field was calculated by subtracting from the total electric field the response of a homogeneous half-space model computed via FE. As shown in Figure 4.13 the agreement between the secondary fields from the finite-element and integral-equation methods is generally good. In particular the mismatch between FE and IE fields are 11.13 percent for the real part and 24.98 percent for the imaginary part of the field. It is thought here that the integral-equation solution is affected by the coarse meshing considered for the scatterer ($2 \times 2 \times 2$ nodes for volume integrations and $5 \times 5 \times 5$ nodes to integrate IE surface integrals; see Farquharson and Oldenburg (2002) for details). The scattered FE field for a frequency of zero is also shown in Figure 4.13. There is good agreement between the FE and DC-resistivity data with the average difference between them being 6.18 percent.

The frequency of 3 Hz used here was considered as the lowest frequency employed in the integral-equation solution of Farquharson and Oldenburg (2002). Here however the $\mathbf{A}-\phi$ finite-element approach enabled using an absolute frequency of zero. For this scenario all off-diagonal terms in equation 3.27, which are functions of frequency, will

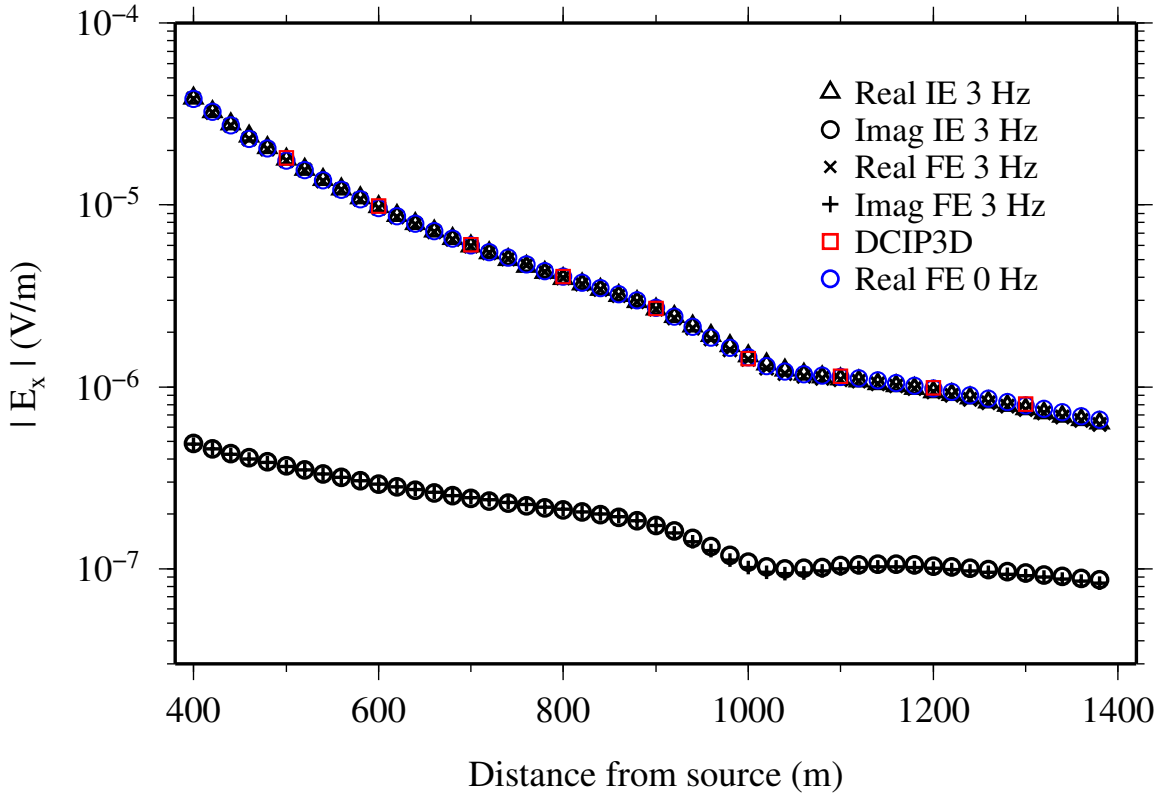

Figure 4.12: The x-component of the electric field, E_x, along a profile directly over the conductive prism. The cross and plus symbols are the real and imaginary parts of the electric field calculated using the $\mathbf{A} - \phi$ decomposed approach for a frequency of 3 Hz. The triangles and circles are the real and imaginary parts of the electric field calculated using the integral equation approach of Farquharson and Oldenburg (2002) again for 3 Hz. Circles in blue are the real part of the electric field for the decomposed approach for a zero frequency. Squares shown in red are data calculated using the DC resistivity forward modeling code, DCIP3D, of Li et al. (1999).

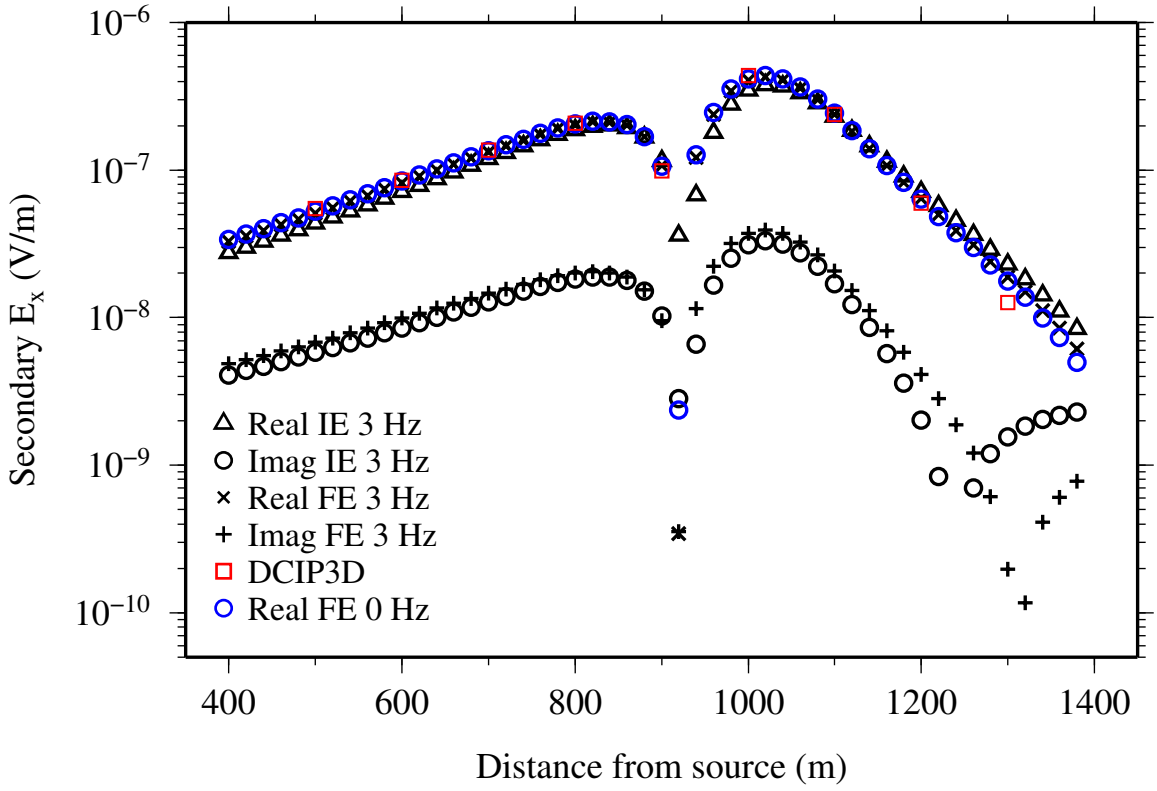

Figure 4.13: The real and imaginary parts of the secondary electric field computed using the finite-element method in this paper (cross and plus symbols), the integral-equation approach of Farquharson and Oldenburg (2002) (triangles and circles), and the DC resistivity modeling program of Li et al. (1999). Circles in blue are the real part of the secondary field for the finite-element approach for a zero frequency.

disappear, therefore a faster solution to the simplified system is obtained. Figure 4.14 shows the behavior of the residual norm for iterative solutions for frequencies of 3 and 0 Hz. For the $\mathbf{A} - \phi$ run whose results are presented above a Krylov subspace of 200 for the GMRES solver and a fill-in factor of $lfil = 3$ for the ILUT preconditioner were used. It is seen in Figure 4.14 that for a frequency of 3 Hz the iterative solver reduces to an approximate residual norm of 10^{-11} after approximately 6000 iterations. The computation time for this run was roughly 42 minutes. Here also a relative residual norm of 2.91×10^{-9} is obtained for the final solution of the iterative solver. By comparison, the convergence for the frequency of zero is significantly faster as a relatively smaller residual norm of approximately 10^{-14} is given after only 3000 iterations.

An explanation for the quick convergence of the decomposed solution for the frequency of 3 Hz is provided in Table 4.1. The elements of the coefficient matrix for three points (i.e. the center of three particular edges and their connected nodes) located in three regions of the mesh are shown. The first point, which corresponds to region 1 in Table 4.1, is located just below the surface along the profile of observation locations at $(x, y, z) = (211, 0.5, 1)$ m. The average volume of the tetrahedrons surrounding this edge is 2.01 m^3. The second point (region 2 in the table) corresponds to an edge within the conductive prism with coordinates of $(x, y, z) = (1020, -15, 350)$ m. The average volume of the cells around this edge is 260 m^3. The third edge is chosen to be far from the line source and deeper in the homogeneous half space at $(x, y, z) = (1400, -330, 700)$ m. As seen in Table 4.1 (region 3) its length is greater than the first and second edges. Also the average volume of the cells surrounding this edge is approximately 560000 m^3. It is seen here that the additional conductivity term $\mathbf{H}$ in conjunction with $\mathbf{C}$ preserve the diagonal dominance of the coefficient matrix despite the vanishing term, $\omega\mu_0\mathbf{D}$.

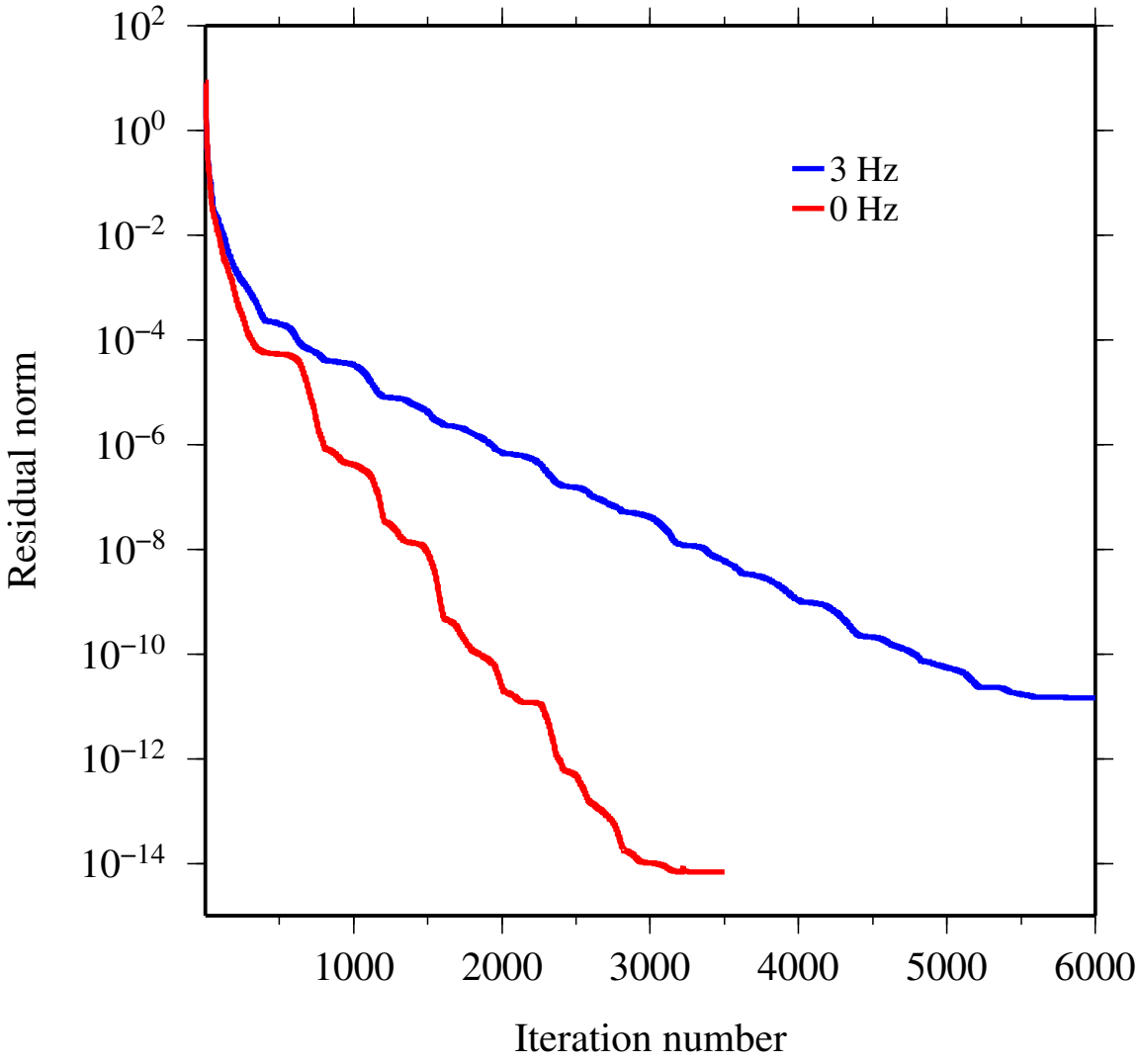

Figure 4.14: The convergence curves for the $\mathbf{A} - \phi$ finite-element solutions for frequencies of 3 Hz (shown in blue) and zero (shown in black) for the line source and conductive prism example.

Table 4.1: A sample of the entries of the coefficient matrix (see equation 3.27) for the prism and line source example. The numbers correspond to a specific edge and its connected nodes located in the half-space (regions 1 and 3) and in the conductive prism (region 2).

Elements of the coefficient matrix								
region	freq (Hz)	C_{ij}	$\omega\mu_0 D_{ij}$	$\mu_0 F_{il}$	ωG_{lj}	H_{ll}	σ (S/m)	ℓ (m)
1	3	24.85	2.46×10^{-6}	5.68×10^{-8}	0.852	0.203	0.02	3.06
2	3	67.76	3.36×10^{-3}	2.33×10^{-5}	349.21	15.45	0.2	11.90
3	3	2122.96	1.66	7.63×10^{-4}	10745.41	22.15	0.02	192.42

Investigation of the inductive and galvanic components was also carried out. A horizontal plane of nodes was inserted into the mesh at a depth of $z = 120$ m which corresponds to 20 m below the top of the prism. This plane of nodes is introduced only to obtain vector plots of better quality, not to improve convergence or accuracy of the solution. Fields and current densities were calculated at these nodes and the results for a frequency of 3 Hz are shown in Figures 4.15 and 4.17. In Figure 4.15, both real and imaginary components of the galvanic part (see panels c and d) decrease in strength in the conductive prism. In fact, the strength and direction of the galvanic part are almost the same as for the total field (see panels e and f). This is clear evidence of the extent to which the galvanic part is dominant in reducing the field in the underground body for a low frequency. In order to show the channelling of the electric field from the resistive host into the conductive body here the arrows of the galvanic and total fields are being replotted in a different color scale (see Figure 4.16). In particular here, the electric field tends to enter and leave the body from its sharp corners. In contrast to the fields, both inductive and galvanic parts of the current density (Figure 4.17) increase in magnitude in the conductive prism. Again, because it significantly resembles the total current density, the galvanic part is the dominant component.

In order to demonstrate the continuity conditions, the behaviors of the electric field

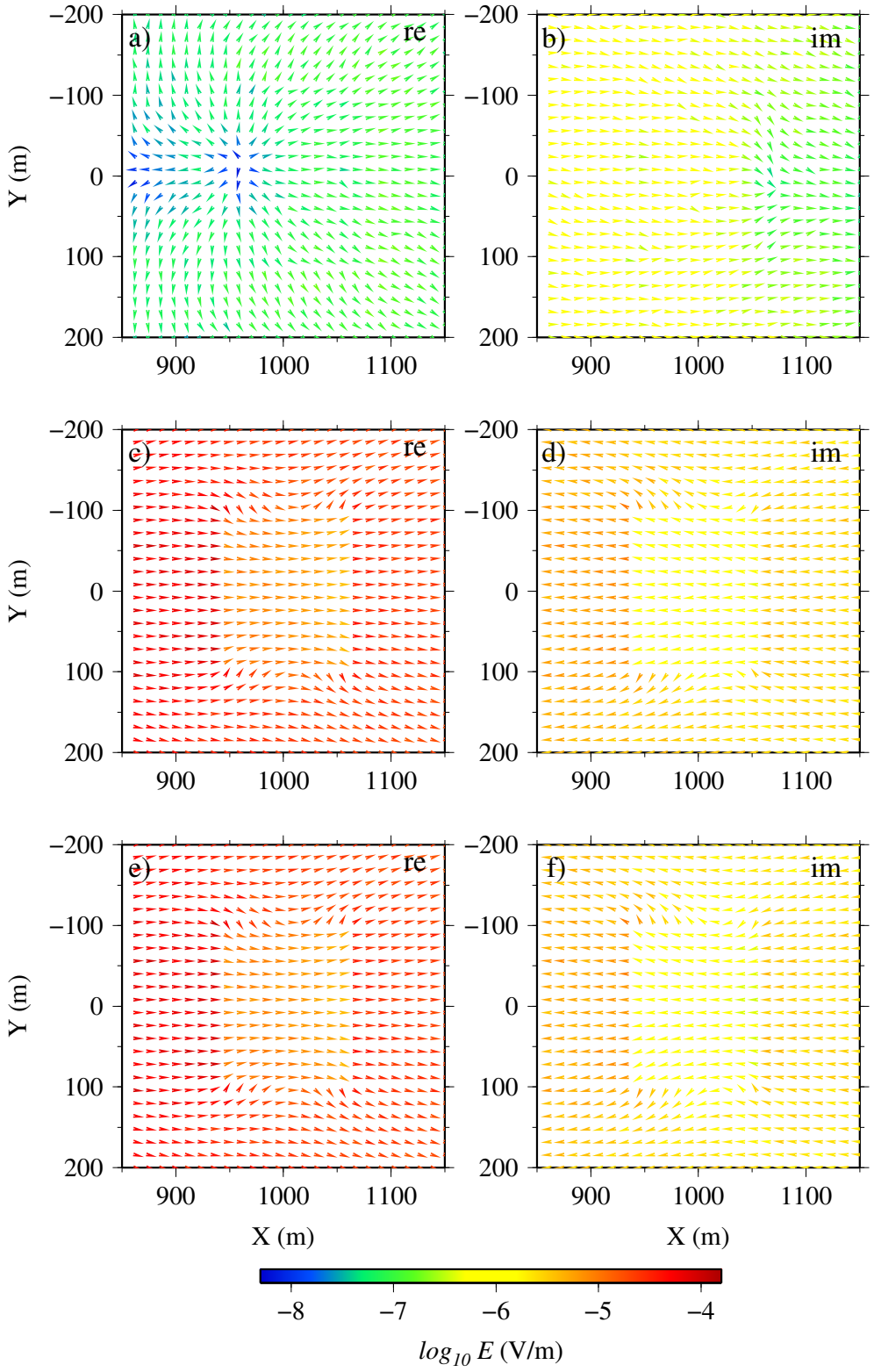

Figure 4.15: The inductive part of the electric field, the galvanic part, and the total electric field in the xy plane for the prism and line source example for a frequency of 3 Hz. All six panels show the horizontal component of the fields at a depth of 120 m in the ground: the real (a) and imaginary (b) components of the inductive part; the real (c) and imaginary (d) components of the galvanic part; and the real (e) and imaginary (f) components of the total electric field.

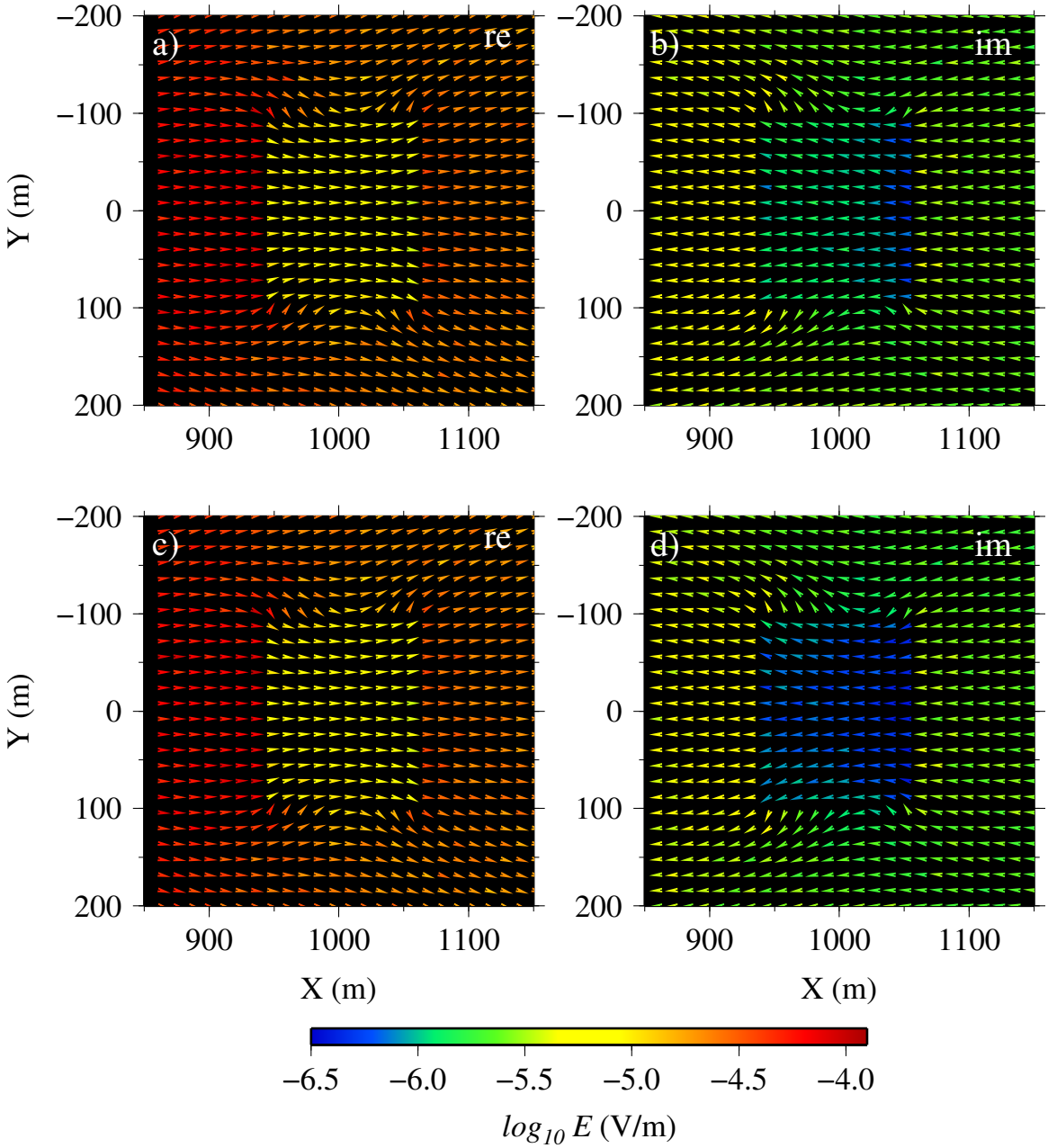

Figure 4.16: The channelling of the fields. The galvanic part and the total electric field in the xy plane for a frequency of 3 Hz. All four panels show the horizontal component of the fields at a depth of 120 m in the ground: the (a) real and (b) imaginary components of the galvanic part, and the real (c) and imaginary (d) components of the total electric field.

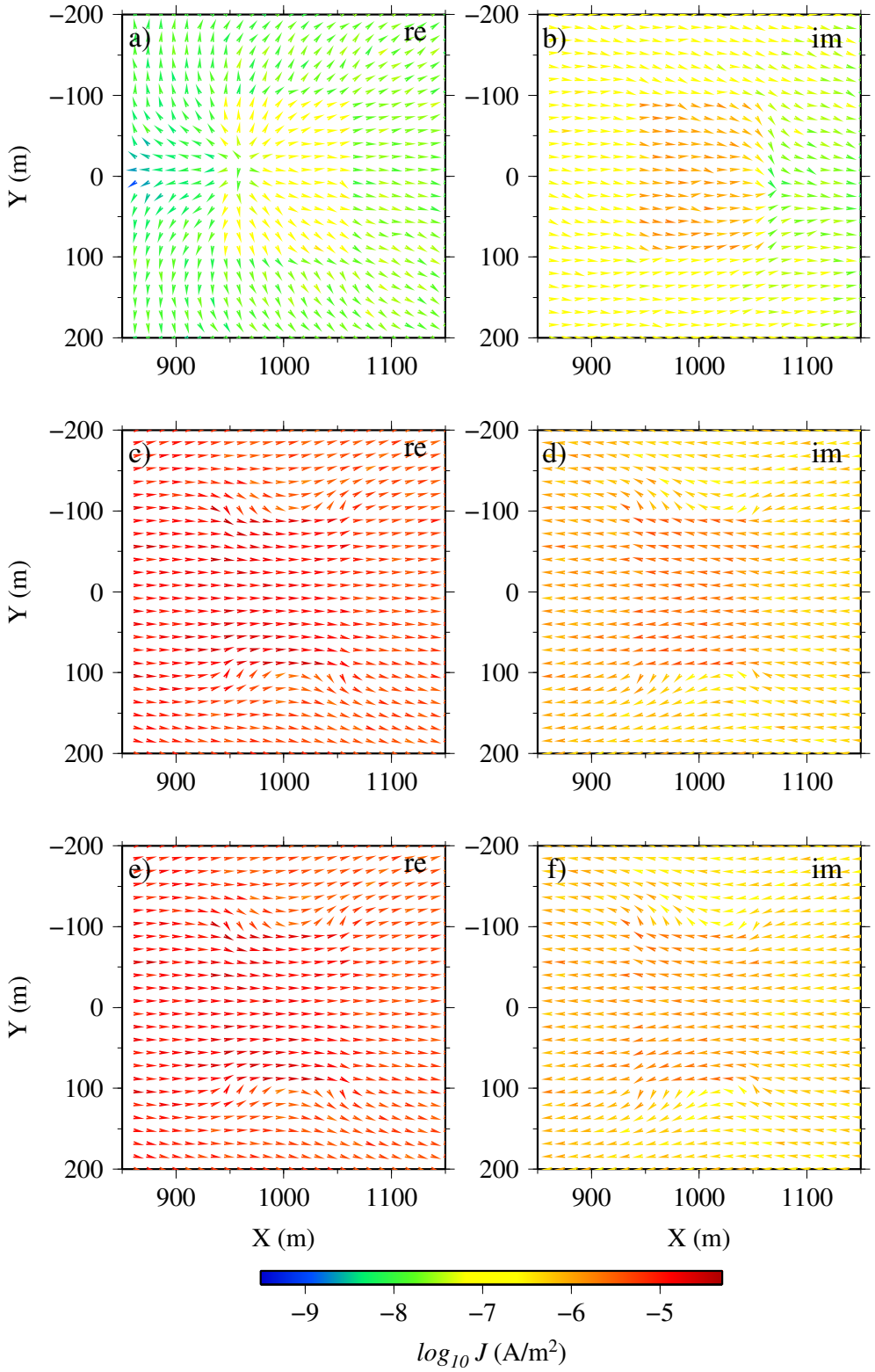

Figure 4.17: The inductive part of the current density, the galvanic part and the total current density in the xy plane for the prism and line source example for a frequency of 3 Hz. All six panels show the horizontal component of the current densities at a depth of 120 m in the ground: the real (a) and imaginary (b) components of the inductive part; the real (c) and imaginary (d) components of the galvanic part; and the real (e) and imaginary (f) components of the total current density.

and current density are investigated across the conductivity interface between the prism and the surrounding host. Figure 4.18 shows the discontinuity (continuity) of the normal component of the electric field (current density), and the continuity (discontinuity) of the tangential component of the electric field (current density) respectively. Here, the plots shown in panels (a)-(d) are the x-components of the electric field and current density for an x-directed profile of observation that passes through the anomalous region at $y = 0$ and $z = 120$. The corresponding plots in panels (e)-(f) are again the x-components of the field and current for a profile parallel to the y-axis at $x = 1000$ and $z = 120$.

4.2.2 Graphite cube immersed in brine and magnetic dipole source

The example presented here verifies the code for models containing large conductivity contrasts. The model is for a graphite cube immersed in brine as shown in Figure 4.19. The conductivity ratio of the graphite to the background brine is very large, namely,: 8630 : 1, which is a challenge for any numerical modeling process. The conductivities of the graphite cube and the brine solution are 6.3×10^4 and 7.3 S/m respectively. The center of the graphite cube is located below $x = 25$ cm. A horizontal coplanar loop transmitter-receiver configuration is considered. The transmitter-receiver pair moves at a height of 2 cm above the surface of the brine. The actual apparatus used to obtain the physical scale modeling data is a tank of brine which is 5 m long, 3 m wide, and 1.3 m deep (Farquharson et al., 2006). Transmitter and receiver coils are also small loops of wires. Because of the small ratio of the cube depth to the coil separation (0.1 here) a strong response for the secondary magnetic field is expected (Farquharson et al., 2006). For frequencies, conductivities and dimensions of the problem considered for this model the induction number, $\sigma f l^2$, is comparable

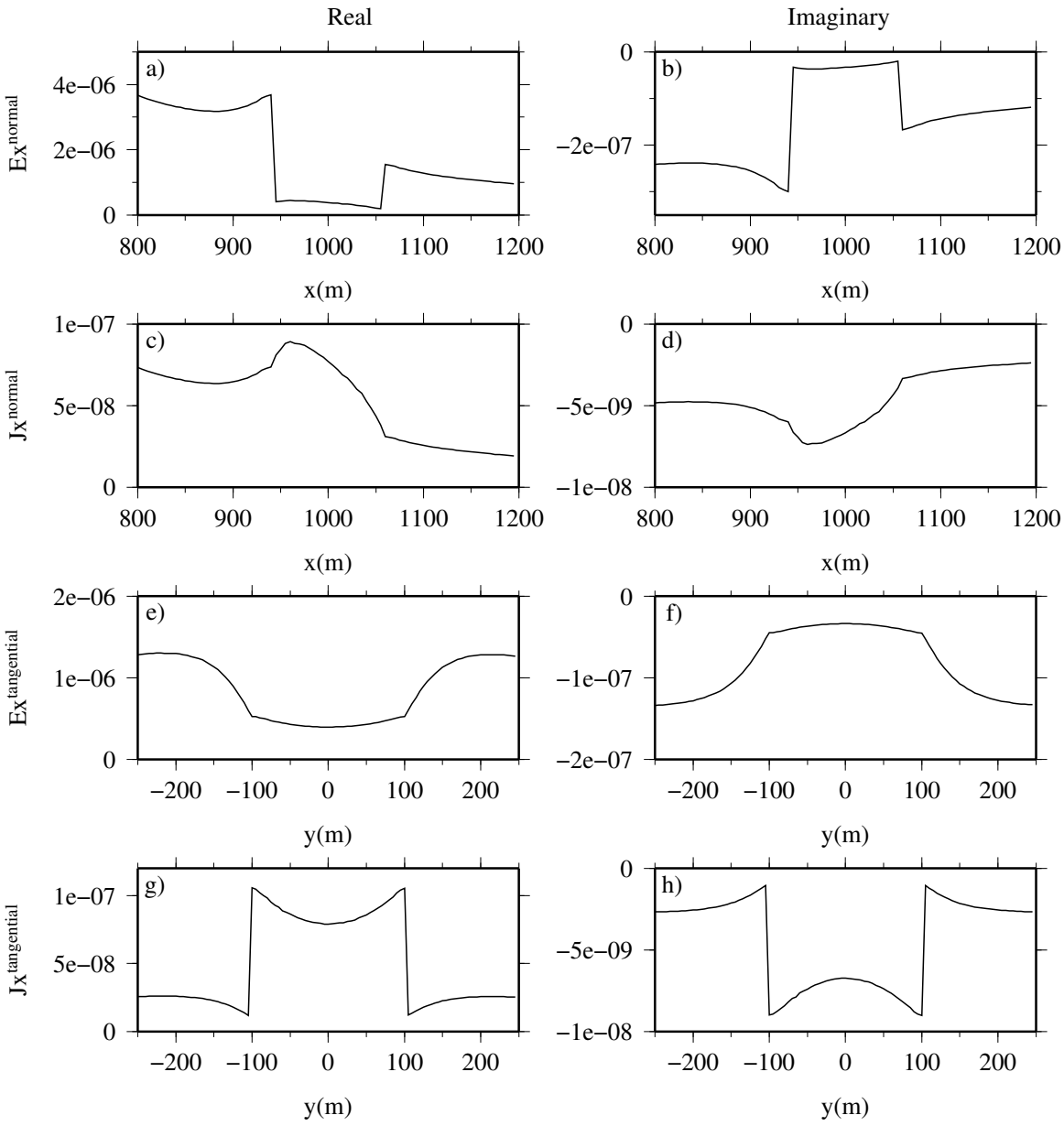

Figure 4.18: Line continuity plots for the electric field and current density. Panels (a and b) show the x-component of the electric field, and panels (c and d) show the x-component of the current density for the horizontal line of observations at $y = 0$ m and $z = 120$ m. Panels (e and f) show the x-component of the electric field, and panels (g and h) show the x component of the current density for the horizontal line of observations at $x = 1000$ m and $z = 120$ m.

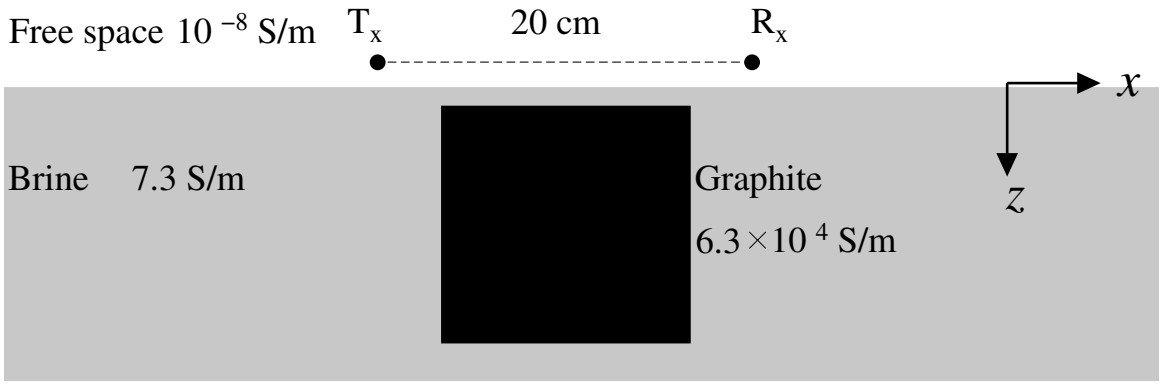

Figure 4.19: The graphite-cube-in-brine model. The graphite cube with a conductivity of 6.3×10^4 S/m is submerged in brine with a conductivity of 7.3 S/m. The 20 cm apart transmitter-receiver pair is in free-space (10^{-8} S/m) and moves along at a height of 2 cm above the surface of the brine.

with those observed in geophysical exploration scenarios. The computational domain of $10 \times 10 \times 10$ m is subdivided into tetrahedral elements. Figure 4.20 shows the main area of the mesh including the line of transmitter-receiver locations and the conductive cube where the mesh is locally refined. For this example the computational domain is subdivided into 592264 elements which gives 688962 edges and 96350 nodes.

A fill-in parameter of 3 was again chosen for the ILUT preconditioner, the GMRES solver was used, and the dimension of the Krylov subspace was set to 200. The z-component of the secondary magnetic field (total field minus free-space field normalized by the free-space field) was calculated using the resulting potentials. Figure 4.21 shows the responses for frequencies of 1, 10, 100, 200, and 400 kHz. Here I was not concerned with modeling the effects of dielectric permittivity (i.e. non-quasi-static situations). The system of equations was solved for 50 measurement locations along a profile directly over the cube. Figure 4.21 also shows the physical scale modeling results obtained for this scenario by Farquharson et al. (2006). Similar to the previous example the agreement between FE and physical scale modeling responses is quanti-

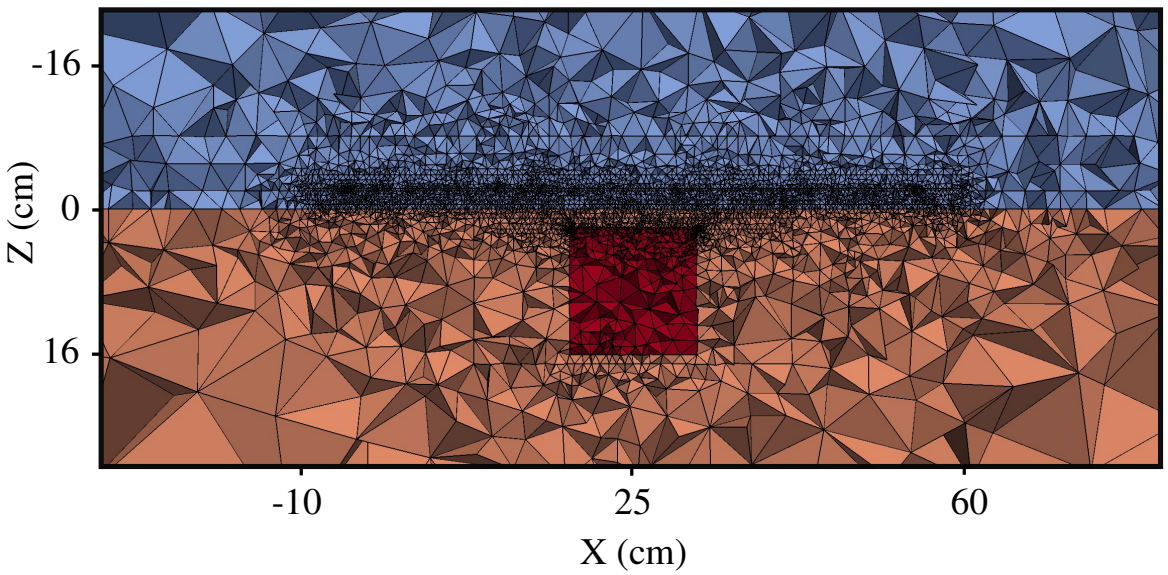

Figure 4.20: An enlarged xz cross-section of the central part of the tetrahedral mesh used for the graphite cube in brine example. The free-space and conductive brine are shown in light blue and brown respectively. The conductive cube is shown in red.

fied here (e.g., $\delta = (\sum_{i=1}^{n_{obs}} |\Delta \mathbf{H}_i|)/n_{obs})$). The average differences for a frequency of 1 kHz are 1.46 percent for the in-phase part and 1.84 percent for the quadrature part. For frequencies of 10, 100, 200, and 400 kHz the differences, in in-phase and quadrature pairs, are $(1.20\%, 2.09\%)$, $(1.97\%, 1.18\%)$, $(2.51\%, 0.99\%)$, and $(5.59\%, 1.09\%)$ respectively. Overall, the agreement between the FE results and the physical scale modeling results is good. However, a relatively high mismatch is seen for the in-phase component at 400 kHz. Here the physical scale modeling data are thought to be affected by the capacitive effects from the nonconductive materials in the laboratory (Farquharson et al., 2006).

The galvanic and inductive components of the response were again investigated. A horizontal plane which has nodes and cells in the graphite cube was introduced at a depth of 2.2 cm below the brine surface in order to give detailed vector plots. The inductive, galvanic and total fields for a frequency of 100 kHz and the transmitter over

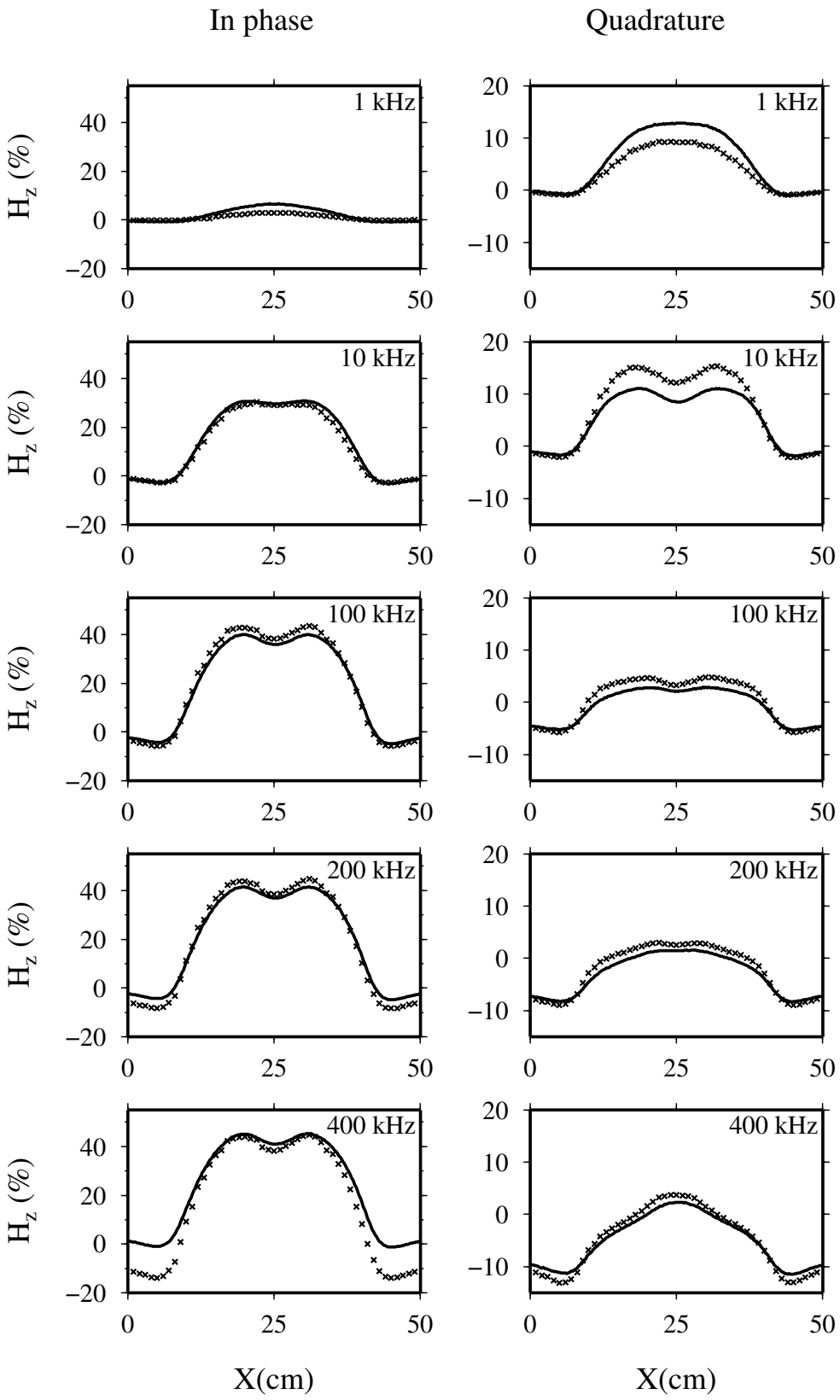

Figure 4.21: The responses for the cube-in-brine model. Crosses are the FE solutions; the solid lines are the physical scale modeling measurements from Farquharson et al. (2006). The vertical component of the secondary magnetic field H_z (here total field minus free-space field normalized by the free-space field) is plotted versus the location of the center of the transmitter-receiver pair.

the center of the cube are shown in Figure 4.22 for the electric field. As can be seen from Figure 4.22, the inductive component is dominant and resembles the total electric field for this example. The galvanic fields shown in panels (c) and (d) are very small in magnitude and show a noisy behavior. However, the imaginary part of the galvanic component provides a hint of the boundary between the brine and the graphite cube where it moderately contributes to the total electric field. The corresponding arrows for the inductive, galvanic and total current densities are shown in Figure 4.23. Here again it is the inductive part (panels (a) and (b)) which significantly contributes in forming the total current density in the horizontal plane.

For this example also, the behavior of the residual norms of the iterative solver is shown. A configuration in which the transmitter is located above the center of the cube is considered. Figure 4.24 shows the residual norm for the $\mathbf{A} - \phi$ decomposed solution. Again, because of the effective contribution from the conductivity term $\mathbf{H}$ (see equation 3.27), the $\mathbf{A} - \phi$ solution converges rapidly. However, the small scale of the problem and very high frequencies used here generate large off-diagonal elements of $\mathbf{G}$, particularly in the graphite cube (see equation 3.27), in the coefficient matrix. Therefore a poorer convergence is observed in comparison to those seen in the previous example. The relative residual norm for the final solution is 6.15×10^{-5}.

4.2.3 Canonical disk model: A hydrocarbon exploration scenario

The example presented here considers a marine geophysical model (e.g, see Constable and Weiss,2006; and Weiss and Constable,2006 for similar examples). Figure 4.25 illustrates a sketch of the model. Panel (a) in Figure 4.26 shows the meshed geometry of the problem. The model consists of a circular disk of 0.01 S/m surrounded by con-

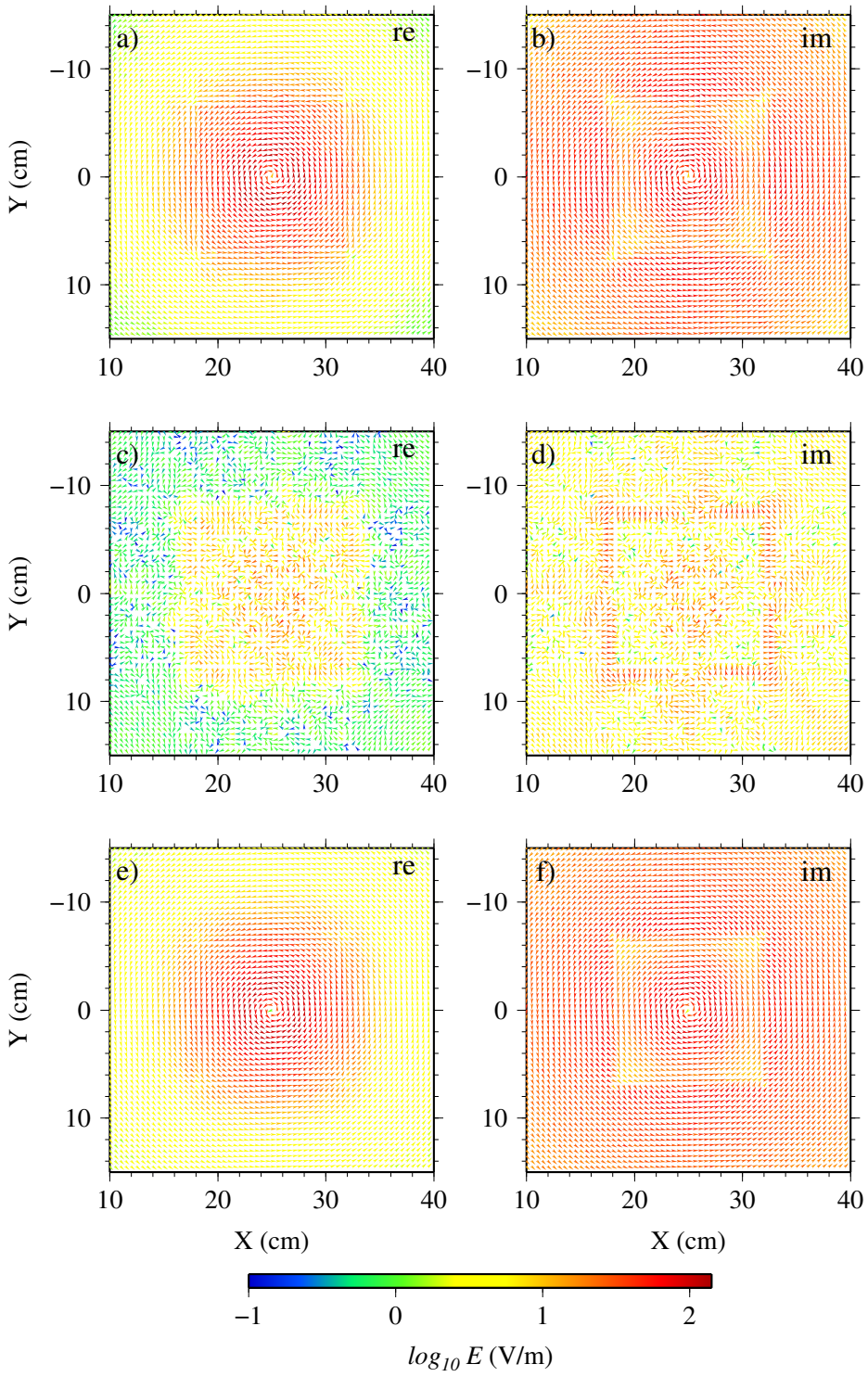

Figure 4.22: The inductive part, galvanic part and total electric field for the graphite-in-brine model for a frequency of 100 kHz. All six panels show the horizontal component of the fields at a depth of 2.2 cm below the brine surface, i.e., 0.2 cm below the top of the cube.

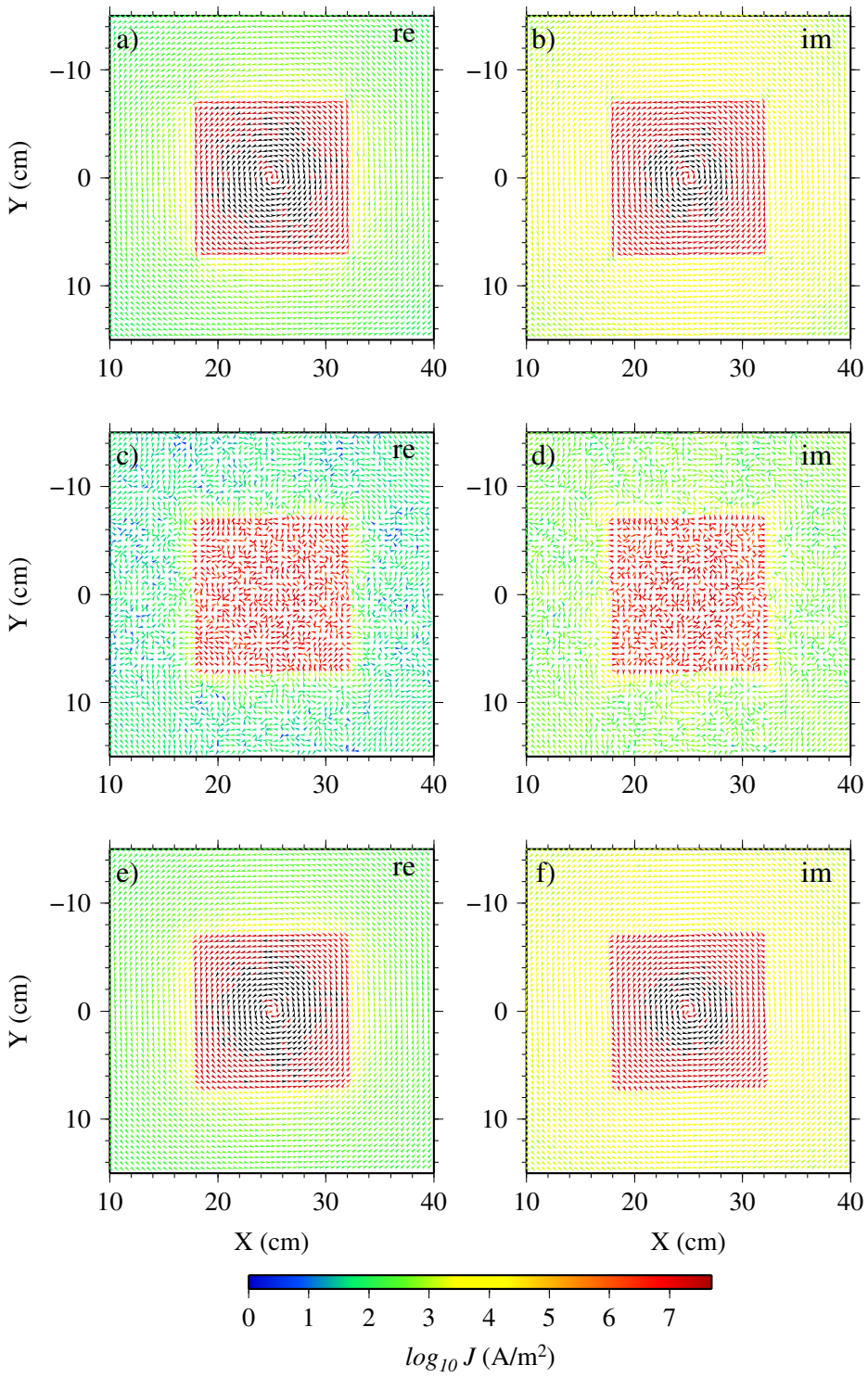

Figure 4.23: The inductive part, galvanic part and total current density for the graphite-in-brine model for a frequency of 100 kHz. All six panels show the horizontal component of the currents at a depth of 2.2 cm below the brine surface.

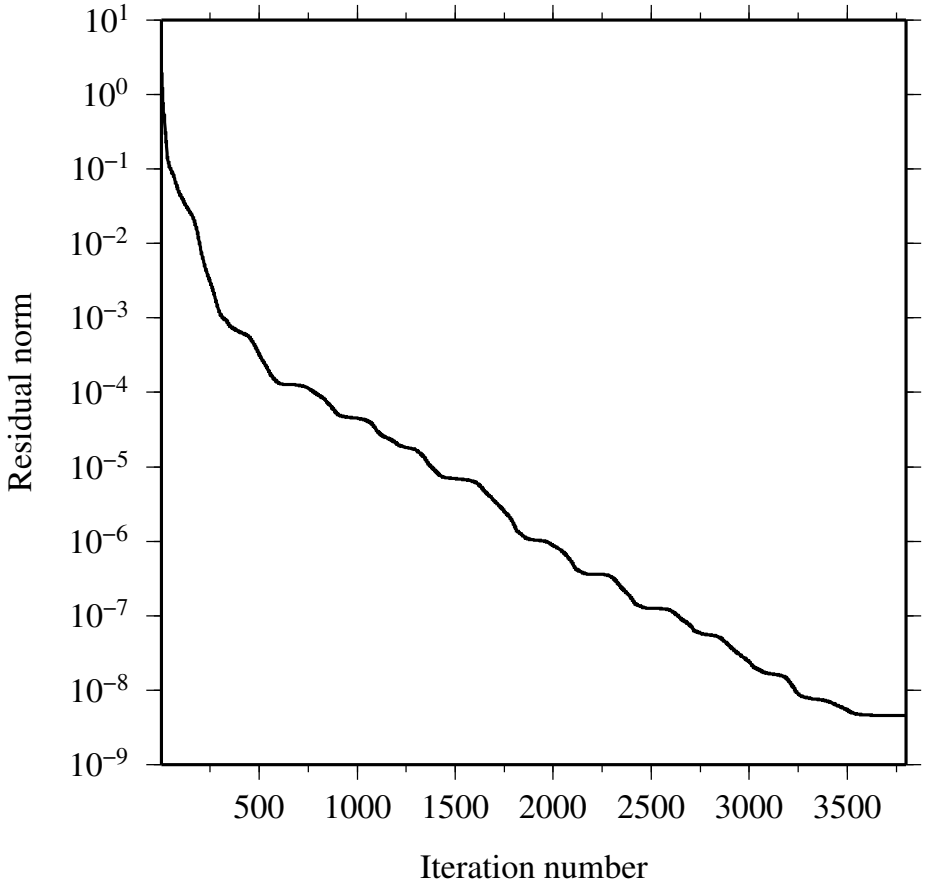

Figure 4.24: The convergence curve for the $\mathbf{A} - \phi$ solution for a frequency of 100 kHz for the cube-in-brine example.

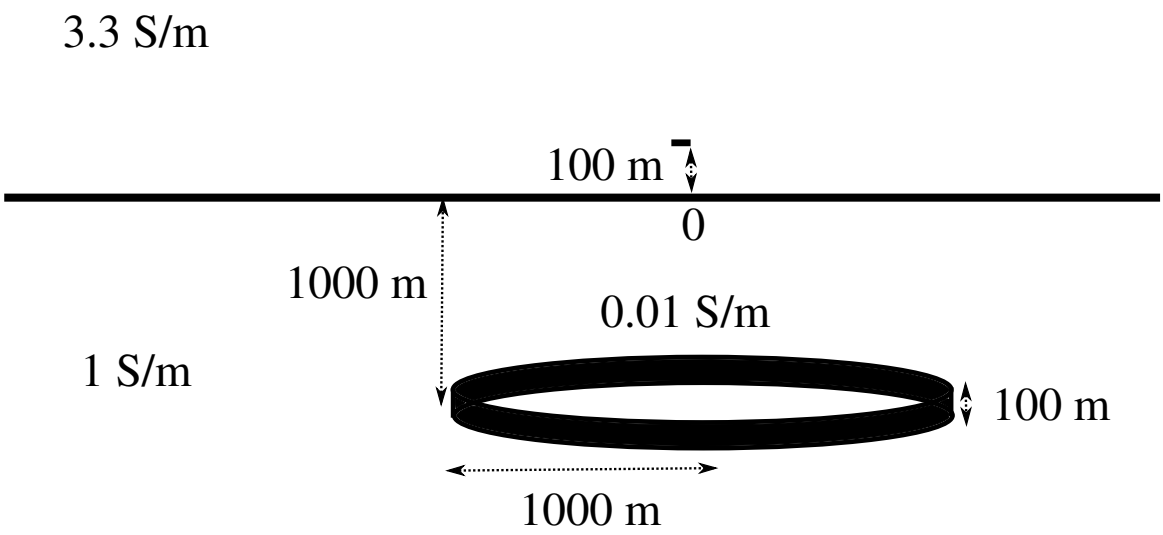

Figure 4.25: The geometry of the canonical disk model example. The conductivities of sea water, sediments and the canonical disk are 3.2, 1 and 0.01 S/m respectively.

ductive sea sediments of 1 S/m. The center of the 100 m thick and 2000 m diameter disk is at $(x, y, z) = (0, 0, 1000)$ m. The model also includes an x-directed electric dipole source extending from $x = 100$ to 0 m located in conductive sea water of 3.2 S/m at a height of 100 m above the sea floor. Similar to previous examples the mesh is locally refined at the source and observation locations. Panel (b) in Figure 4.26 shows a horizontal view of the central part of the mesh at a depth of $z = 1000$ m. This is a typical example of how unstructured tetrahedral meshes are capable of easily generating curved boundaries in the model. Here the entire dimension of the mesh is $20 \times 20 \times 20$ km in the x-, y- and z- directions. The mesh consists of 696498 cells, 113641 nodes and 647526 edges. The solution from the approach presented in this thesis is compared against the finite-volume solution of Weiss (2013). For a frequency of 1 Hz the normalized amplitude and the phase for the x-component of the electric field at the water-sediments interface are shown in Figure 4.27. Figure 4.28 shows the residual norm due to the iterative solution. For a Krylov subspace of 200 the solution obtained after 2900 iterations is adequate to match the corresponding solution

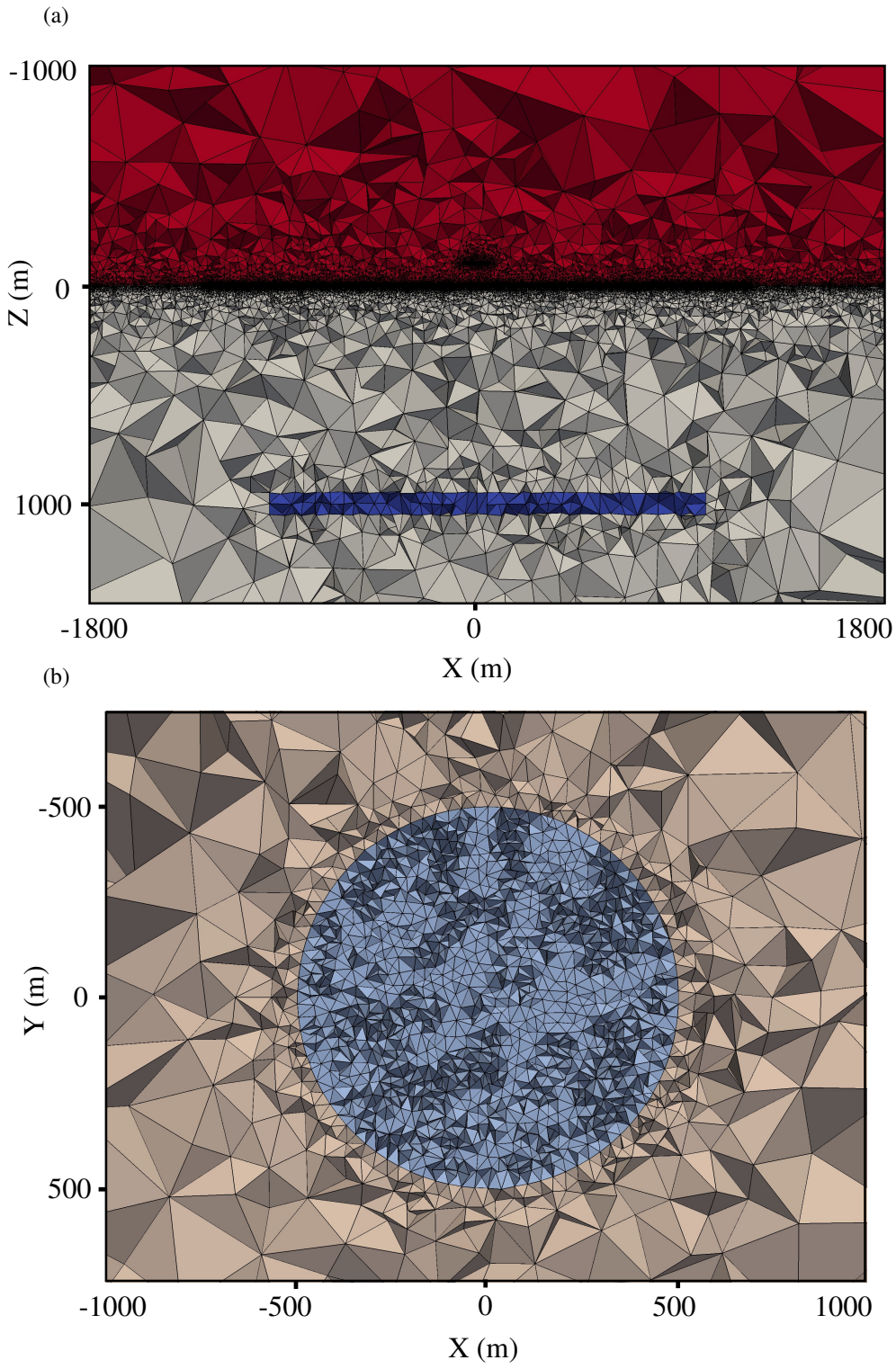

Figure 4.26: (a) The geometry of the enlarged xz cross-section of the central part of the mesh for the canonical disk model. The 100 m dipole source is located in sea water (shown in red) 100 m above the sediments-water interface. The center of the resistive circular disk (shown in blue) is at $z = 1000$ m in the sediments. b) An enlarged xy cross-section of the central part of the mesh at $z = 1000$ m. The circular disk is optimally reproduced using unstructured tetrahedral meshes.

of Weiss (2013). The relative residual norm (e.g., $\frac{||Ax-b||}{||b||}$) was 2.87×10^{-9} for the final solution presented here.

Inductive and galvanic components are also investigated for this example. A horizontal plane of nodes that cuts through the circular disk is inserted into the mesh at a depth of 1000 m in the conductive sediments to generate the results for the plotting. Figures 4.29 and 4.30 respectively show the directions of the component of the electric field and current density on this plane of nodes for a frequency of 1 Hz. It is seen here that both inductive (see panels a and b) and galvanic (see panels c and d) parts of the electric field and current density increase and decrease in the resistive disk respectively. Furthermore, in contrast to the previous examples where the total field was dominated only by inductive or galvanic field, here the total field (see panels e and f) is a mixture of inductive and galvanic components in the horizontal plane.

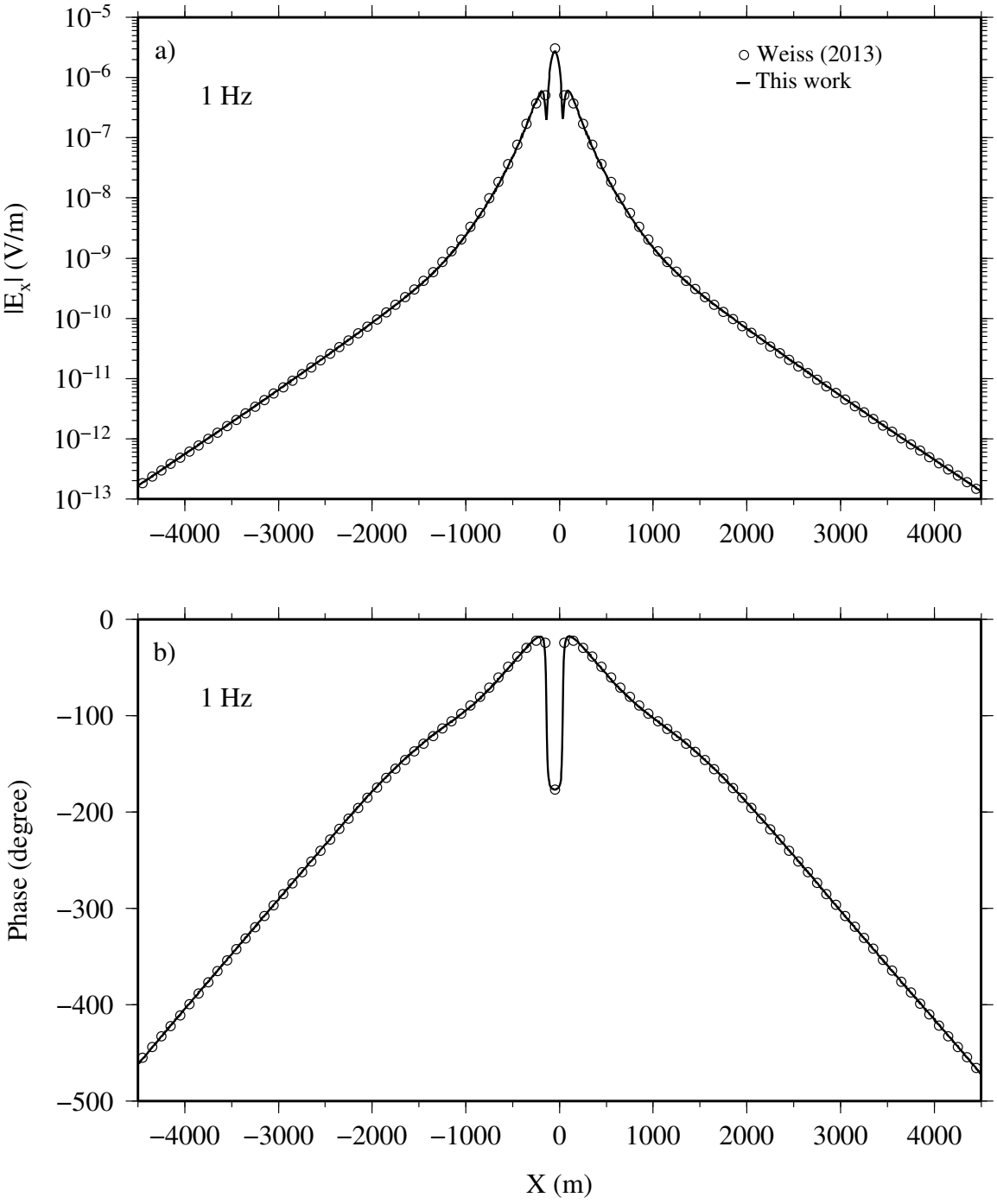

Figure 4.27: a) The normalized amplitude and b) the phase for the x-component of the electric field measured on the ocean floor for a frequency of 1 Hz for the marine model. A comparison of the FE solution (solid line) with the finite-volume solution of Weiss (2013) (shown in circles) is shown in each panel.

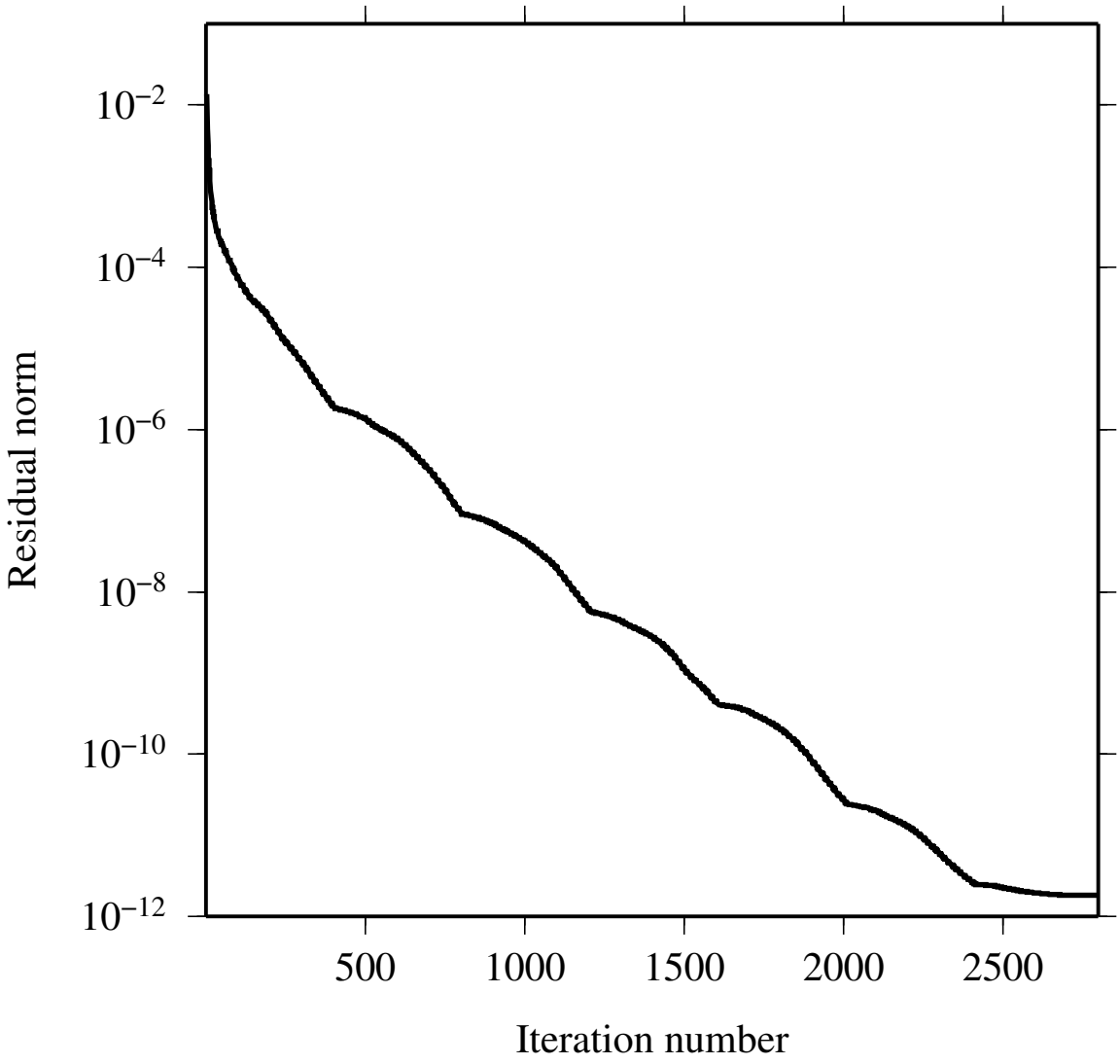

Figure 4.28: The convergence curve for the $\mathbf{A} - \phi$ solution for a frequency of 1 Hz for the marine example.

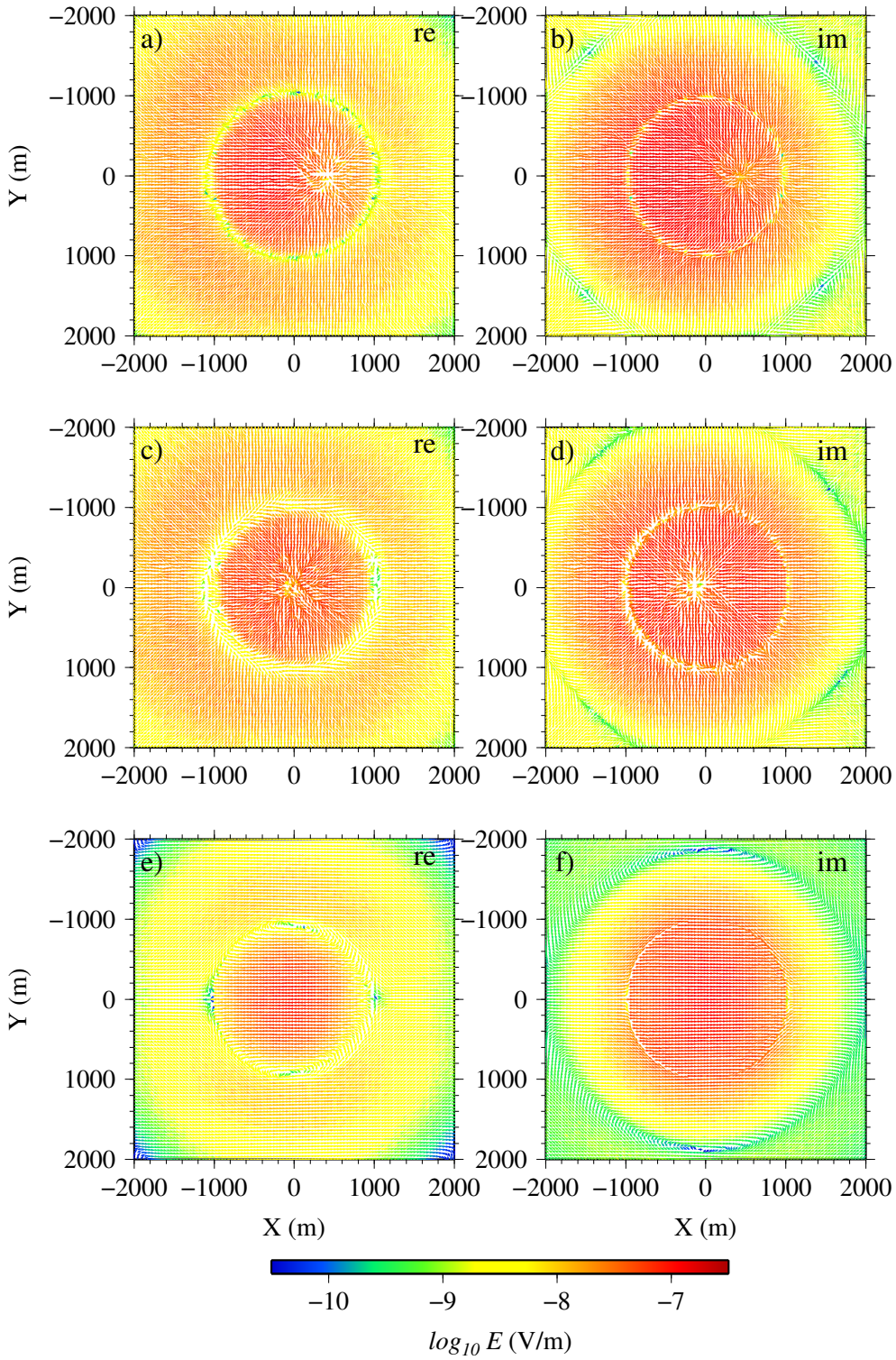

Figure 4.29: The inductive part, galvanic part and total electric field for the canonical disk model for a frequency of 1 Hz. All six panels show the horizontal component of the fields at a depth of 1000 m below the water-seabed interface, i.e., within the disk.

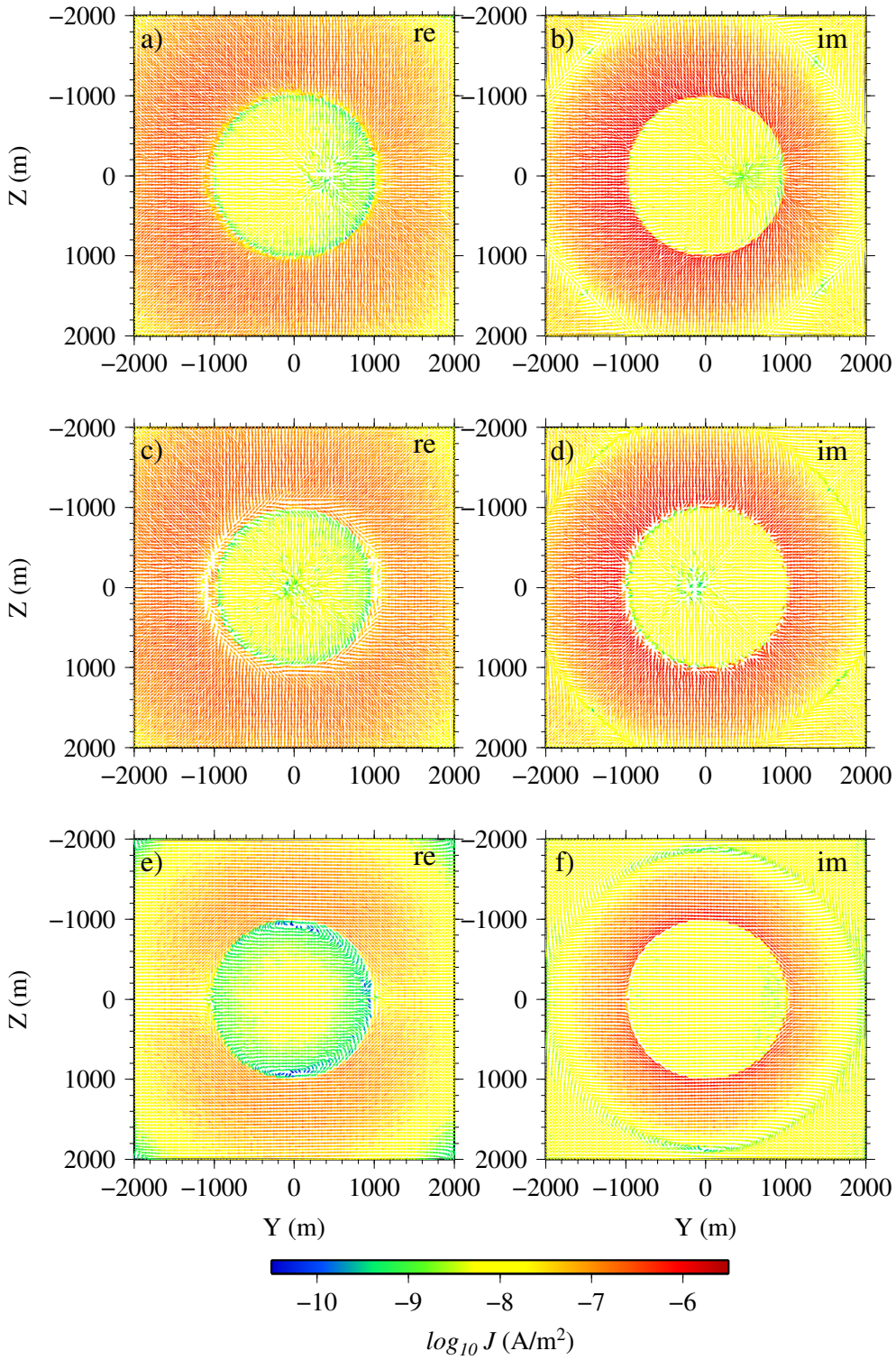

Figure 4.30: The inductive part, galvanic part and total current density for the canonical disk model for a frequency of 1 Hz. All six panels show the horizontal component of the fields at a depth of 1000 m below the water-seabed interface.

Chapter 5

Field characteristics, gauged and un-gauged potential formulations

5.1 Introduction

The contribution of the inductive and galvanic parts to the total electric field depends on the type of formulation used for the $\mathbf{A} - \phi$ decomposition method. Examples presented in the previous chapter consider the inductive and galvanic fields for the un-gauged $\mathbf{A} - \phi$ formulation i.e., with the term $\nabla \cdot (\sigma \mathbf{A})$ existing in the system (see equation 3.7). Despite implicitly enforcing the Coulomb gauge condition by choosing edge-element basis functions for the vector potential therein, the $\mathbf{A} - \phi$ formulation is explicitly un-gauged. In other words although edge-element basis functions satisfy the requirement of $\nabla \cdot \mathbf{A} = 0$ within a cell, there is no explicit condition enforcing $\nabla \cdot \mathbf{A}$ to zero across an interface. This condition might result in a peculiar behavior for the inductive and galvanic components. In fact I become suspicious about this behavior from the non-symmetric inductive and galvanic parts for the canonical disk model in Chapter 4 (see Figure 4.29) and also spurious fields observed for the plate example

presented later in this chapter. In this chapter, in addition to demonstrating these issues using a specific example, I present the solution to the corresponding explicitly Coulomb-gauged system of equations.

Examples presented in this thesis thus far have investigated the electromagnetic response of models with an isolated three-dimensional target situated in an otherwise homogeneous host of different conductivity and for simple sources. In real geophysical surveys, large-layout transmitter systems are often used and more complicated Earth models, including layered or stratified backgrounds, are considered. The response of the large-loop Turam system to a large rectangular thin plate anomaly has been investigated in a number of studies particularly concerned with investigating the relative importance of inductive and galvanic effects (e.g, Lamontage and West, 1971; Lajoie and West, 1976; Hanneson and West, 1984). In particular, as discussed by Lajoie and West (1976), the EM response is significantly affected and altered by the presence of conductive overburden in the model. The integral equation approach of Lajoie and West (1976) was developed for a significantly thin conductive plate. For this example the electromagnetic response as calculated by the $\mathbf{A} - \phi$ FE formulation presented in this thesis with its corresponding inductive and galvanic fields, is investigated in this chapter. The marine example presented in Chapter 4 is also revisited in terms of finding the gauged solution. For the examples mentioned above the continuity of the potentials and fields at conductivity gradients is also investigated for the type of formulations used.

5.2 The thin plate problem

5.2.1 Vertical plate and large fixed-loop system

This example concerns simulating the behavior of inductive and galvanic responses for a plate buried in a half-space of varying conductivity (same example as considered by Lajoie and West, 1976). The model is excited with a fixed large loop of current. Panel (a) in Figure 5.1 shows the geometry of the model for this example. The model comprises a conductive half-space, a narrow conductive plate, and an air layer of 10^{-8} S/m. Here the conductance of the rectangular plate, which is the product of conductivity and thickness, was set to 10.5 Siemens. The top of the conductive plate is 50 m deep in the ground and is located 250 m to the side of the transmitting loop. Also, its dimensions are 500 m and 250 m in the y- and z-directions respectively. A small thickness of 4 m in the FE modeling is considered for the plate which is negligible relative to its strike length. The frequency of the current in the transmitter is 500 Hz. The transmitter loop has dimensions of 500 m and 1000 m in the x- and y-directions respectively, and sits on the Earth surface. Also, a current of 1 A runs through the wires in the loop and builds a positive magnetic moment purely in the z-direction. Panel (b) in Figure 5.1 shows the xz-cross-section of the entire unstructured mesh. As illustrated here the tetrahedral cells gradually increase in size away from the central part of the simulation grid. The dimension of the whole mesh used in this example is 10 km $\times$ 10 km $\times$ 10 km. Panel (c) in Figure 5.1 shows an xy-cross-sectional view of the central part of the mesh. As illustrated here the mesh is slightly refined around the wires forming the rectangular loop of current. In contrast, in order to obtain precise magnetic fields, the mesh is significantly refined at the observation locations along the x-axis (line in red). Panel (d) in Figure 5.1 also shows a yz-cross-section of the central part of the mesh at $x = 500$ m.

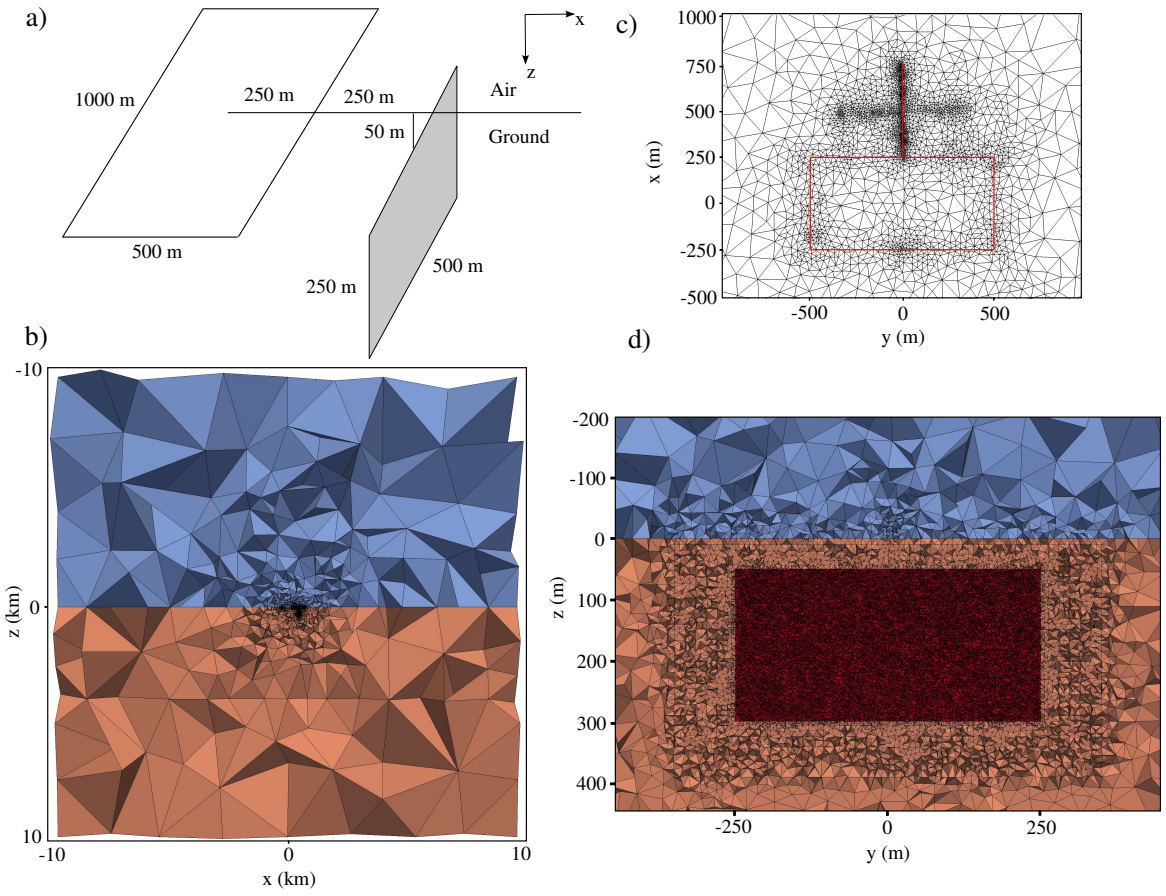

Figure 5.1: The geometry and mesh used for the plate and large loop example. a) The loop of current is located at the air-ground interface with its center at the origin. The narrow vertical plate is 50 m deep and 250 m away from the nearest long edge of the transmitter loop. b) The entire view of the tetrahedral mesh. The conductive ground and the resistive air are shown in orange and blue respectively. c) An xy-cross-section of the central part of the mesh at $z = 0$. Lines shown in red depict the geometry of the rectangular source and observation locations. d) A central yz-cross-section of the mesh at $x = 500$ m. The conductive plate is shown in red.

For the specific example presented here the small thickness of the plate with its two other large dimensions does not favor the meshing program. In particular, TetGen automatically generates a significant number of fine cells within the rectangular plate and somewhat abruptly produces cells of larger dimensions in the surrounding host. This issue affects the convergence of the problem in the iterative solver particularly for large conductivity contrasts. In order to counteract this difficulty the mesh is locally refined also around the conductive plate to maintain the gradual increase for the cells sizes. The mesh used here consists of 886244 cells, 145192 nodes and 1033610 edges.

The solution parameters are set to $lfil = 3$ for the fill-in factor of the ILUT preconditioner and a dimension of 200 for the Krylov subspace in GMRES. Figure 5.2 shows the z-component of the total magnetic field along the line of observations for hosts of different conductivities. Here the data points in black represent the calculated fields for the model including the conductive plate. Also, the red-colored solid lines indicate the calculated field for the homogeneous background host for which the conductive plate is absent. It is seen here that, unlike the real part, the imaginary part of the magnetic field is significantly sensitive to the varying host conductivities. In order to identify the cross-over inflection of the vertical component anomaly along the observation locations the corresponding normalized magnetic fields were also calculated. For different conductivities of the host Figure 5.3 shows the normalized magnetic field calculated by subtracting the free-space field from the total field and then dividing by the free-space field. The data shown using cross symbols are the normalized fields at each observation location in the presence of the conductive plate. The corresponding normalized magnetic fields for only the conductive background host are shown in circles. It is seen here that the increase in the conductivity of the host medium

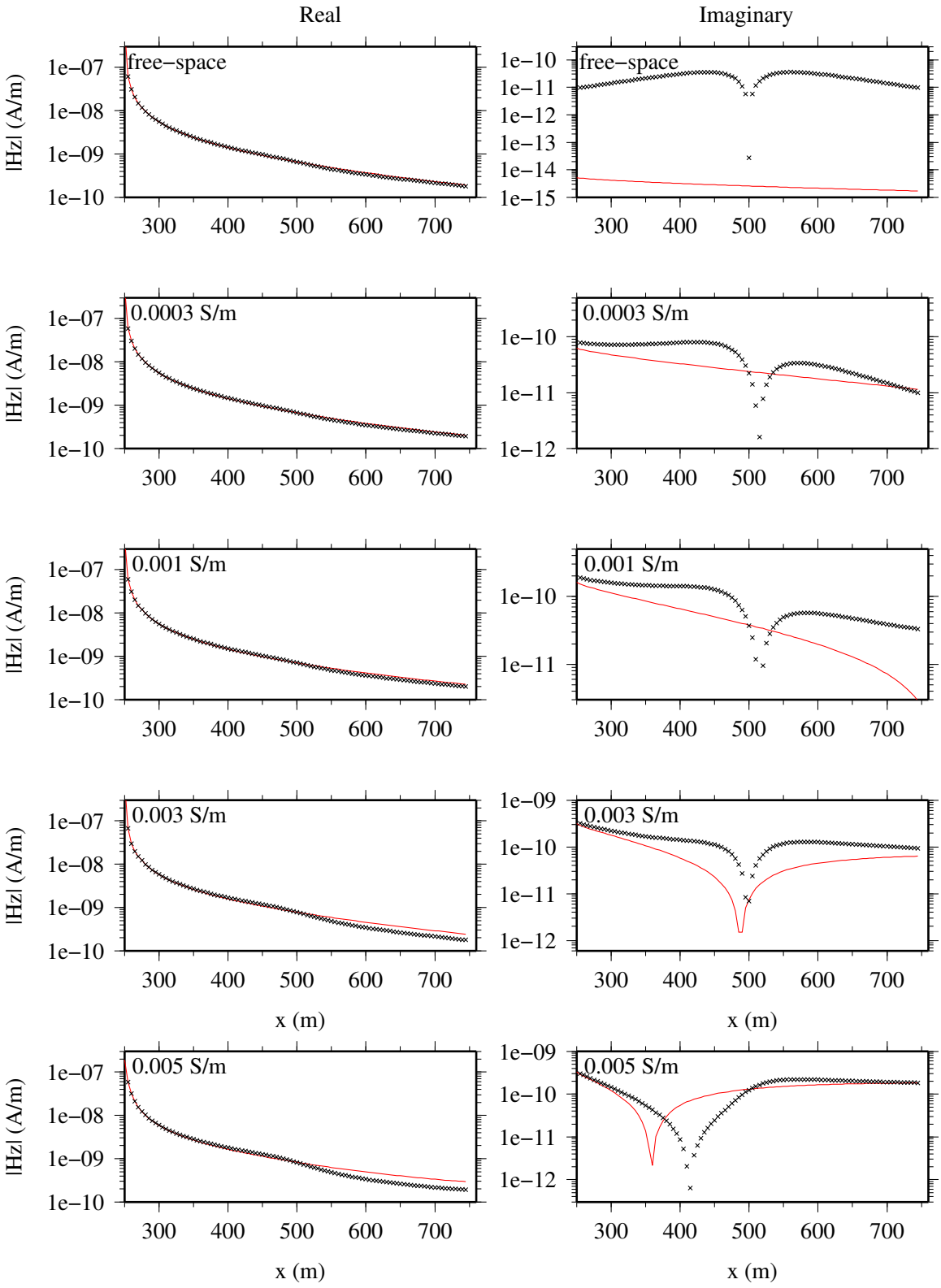

Figure 5.2: The real and imaginary parts of the magnetic field for the plate in half-spaces of varying conductivity. The observation points along the horizontal axis are over the center of the plate on the surface. The conductance of the rectangular plate is 10.5 S. The vertical axis is the z-component of the total magnetic field. Data points (in black) and solid lines (in red) are magnetic fields in the presence and absence of the conductive plate respectively.

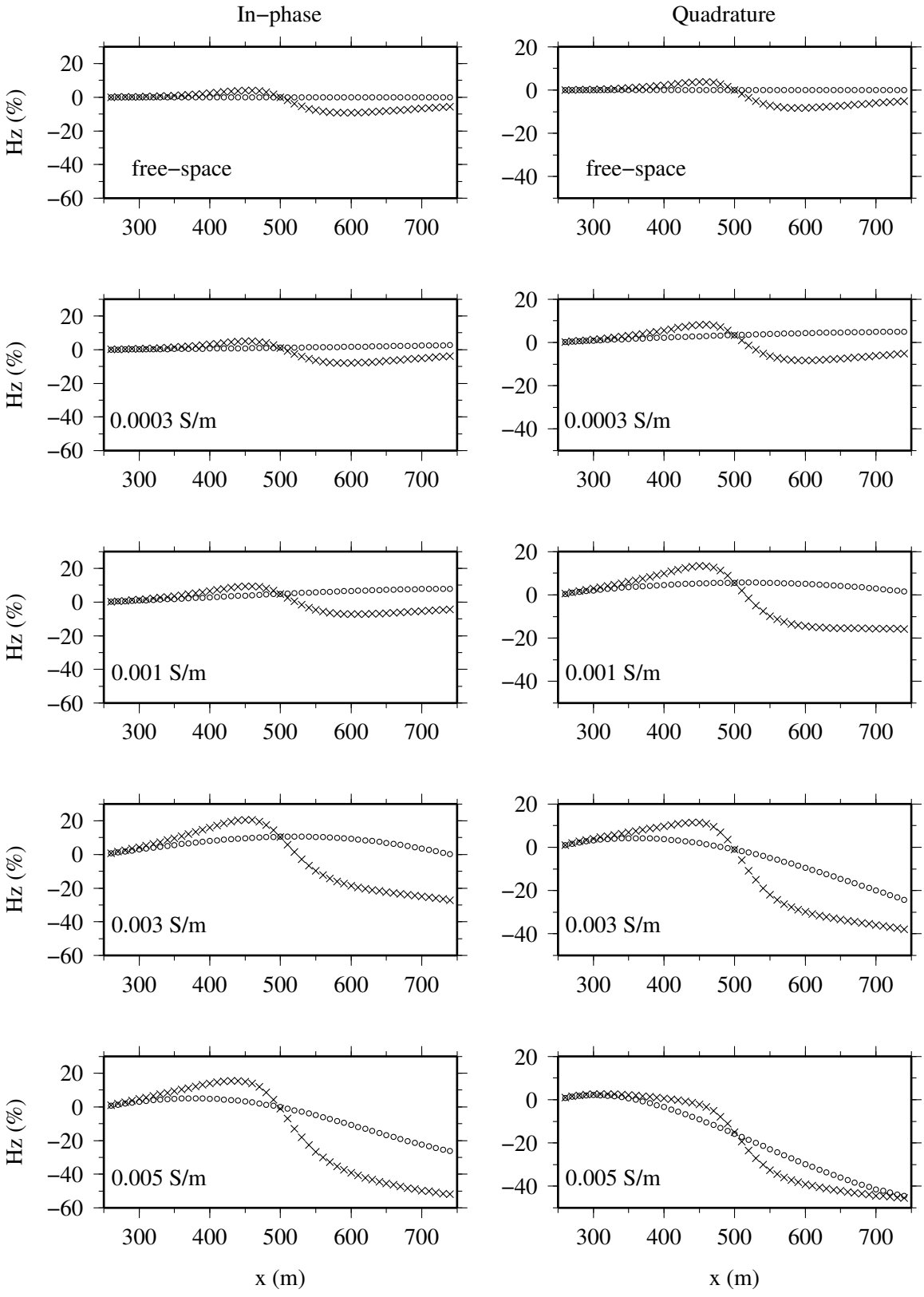

Figure 5.3: The in-phase and quadrature parts of the normalized magnetic field, i.e., total minus free-space field normalized by free-space field, for the plate in half-spaces of varying conductivity. Data shown using cross symbols and circles are respectively the normalized fields for the model in the presence and absence of the conductive plate (for comparison see Lajoie and West, 1976, page 1148).

increases the amplitude of the anomalous field. Also as expected the cross-over point in all panels in Figure 5.3 occurs at $x = 500$ m which is the point corresponding to the center of the conductive plate projected to the surface.

The normalization method used above attenuated the measured data near the transmitter loop while magnified data far from the loop wire. In order to obtain a balanced view of the field on the surface a fixed normalization is also used. Here the free-space field at only the cross-over point was used for normalizing the field at all points along the profile. This method of normalization is feasible as the inflection point is already found in Figure 5.3 at $x = 500$ m. Figure 5.4 shows the fixed-point normalization fields relative to the conductivity contrasts shown in Figure 5.3. Here an odd-symmetric curve for the normalized magnetic field, namely the peak-to-peak anomalous field of Lajoie and West (1976), is obtained. For the range of host conductivities considered here it is seen that the peak-to-peak anomaly, i.e., the difference in local anomaly peaks on either sides of the plate, increases as the conductivity of the host increases. The normalized anomaly in Figure 5.3 is also modified (i.e., begins to rotate here) for hosts with higher conductivities.

In order to picture a summary of the peak-to-peak responses for a variety of conductivities of the host phasor diagrams are used (see Figure 5.5). Data points shown on each individual curve correspond to the peak-to-peak response for a range of conductances of the plate located within the relevant host of constant conductivity. The data obtained for this example are comparable to those shown in Lajoie and West (1976). However, because of the non-negligible thickness of the plate considered here, the amplitude of the anomaly is slightly scaled. The responses shown in black (see Figure 5.5) are the phasor curve for the plate situated in free-space ($\sigma = 10^{-8}$ S/m).

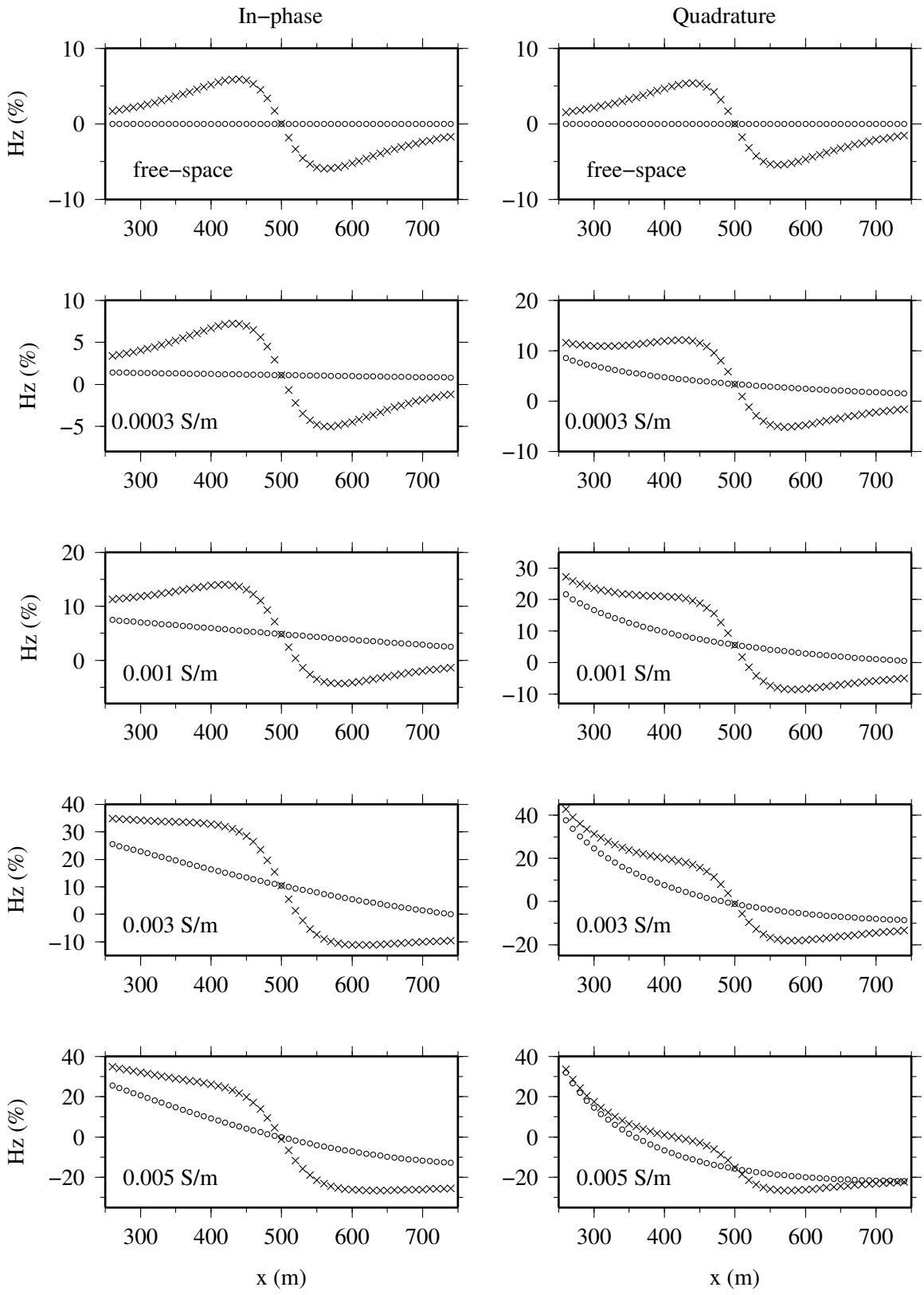

Figure 5.4: The in-phase and quadrature parts of the fix-point normalized magnetic field, i.e., total minus free-space field normalized by the free-space field at the cross-over point. Data shown using cross symbols and circles are respectively the normalized fields for the model in the presence and absence of the conductive plate.

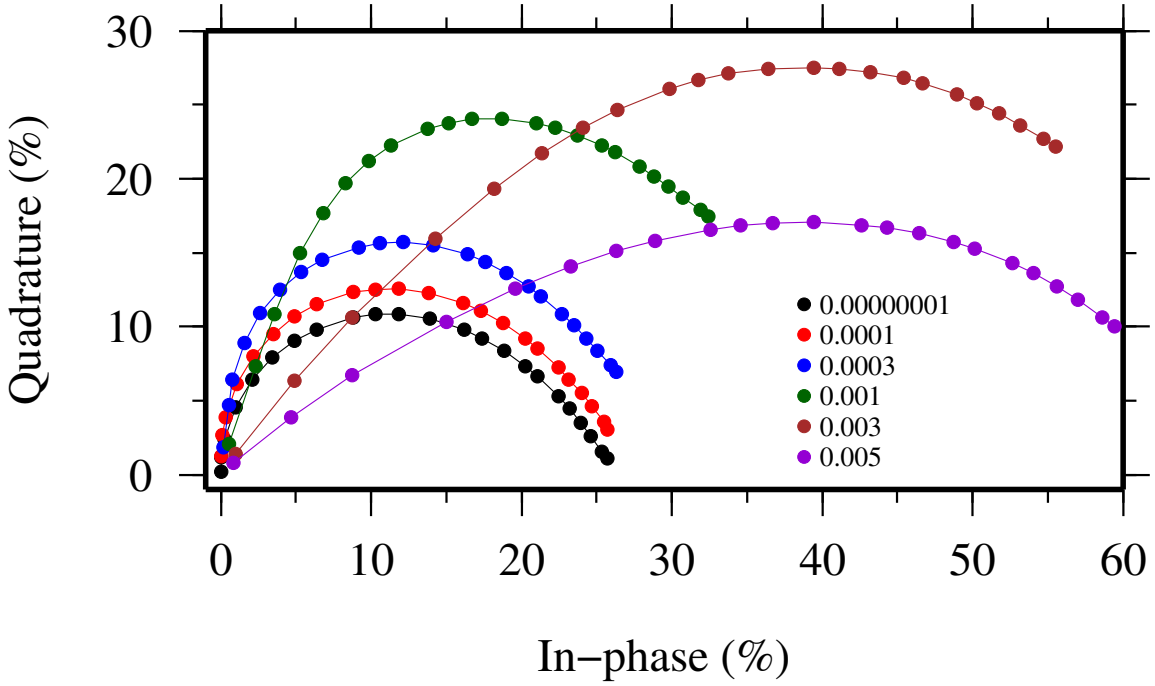

Figure 5.5: Phasor diagram for the in-phase and quadrature normalized anomalous field. Five graphs are shown in different colors which correspond to hosts of different conductivities. Data points in each curve correspond to the in-phase-quadrature response for low to high conductivities of the plate.

In particular it shows the anomalous in-phase versus quadrature response as the plate conductance increases from a small value of 0.1 S to a high value of 1000 S. Phasor curves shown in red, blue, green, brown and violet colors are for increasing host conductivities of 0.0001, 0.0003, 0.001, 0.003 and 0.005 S/m respectively. It is seen here that the increase in conductivity of the host enhances the anomalous response of the plate. In fact this amplitude increase is seen for higher host conductivities as a larger portion of current is induced in the host medium (see the real part of H_z for conductivities of 0.003 and 0.005 S/m in Figure 5.2) and subsequently more current is available to be channelled into the conductive plate. For higher conductivities of the host, e.g., 0.005 S/m, the phasor diagram begins to rotate towards the in-phase axis. The main reason, as illustrated for example in the fifth panel in Figure 5.2, is because the total magnetic field changes sign (see the imaginary component) in passing through the conductive host prior to sensing the conductive plate.

5.2.2 Inductive and Galvanic components

Investigations of the inductive and galvanic components of the electric field and current density for varying conductivities of the host and plate is performed. A vertical plane of nodes is inserted in the mesh that passes through the center of the conductive plate in the y-plane ($x = 500$). For the host conductivity of 0.0003 S/m (indicated in blue-colored data points in Figure 5.5) Figures 5.6 and 5.7 show the inductive, galvanic and total electric fields for two plate conductances 6 and 25 S respectively. Figures 5.8 and 5.9 also show the corresponding inductive, galvanic and total current densities. It is seen here that the vortex fields and currents inside the conductive plate are mostly provided by the contribution from the inductive part (see panels a and b in all figures) of the electric field. In terms of the fields and currents outside the plate, i.e., in the host medium, the galvanic component is dominant. In particular,

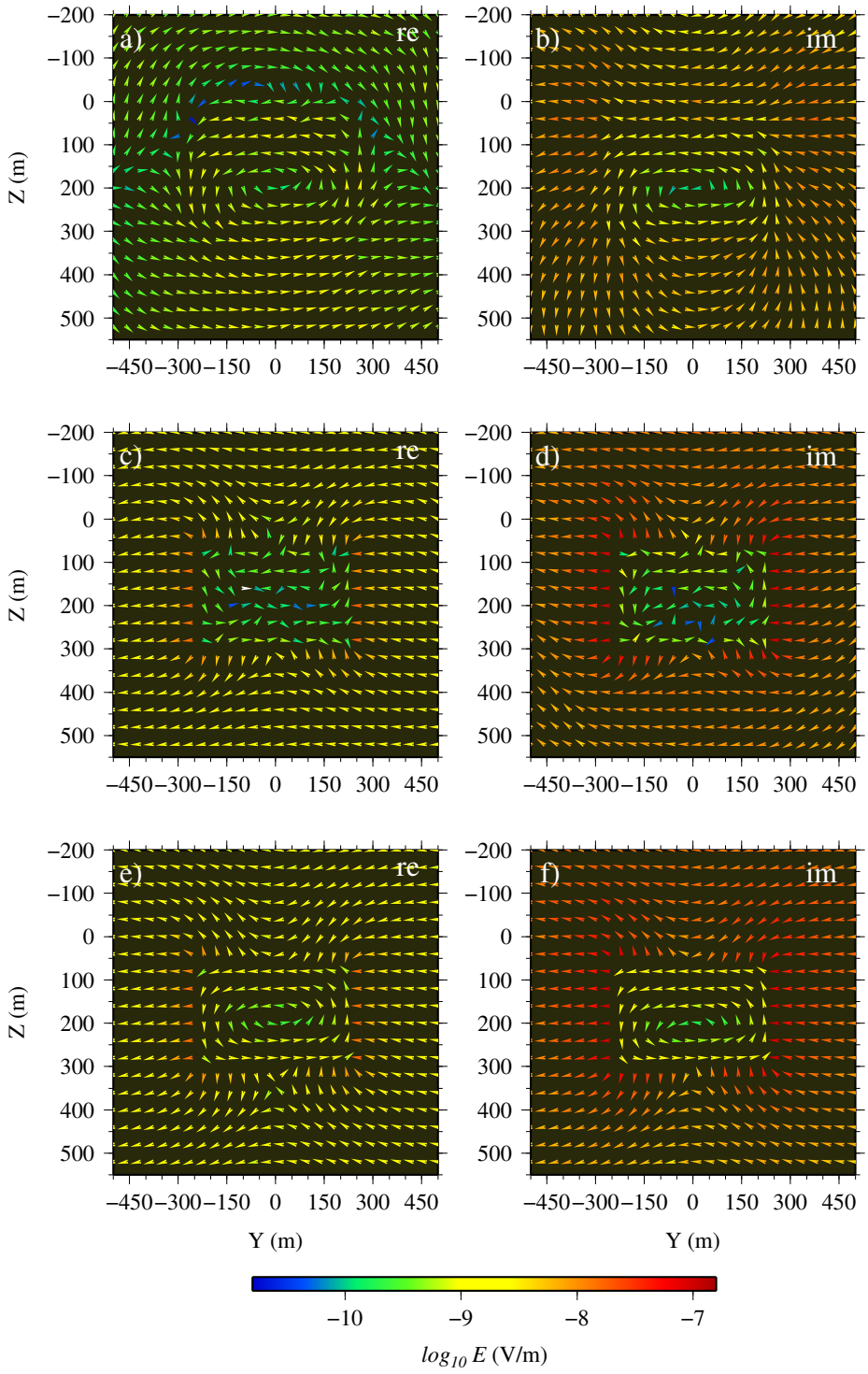

Figure 5.6: The inductive part, galvanic part and total electric field for the plate example for a frequency of 500 Hz and a plate conductance of 6 Siemens. All six panels show the yz-component of the fields in a plane of nodes at $x = 500$ m: the real (a) and imaginary (b) components of the inductive part; the real (c) and imaginary (d) components of the galvanic part and the real (e) and imaginary (f) components of the total electric field.

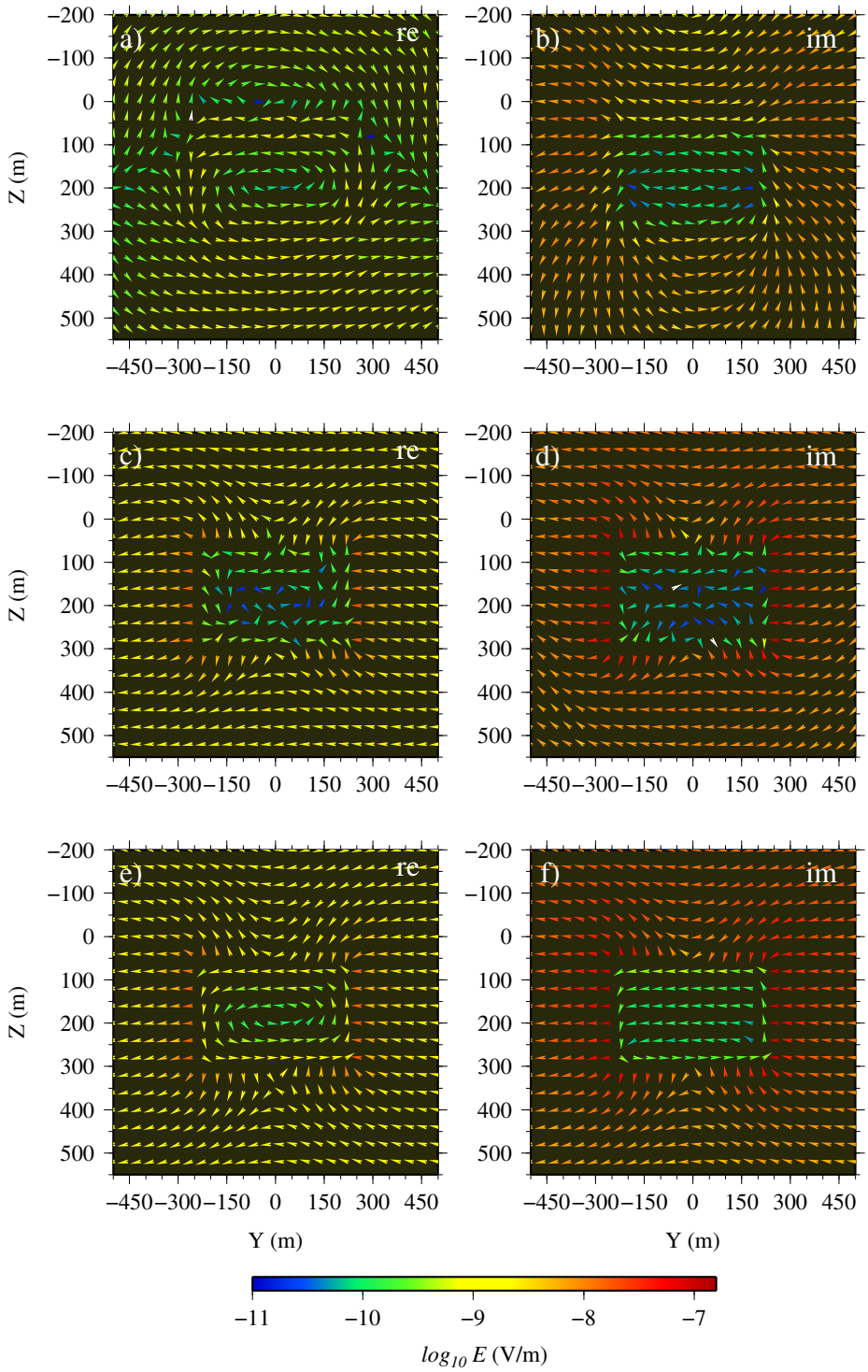

Figure 5.7: The inductive part, galvanic part and total electric field for the plate example for a frequency of 500 Hz and a plate conductance of 25 Siemens. All six panels show the yz-component of the fields in a plane of nodes at $x = 500$ m: the real (a) and imaginary (b) components of the inductive part; the real (c) and imaginary (d) components of the galvanic part and the real (e) and imaginary (f) components of the total electric field.

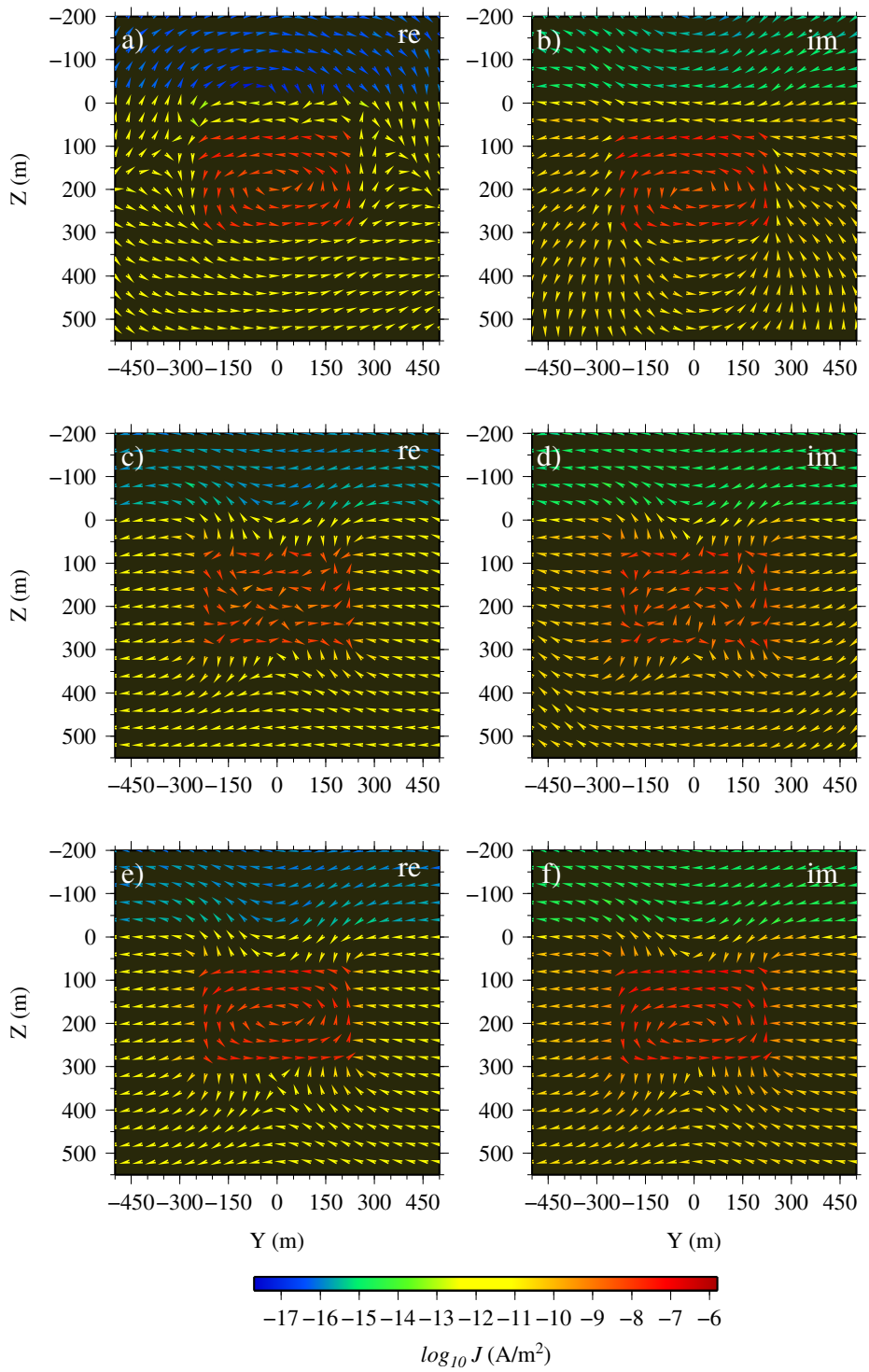

Figure 5.8: The inductive part, galvanic part and total current density for the plate example for a frequency of 500 Hz and a plate conductance of 6 Siemens. All six panels show the yz-component of the currents in a plane of nodes at $x = 500$ m.

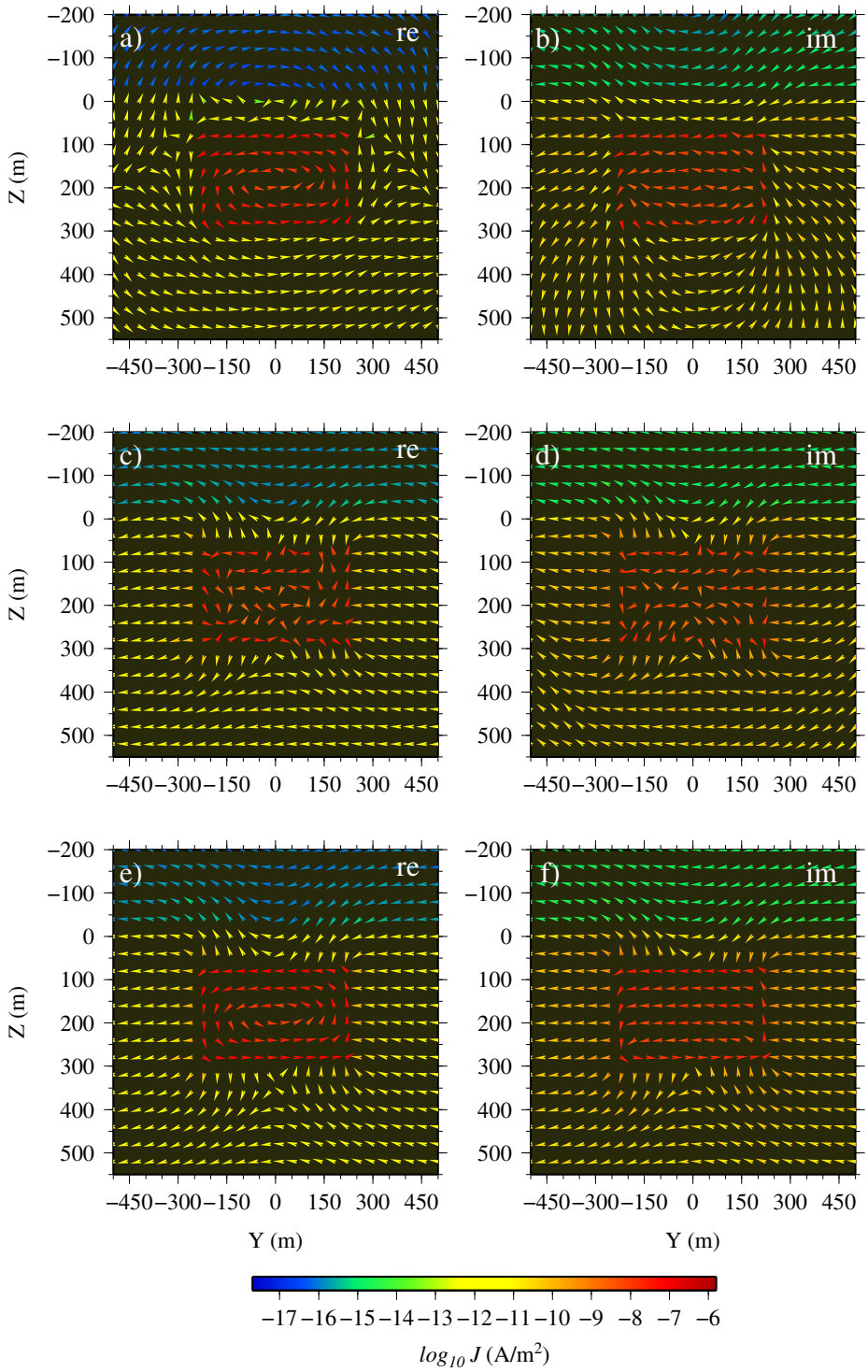

Figure 5.9: The inductive part, galvanic part and total current density for the plate example for a frequency of 500 Hz and a plate conductance of 25 Siemens. All six panels show the yz-component of the currents in a plane of nodes at $x = 500$ m.

the galvanic component is responsible for simulating the current channelling effects at locations where both fields and currents approach and leave the conductive plate.

It is seen in the above figures that despite the well-oriented arrows of the total fields (see panels e and f) for the frequency considered here, the iterative solution of the $\mathbf{A} - \phi$ decomposed system has produced some distorted suspicious inductive (e.g., around the conductive plate) and galvanic (e.g., inside the conductive plate) fields. However, as seen later in this chapter for a lower frequency, the distortion of the fields disappears as a result of greater skin depth of the field in the plate.

5.2.3 Continuity of the fields and currents

For the iterative $\mathbf{A}-\phi$ solution presented here the continuity of the normal components of the fields and currents across the inter-element boundaries is investigated. Here the normal component due to the vector potential, $\mathbf{A} \cdot \mathbf{n}$ (with $\mathbf{n}$ being the outward normal of the considered plane), the gradient of the scalar potential, $\nabla\phi \cdot \mathbf{n}$, and the total electric field, $\mathbf{E} \cdot \mathbf{n} = (-i\omega\mathbf{A} - \nabla\phi) \cdot \mathbf{n}$ are calculated across the jumps in conductivity. For the example presented above, a vertical plane of nodes that shares the outer boundary of the thin plate for the y and z extents of the plate at $x = 498$ m is considered. The inserted nodes on this plane, which are part of some but not all triangular faces, are being shared between the plate and the surrounding host of distinct conductivities. The normal discontinuities are calculated by subtracting the average normal fields on either sides of the conductivity gradient ($x = 498$ here).

For the iterative solution to the model introduced in the preceding section, Figures 5.10 and 5.11 show the discontinuities in the normal components of the potentials and total field. Data provided here are the logarithm of the magnitude of the difference in relevant field component. It is seen here that the discontinuity coming from

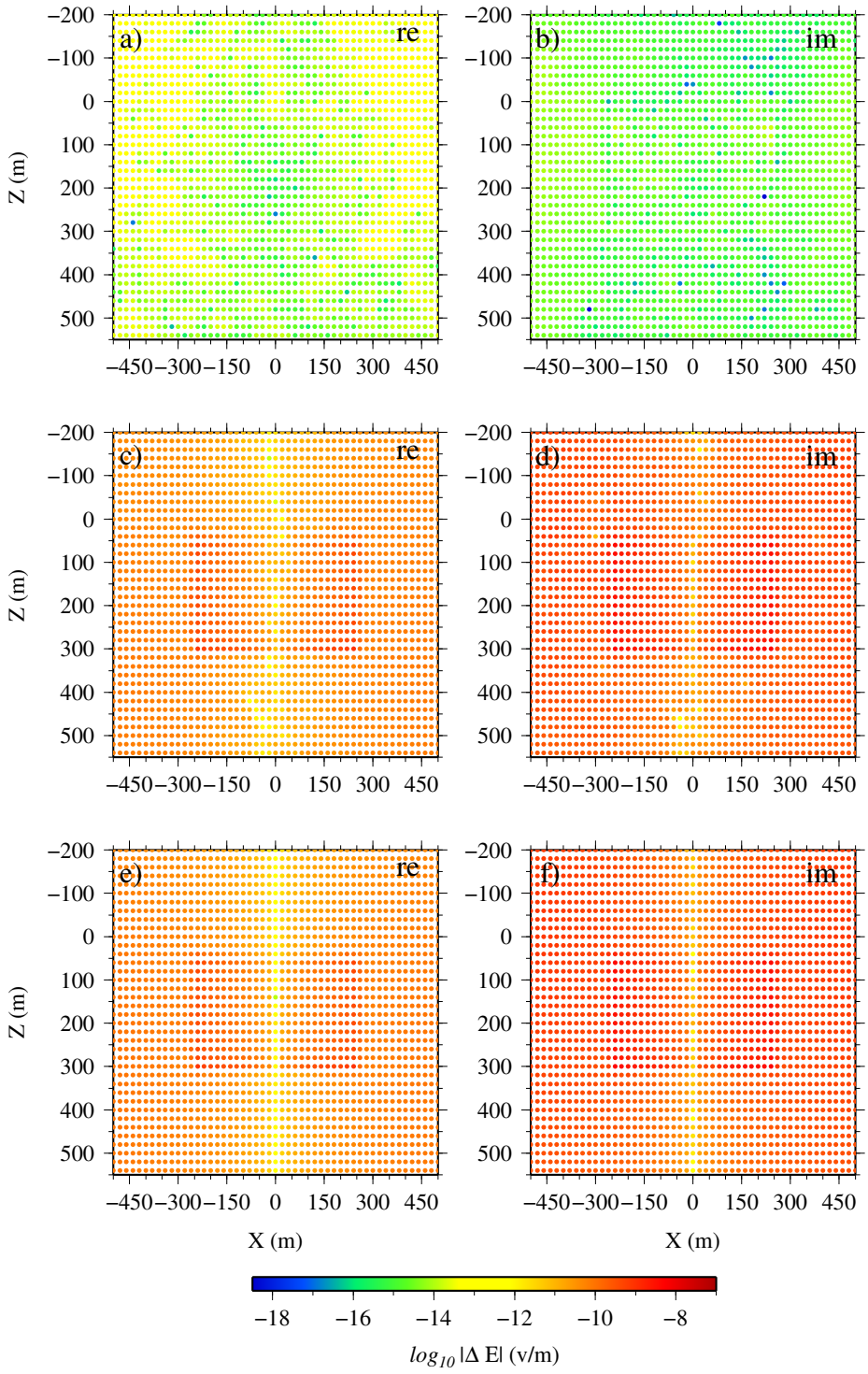

Figure 5.10: Discontinuity in the normal components of the fields for the inductive part, galvanic part and total electric field, for a plate conductance of 6 S, for a frequency of 500 Hz. The vertical plane of nodes is located at $x = 498$ m. Panels (a) and (b) are respectively the discontinuity in the real and imaginary components of the inductive part. Panels (c) and (d) are discontinuity due to the corresponding galvanic parts; and panels (e) and (f) are the corresponding total field discontinuities.

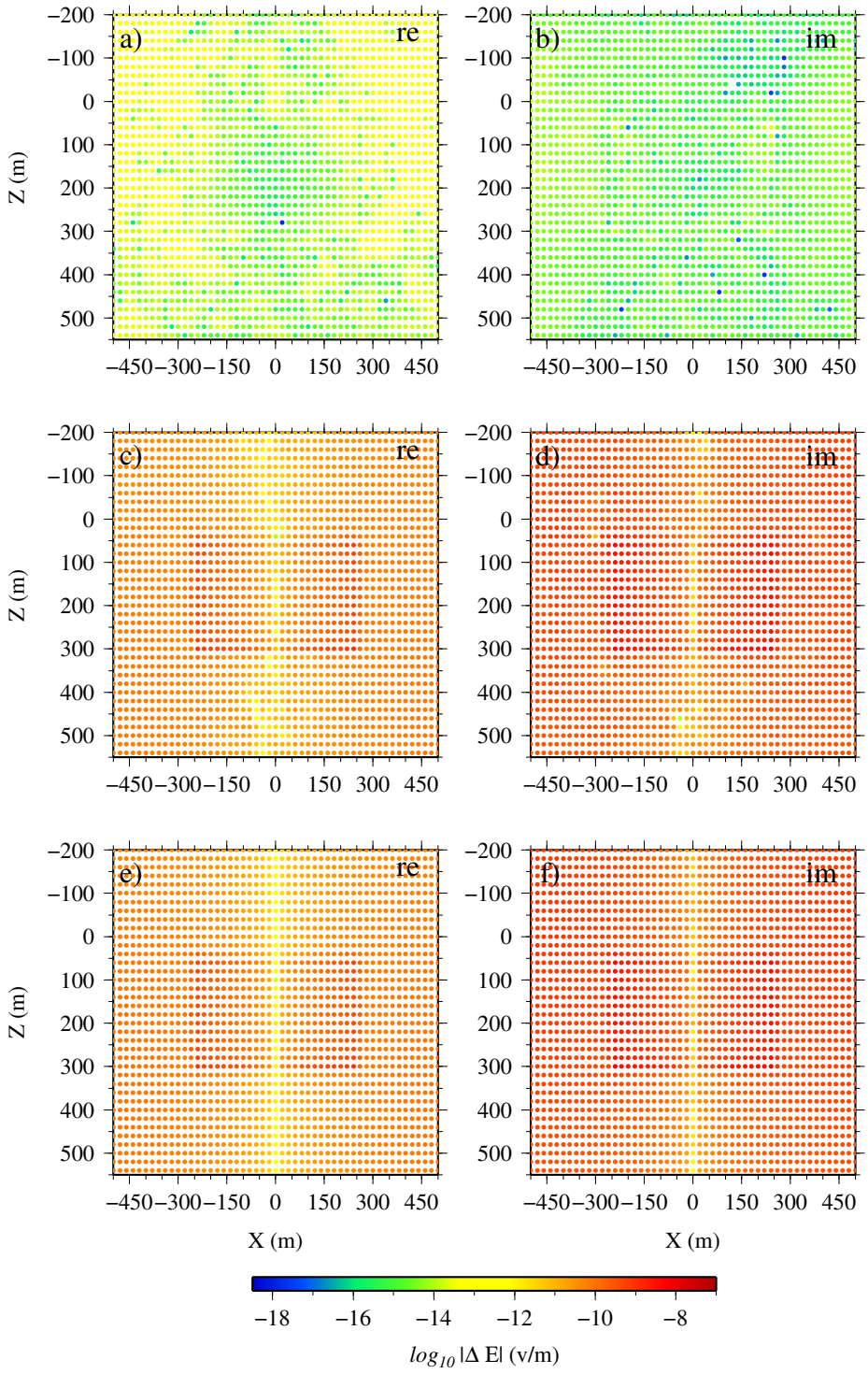

Figure 5.11: Discontinuity in the normal components of the fields for the inductive part, galvanic part and total electric field, for a plate conductance of 25 Siemens, for a frequency of 500 Hz. The vertical plane of nodes is located at $x = 498$ m. Panels (a) and (b) are respectively the discontinuity in the real and imaginary components of the inductive part. Panels (c) and (d) are the discontinuities due to the corresponding galvanic parts; and panels (e) and (f) are the corresponding total field discontinuities.

the scalar potentials, $\nabla\phi$, (see panels c and d) is dominant over those of the vector potentials (see panels a and b). This is compatible with the fact that the normal component of the vector potential is continuous across the inter-elements of different conductivities. This phenomenon is as expected here, because I am aiming for the Coulomb gauge ($\nabla \cdot \mathbf{A} = 0$) to hold across interfaces as well as within cells. Therefore the discontinuity in the normal component of the total electric field shown in panels (e) and (f) is mainly provided through the discontinuity in the normal component of the gradient of the scalar potential. The high value of discontinuity for the normal components of the galvanic and total fields around the conductive plate (in the host medium) where there is no conductivity gradient (see panels c to f in Figures 5.10 and 5.11) can be justified by the large range of the color scale used here. This concern can be mitigated if these discontinuities are normalized by the magnitude of the corresponding fields in each panel. Figures 5.12 and 5.13 show the normalized discontinuities for plate conductances of 6 and 25 S respectively. It is seen here that despite the significant discontinuity of the normal components of the total field at the boundary of the conductive plate (indicated in red dots), the discontinuity is zero in the host medium (indicated in blue dots) where there is no conductivity variation. The noisiness of the normalized inductive fields in panels (a) and (b) of the above-mentioned figures is because of the small size of the inductive part of the electric field for these examples.

The normal components of the current densities due to the inductive part, $\sigma\mathbf{A} \cdot \mathbf{n}$, the galvanic part, $\sigma\nabla\phi \cdot \mathbf{n}$, and the total current, $\sigma\mathbf{E} \cdot \mathbf{n}$, are also shown in Figures 5.14 and 5.15 for plate conductances of 6 and 25 S respectively. Here, as anticipated theoretically, the normal component of the total current density (see panels e and f) has the smallest discontinuity at the surface of the plate. The normal components due to the individual inductive and galvanic parts are however nicely discontinuous

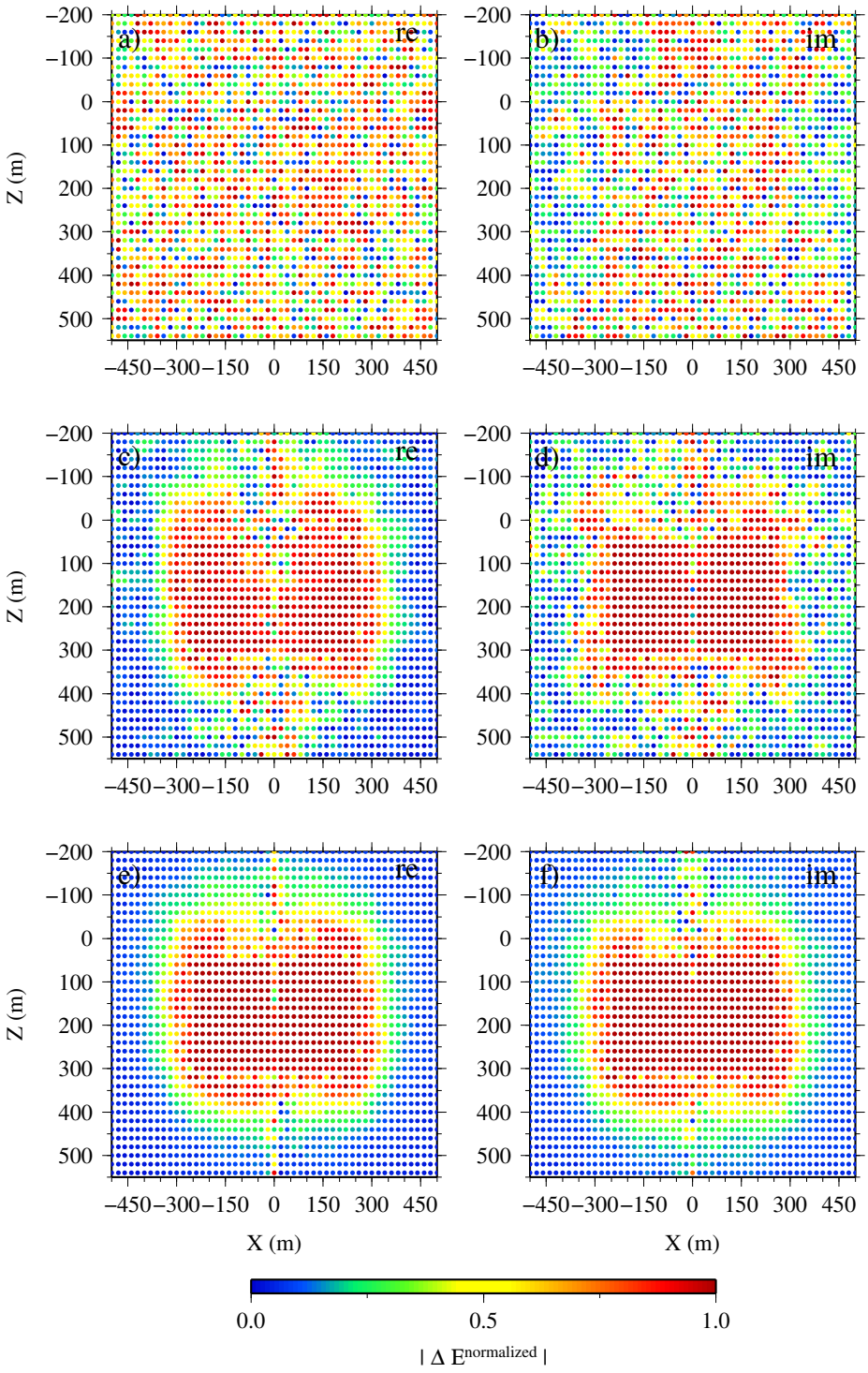

Figure 5.12: Normalized discontinuities in the normal components of the fields for the inductive part, galvanic part and total electric field, for a plate conductance of 6 Siemens, for a frequency of 500 Hz. The vertical plane of nodes is located at $x = 498$ m. Panels (a) and (b) are respectively the normalized discontinuity in the real and imaginary components of the inductive part. Panels (c) and (d) are the discontinuities due to the corresponding galvanic parts; and panels (e) and (f) are the corresponding total field discontinuities.

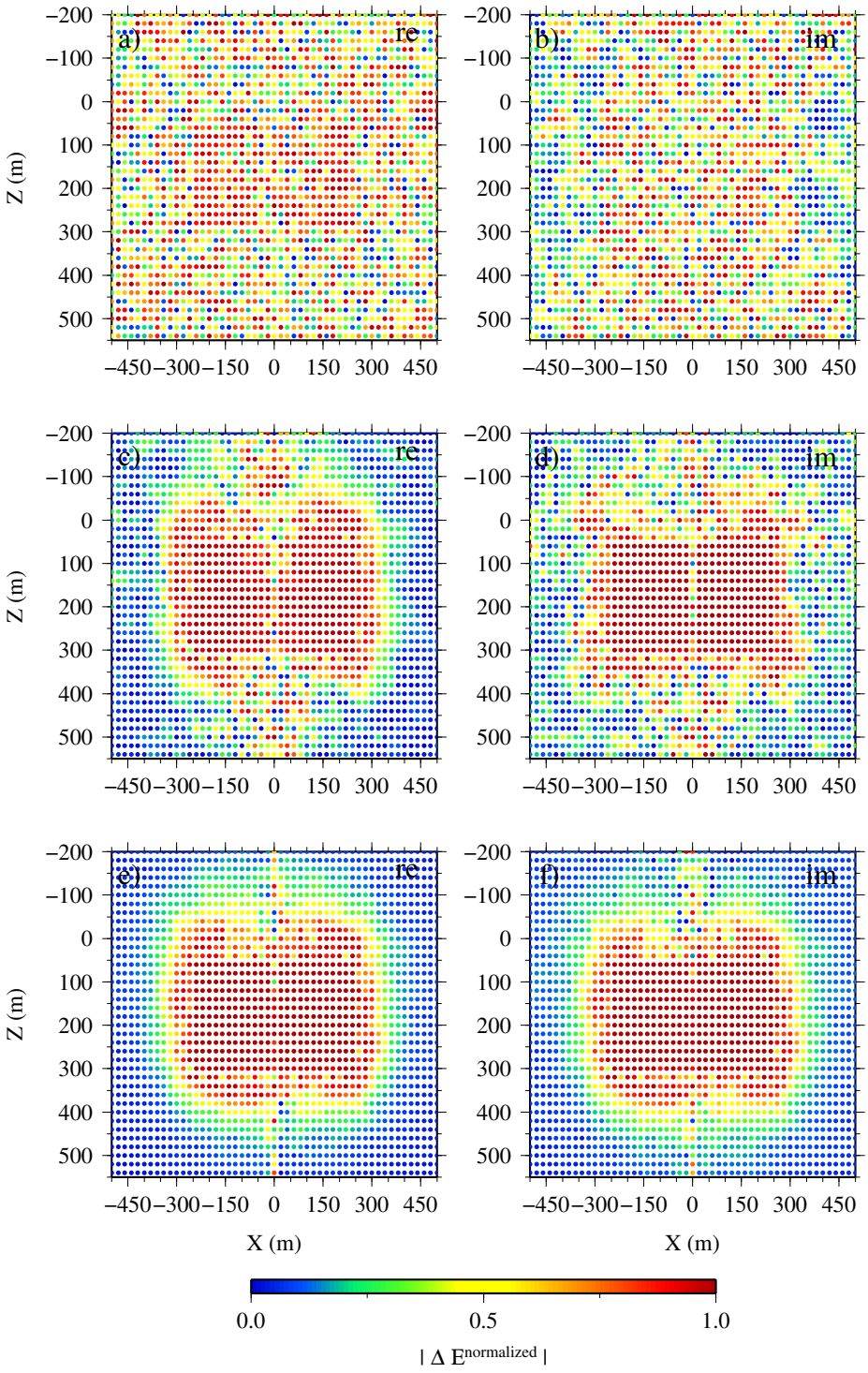

Figure 5.13: Normalized discontinuities in the normal components of the fields for the inductive part, galvanic part and total electric field, for a plate conductance of 25 Siemens, for a frequency of 500 Hz. The vertical plane of nodes is located at $x = 498$ m. Panels (a) and (b) are respectively the normalized discontinuity in the real and imaginary components of the inductive part. Panels (c) and (d) are the discontinuities due to the corresponding galvanic parts; and panels (e) and (f) are the corresponding total field discontinuities.

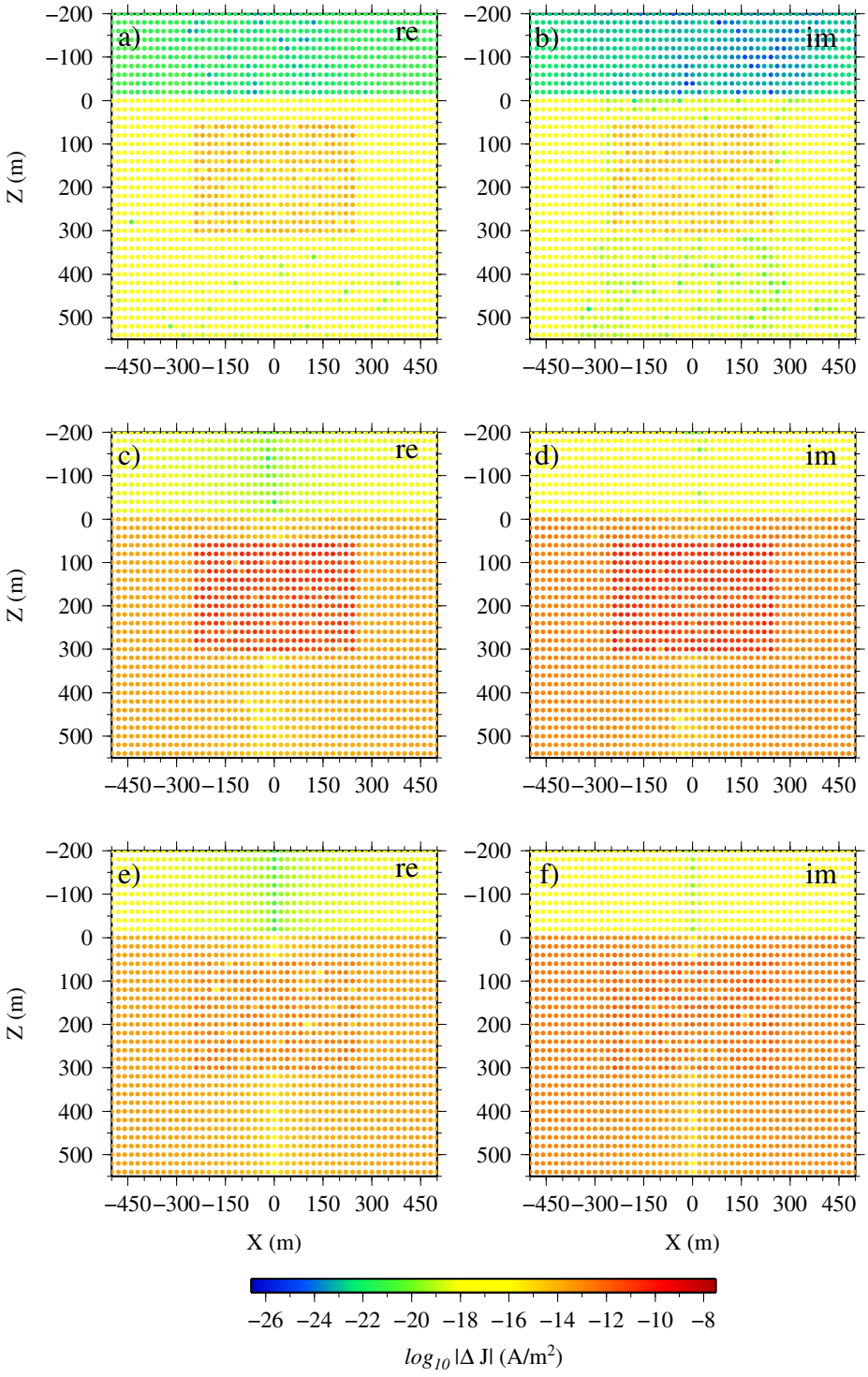

Figure 5.14: Normalized discontinuities in the normal components of the current densities for the inductive part, galvanic part and total electric field, for a plate conductance of 6 S, for a frequency of 500 Hz. The vertical plane of nodes is located at $x = 498$ m.

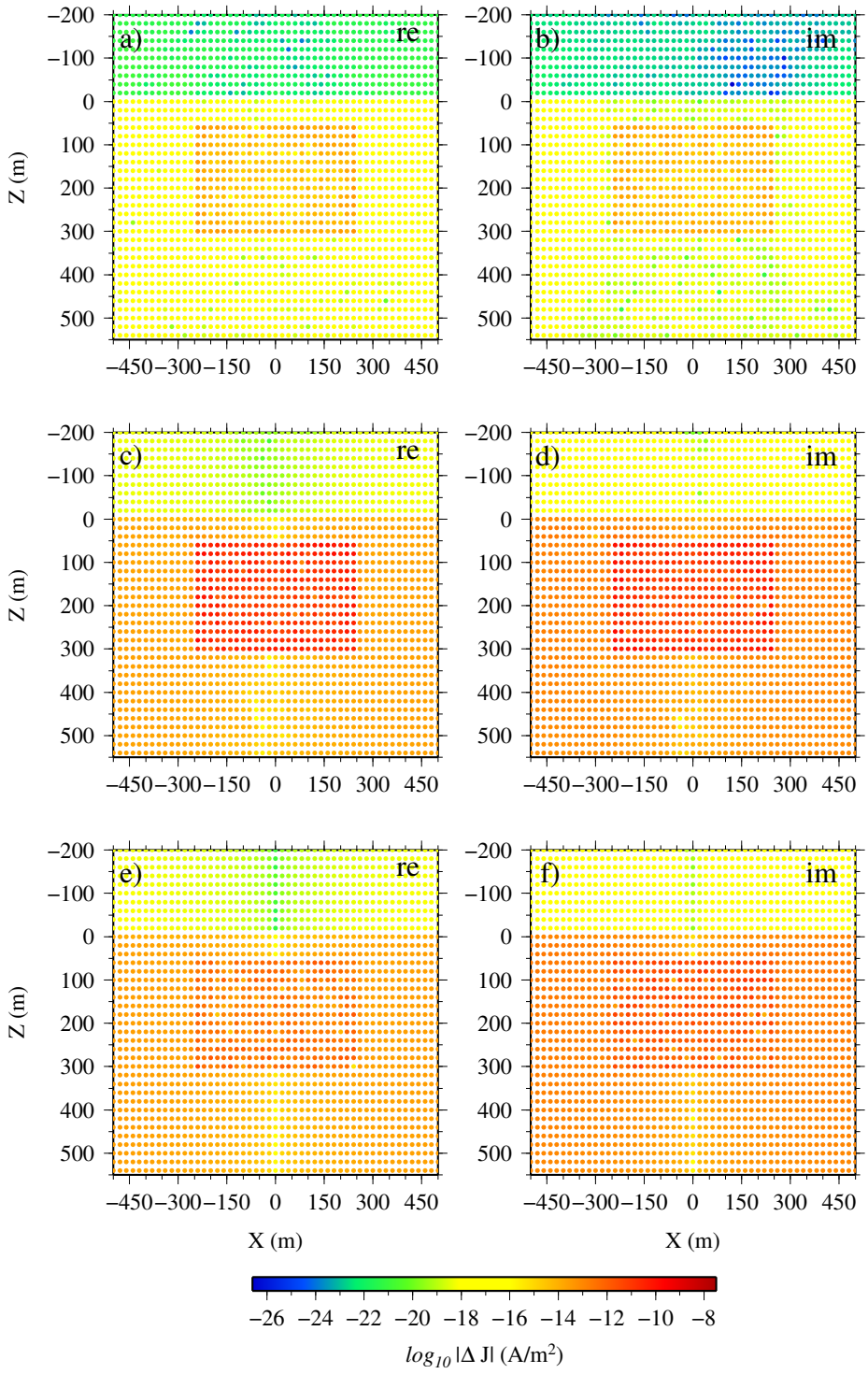

Figure 5.15: Normalized discontinuities in the normal components of the currents for the inductive part, galvanic part and total electric field, for a plate conductance of 25 S, for a frequency of 500 Hz. The vertical plane of nodes is located at $x = 498$ m.

across the interface. Similar to the fields, the discontinuities of the currents are also normalized here. Figures 5.16 and 5.17 show the normalized discontinuities of the currents for plate conductances of 6 and 25 S respectively. As anticipated it is seen that the total current, compared to the inductive and galvanic currents, is again less discontinuous at the surface of the plate. Also, the discontinuity of the total field at the surrounding medium is zero.

The problem of distorted inductive and galvanic fields, e.g. noisy inductive and galvanic arrows (see panels a, c, and d in Figures 5.6 and 5.7) compared to the solid-looking total fields (see panels e and f in Figures 5.6 and 5.7), for a higher frequency of 500 Hz used here could be counteracted using the choice of explicit Coulomb gauge condition.

5.3 Coulomb gauged solution

The $\mathbf{A} - \phi$ system of equations presented in Chapter 3 (see equations 3.5 and 3.6) is implicitly gauged through the choice of edge-element basis functions for the vector potential. This choice was made as a result of $\nabla \cdot \mathbf{A}$ being explicitly zero within a cell. However, this condition does not necessarily hold across the interfaces. In terms of simulating the total electric and magnetic fields this method has produced accurate and elegant results for the examples yet presented in this thesis. However, as demonstrated in the above example, this formulation can generate peculiar results for the individual vector and scalar potential electric fields. In order to remedy these issues the Coulomb gauge condition, i.e., $\nabla \cdot \mathbf{A} = 0$, is directly used in the discretization procedure. To demonstrate the gauged system, the weighted equations are reiterated

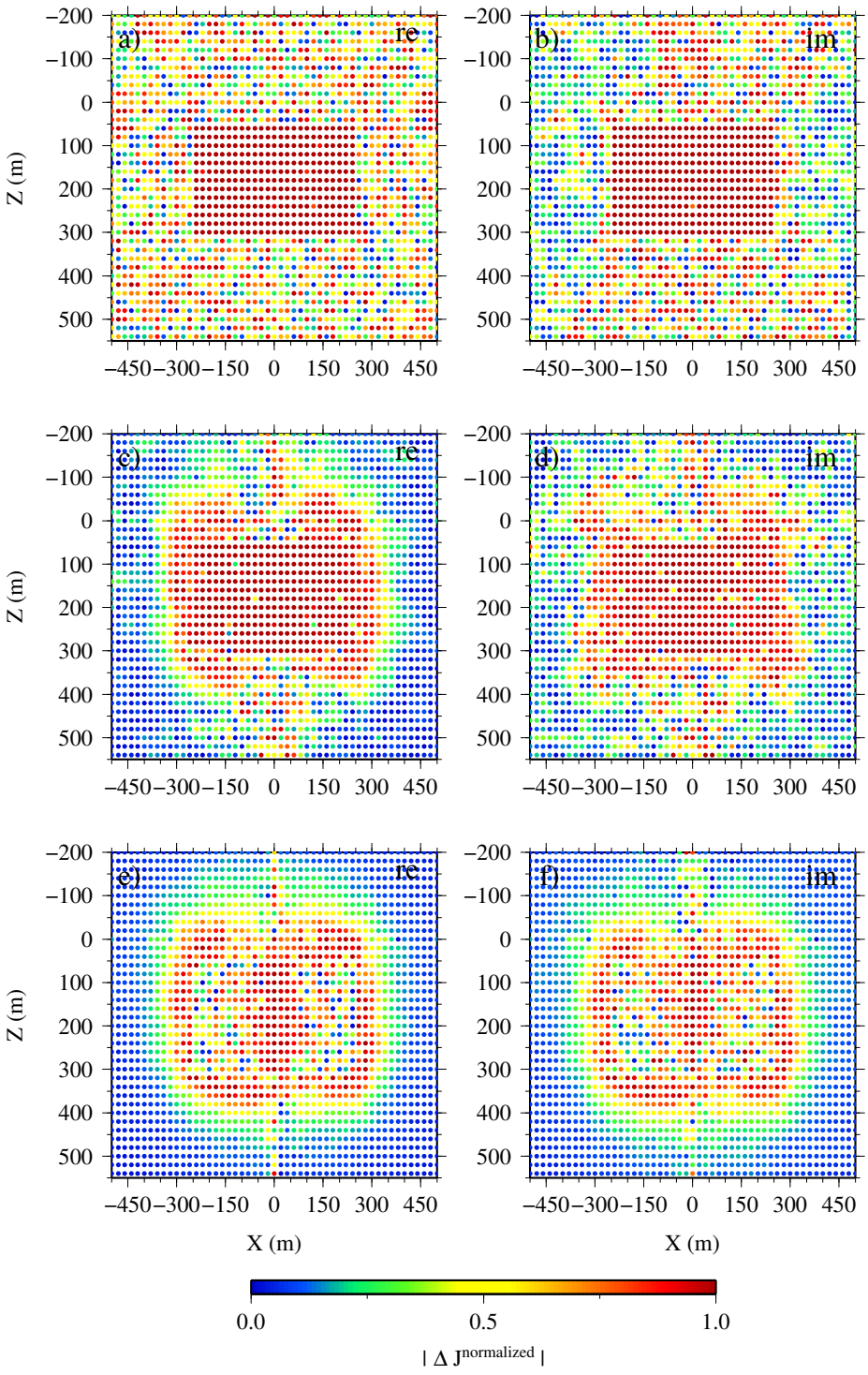

Figure 5.16: Normalized discontinuities in the normal components of the current densities for the inductive part, galvanic part and total electric field, for a plate conductance of 6 S, for a frequency of 500 Hz. The vertical plane of nodes is located at $x = 498$ m.

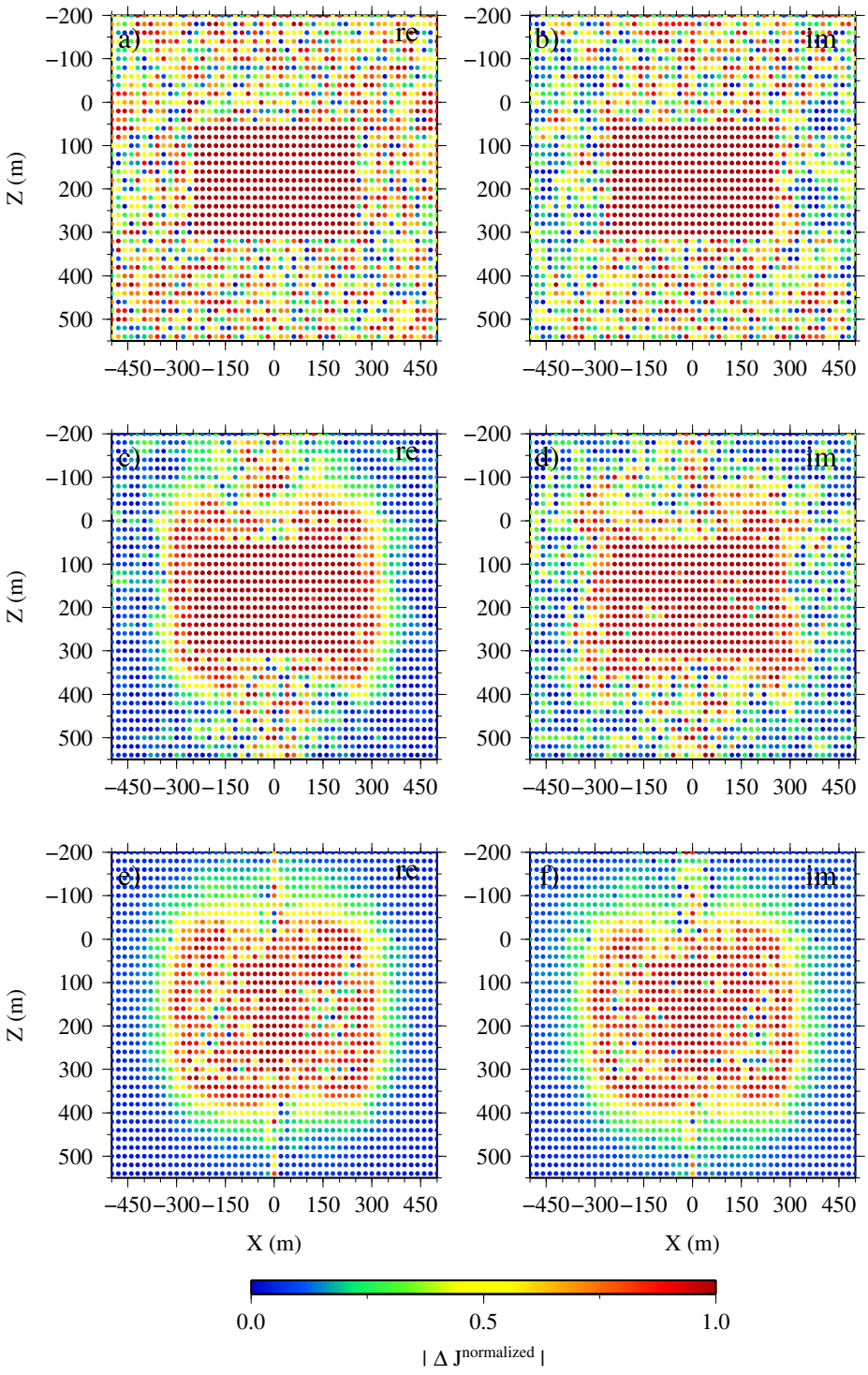

Figure 5.17: Normalized discontinuities in the normal components of the current densities for the inductive part, galvanic part and total electric field, for a plate conductance of 25 S, for a frequency of 500 Hz. The vertical plane of nodes is located at $x = 498$ m.

here from Chapter 3:

$$\int_\Omega \mathbf{W}\cdot(\nabla\times\nabla\times\tilde{\mathbf{A}})\ d\Omega\ + i\omega\mu_0\int_\Omega \sigma\ \mathbf{W}\cdot\tilde{\mathbf{A}}\ d\Omega\ + \mu_0\int_\Omega \sigma\ \mathbf{W}\cdot\nabla\tilde{\phi}\ d\Omega = \mu_0\int_\Omega \mathbf{W}\cdot\mathbf{J^s}\ d\Omega, \tag{5.1}$$

$$-i\omega\int_\Omega v\nabla\cdot(\sigma\tilde{\mathbf{A}})\ d\Omega\ - \int_\Omega v\nabla\cdot(\sigma\nabla\tilde{\phi})\ d\Omega\ = -\int_\Omega v\ \nabla\cdot\mathbf{J^s}\ d\Omega. \tag{5.2}$$

The imposition of the Coulomb gauge condition would require splitting the $\nabla\times\nabla\times\mathbf{A}$ into $\nabla(\nabla\cdot\mathbf{A})-\nabla^2\mathbf{A}$ (Ward and Hohmann, 1988) in equation 5.1. However this implementation is not tractable as edge-elements are chosen for the vector potential here. In particular, replacing the term $\nabla^2\mathbf{A}$ for $\nabla\times\nabla\times\mathbf{A}$ in the left hand side of equation 5.1 produces zero integrals (see section B.2 for details). The first term in equation 5.2 can however be gauged if the parameter σ is considered constant within each volume:

$$-i\omega\int_\Omega v\ \sigma\ \nabla\cdot\tilde{\mathbf{A}}\ d\Omega \rightarrow 0 - \int_\Omega v\nabla\cdot(\sigma\nabla\tilde{\phi})\ d\Omega\ = -\int_\Omega v\ \nabla\cdot\mathbf{J^s}\ d\Omega. \tag{5.3}$$

A new system of equations is then formed using equations 5.1 and 5.3,

$$\begin{pmatrix} \mathbf{C}+i\omega\mu_0\mathbf{D} & \mu_0\mathbf{F} \\ \mathbf{0} & \mathbf{H} \end{pmatrix}\begin{pmatrix} \tilde{A} \\ \tilde{\phi} \end{pmatrix} = \begin{pmatrix} \mu_0 S_1 \\ S_3 \end{pmatrix}. \tag{5.4}$$

In order to remove the problem of ill-shaped inductive and galvanic arrows for the examples presented in the previous section, the new system given by equation 5.4 is solved in preference to the system in equation 3.27. The gauged system however does not produce a scalar potential if a magnetic dipole or a loop of current is used as the source of excitation. In particular, as a result of the source term from the equation of conservation of charge (S_3 in equation 5.4) being zero for a magnetic dipole or a

current loop source, the parameter $\tilde{\phi}$ would then be zero after solution. Hence, the total electric field approximation is provided by the contribution only from the vector potential.

The plate example presented in Section 5.2 is modelled using the new system. In order to judge the correctness of the solution for the gauged system in equation 5.4 a comparison with the results from the original decomposed system of equation 3.27 is performed. In order to efficiently use the direct solver in terms of the memory usage in the computer a smaller mesh is used here. The new mesh consists of 358458 cells, 58490 nodes, and 417459 edges. The dimension of the mesh is also $13 \times 13 \times 13$ km in the x-, y- and z-directions. The dimension of the Krylov subspace used here is 300 for the GMRES solver. Figure 5.18 shows the z-component of the magnetic field for the iterative solutions to the original and gauged $\mathbf{A} - \phi$ systems. It is seen here that the iterative gauged solution of the system in equation 5.4 (shown in blue triangles and circles), particularly in the imaginary part, does not match the solution from the original decomposed system (shown using cross and plus symbols). The reason for the inadequate solution of the gauged system lies in the slow convergence of the iterative solver for this example. This issue is demonstrated in Figure 5.19 where the preconditioned residual norms due to the two solutions are shown. It is seen here that an adequate solution to the original $\mathbf{A} - \phi$ system is obtained after approximately 7500 iterations of the iterative solver. The decrease of the residual norm due to the gauged system is however very slow.

5.3.1 Direct solution

In order to provide the final solution for the gauged system the direct solver MUMPS is used. The non-symmetric coefficient matrix seen in equation 5.4 with the relevant

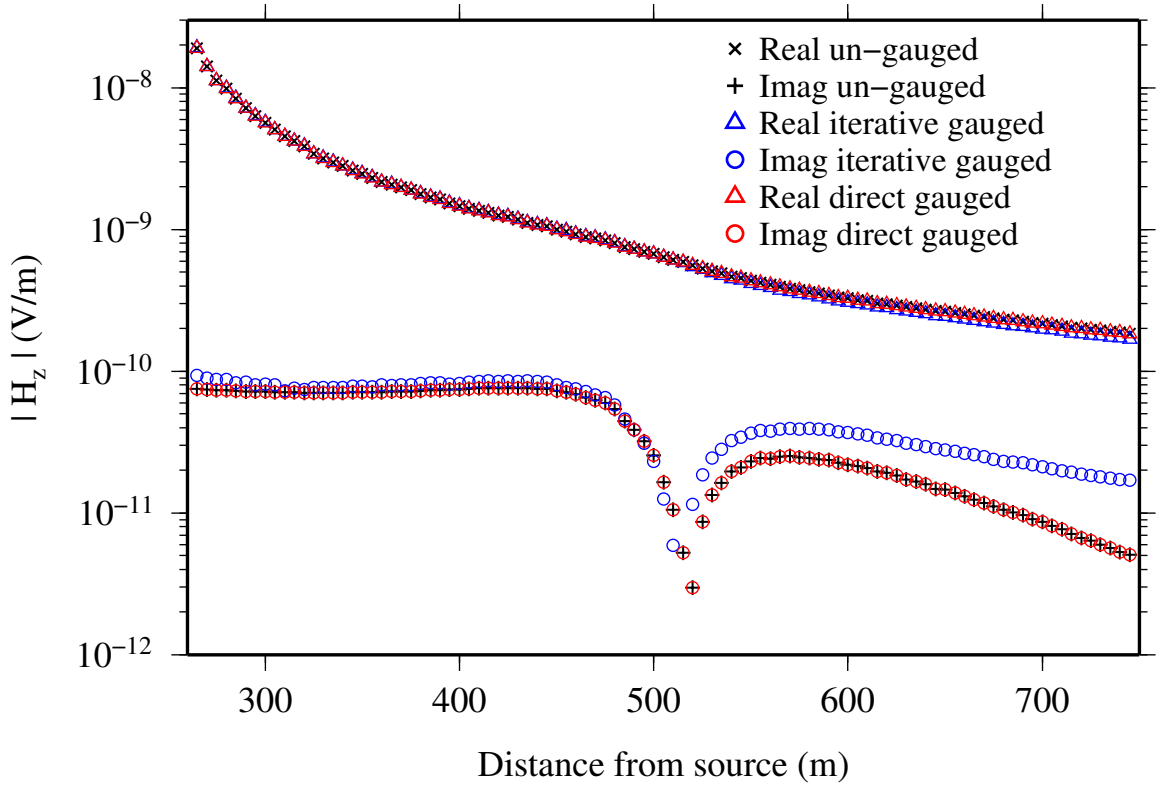

Figure 5.18: A comparison of the z-component of the real and imaginary parts of the total magnetic field observed on the Earth's surface for the plate example (see Figure 5.1). Data are synthesized using the iterative solution to the original decomposed (i.e., un-gauged here) system (cross and plus symbols in black), the iterative solution to the gauged system (triangles and circles in blue), and the direct solution to the gauged system (triangles and circles in red).

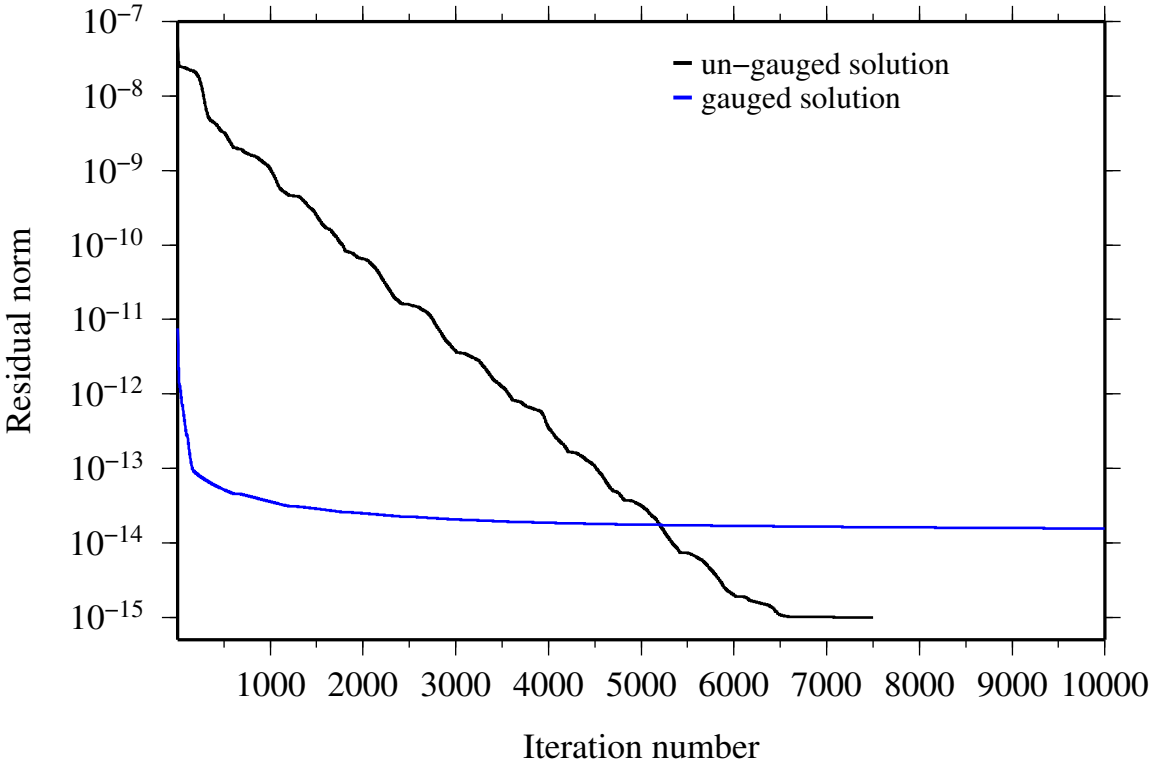

Figure 5.19: The convergence curves for the original decomposed solution (black), and the decomposed gauged solution shown (blue) for a frequency of 500 Hz for the plate example.

source term on the right hand side are introduced into MUMPS in sparse format. The total field results for the direct solution to the above example are shown in Figure 5.18. It is seen that the direct gauged solution is coincident with the ungauged iterative solution for both the real and imaginary parts of the magnetic field. The direct solution however uses significant more space in the memory of the computer specifically, 21.3 Gbytes for the mesh used in this example. The memory usage for the iterative ungauged solution was however only 4 Gbytes.

In order to further investigate the correctness of the three solutions observed in Figure 5.18 the total field and current density are plotted in the same $x = 500$ m plane as used in Figures 5.6 to 5.9. Figure 5.20 shows the arrows of the total electric fields due to the three solution methods presented above. Figure 5.21 shows the corresponding current densities. It is seen in both figures that the fields and currents produced from the direct solution of the gauged system (see panels c and d) resemble those of the iterative solutions from the original decomposed system (see panels e and f). However, the results from the iterative solution (see panel a and b) to the gauged system are not adequate.

Comparison of the solutions from the direct and iterative solvers will further be investigated in future sections. However, in the next section I will be investigating the large loop and plate example to gather more information on galvanic and inductive effects, and also more evidence for needing gauged versus ungauged solutions.

5.3.2 The effect of conductive host and overburden

An investigation of the electromagnetic phasor response for plate models including a conductive overburden layer is presented in Lajoie and West (1976). Here, in order to observe the effect of the overburden and the host on the resulting fields for a number

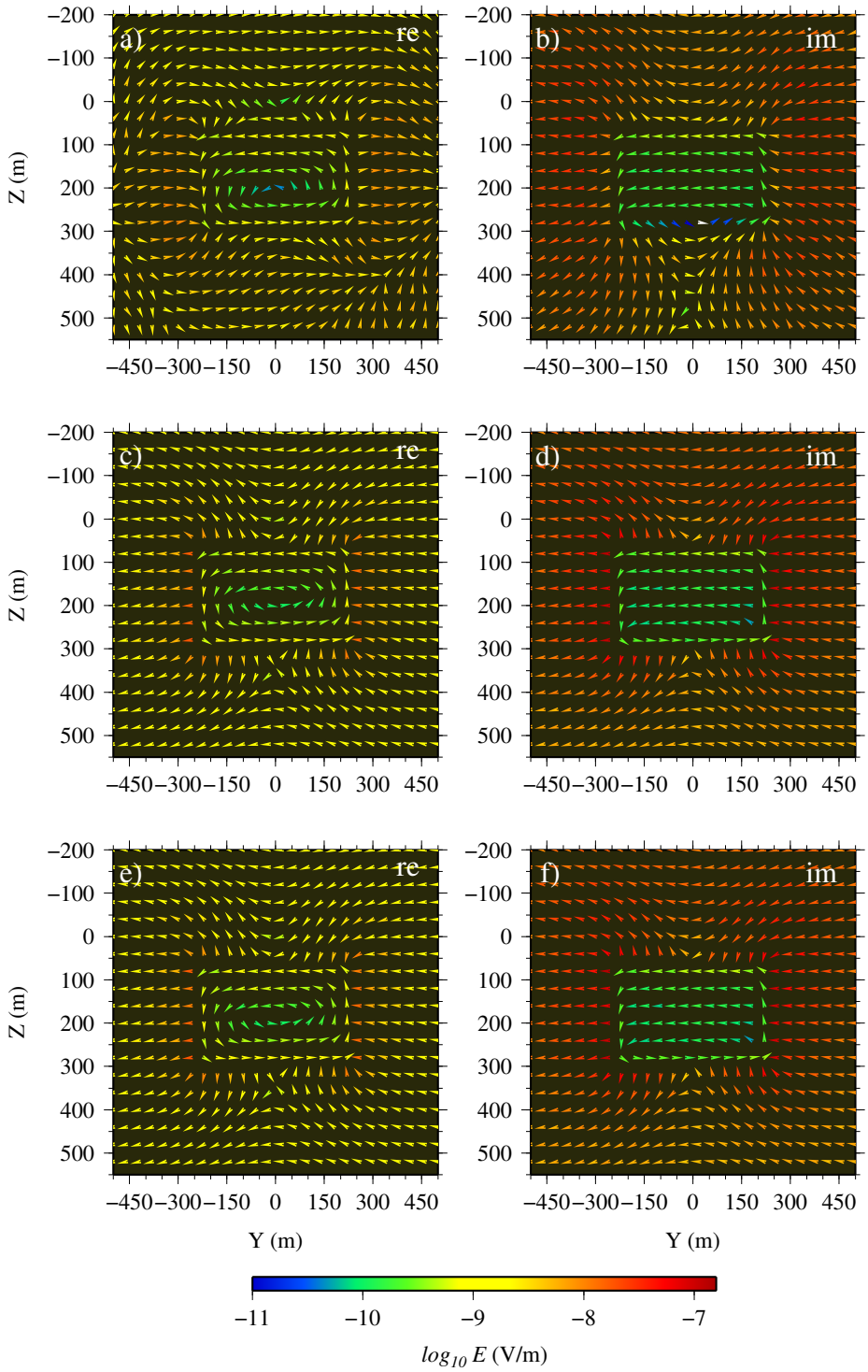

Figure 5.20: Arrows of the total electric field for three solutions for a frequency of 500 Hz and a plate conductance of 25 Siemens. All six panels show the yz-component of the total electric fields in a plane of nodes at $x = 500$ m: the real (a) and imaginary (b) components for the iterative solution to the gauged system; the real (c) and imaginary (d) components for the direct solution to the gauged system, and the real (e) and imaginary (f) components for the iterative solution to the original ungauged system.

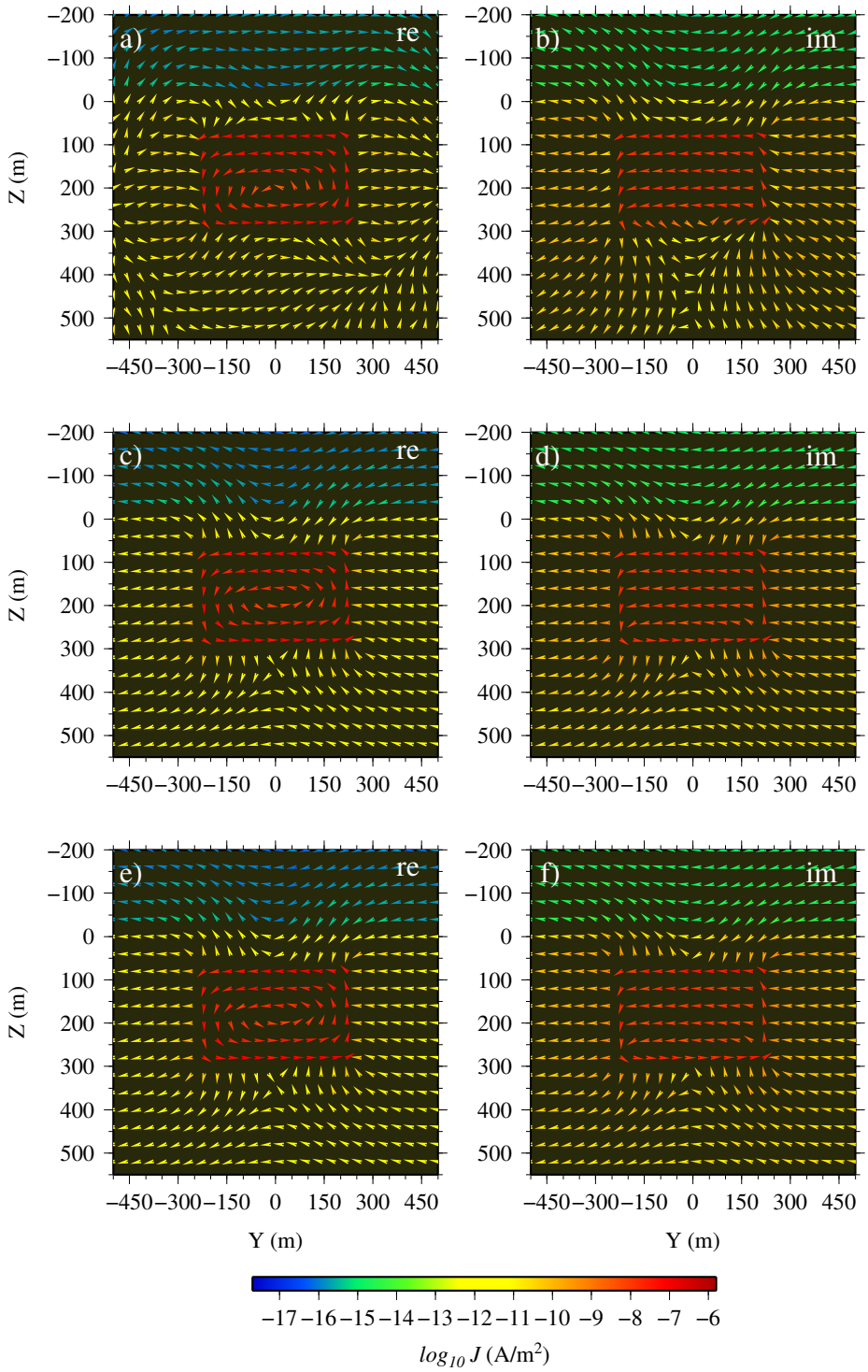

Figure 5.21: Arrows of the current density for three solutions for a frequency of 500 Hz and a plate conductance of 25 S. All six panels show the yz-component of the total current density in a plane of nodes at $x = 500$ m: the real (a) and imaginary (b) components for the iterative solution to the gauged system; the real (c) and imaginary (d) components for the direct solution to the gauged system, and the real (e) and imaginary (f) components for the iterative solution to the original ungauged system.

of conductivities and frequencies, I modified slightly the model presented above. In fact, the plate is now overlain by 100 m (instead of 50 m in the original model) of an overburden layer (see Figure 5.22). The reason for this modification was the high number of tetrahedral elements generated for the model that includes a thinner overburden layer. The depth to the top of the conductive plate is 200 m here. In order to see both the inductive and galvanic parts, solutions due to the un-gauged system are shown. Also in order for the source signal to adequately pass through the top conductive layer and sense the plate, a lower frequency of 10 Hz is used.

For the first experiment the overburden layer is ignored in the model. In particular, the fields and currents for the conductive plate, again with a conductance of 10.5 S, are only investigated for two different hosts of 0.0003 and 0.003 S/m. Figure 5.23 shows the inductive, galvanic and total electric fields (only the real components) for these two hosts. By comparison amongst the different panels in this figure, the inductive component has slightly increased in size for the higher conductivity of 0.003 S/m. Also, it can be seen here that the galvanic component has increased in the host and particularly around the plate for the higher host conductivity of 0.003 S/m. Furthermore, for the frequency used here, the total field seen inside the conductive plate is a combination of inductive and galvanic fields. The corresponding plot for the current densities is shown in Figure 5.24. Here the current density has increased in all of the inductive, galvanic and total fields. Moreover, for the host with the higher conductivity of 0.003 S/m, the orientation of the total current (see panel f) in the background is dominated by the contribution from the galvanic part.

The effects of the conductive overburden are also investigated for this example. For a host conductivity of 0.003 S/m, Figure 5.25 shows the resulting inductive, galvanic

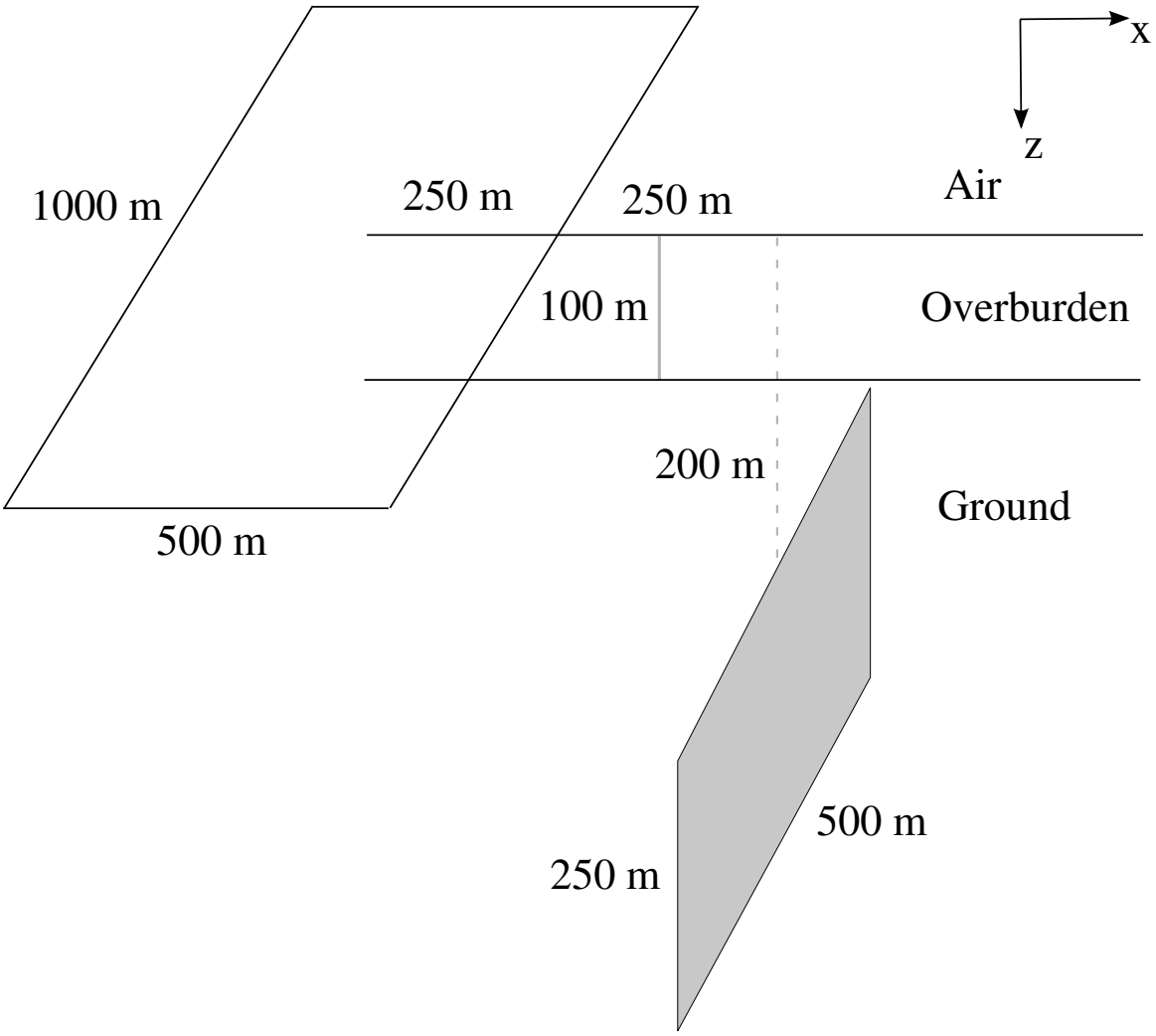

Figure 5.22: The geometry of the model for the deep plate and overburden example. The loop of current is located at the air-ground interface with its center at the origin. The narrow vertical plate is 200 m deep and 250 m away from the nearest long edge of the transmitter loop. The thickness of the overburden layer is 100 m.

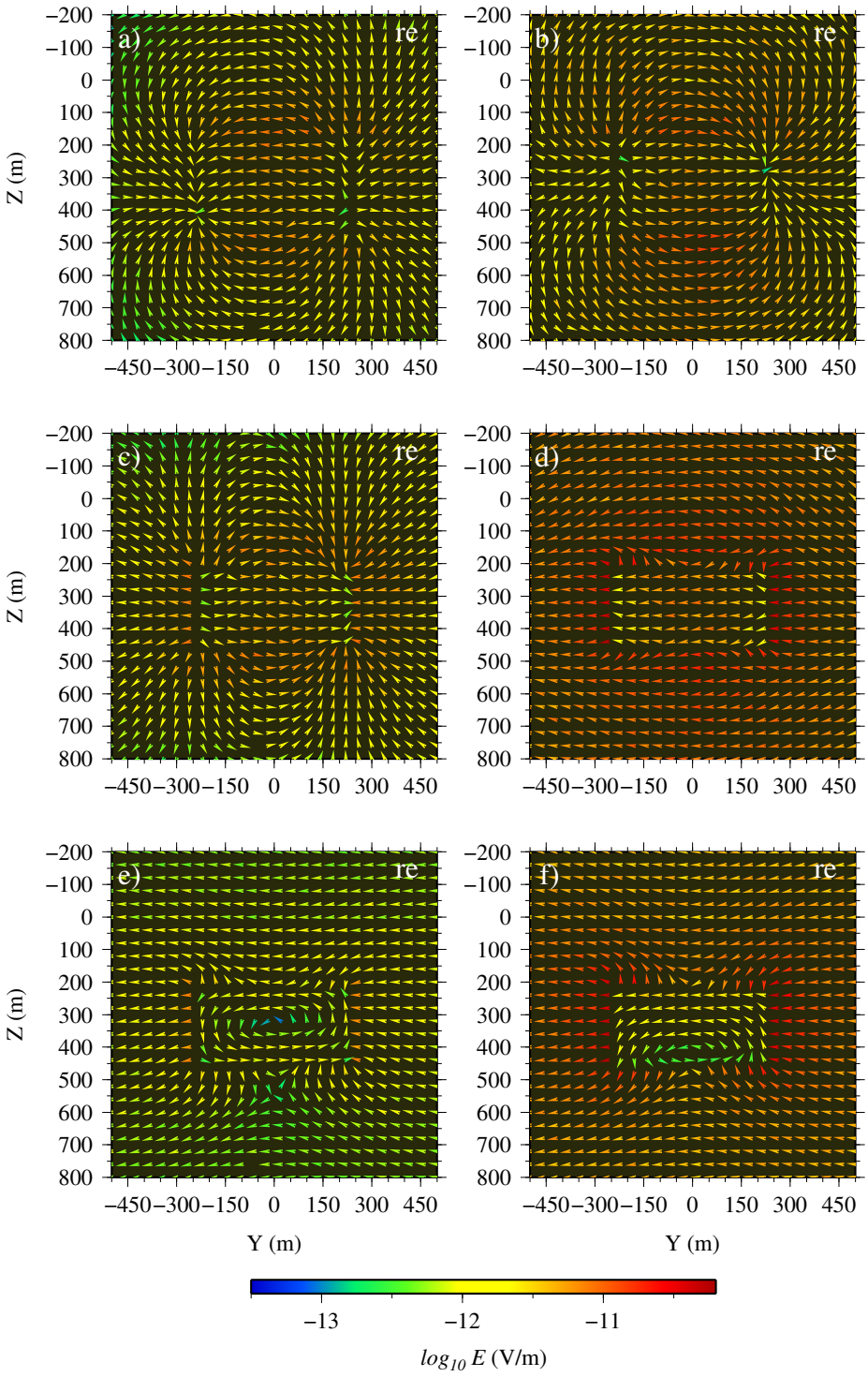

Figure 5.23: Arrows of the fields for the un-gauged solutions to the deep plate example for a frequency of 10 Hz and a plate conductance of 10.5 S. Panels (a), (c) and (e) on the left are respectively the real components of the inductive, galvanic and total fields for a host conductivity of 0.0003 S/m. Panels (b), (d) and (f) on the right are the corresponding fields for a host conductivity of 0.003 S/m.

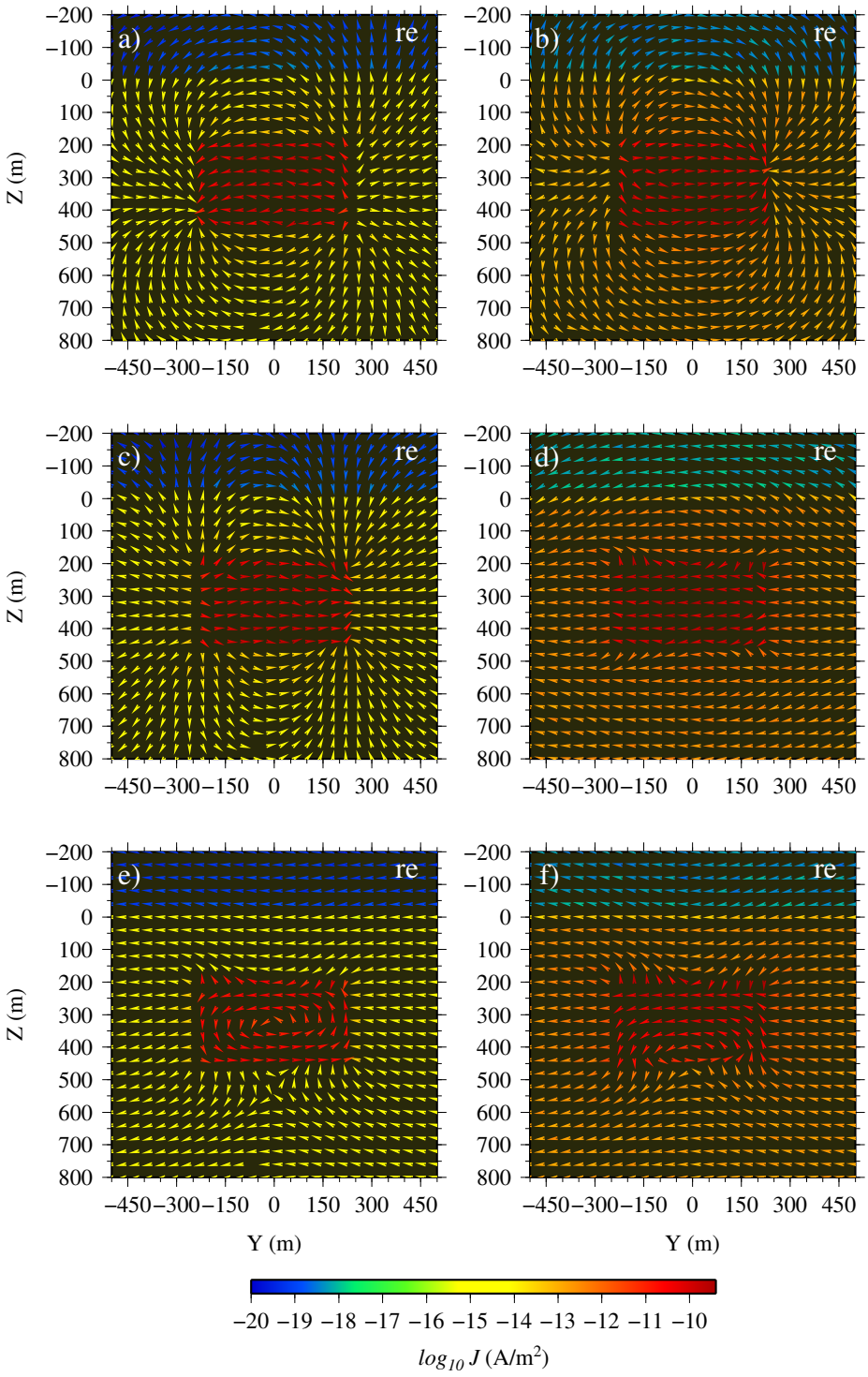

Figure 5.24: Arrows of the currents for the un-gauged solutions to the deep plate example for a frequency of 10 Hz and a plate conductance of 10.5 S. Panels (a), (c) and (e) on the left are respectively the real components of the inductive, galvanic and total current densities for a host conductivity of 0.0003 S/m. Panels (b), (d) and (f) on the right are the corresponding currents for a host conductivity of 0.003 S/m.

and total electric fields for increasing conductivities of the overburden layer. Three conductivities of 0.01, 0.045, and 0.1 S/m are chosen for the overburden layer. It can be noticed here that the galvanic part (see panels d, e and f) increases in the host and around the target for the increasing overburden conductivities. A hint of vortex fields can also be seen in the inductive component (see panels a, b and c) as the overburden conductivity increases. Figure 5.26 shows the corresponding inductive, galvanic and total current densities. Here however, because of the broad range of current magnitudes shown, the increase in the current densities is not as evident (except for the overburden layer).

The discontinuities in the normal component of the inductive, galvanic and total electric fields for the plane $x = 498$ m are shown in Figure 5.27. Figure 5.28 shows the corresponding discontinuities in the normal component of the current densities. As for the situations described in Section 5.2.3 it is the galvanic part of the electric field that predominantly contributes in forming the total discontinuity of the electric field across the interface. The continuity in the normal component of the total current density (see Figure 5.28) is however the result of discontinuities in both the inductive and galvanic currents. Also, similar to the plots shown, for example in Figures 5.12 and 5.13, in order to relatively compare the continuity conditions of the inductive, galvanic, and total fields, the data are normalized. Figure 5.29 shows the discontinuity of the fields for the corresponding fields shown in Figure 5.27. It is seen here that despite the predominant contribution from the galvanic parts (see panels d, e, and (f) in Figure 5.29) the inductive components (see panels a, b, and c in Figure 5.29) insignificantly contribute to forming the discontinuity of the total electric fields (see panels g, h, and i in Figure 5.29) on the surface of the plate. The corresponding normalized data for the current density are also shown in Figure 5.30. Here, in contrast

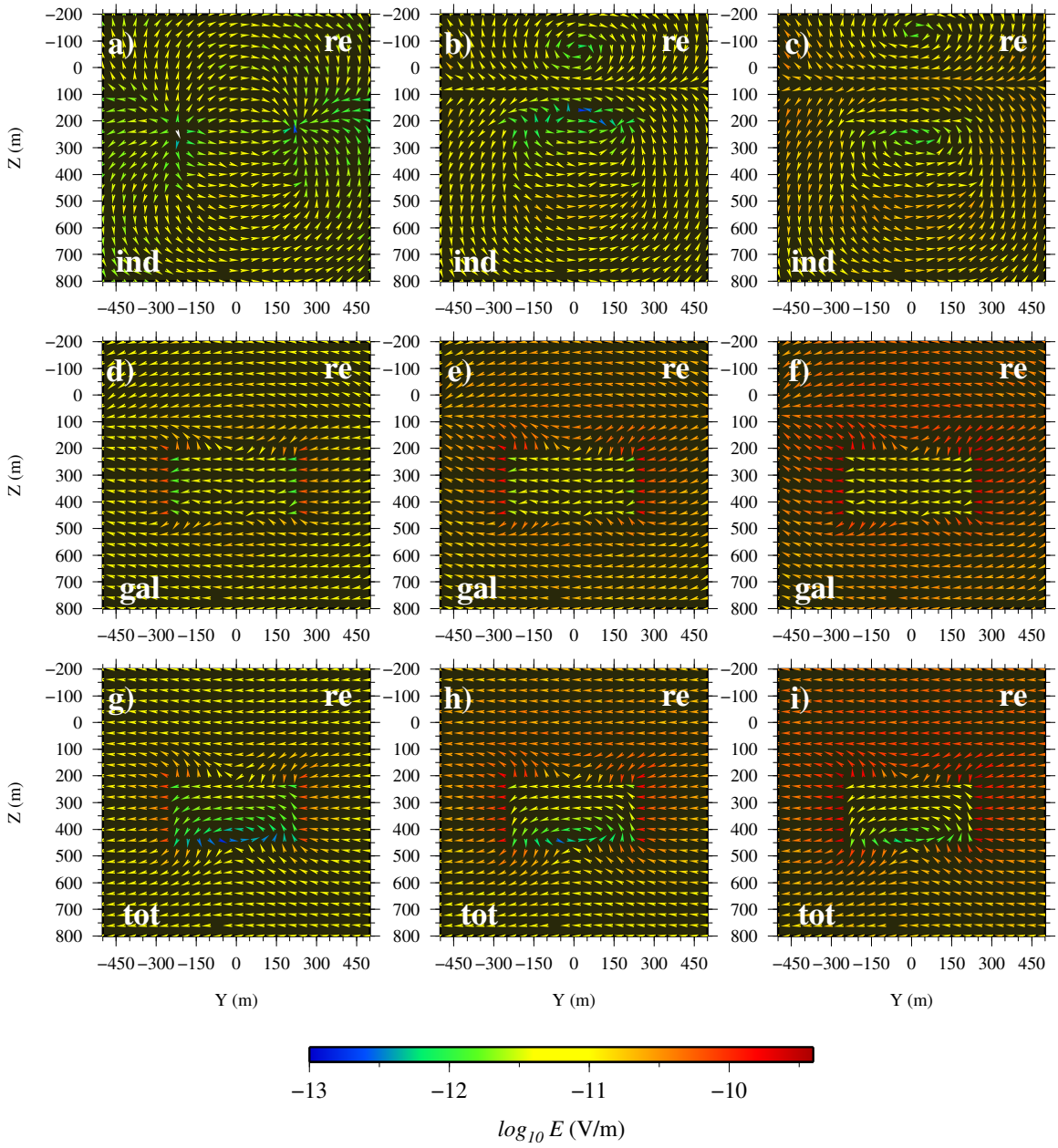

Figure 5.25: Arrows of the fields (only real components) for a host conductivity of 0.003 S/m, and for a range of conductivities of the overburden layer. Panels (a), (b), and (c) are the inductive parts for overburden conductivities of 0.01, 0.045, and 0.1 S/m respectively. Panels (d), (e) and (f) are the corresponding galvanic parts. Panels (f), (g) and (h) are the corresponding total fields.

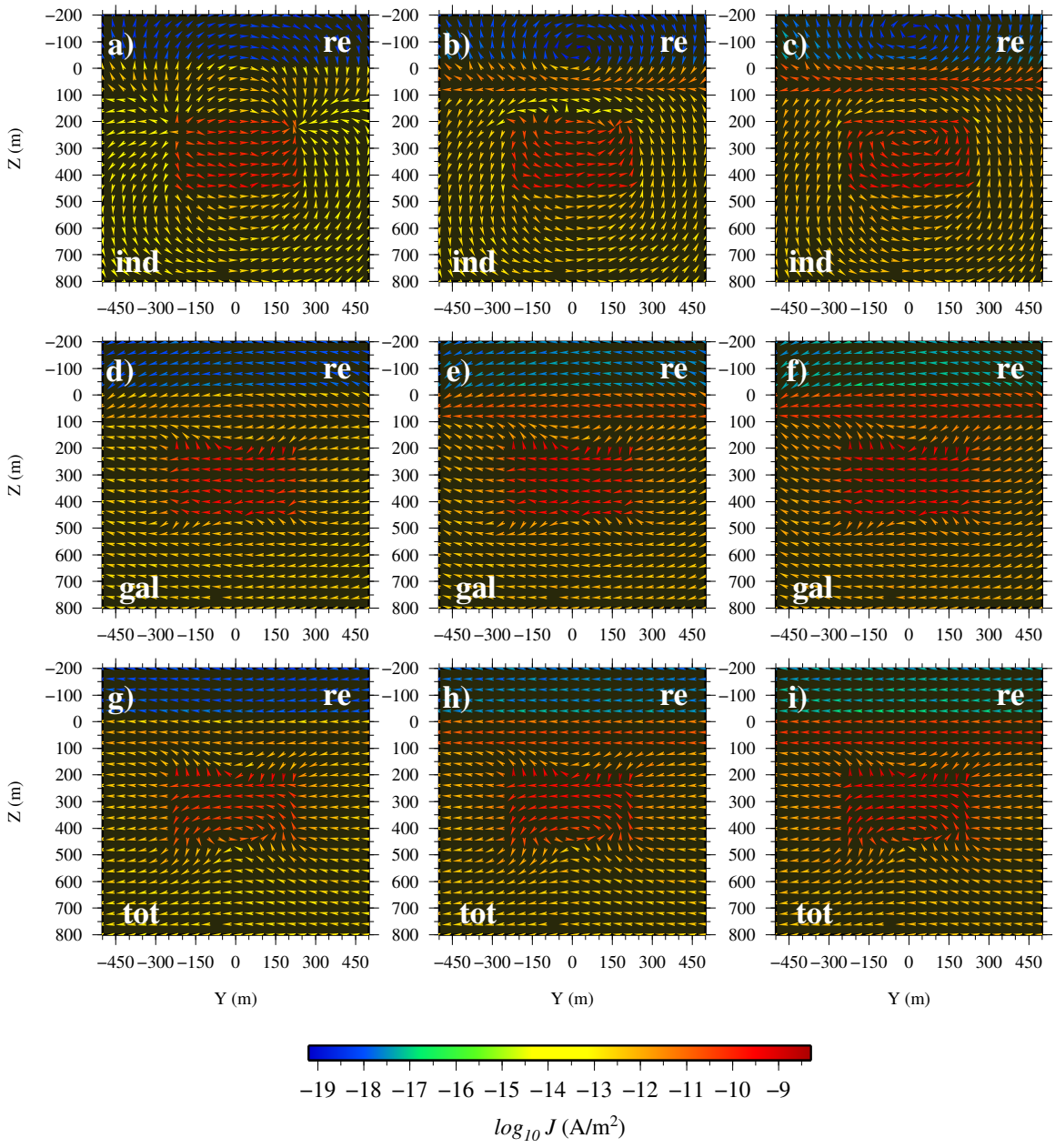

Figure 5.26: Arrows of the current densities (only real components) for a host conductivity of 0.003 S/m, and for a range of conductivities of the overburden layer. Panels (a), (b), and (c) are the inductive parts for overburden conductivities of 0.01, 0.045, and 0.1 S/m respectively. Panels (d), (e) and (f) are the corresponding galvanic parts. Panels (f), (g) and (h) are the corresponding total currents.

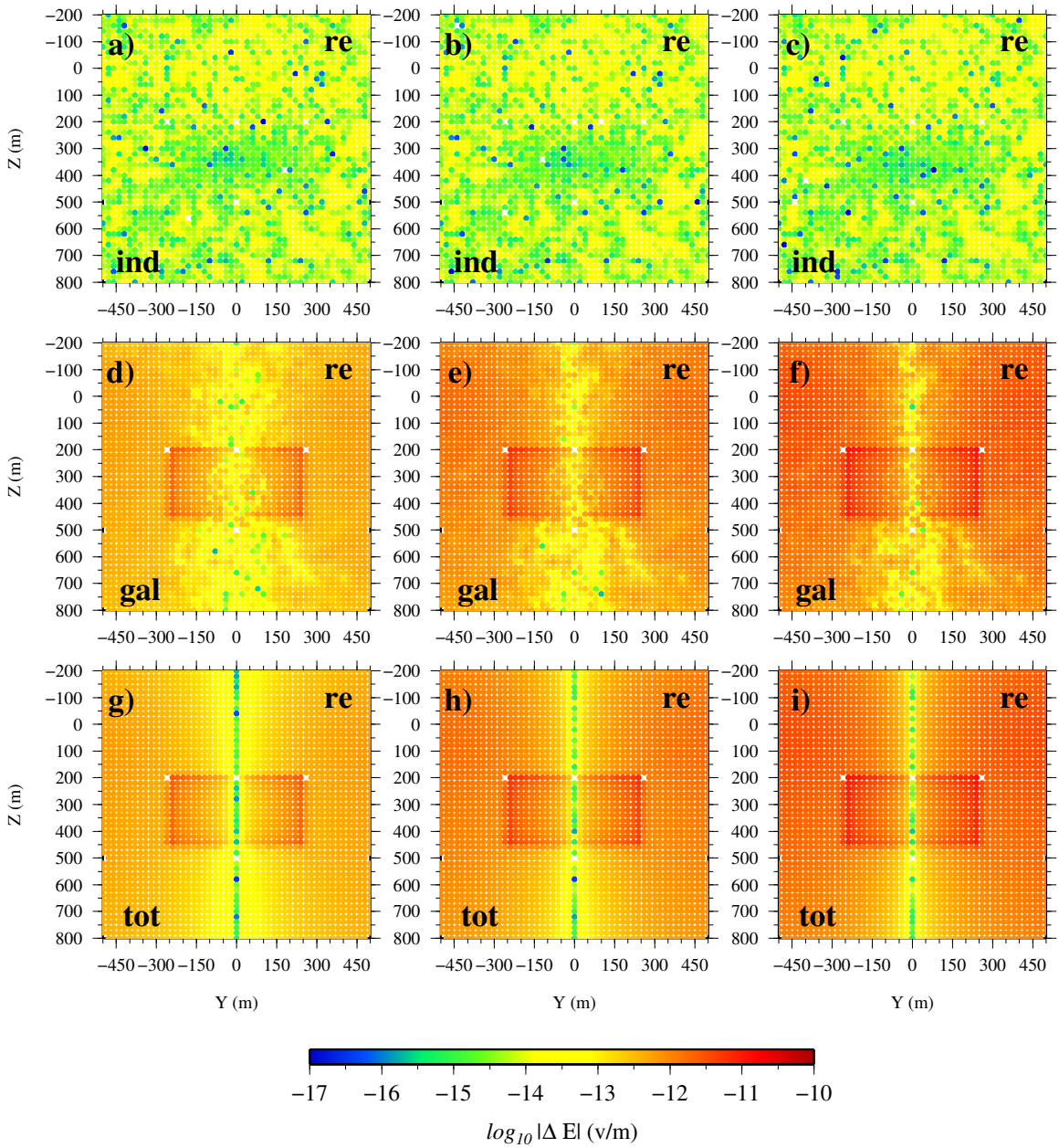

Figure 5.27: Discontinuity in the normal components of the fields for the inductive part, galvanic part and total electric field for a host conductivity of 0.003 S/m and for a range of conductivities of the overburden layer. Panels (a), (b), and (c) are the inductive parts for overburden conductivities of 0.01, 0.045, and 0.1 S/m respectively. Panels (d), (e) and (f) are the corresponding galvanic parts. Panels (f), (g) and (h) are the corresponding total fields.

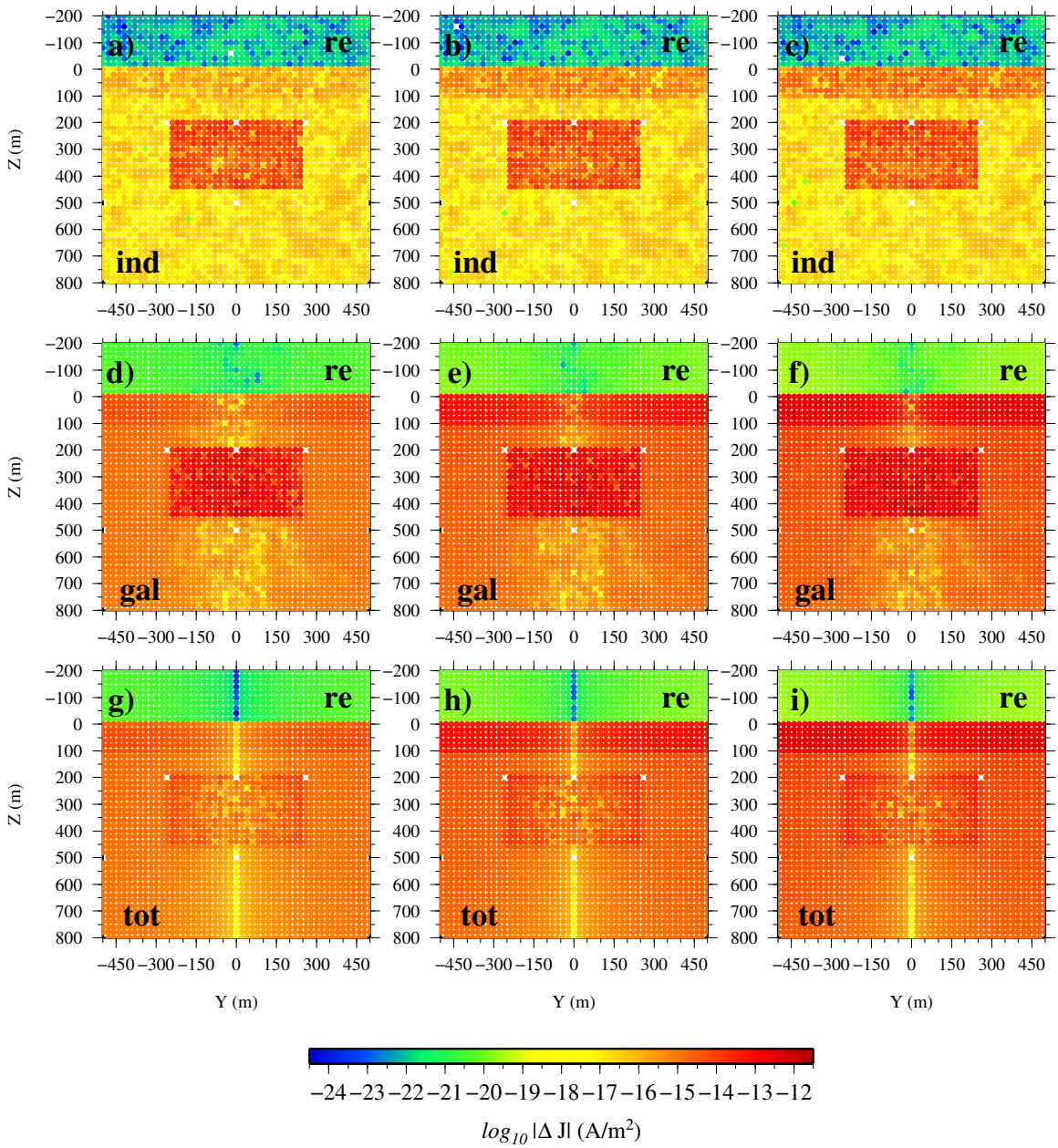

Figure 5.28: Discontinuities of the normal components of the current densities for the inductive part, galvanic part and total current for a host conductivity of 0.003 S/m and for a range of conductivities of the overburden layer. Panels (a), (b), and (c) are the inductive parts for overburden conductivities of 0.01, 0.045, and 0.1 S/m respectively. Panels (d), (e) and (f) are the corresponding galvanic parts; panels (f), (g) and (h) are also the corresponding currents.

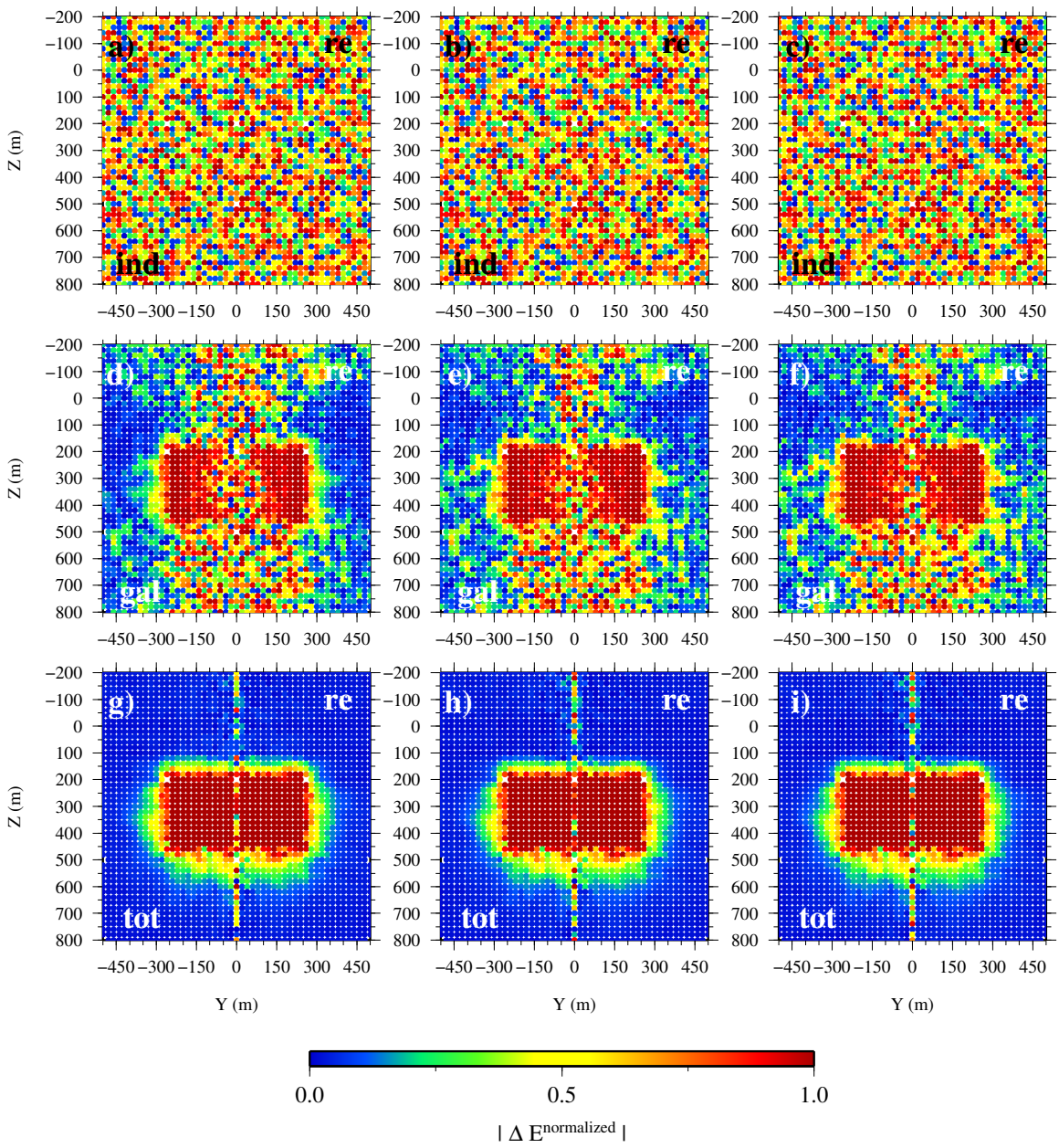

Figure 5.29: Normalized discontinuities in the normal components of the fields for the real components of the inductive part, galvanic part and total electric field for a host conductivity of 0.003 S/m and for a range of conductivities of the overburden layer. Panels (a), (b), and (c) are the inductive parts for overburden conductivities of 0.01, 0.045, and 0.1 S/m respectively. Panels (d), (e) and (f) are the corresponding galvanic parts. Panels (f), (g) and (h) are the corresponding total fields.

to the fields, both the inductive and galvanic components contribute to continuity of the total current density on the surface of the plate.

5.4 Marine disk model revisited

The inductive and galvanic components were calculated for the marine example presented in Chapter 4. In order to observe the behavior of the fields for the explicitly gauged solution, the system in equation 5.4 is solved for this model. The mesh used for this example consists of 299532 tetrahedral elements, 48972 nodes, and 348797 edges. This choice of a smaller mesh compared to the mesh used in Chapter 4 is for the sake of solving the system using the direct MUMPS solver. The dimension of the problem is 20 km $\times$ 20 km $\times$ 20 km in the x-, y- and z-directions. Here, for the iterative solution, the ILUT preconditioner with $lfil = 3$ and the GMRES solver with a Krylov subspace of 300 are used. The discretized system is also solved using the direct solver MUMPS. Figure 5.31 shows a comparison for the magnitude of the electric field, E_x, obtained using the different solution approaches. It is seen here that the fields that correspond to iteratively solving the un-gauged system and to directly solving the gauged and un-gauged systems coincide with the finite-volume solution of Weiss (2013). However, the iterative solution of the gauged system does not match the other solutions. This mismatch is a result of the slow convergence of the iterative solver due to the non-symmetric gauged system. It is evident from Figure 5.32 that the decrease in the preconditioned residual norm of the iterative solution for the gauged system is very slow compared to that seen for the un-gauged system.

The iterative solution for the gauged system is tried with increasing dimensions of the Krylov subspace and increasing numbers of iterations. Table 5.1 lists information regarding the parameters for the iterative solver and the relevant computation costs for

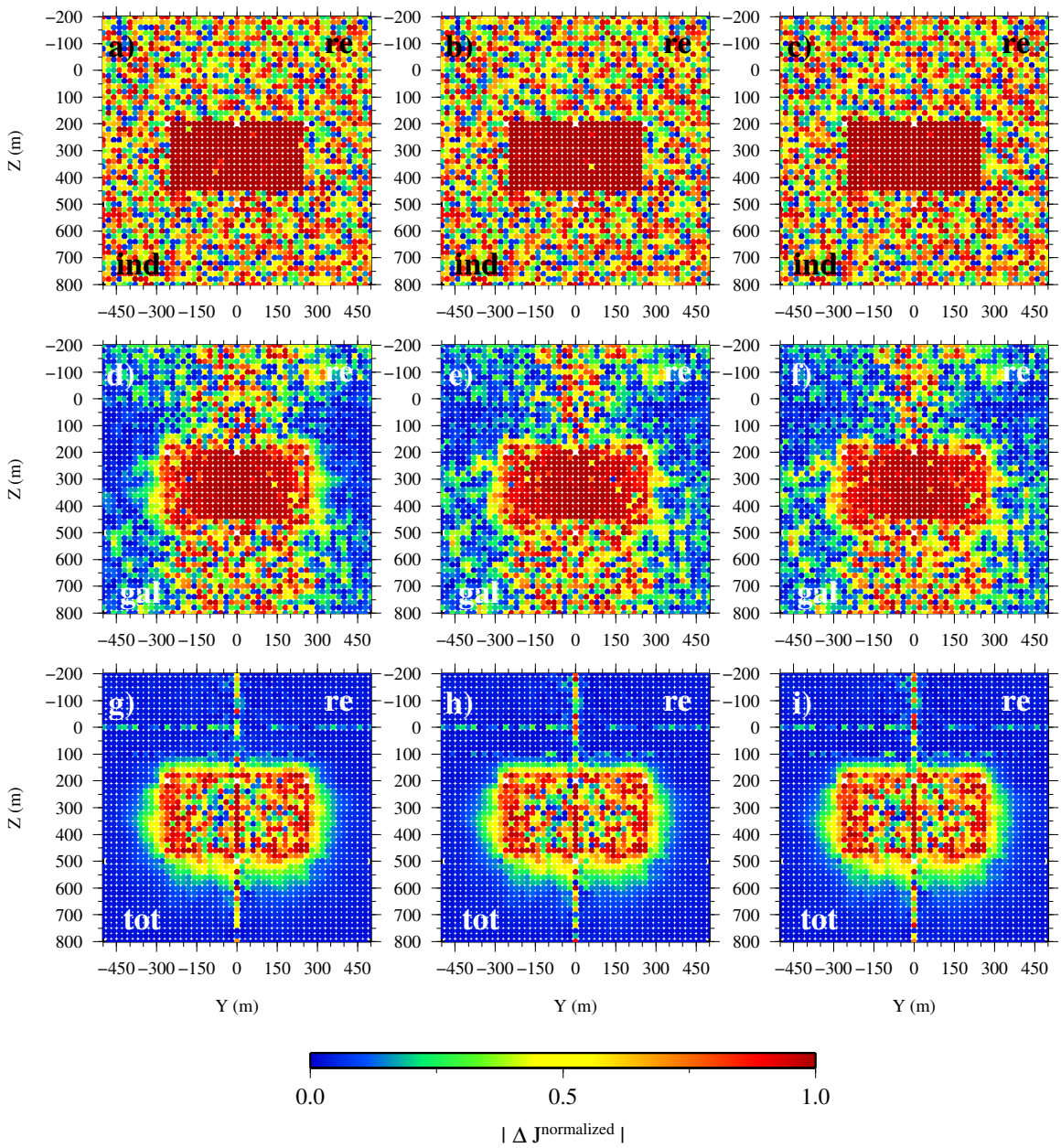

Figure 5.30: Normalized discontinuities in the normal components of the current densities for the inductive part, galvanic part and total current for a host conductivity of 0.003 S/m and for a range of conductivities of the overburden layer. Panels (a), (b), and (c) are the inductive parts for overburden conductivities of 0.01, 0.045, and 0.1 S/m respectively. Panels (d), (e) and (f) are the corresponding galvanic parts; panels (f), (g) and (h) are also the corresponding currents.

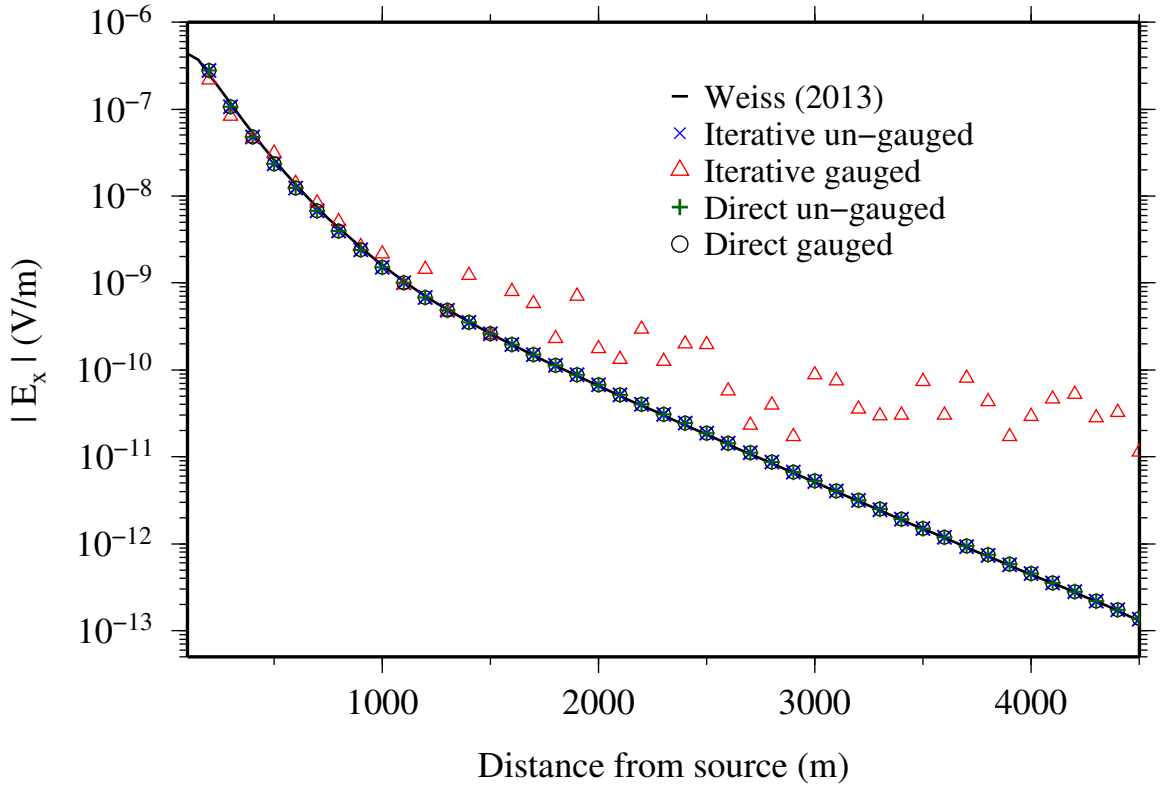

Figure 5.31: A comparison of the x-component of the amplitude of the electric field for the marine example for a frequency of 1 Hz. Data obtained using the iterative solutions to the original un-gauged system (shown with crosses) and to the gauged system (shown with triangles), and the direct solutions to the original un-gauged system (shown with pluses) and to the gauged system (shown with circles). The finite-volume solution of Weiss (2013) is also shown using the solid line.

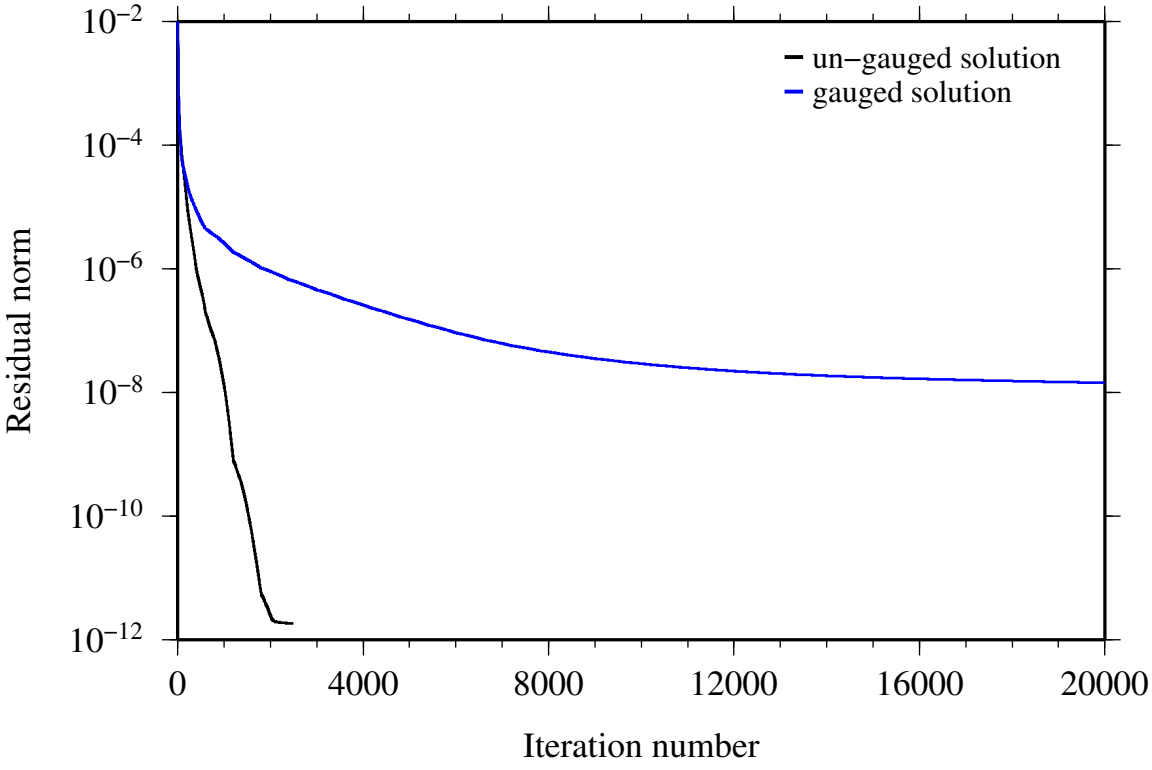

Figure 5.32: The convergence curves for the original $\mathbf{A} - \phi$ decomposed solution (black) and the decomposed gauged solution (blue) for a frequency of 1 Hz for the marine example.

Table 5.1: The iterative solver parameters for three runs of the gauged system (equation 5.4) for the marine example.

Solution parameters and computation costs				
Run no.	Krylov	Iterations	Memory (Gbytes)	Computation time (sec)
1	600	50000	5.2	20025
2	1500	50000	10.6	41236
3	2500	100000	16.5	136280

a range of possibilities. The behavior of the iterative solver and the corresponding final field values are shown in Figures 5.33 and 5.34 respectively. It is seen in Figure 5.33 that even for a high Krylov subspace dimension of 2500 the convergence of the iterative solver is very slow. The corresponding electric field solutions are also inadequate (see Figure 5.34) for all the final residual norms obtained here.

5.4.1 Fields in the horizontal plane

Investigations of the inductive and galvanic components for the different solution methods presented above are performed here and in the next section. A horizontal plane that slices through the center of the resistive disk is considered. The source is a 100 m electric dipole located in the conductive sea water at a height of 100 m above the sea floor (see Section 4.2.3). As seen in Chapter 4 (see Figures 4.29 and 4.30), for the original un-ungauged system, Figure 5.35 shows the components of the fields in the plane and Figure 5.36 shows the current densities. Figures 5.37 and 5.38 show the corresponding arrows for the gauged system. The system here is solved using the direct solver. For the sake of memory efficiency due to the direct solver a new mesh compared to the mesh used for Figures 4.29 and 4.30 is used. The mesh consists of 305995 cells, 49922 nodes, and 356250 edges. MUMPS used a memory of 18.4 Gbytes to solve the gauged system with a computation time of 765 seconds. From panels (e) and (f) in Figures 5.35 and 5.37 it can be seen that total electric field is the same for both these

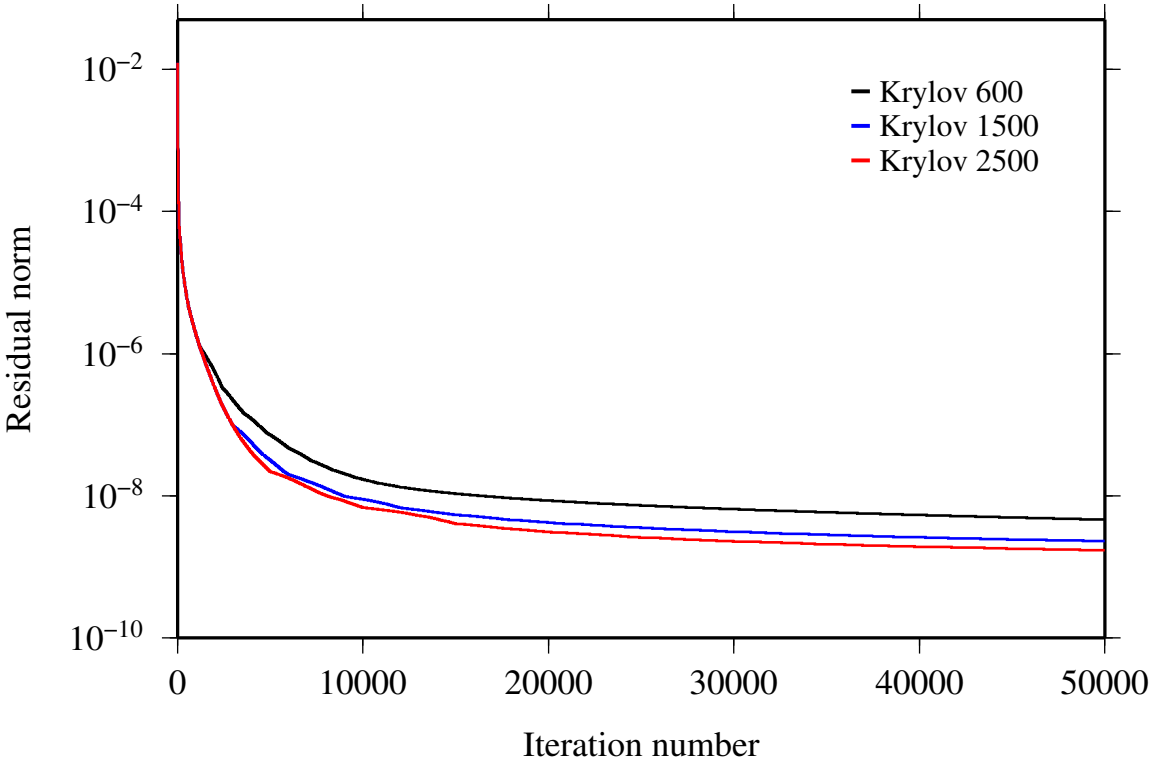

Figure 5.33: The preconditioned residual norm for runs with different dimensions for the Krylov subspace for the gauged marine example: 600 in black, 1500 in blue, and 2500 in red.

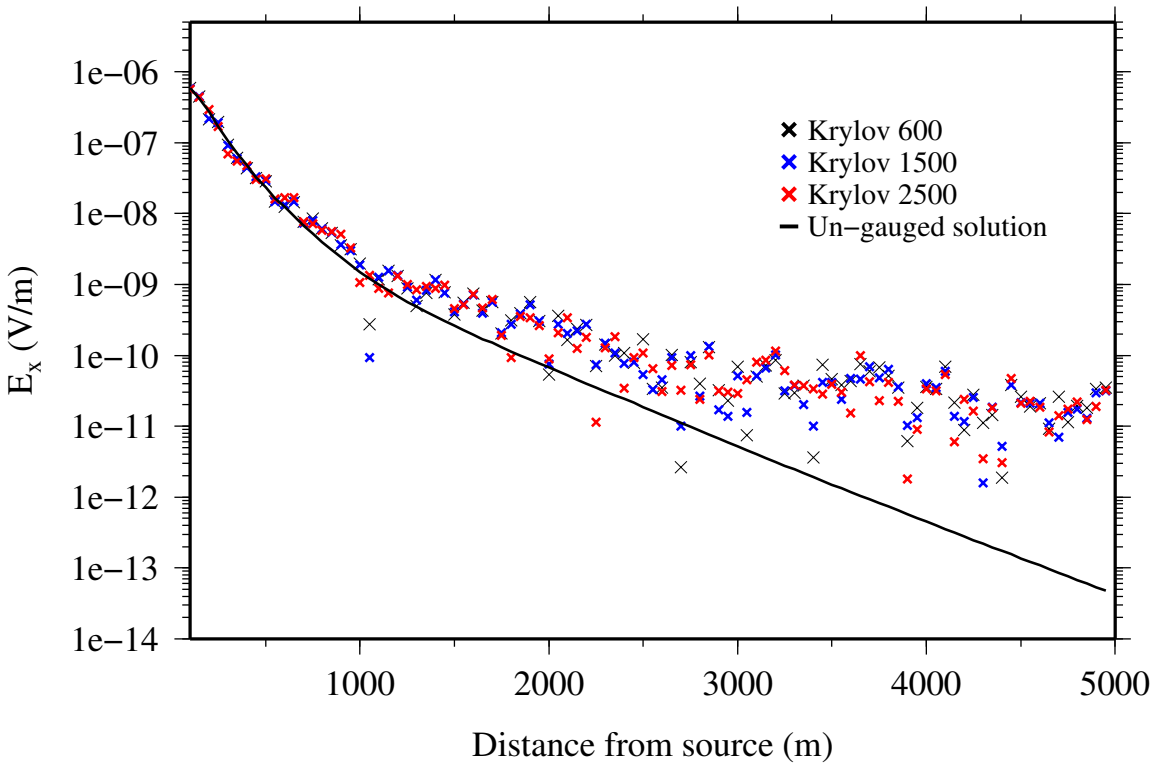

Figure 5.34: The electric field data for runs with different dimensions of the Krylov subspace and 50000 iterations in the GMRES solver for the gauged marine example: 600 in black, 1500 in blue, and 2500 in red. The solid line in black is the solution due to the original un-gauged system.

solutions. The components of the electric field coming from the individual vector ($\mathbf{A}$) and scalar (ϕ) potentials are however non-unique numerically as the inductive and galvanic pairs are different for the gauged and un-gauged scenarios. The solution to the gauged system produced zero vectors for the imaginary component of the galvanic part (see panel d in Figure 5.37), therefore, the corresponding imaginary part of the total electric field is solely given by the contribution from the inductive part.

The un-gauged original system is also solved using the direct solver (see Figures 5.39 and 5.40). Here MUMPS required 22 Gbytes of memory to solve the system of equations. The computation time was 1140 seconds. Here in Figure 5.39 the numerical non-uniqueness of the inductive and galvanic parts is further demonstrated as the contribution from the inductive and galvanic components differ from those obtained for the iterative solution of the un-gauged system and the direct solution of the gauged system. The total field is however unique across all solution techniques.

5.4.2 Fields in the vertical plane

Inductive and galvanic components for the marine example are also studied for a plane that cuts vertically through the circular disk. A plane of nodes is again inserted into the mesh, this time at $y = 0$. The computational domain is subdivided into 306199 cells, 49839 nodes, and 356360 edges. For the solution to the original un-gauged system, Figures 5.41 and 5.42 show the inductive, galvanic and total components of the electric field and current density respectively. For the next experiment, the gauged system is solved directly using MUMPS. Figures 5.43 and 5.44 show the corresponding field and current densities respectively. In the third experiment, a direct solution to the original un-gauged system is performed. For this solution the corresponding fields and current densities are shown in Figures 5.45 and 5.46. A comparison of the

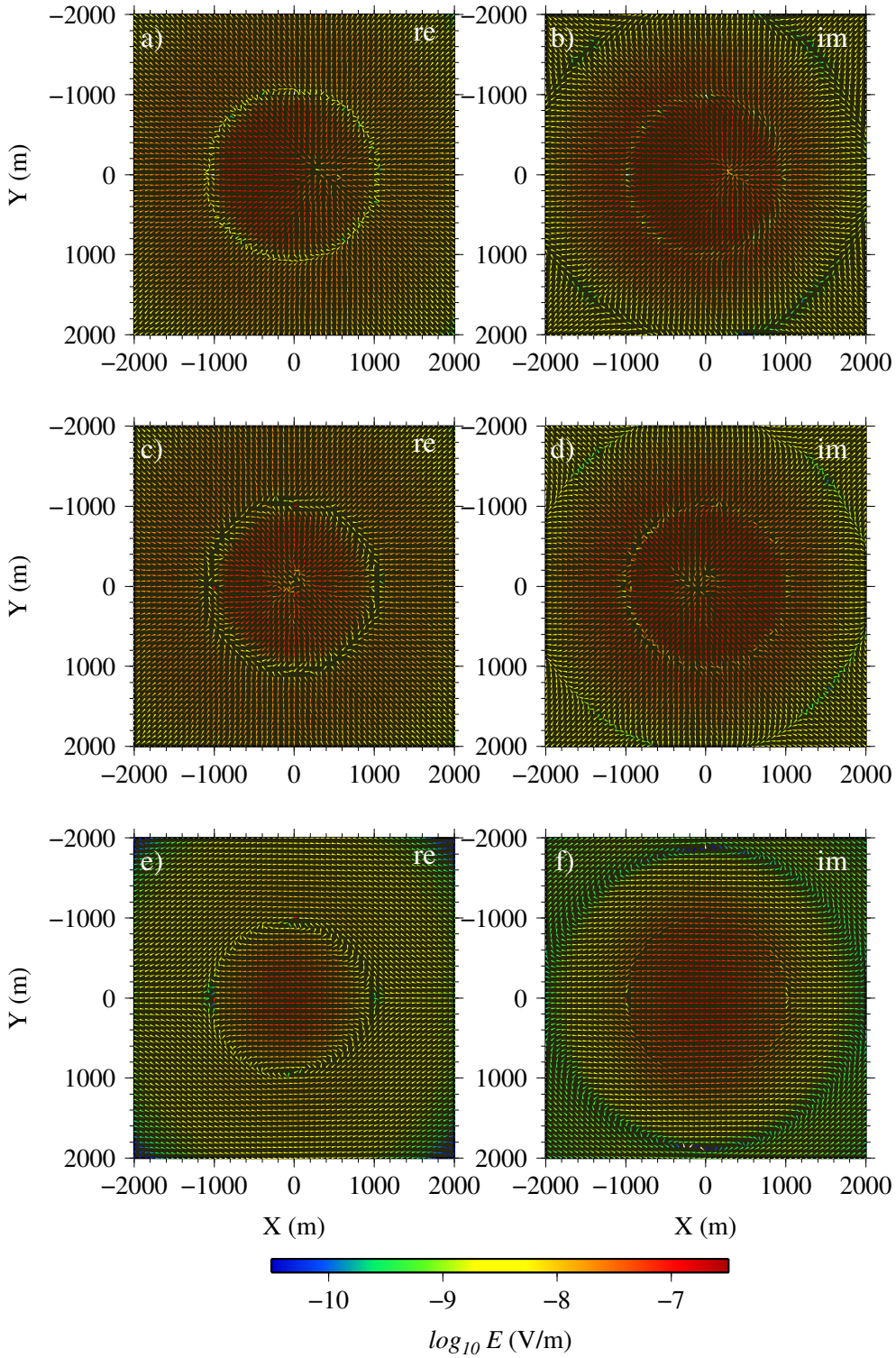

Figure 5.35: The inductive part, galvanic part and total electric field for the solution to the un-gauged system, for the canonical disk model for a frequency of 1 Hz. All six panels show the horizontal component of the fields at a depth of 1000 m below the water-seabed interface, i.e., in the center of the disk: the real (a) and imaginary (b) components of the inductive part; the real (c) and imaginary (d) components of the galvanic part; and the real (e) and imaginary (f) components of the total electric field.

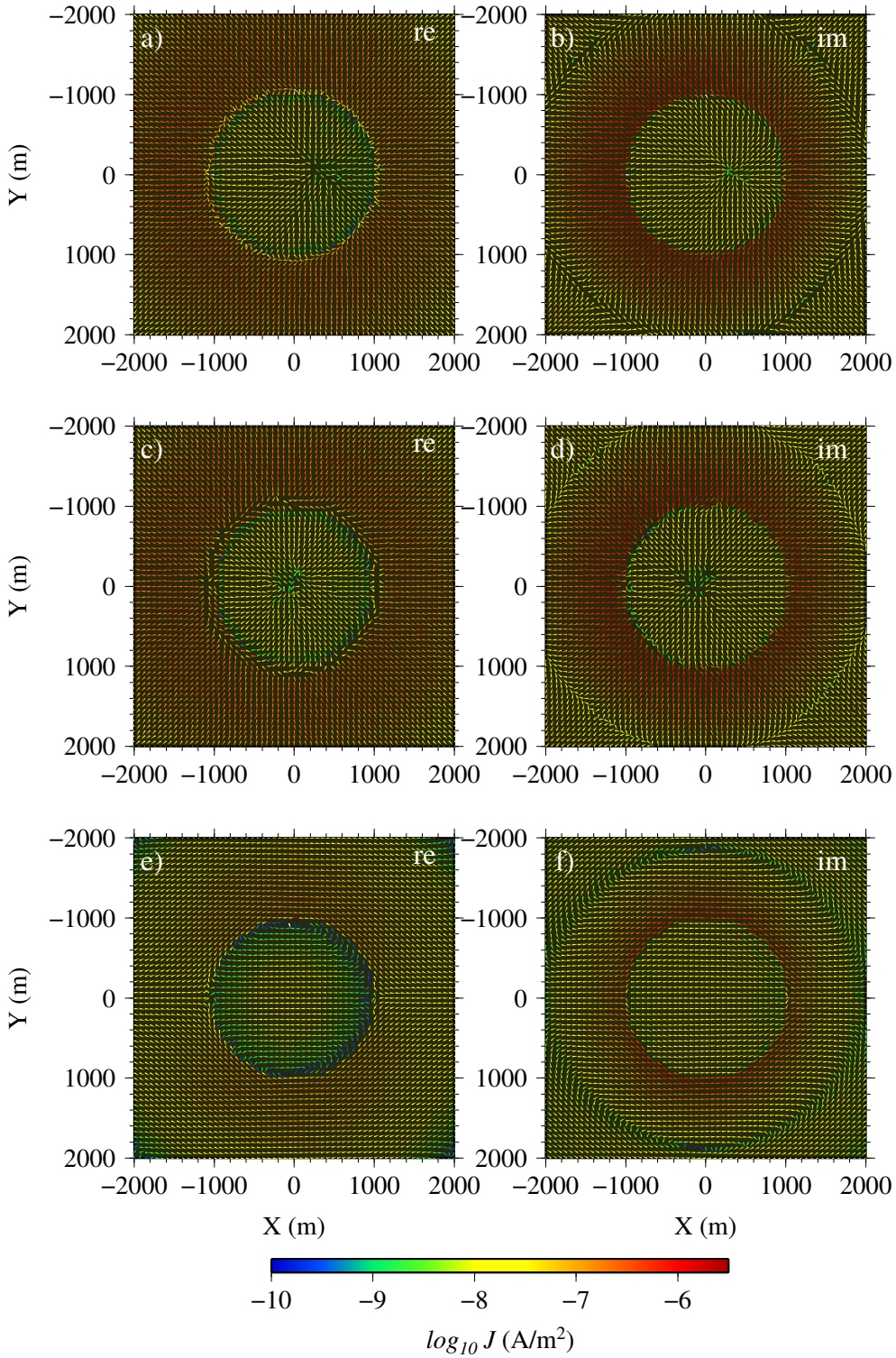

Figure 5.36: The inductive part, galvanic part and total current density for the solution to the un-gauged system, for the canonical disk model for a frequency of 1 Hz. All six panels show the horizontal component of the currents at a depth of 1000 m below the water-seabed interface, i.e., in the center of the disk: the real (a) and imaginary (b) components of the inductive part; the real (c) and imaginary (d) components of the galvanic part; and the real (e) and imaginary (f) components of the total current density.

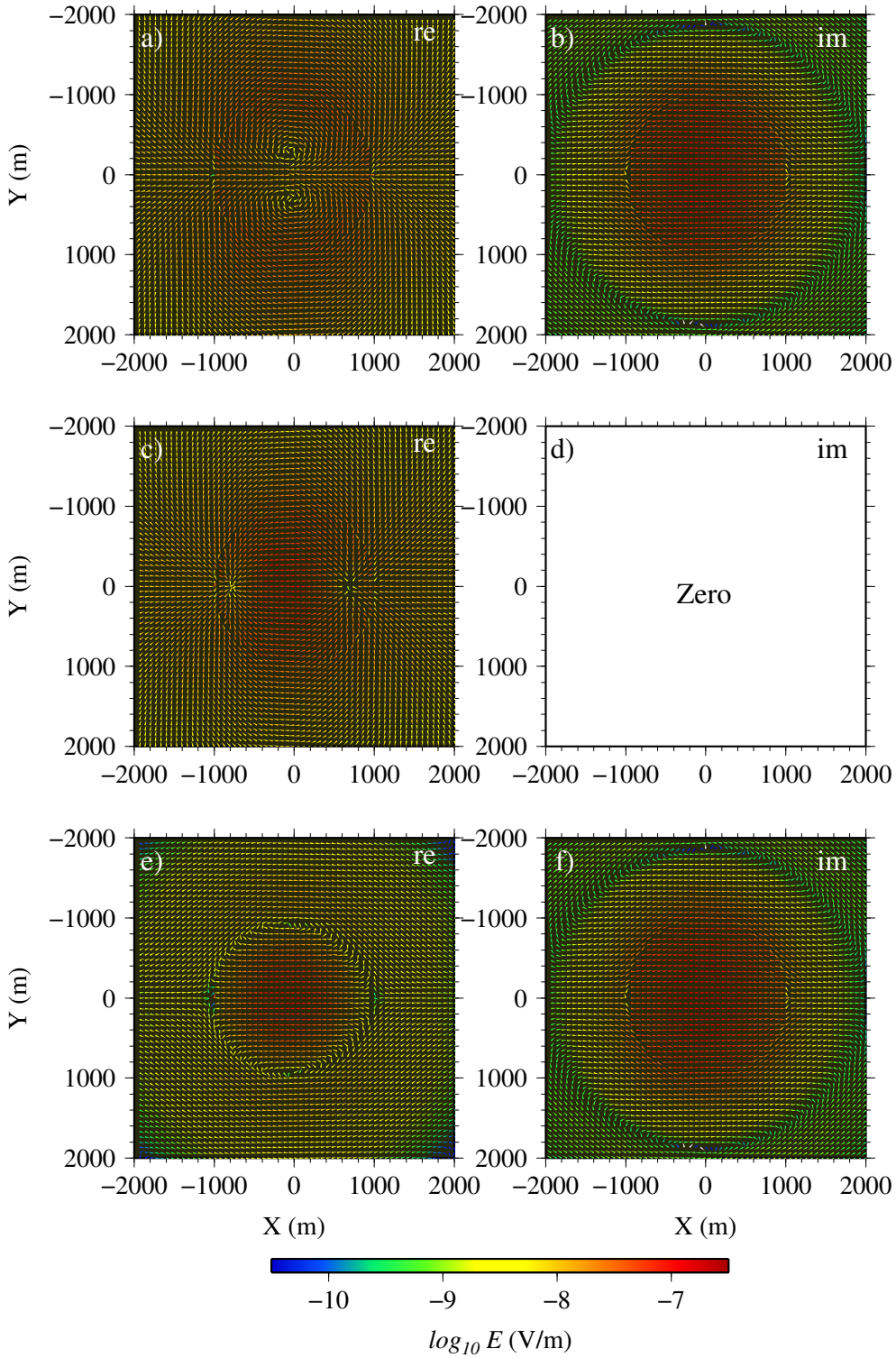

Figure 5.37: The inductive part, galvanic part and total electric field for the solution to the gauged system, for the canonical disk model for a frequency of 1 Hz. All six panels show the horizontal component of the fields at a depth of 1000 m below the water-seabed interface, i.e., in the center of the disk.

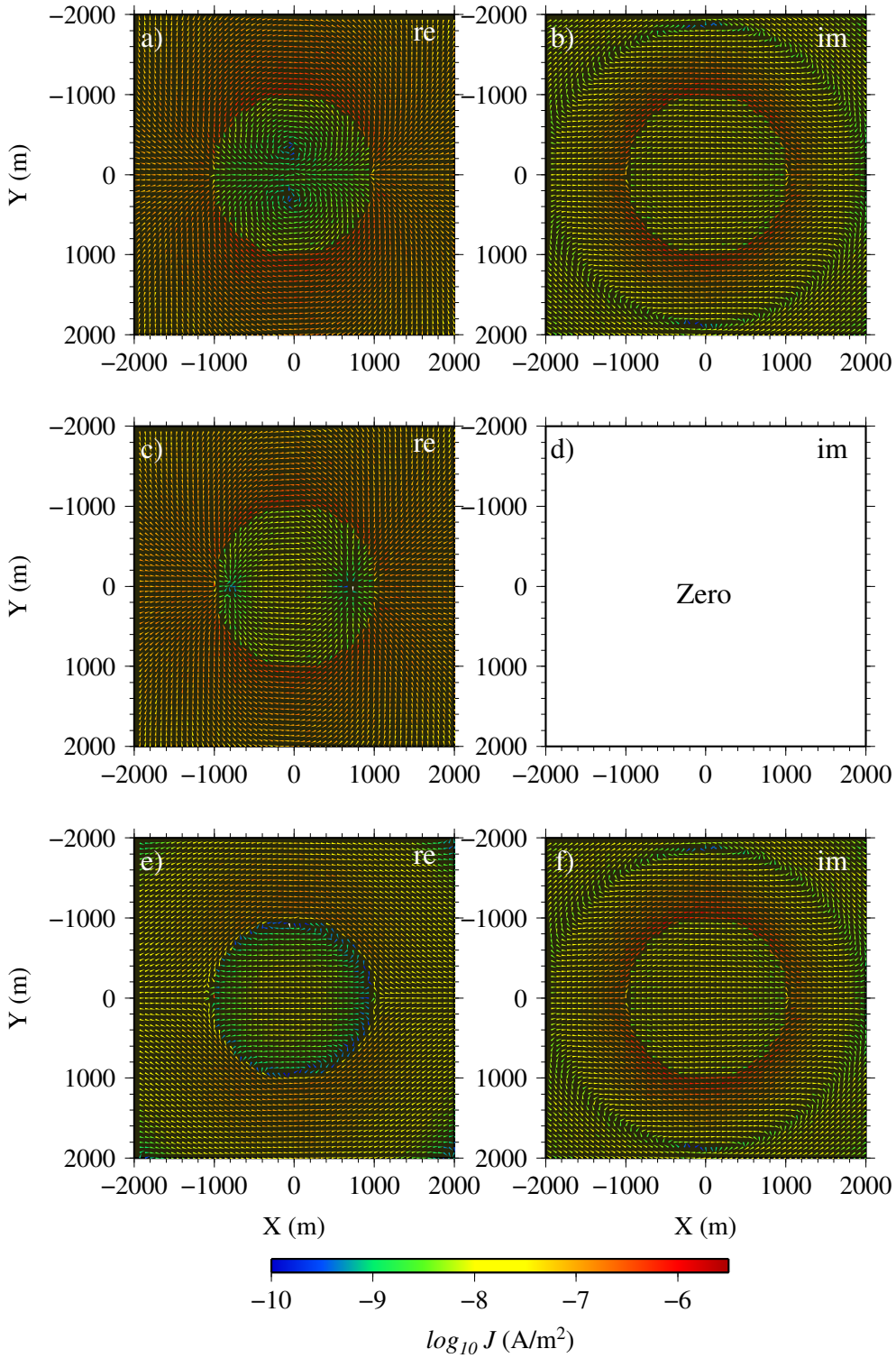

Figure 5.38: The inductive part, galvanic part and total current density for the solution to the gauged system, for the canonical disk model for a frequency of 1 Hz. All six panels show the horizontal component of the currents at a depth of 1000 m below the water-seabed interface, i.e., in the center of the disk.

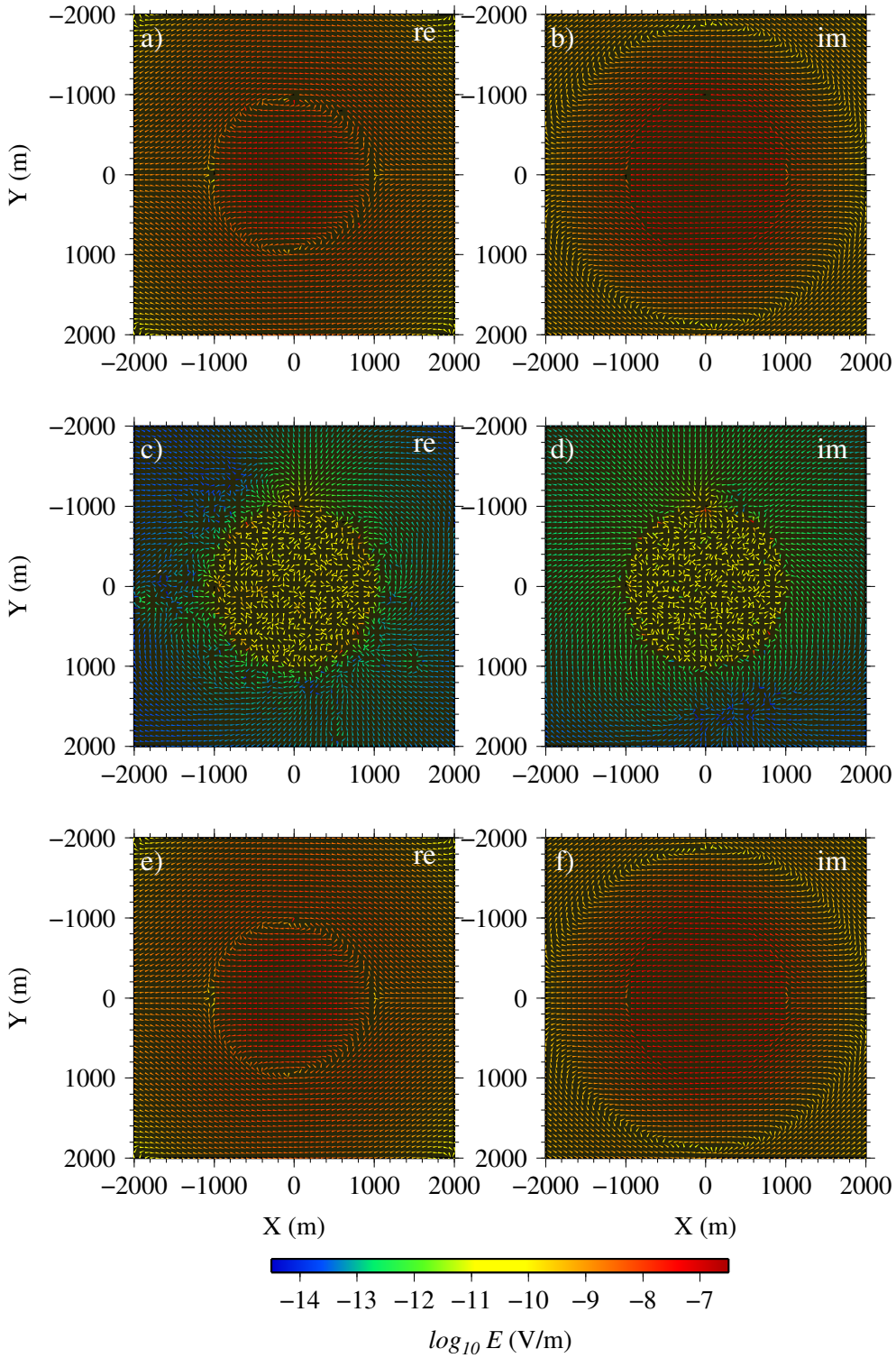

Figure 5.39: The inductive part, galvanic part and total electric field for the direct solution to the original un-gauged system, for the canonical disk model for a frequency of 1 Hz. All six panels show the horizontal component of the fields at a depth of 1000 m below the water-seabed interface, i.e., in the center of the disk.

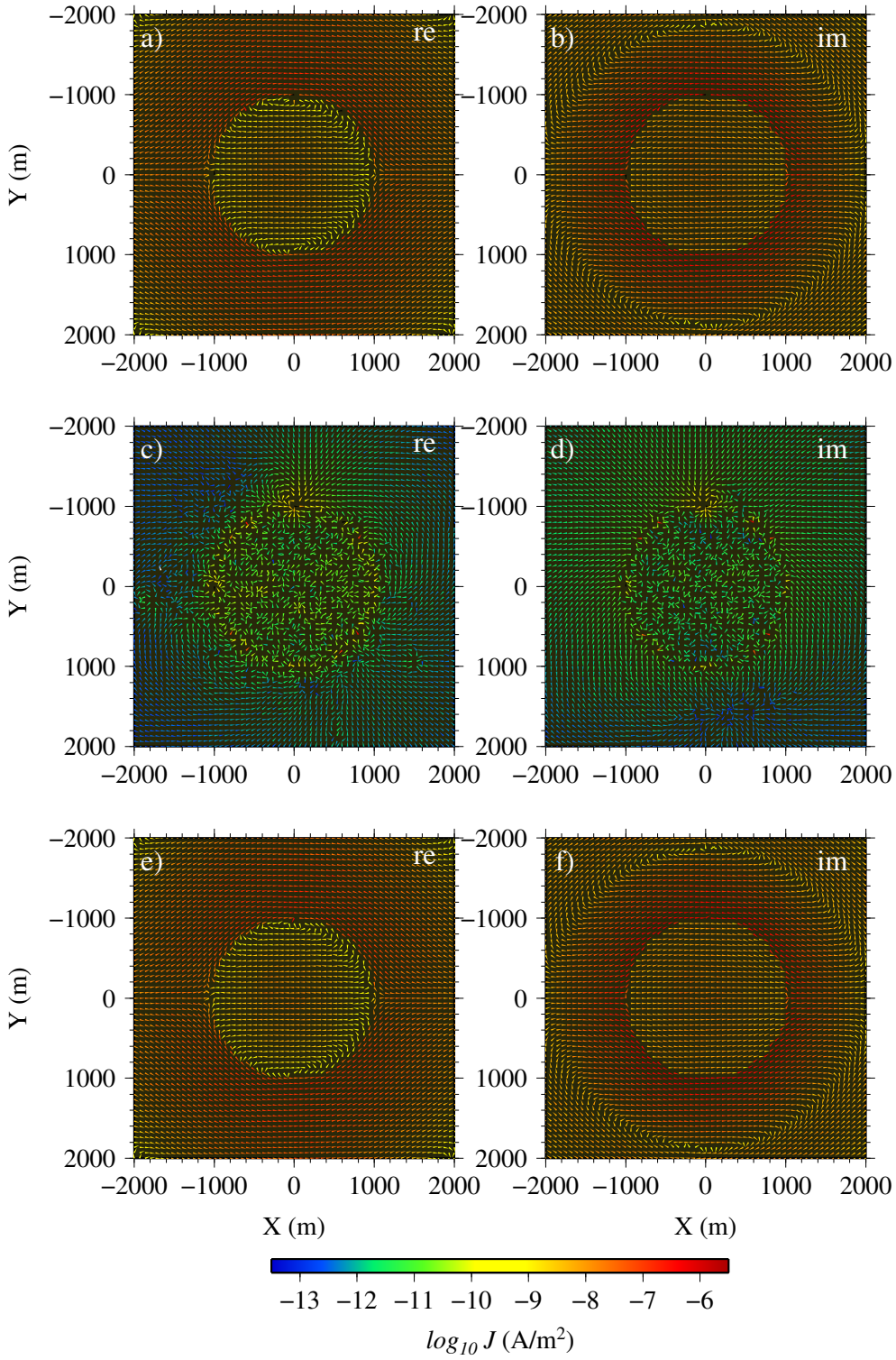

Figure 5.40: The inductive part, galvanic part and total current density for the direct solution to the original un-gauged system, for the canonical disk model for a frequency of 1 Hz. All six panels show the horizontal component of the currents at a depth of 1000 m below the water-seabed interface, i.e., in the center of the disk.

above figures again demonstrates the consistency and uniqueness of the total electric fields and current densities (see panels e and f in all figures) obtained from the three solution methods. The individual inductive and galvanic components are however non-unique for the different types of solutions and systems considered. For the first two experiments presented above the total field and current density are formed by a combination of the inductive and galvanic components. In particular, in terms of the directions of the arrows, the galvanic field in Figure 5.41 provides a hint of the disk for the final un-gauged solution. The strength and direction of the total field is however formed by an interplay between the inductive and galvanic components. The contributions of the potentials to the gauged solutions are shown in Figures 5.43 and 5.44. Here the imaginary part of the total field and currents is provided by only the inductive component. For the real part, however, a combination of fields and currents forms the total field in the plane. It is noteworthy to mention that the total electric field and current density for the direct solution of the original ungauged system are dominated by the so-called inductive part (see Figures 5.45 and 5.46).

5.4.3 Continuity of the fields and currents

For the different types of solutions presented above, the continuity of the normal components of the fields and currents across the inter-element boundaries is investigated for this marine example. A horizontal plane of nodes is firstly considered in the $z = 950$ m plane. Here, the inserted nodes on this plane are shared between the disk and the host. For the iterative solution to the original un-gauged system (e.g., with field arrows shown in Figure 5.35) Figure 5.47 shows the discontinuity in the normal components of the combinations to the electric field from the individual potentials and the total field. Similar to the plate example in Section 5.2.3, the scalar potential again dominates the vector potential in contributing to the total field discontinuity of

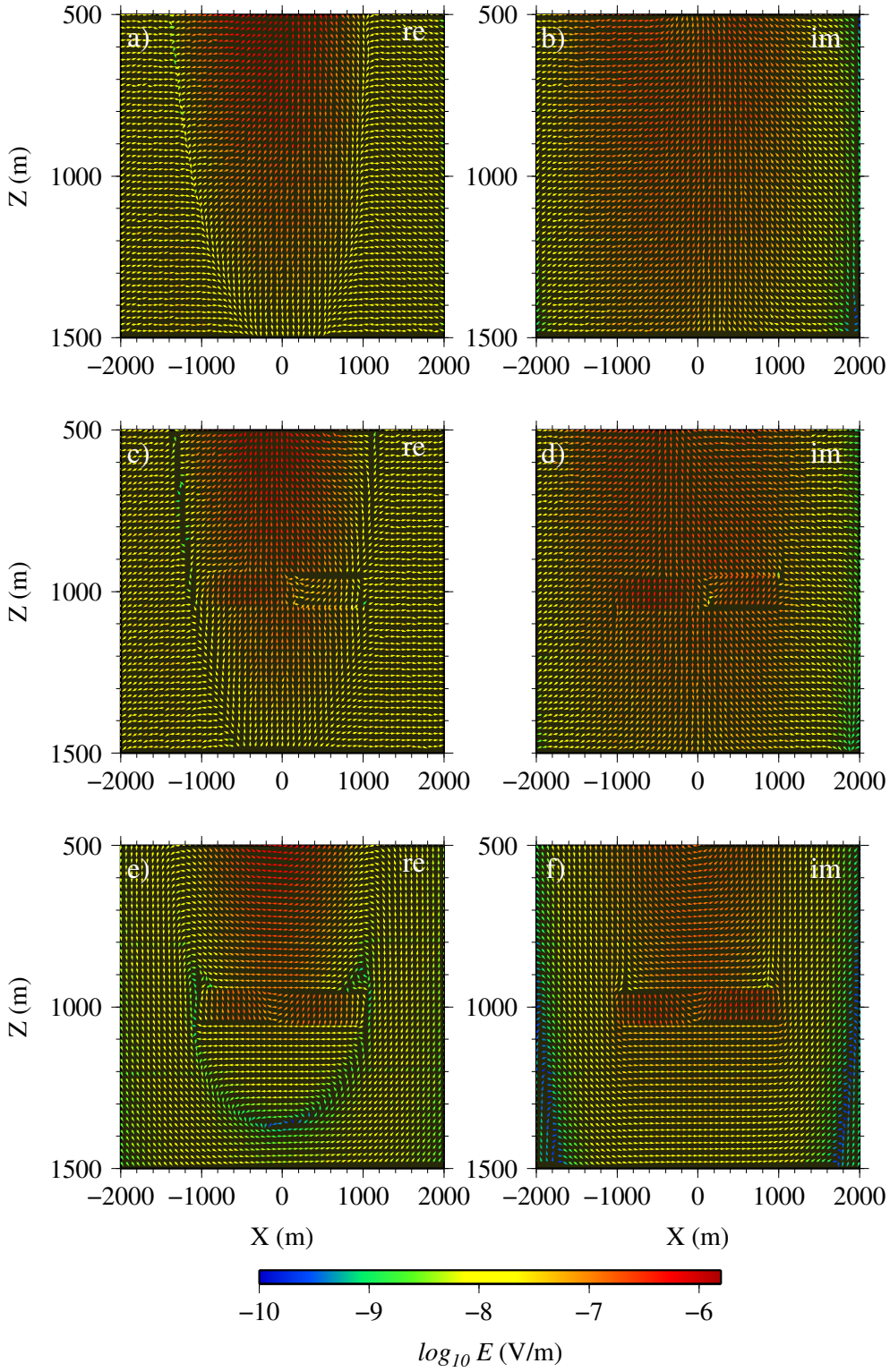

Figure 5.41: The inductive part, galvanic part and total electric field for the iterative solution to the original un-gauged system for the canonical disk model and for a frequency of 1 Hz. All six panels show the xz-component of the fields on a vertical plane passing through the center of the disk: the real (a) and imaginary (b) components of the inductive part; the real (c) and imaginary (d) components of the galvanic part; and the real (e) and imaginary (f) components of the total electric field.

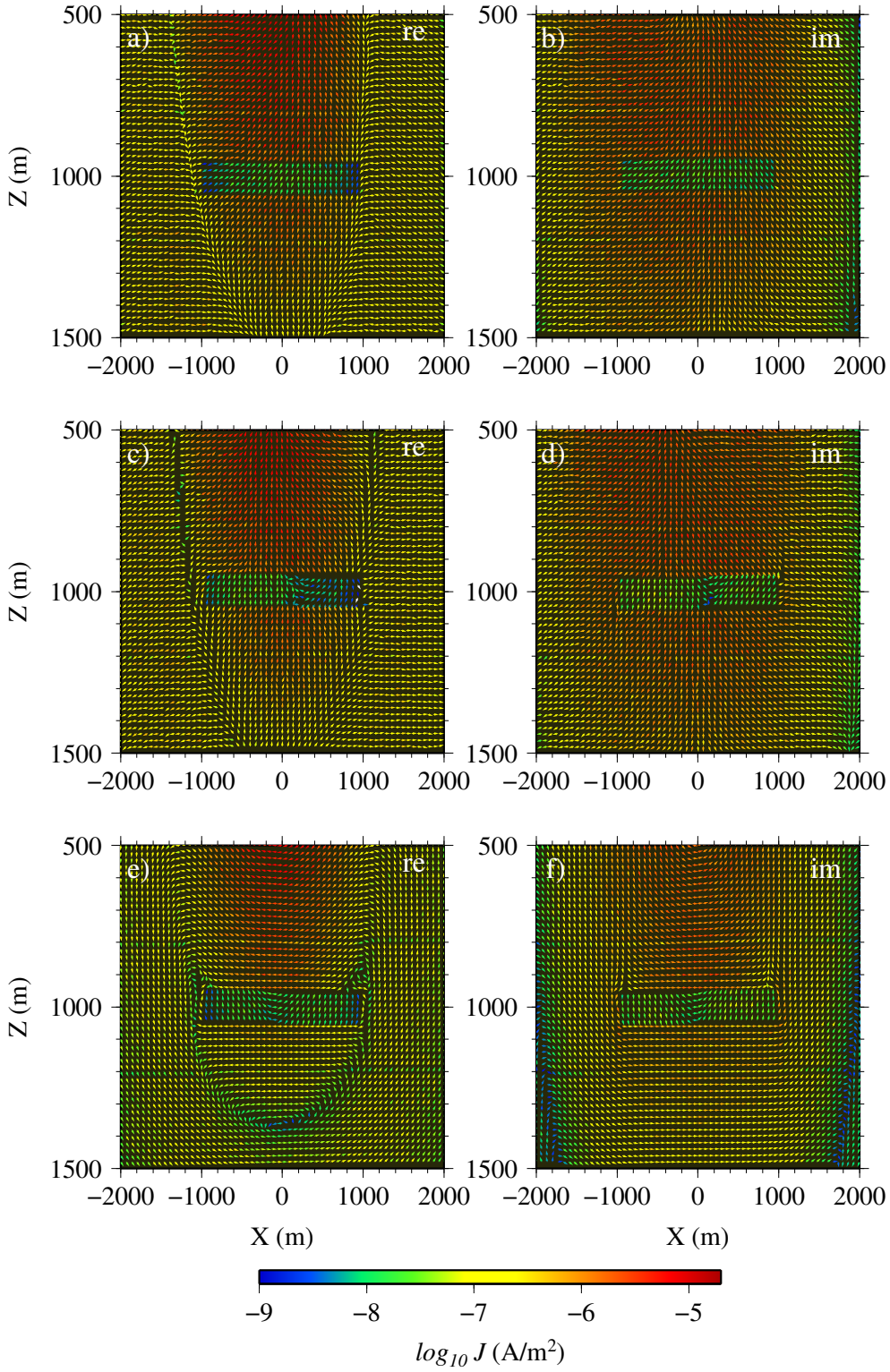

Figure 5.42: The inductive part, galvanic part and total current density for the iterative solution to the original un-gauged system for the canonical disk model and for a frequency of 1 Hz. All six panels show the xz-component of the currents on a vertical plane passing through the center of the disk: the real (a) and imaginary (b) components of the inductive part; the real (c) and imaginary (d) components of the galvanic part; and the real (e) and imaginary (f) components of the total current density.

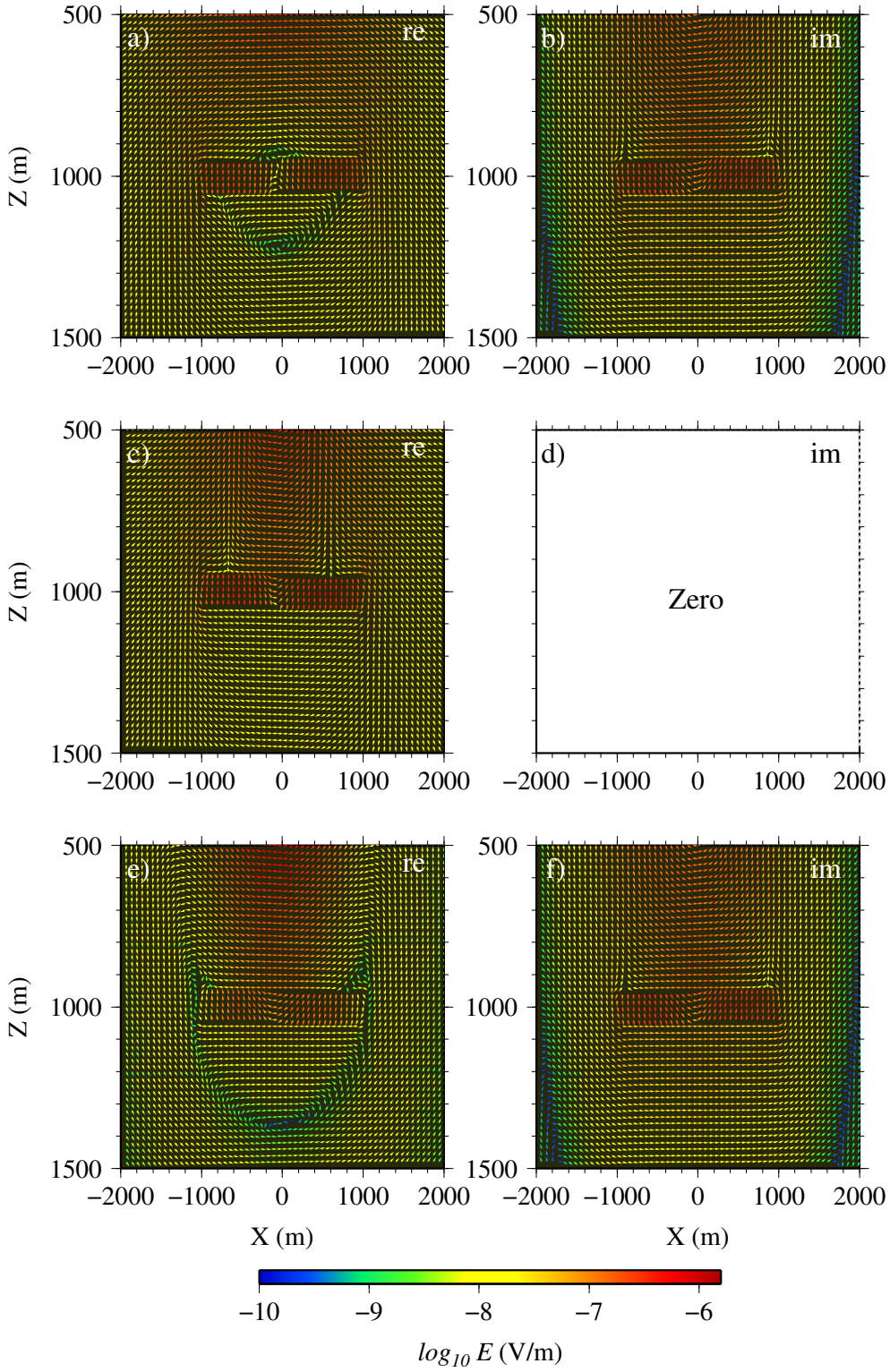

Figure 5.43: The inductive part, galvanic part and total electric field for the direct solution to the gauged system for the canonical disk model and for a frequency of 1 Hz. All six panels show the xz-component of the fields on a vertical plane passing through the center of the disk.

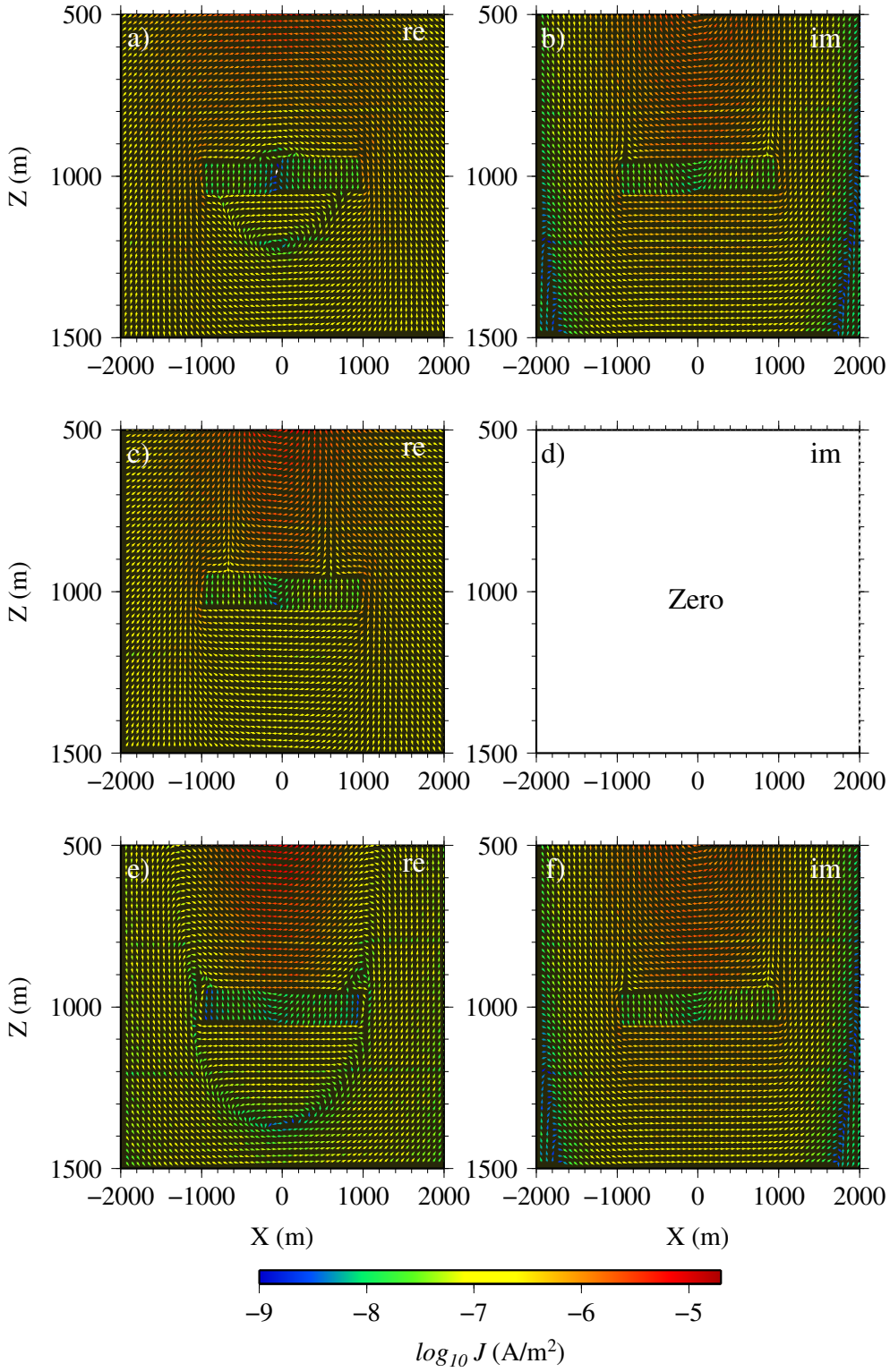

Figure 5.44: The inductive part, galvanic part and total current density for the direct solution to the gauged system for the canonical disk model and for a frequency of 1 Hz. All six panels show the xz-component of the currents on a vertical plane passing through the center of the disk.

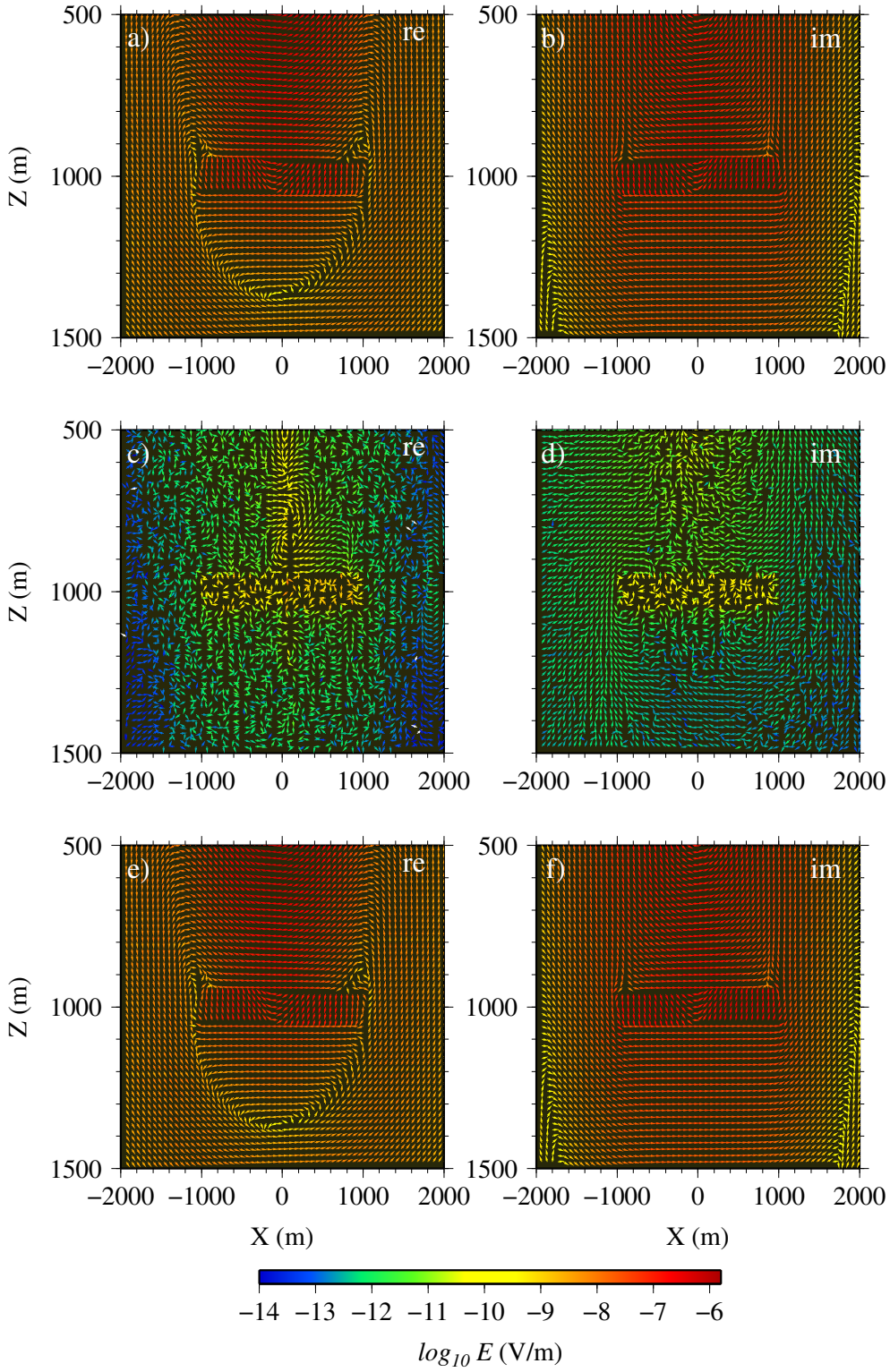

Figure 5.45: The inductive part, galvanic part and total electric field for the direct solution to the original un-gauged system for the canonical disk model and for a frequency of 1 Hz. All six panels show the xz-component of the fields on a vertical plane passing through the center of the disk (note that the color scale is different from that in Figures 5.41 and 5.43).

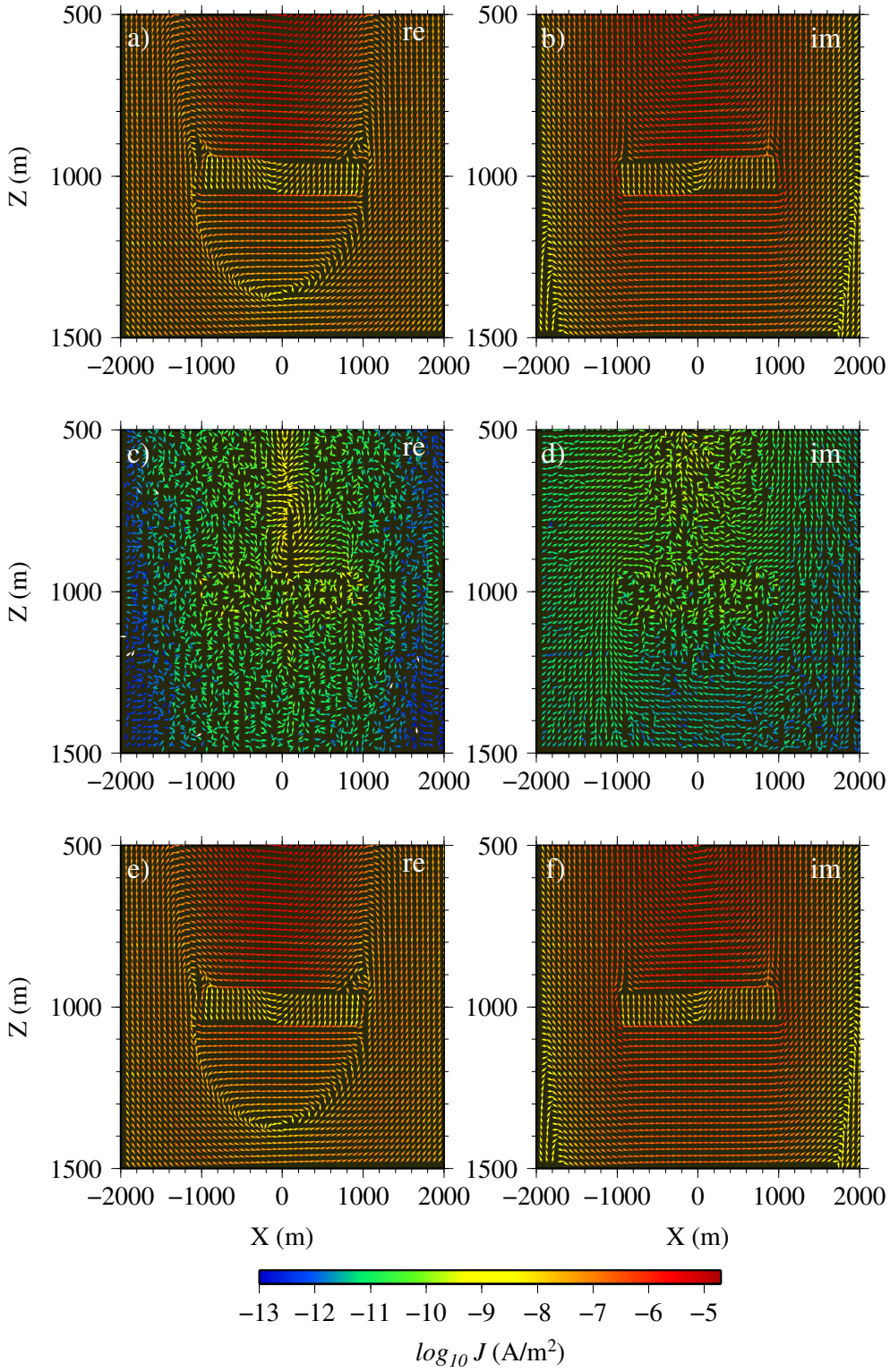

Figure 5.46: The inductive part, galvanic part and total current density for the direct solution to the original un-gauged system for the canonical disk model and for a frequency of 1 Hz. All six panels show the xz-component of the currents on a vertical plane passing through the center of the disk.

the normal component of the electric field on the surface of the disk. The normal components of the current densities are also shown in Figure 5.48. Here again, the normal component of the total current density (see panels e and f) is continuous across the conductivity contrast at the top surface of the disk while the normal components due to the individual inductive and galvanic parts are discontinuous across the interface.

The continuity of the fields from directly solving the gauged system is also investigated. Figure 5.49 shows the continuity of the normal component of the fields for the direct solution to the gauged system. For the type of solution presented here the discontinuity from the real part of $\nabla\phi$ is again dominant over the discontinuity in the corresponding $\mathbf{A}$ in forming a discontinuous real total field. The interface condition for the imaginary part of the electric field is however given by only the corresponding vector potential solution (e.g., scaled by ω and seen in panel f). For this solution the continuity of the normal components of the current densities are shown in Figure 5.50. In contrast to the iterative solution of the un-gauged system (see Figure 5.48) there is a significantly lower discontinuity in both inductive and galvanic currents produced by the gauged system. The continuity of the total current density is however unique if compared to the un-gauged solution.

The interface condition for the direct solution of the un-gauged system is also shown here. Figure 5.51 shows the normal discontinuity of the fields for the disk model. It is seen here that the discontinuity in $\nabla\phi$ (panels c and d) is negligible in comparison to those in $\mathbf{A}$ (panels a and b). Here the normal components produced for the total field are again unique if compared to the results from the previous solutions (e.g., in the same color scale). The results for the current densities due to this solution are also shown in Figure 5.52. Here the continuity in the total current density is provided by the absolutely dominant inductive components.

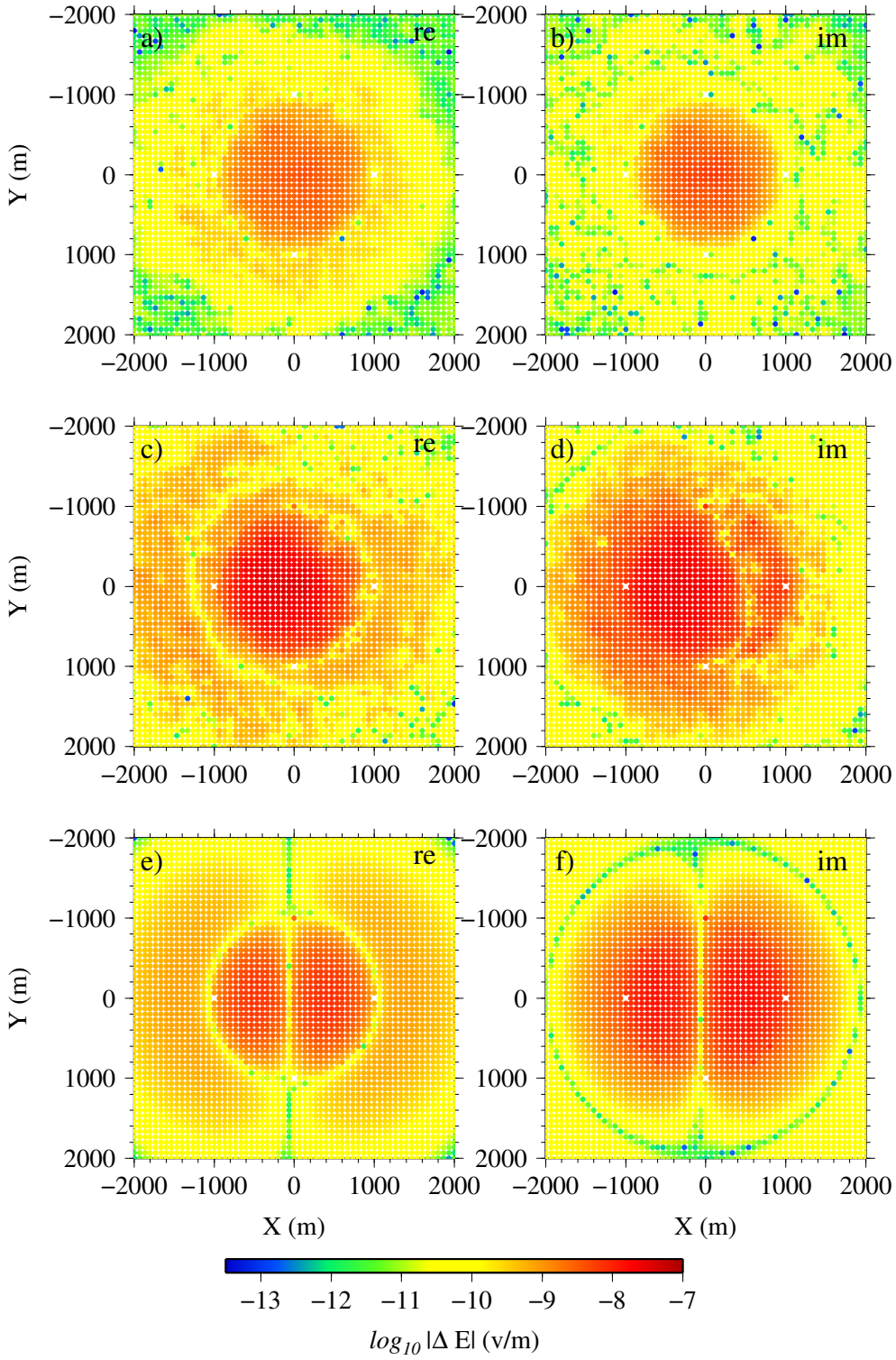

Figure 5.47: Discontinuity in the normal field components for the inductive part, galvanic part and total electric field for the iterative solution to the original un-gauged system for the canonical disk model and for a frequency of 1 Hz. The horizontal plane of nodes is located at $z = 950$ m immediately on the top of the circular disk: the real (a) and imaginary (b) components of the inductive part; the real (c) and imaginary (d) components of the galvanic part; and the real (e) and imaginary (f) components of the total electric field.

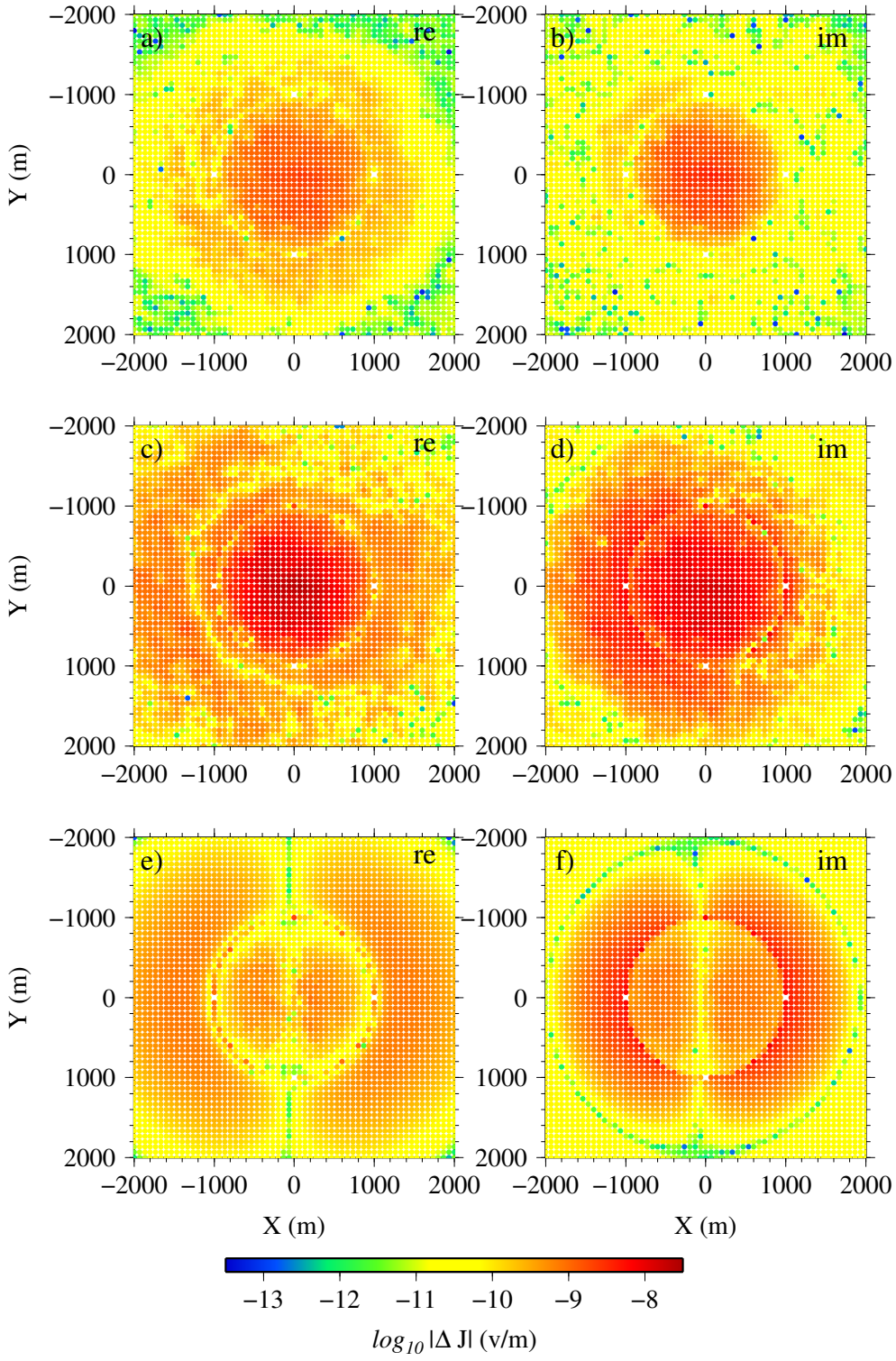

Figure 5.48: The discontinuity in the normal current density components for the inductive part, galvanic part and total current density for the iterative solution to the original un-gauged system for the canonical disk model and for a frequency of 1 Hz. The horizontal plane of nodes is located at $z = 950$ m immediately on the top of the circular disk: the real (a) and imaginary (b) components of the inductive part; the real (c) and imaginary (d) components of the galvanic part; and the real (e) and imaginary (f) components of the total current density.

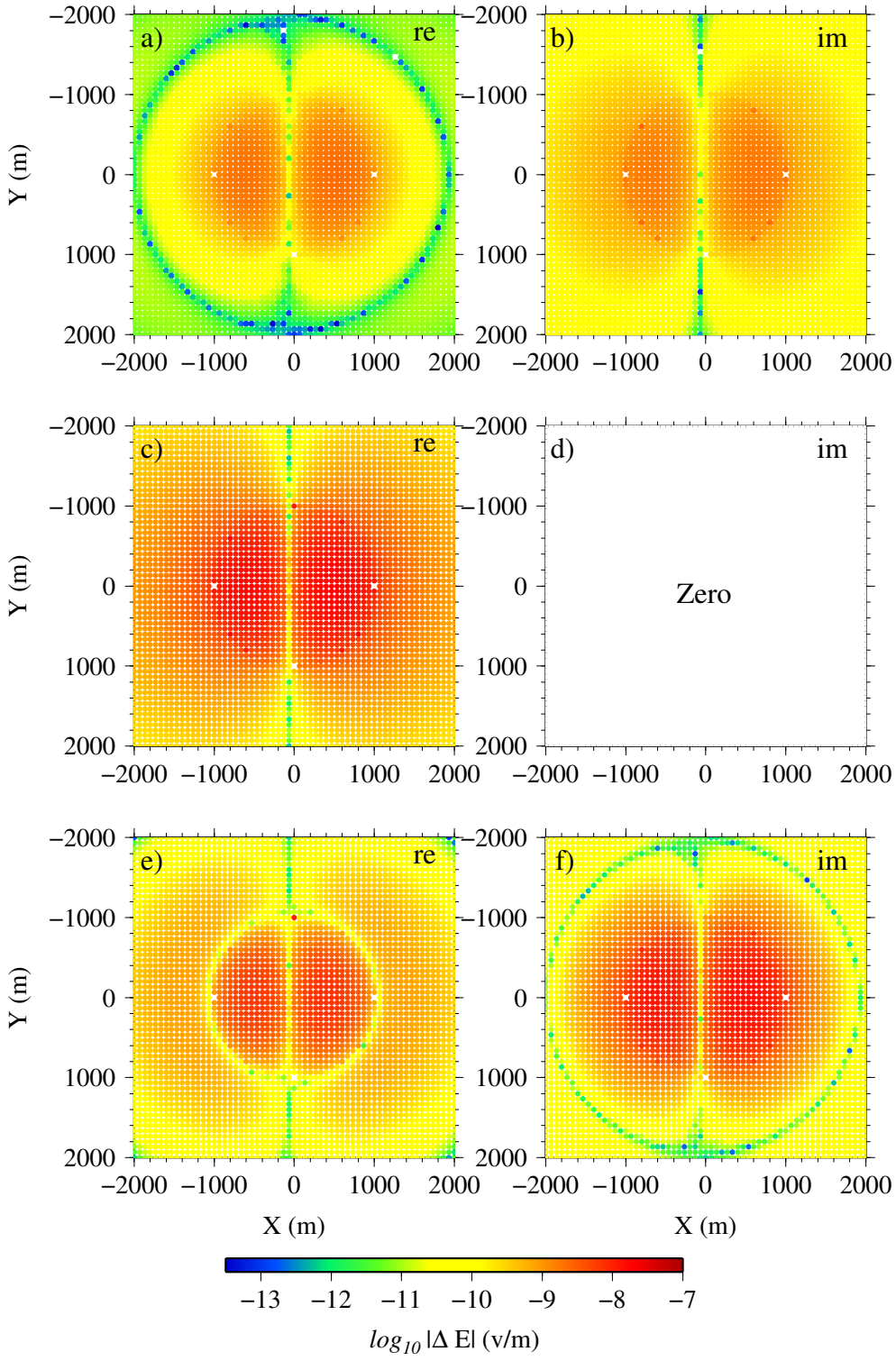

Figure 5.49: The discontinuity in the normal field components for the inductive part, galvanic part and total electric field for the direct solution to the gauged system for the canonical disk model and for a frequency of 1 Hz. The horizontal plane of nodes is located at $z = 950$ m immediately on the top of the circular disk.

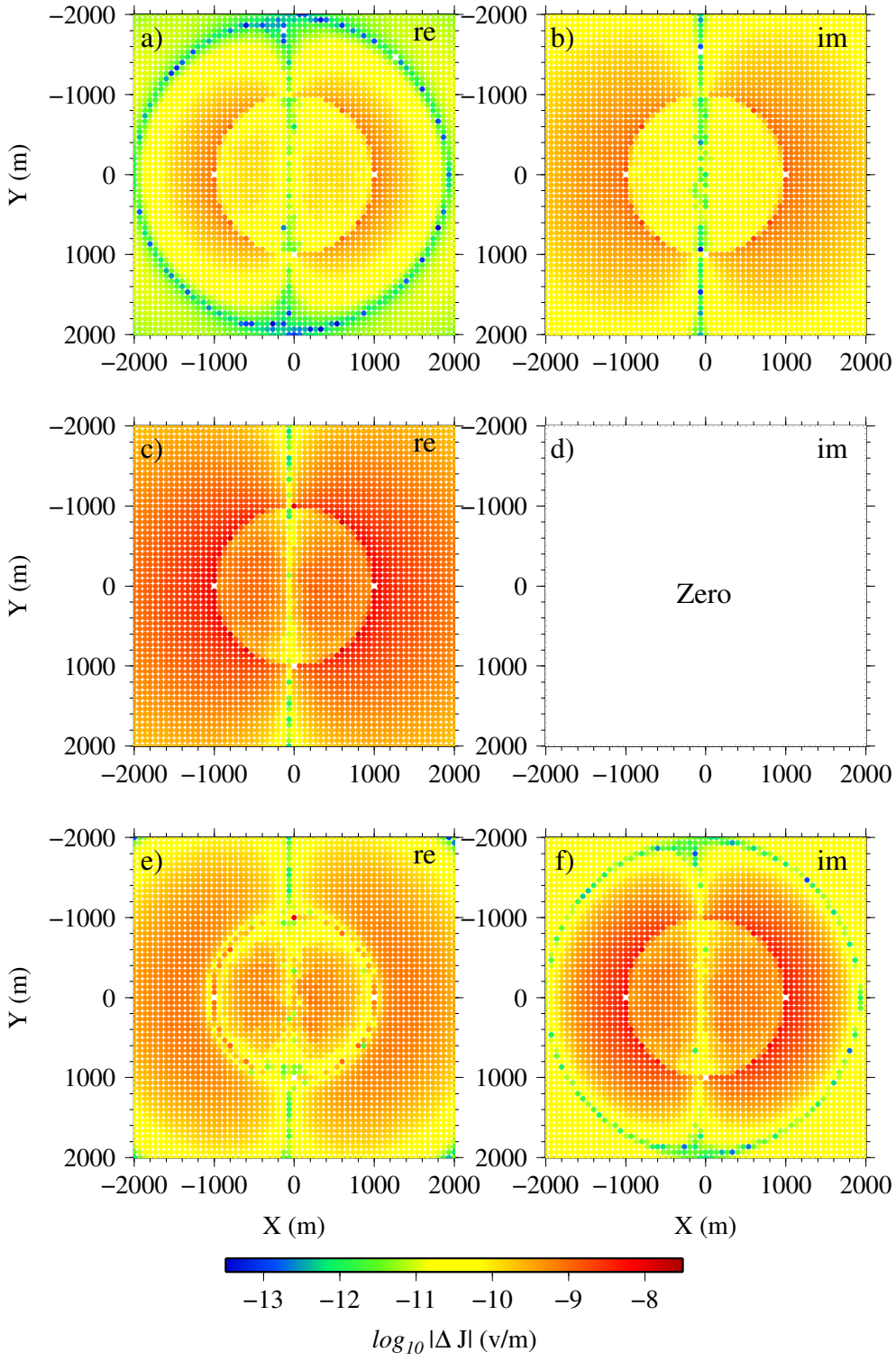

Figure 5.50: The discontinuity in the normal current density components for the inductive part, galvanic part and total current density for the direct solution to the gauged system for the canonical disk model and for a frequency of 1 Hz. The horizontal plane of nodes is located at $z = 950$ m immediately on the top of the circular disk.

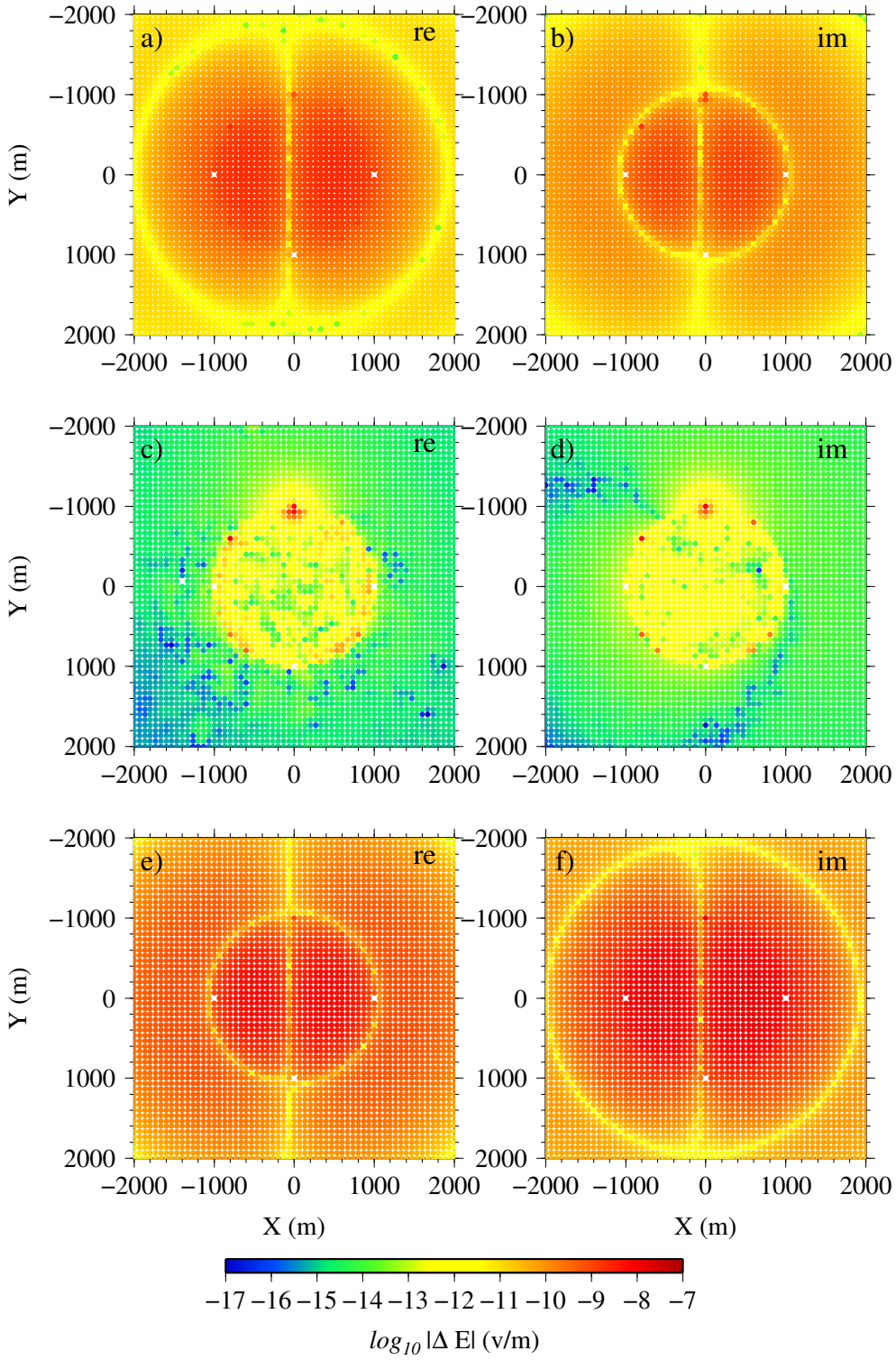

Figure 5.51: The discontinuity in the normal field components for the inductive part, galvanic part and total electric field for the direct solution to the un-gauged system for the canonical disk model and for a frequency of 1 Hz. The horizontal plane of nodes is located at $z = 950$ m immediately on the top of the circular disk.

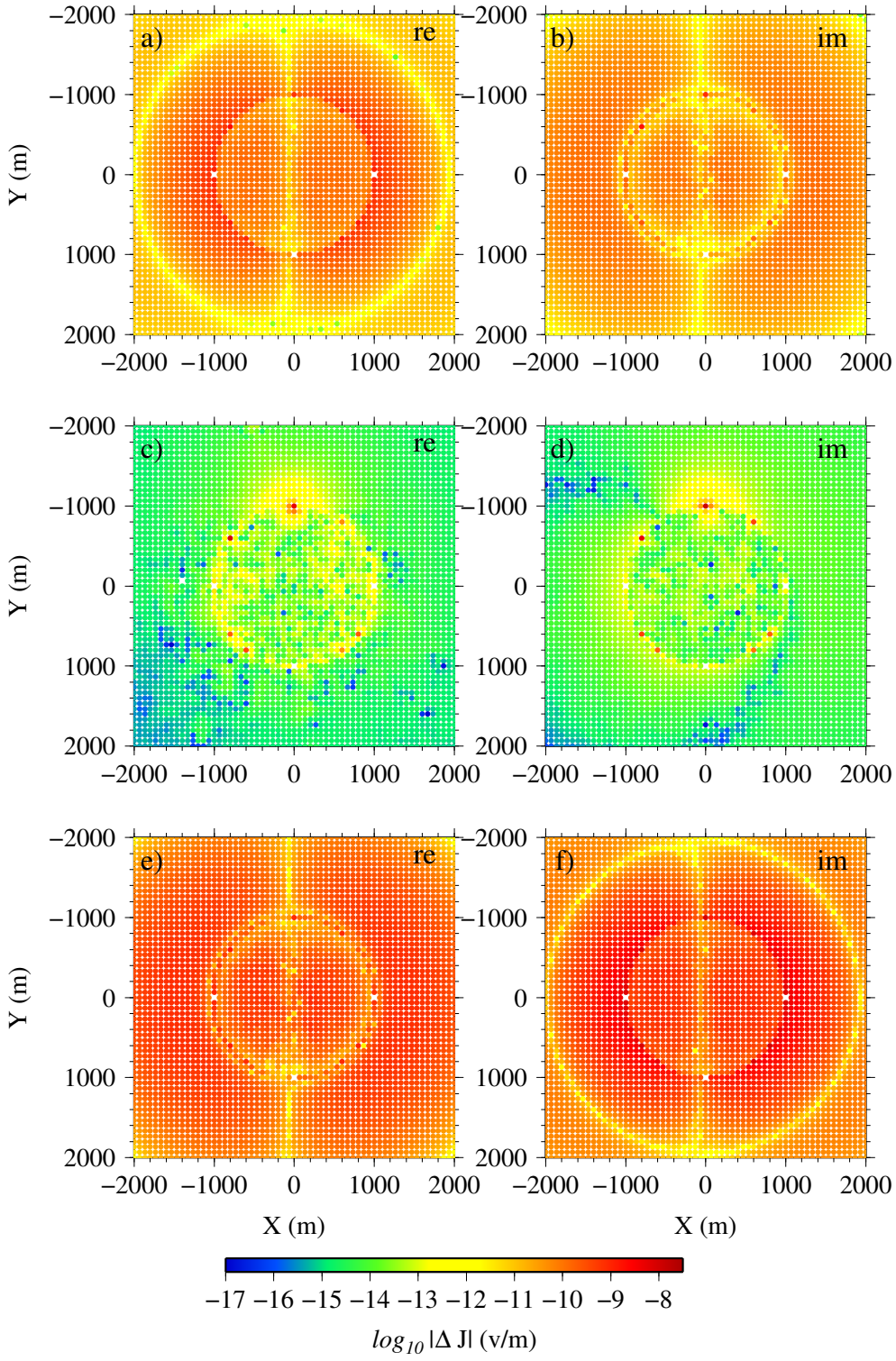

Figure 5.52: The discontinuity in the normal current density components for the inductive part, galvanic part and total current density for the direct solution to the un-gauged system for the canonical disk model and for a frequency of 1 Hz. The horizontal plane of nodes is located at $z = 950$ m immediately on the top of the circular disk.

5.4.4 Concluding remarks

The characteristics of the EM fields were investigated for four solution possibilities for the marine disk example. These solution methods involve iterative and direct solutions to the un-gauged and gauged systems. It was demonstrated that the convergence to the iterative solution of the $\mathbf{A}-\phi$ gauged system is very slow. It was also observed that results for the iterative and direct solutions to the un-gauged system, and direct solution the gauged system, produced the same total electric fields and current densities. However, the contributions from the individual $\mathbf{A}$ and ϕ parts of the total fields were different. This demonstrates the non-uniqueness of the $\mathbf{A}$ and ϕ as a result of non-zero $\nabla \cdot \mathbf{A}$ across cell interfaces. By enforcing zero divergence for $\mathbf{A}$ the explicitly gauged solutions (see e.g., Figures 5.37, 5.43, and 5.49) were found to produce the most reasonable results in terms of the both behavior and continuity conditions of the inductive and galvanic fields. However, in order to accurately solve the gauged system a direct solver needs to be used which demands a larger memory space in the computer. Hence, if only $\mathbf{E}$ and $\mathbf{H}$ fields are required the iterative solution to the original un-gauged system can be computationally efficient and so can handle meshes with more cells.

Chapter 6

Summary and Conclusions

In this thesis forward modeling software has been developed for numerically solving the three-dimensional geophysical electromagnetic boundary value problem. Using Maxwell's equations the relevant partial differential equations were derived in terms of the stand-alone electric field and the combined vector-scalar potentials. The method used and the code developed here are for frequency domain EM problems and arbitrary EM sources. The crux of the numerical implementation applied to the above equations is based on the method of weighted residuals and the Galerkin finite-element method. The numerical modeling is executed on unstructured tetrahedral meshes. The rationale for using this type of mesh is to optimally generate Earth models with complicated geometries and to accurately reproduce general topographic features. The TetGen library is used to produce the grid of tetrahedral elements. In order to fully take advantage of unstructured meshes the problem is formulated for the total field approximation. In particular, the total field formulation can enable the correct simulation of the field for the topographic Earth models in addition to solving the traditionally-modelled flat Earth.

The numerical modeling was firstly implemented on the conventional form of the Helmholtz equation that includes only the electric field as the unknown physical quantity to be solved for. The numerical solution of this partial differential equation, which is referred as to the E-field equation in this context, was attempted using the finite-element method. To begin the discretization process, the E-field equation was firstly minimized using the method of weighted residuals. Edge-element basis functions were used to approximate the electric field within each tetrahedral element in the mesh. The physical justification for this choice was to best satisfy the continuity of the tangential component of the electric field while allowing the normal component to remain discontinuous across the interfaces of distinct conductivities and satisfy the condition that the electric field is divergence-free within a cell. The discrete form of the E-field partial differential equation was solved using both iterative and direct solvers. The reason for making use of an iterative solver was for the sake of memory efficiency in the computer. The E-field solution was investigated for a number of preliminary models, e.g., the conductive whole-space and half-space problems. However, it was found that the total-field solution of the E-field equation, for unstructured meshes and for the range of frequencies and conductivities used here, did not converge to the correct solution in the entire computational domain. The slow convergence of the iterative solver for these scenarios is attributed to the vanishing conductivity term in the E-field equation. Instead, the direct solver, MUMPS, correctly simulated the electric field using the E-field system. The direct solution was however computationally more expensive in comparison to the corresponding iterative solution (e.g. 18.5 Gbytes for the direct solution of the E-field system in Chapter 2).

From the physical standpoint, the non-adequate iterative solution obtained for the E-field equation is an indication of the concept that the low-frequency behavior of the

electromagnetic field is affected by the direct current flow in the conducting medium in addition to the inducing eddy currents. In order to accurately model both of these two effects the electric field is decomposed into vector and scalar potentials. Also the equation of conservation of charge is used in conjunction with the Helmholtz equation. The system of equations for the potentials is again solved using the finite-element method. The vector residual from the Helmholtz equation and the scalar residual from the equation of conservation of charge are minimized using the method of weighted residuals. Similar to the situation where the electric field is approximated, edge-element basis functions are used for the vector potentials. Also nodal basis functions are used for the approximation of the scalar potentials. Here the continuity of the tangential components of the vector potential and the discontinuity in the normal component of the gradient of the scalar potential are thought to better satisfy the behavior of the fields across interfaces in the grid. Upon imposing appropriate boundary conditions the sparse algebraic form of the decomposed system is solved again using an iterative solver with appropriate preconditioning of the system. The approximate electric and magnetic fields are reproduced using the calculated potentials. Here, for the comparable examples presented for the E-field solution, a significantly faster convergence of the iterative solver and subsequently an accurate numerical solution for the fields are observed. The memory usage of this iterative solution was significantly smaller than those of direct solutions of the E-field system (e.g., memory usages of 8 and 4 Gbytes for the examples presented in Chapters 3 and 5).

The decomposition of the electric field into magnetic vector potential and electric scalar potential is performed with the intention of separating the inductive and galvanic components of the electromagnetic field. In the third phase of this thesis the solution from the $\mathbf{A} - \phi$ decomposition approach was validated for a number of examples published in the geophysical literature and the inductive and galvanic parts

of the field investigated. The first example presented is for a mineral exploration scenario where a conductive prism is located within a homogeneous half-space of otherwise uniform conductivity. This conductivity structure is stimulated using an electric line source of current (e.g., a grounded wire) with a fairly low frequency. The finite element solution of the decomposed system is obtained in agreement with the solution from an integral-equation approach. For this example it is also found that the galvanic part of the field dominates the inductive component in reducing the electric field in the conductive prism. The next example presented in this section verifies the finite-element solution against the data from the physical scale modeling method. The laboratory-scaled model considers a highly conductive graphite cube immersed in conductive brine. Here the normalized magnetic field is measured using a source-receiver magnetic dipole pair moving above the brine solution in free-space. Considering the conductivities of the graphite cube and the brine host, and also the range of frequencies used for the dipole source, the EM response of this model is representative of those observed in the geophysical exploration scenarios. A reasonable agreement of the numerical magnetic fields against the experimental physical scale modelings are observed for different frequencies. It is also observed that for a particular source-receiver configuration the inductive part dominates the galvanic part in forming the total electric field in the conductive graphite. The last example in this section verifies the finite-element total field solution for unstructured meshes against the finite-volume total field solution for structured meshes. The model presented simulates a hydrocarbon exploration scenario where a resistive disk model is located in the conductive seabed sediments. In terms of simulating the fields around the resistive disk it is observed that for the configuration presented here the total field is a combination of the inductive and galvanic components.

The $\mathbf{A} - \phi$ formulation of the electromagnetic problem is implicitly gauged through the choice of edge-element basis functions for the vector potential. This approach however caused peculiar behaviors for the inductive and galvanic fields, e.g., for higher frequencies used for the large loop of current and plate example presented in Chapter 5. This is because the potential formulation is stymied by the non-uniqueness of the vector potential. An explicit gauging of the system of equations was therefore derived. The gauged decomposed system is correctly solved using the direct solver, and the corresponding inductive and galvanic parts were investigated. In order to further understand the interface conditions due to different solution methods the continuity of the fields and currents at the conductivity gradients in the models are investigated. The uniqueness of the total electric fields and the non-uniqueness of the individual inductive and galvanic parts are demonstrated through comparison of the different solutions (i.e., direct and iterative solutions to the gauged and un-gauged systems) presented in Chapter 5. In particular, the identical $\mathbf{E}$ and $\mathbf{H}$ that are produced from these solutions demonstrated the uniqueness of the total electric and magnetic fields respectively. However, the corresponding inductive and galvanic parts were found to be inherent to the solution types. The enforcement of the explicit gauge condition, $\nabla \cdot \mathbf{A} = 0$, gave rise to obtaining more reasonable inductive and galvanic fields. However, obtaining an accurate solution to the gauged system necessitates solving the system using a direct solver, which in turn requires using a significantly larger computational space. Hence the iterative solution to the original un-gauged system would be more computationally efficient if only the total electric and magnetic fields are required. In terms of future perspectives, in order to optimize the trade-off between the solution accuracy and computation time, adaptive mesh refinement strategies may be required. In particular, based on an error estimation method, e.g., *a posteriori*, adaptive approach refines the mesh only in certain regions, which

causes smaller number of unknowns for the discretized system. The forward modeling code developed here is written in the Fortran programming language that allows for optimizing run time. Also, it is a stand-alone code for assembling the system matrix that can be easily used in inversion schemes.

Appendix A

A.1 Scalar basis functions

In this section a complete description of deriving the scalar basis functions (nodal elements) for a typical tetrahedral element is presented. The following expression represents an arbitrary linear function in a typical tetrahedral element:

$$E^e(x, y, z) = a^e + b^e x + c^e y + d^e z. \tag{A.1}$$

It is possible to find the coefficients a^e, b^e, c^e, and d^e once equation A.1 is constrained at the four nodes of a tetrahedron. Considering $\mathbf{r}_1 = (x_1, y_1, z_1)$, $\mathbf{r}_2 = (x_2, y_2, z_2)$, $\mathbf{r}_3 = (x_3, y_3, z_3)$, and $\mathbf{r}_4 = (x_4, y_4, z_4)$ as the coordinates of the four nodes, the following set of equations is derived:

$$\begin{aligned} E_1 &= a^e + b^e x_1 + c^e y_1 + d^e z_1 \\ E_2 &= a^e + b^e x_2 + c^e y_2 + d^e z_2 \\ E_3 &= a^e + b^e x_3 + c^e y_3 + d^e z_3 \\ E_4 &= a^e + b^e x_4 + c^e y_4 + d^e z_4 \end{aligned} \tag{A.2}$$

where E_1, E_2, E_3, and E_4 mark the values of the function $E^e(\mathbf{r})$ at the respective $\mathbf{r}_1$, $\mathbf{r}_2$, $\mathbf{r}_3$, and $\mathbf{r}_4$ nodal locations. By solving the above set of equations for the coefficients the following expressions are derived (Jin, 2002),

$$a^e = \frac{1}{6V^e}\begin{vmatrix} E_1 & E_2 & E_3 & E_4 \\ x_1 & x_2 & x_3 & x_4 \\ y_1 & y_2 & y_3 & y_4 \\ z_1 & z_2 & z_3 & z_4 \end{vmatrix}, \tag{A.3}$$

$$b^e = \frac{1}{6V^e}\begin{vmatrix} 1 & 1 & 1 & 1 \\ E_1 & E_2 & E_3 & E_4 \\ y_1 & y_2 & y_3 & y_4 \\ z_1 & z_2 & z_3 & z_4 \end{vmatrix}, \tag{A.4}$$

$$c^e = \frac{1}{6V^e}\begin{vmatrix} 1 & 1 & 1 & 1 \\ x_1 & x_2 & x_3 & x_4 \\ E_1 & E_2 & E_3 & E_4 \\ z_1 & z_2 & z_3 & z_4 \end{vmatrix}, \tag{A.5}$$

$$b^e = \frac{1}{6V^e}\begin{vmatrix} 1 & 1 & 1 & 1 \\ x_1 & x_2 & x_3 & x_4 \\ y_1 & y_2 & y_3 & y_4 \\ E_1 & E_2 & E_3 & E_4 \end{vmatrix} \tag{A.6}$$

where V^e is the volume of the tetrahedral element. Expanding each of the above expressions gives,

$$a^e = (\frac{1}{6V_e})(a_1E_1 + a_2E_2 + a_3E_3 + a_4E_4), \tag{A.7}$$

$$b^e = (\frac{1}{6V_e})(b_1E_1 + b_2E_2 + b_3E_3 + b_4E_4), \tag{A.8}$$

$$c^e = (\frac{1}{6V_e})(c_1E_1 + c_2E_2 + c_3E_3 + c_4E_4), \tag{A.9}$$

and

$$d^e = (\frac{1}{6V_e})(d_1E_1 + d_2E_2 + d_3E_3 + d_4E_4) \tag{A.10}$$

where the coefficients a_i, b_i, c_i, and d_i with $i = 1, \cdots 4$ are given by the following equations,

$$a_1 = \begin{vmatrix} x_2 & x_3 & x_4 \\ y_2 & y_3 & y_4 \\ z_2 & z_3 & z_4 \end{vmatrix}, \tag{A.11}$$

$$a_2 = -\begin{vmatrix} x_1 & x_3 & x_4 \\ y_1 & y_3 & y_4 \\ z_1 & z_3 & z_4 \end{vmatrix}, \tag{A.12}$$

$$a_3 = \begin{vmatrix} x_1 & x_2 & x_4 \\ y_1 & y_2 & y_4 \\ z_1 & z_2 & z_4 \end{vmatrix}, \tag{A.13}$$

$$a_4 = -\begin{vmatrix} x_1 & x_2 & x_3 \\ y_1 & y_2 & y_3 \\ z_1 & z_2 & z_3 \end{vmatrix}, \tag{A.14}$$

$$b_1 = -\begin{vmatrix} 1 & 1 & 1 \\ y_2 & y_3 & y_4 \\ z_2 & z_3 & z_4 \end{vmatrix}, \tag{A.15}$$

$$b_2 = \begin{vmatrix} 1 & 1 & 1 \\ y_1 & y_3 & y_4 \\ z_1 & z_3 & z_4 \end{vmatrix}, \tag{A.16}$$

$$b_3 = -\begin{vmatrix} 1 & 1 & 1 \\ y_1 & y_2 & y_4 \\ z_1 & z_2 & z_4 \end{vmatrix}, \tag{A.17}$$

$$b_4 = \begin{vmatrix} 1 & 1 & 1 \\ y_1 & y_2 & y_3 \\ z_1 & z_2 & z_3 \end{vmatrix}, \tag{A.18}$$

$$c_1 = \begin{vmatrix} 1 & 1 & 1 \\ x_2 & x_3 & x_4 \\ z_2 & z_3 & z_4 \end{vmatrix}, \tag{A.19}$$

$$c_2 = -\begin{vmatrix} 1 & 1 & 1 \\ x_1 & x_3 & x_4 \\ z_1 & z_3 & z_4 \end{vmatrix}, \tag{A.20}$$

$$c_3 = \begin{vmatrix} 1 & 1 & 1 \\ x_1 & x_2 & x_4 \\ z_1 & z_2 & z_4 \end{vmatrix}, \tag{A.21}$$

$$c_4 = -\begin{vmatrix} 1 & 1 & 1 \\ x_1 & x_2 & x_3 \\ z_1 & z_2 & z_3 \end{vmatrix}, \tag{A.22}$$

$$d_1 = -\begin{vmatrix} 1 & 1 & 1 \\ x_2 & x_3 & x_4 \\ y_2 & y_3 & y_4 \end{vmatrix}, \tag{A.23}$$

$$d_2 = \begin{vmatrix} 1 & 1 & 1 \\ x_1 & x_3 & x_4 \\ y_1 & y_3 & y_4 \end{vmatrix}, \tag{A.24}$$

$$d_3 = -\begin{vmatrix} 1 & 1 & 1 \\ x_1 & x_2 & x_4 \\ y_1 & y_2 & y_4 \end{vmatrix}, \tag{A.25}$$

$$d_4 = \begin{vmatrix} 1 & 1 & 1 \\ x_1 & x_2 & x_3 \\ y_1 & y_2 & y_3 \end{vmatrix}. \tag{A.26}$$

These are auxiliary coefficients for each node of a tetrahedral cell. By substituting equations A.7, A.8, A.9 and A.10 into equation A.1 a general form for the function E_e is given in terms of the values of the function at the vertices of the tetrahedron:

$$E^e(x, y, z) = \sum_{k=1}^{4} N_k(x, y, z) E_k \tag{A.27}$$

where N_k is the scalar basis function which is given by the following equation,

$$N_k(x, y, z) = \frac{1}{6V^e}(a_k + b_k x + c_k y + d_k z). \tag{A.28}$$

Appendix B

B.1 Applying elemental functions to inner-product integrals

B.1.1 Elements of the coefficient matrix

The first term formulated here is the interaction of the curl of vector basis functions between two particular edges of i and j (e.g., in equation 2.29):

$$C_{ij} = \int_{\Omega} (\nabla \times \mathbf{N}_i) \cdot (\nabla \times \mathbf{N}_j) \, d\Omega \tag{B.1}$$

where the vector basis functions $\mathbf{N}_i$ and $\mathbf{N}_j$ are:

$$\mathbf{N}_i = \ell_i (N_{i1} \nabla N_{i2} - N_{i2} \nabla N_{i1}), \tag{B.2}$$

and

$$\mathbf{N}_j = \ell_j (N_{j1} \nabla N_{j2} - N_{j2} \nabla N_{j1}), \tag{B.3}$$

where N_{i1}, N_{i2} are the nodal elements for the nodes $i1$ and $i2$ respectively, and N_{j1}, N_{j2} are the nodal elements for the nodes $j1$ and $j2$ respectively. Also ℓ_i and ℓ_j are the lengths of the corresponding edges. The curl of the above vector basis functions

are (Jin, 2002):

$$\nabla \times \mathbf{N}_i = 2\ell_i(\nabla N_{i1} \times \nabla N_{i2}), \tag{B.4}$$

and

$$\nabla \times \mathbf{N}_j = 2\ell_j(\nabla N_{j1} \times \nabla N_{j2}), \tag{B.5}$$

where ∇N_k is given by taking the gradient of the nodal element in equation A.28. For example, for a particular node, k

$$\nabla N_k = \frac{1}{6V^e}(b_k\mathbf{x} + c_k\mathbf{y} + d_k\mathbf{z}). \tag{B.6}$$

Using the above equation into equation B.4 and B.5 results in the following expressions for the curl of edge-elements:

$$\nabla \times \mathbf{N}_i = \frac{2\ell_i}{(6V^e)^2}(N_x\mathbf{x} + N_y\mathbf{y} + N_z\mathbf{z}), \tag{B.7}$$

where

$$\begin{aligned} N_x(y,z) &= (a_{i1}b_{i2} - a_{i2}b_{i1}) + y(c_{i1}b_{i2} - c_{i2}b_{i1}) + z(d_{i1}b_{i2} - d_{i2}b_{i1}), \\ N_y(x,z) &= (a_{i1}c_{i2} - a_{i2}c_{i1}) + x(b_{i1}c_{i2} - b_{i2}c_{i1}) + z(d_{i1}c_{i2} - d_{i2}c_{i1}), \\ N_z(x,y) &= (a_{i1}d_{i2} - a_{i2}d_{i1}) + y(c_{i1}d_{i2} - c_{i2}d_{i1}) + x(b_{i1}d_{i2} - b_{i2}d_{i1}). \end{aligned} \tag{B.8}$$

A similar expression also exists for the curl of $\mathbf{N}_j$. Substituting the expressions for $\nabla \times \mathbf{N}_i$ and $\nabla \times \mathbf{N}_j$ into equation B.1 and integrating over the volume Ω results in the following equation for C_{ij}:

$$C_{ij} = \frac{4\ell_i\ell_j}{6^4(V^e)^3}(C_1 + C_2 + C_3), \tag{B.9}$$

where

$$C_1 = (b_{i1}c_{i2} - b_{i2}c_{i1})(b_{j1}c_{j2} - b_{j2}c_{j1}),$$
$$C_2 = (d_{i1}b_{i2} - d_{i2}b_{i1})(d_{j1}b_{j2} - d_{j2}b_{j1}),$$
$$C_3 = (c_{i1}d_{i2} - c_{i2}d_{i1})(c_{j1}d_{j2} - c_{j2}d_{j1}).$$

The second term formulated here is the interaction of the vector basis functions between two neighboring edges i and j:

$$D_{ij} = \int_\Omega \mathbf{N}_i \cdot \mathbf{N}_j \; d\Omega \tag{B.10}$$

By directly substituting equations B.2 and B.3 into the above equation the following equation is given,

$$D_{ij} = \ell_i \ell_j \; [(\nabla N_{i2} \cdot \nabla N_{j2}) \int_\Omega N_{i1} \; N_{j1} \; d\Omega \; - \; (\nabla N_{i2} \cdot \nabla N_{j1}) \int_\Omega N_{i1} \; N_{j2} \; d\Omega \; - \; (\nabla N_{i1} \cdot \nabla N_{j2}) \int_\Omega N_{i2} \; N_{j1} \; d\Omega \; + \; (\nabla N_{i1} \cdot \nabla N_{j1}) \int_\Omega N_{i2} \; N_{j2} \; d\Omega \;] \tag{B.11}$$

Because the integral form of $\int_\Omega N_k N_l \; d\Omega$, with k and l as nodes, is frequently repeated in the above equation, a calculation of its closed-form expression is firstly performed. Using the expression given for the nodal element (equation A.28) in the above integral gives:

$$G_{ij} = \int_\Omega N_k \; N_l \; d\Omega = \frac{1}{(6V^e)^2} \int_\Omega (a_k + b_k x + c_k y + d_k z)(a_l + b_l x + c_l y + d_l z) \; dx \; dy \; dz. \tag{B.12}$$

In order to counteract the problem of finding the lower and upper bounds of the above integral, a transformation to the normalized coordinate system is performed. An arbitrary point $\mathbf{r} = (x, y, z)$ in a tetrahedron can be related to four tetrahedral

vertices through the following linear combination (Xu, 2001):

$$\mathbf{r} - \mathbf{r}_4 = L_1(\mathbf{r}_1 - \mathbf{r}_4) + L_2(\mathbf{r}_2 - \mathbf{r}_4) + L_3(\mathbf{r}_3 - \mathbf{r}_4), \tag{B.13}$$

where $\mathbf{r}_1 = (x_1, y_1, z_1)$, $\mathbf{r}_2 = (x_2, y_2, z_2)$, $\mathbf{r}_3 = (x_3, y_3, z_3)$, and $\mathbf{r}_4 = (x_4, y_4, z_4)$ are the coordinates of the vertices. Here, because the arbitrary point is in the tetrahedron, L_1, L_2, L_3, and L_4 are varying between zero and 1. Rearranging the above equation gives,

$$\mathbf{r} = L_1\mathbf{r}_1 + L_2\mathbf{r}_2 + L_3\mathbf{r}_3 + L_4\mathbf{r}_4, \tag{B.14}$$

where the parameter L_4 is

$$L_4 = 1 - L_1 - L_2 - L_3 \tag{B.15}$$

which indicates that only three of these linear elements, L_i, are independent. Expanding equation B.14 for three Cartesian components gives,

$$\begin{aligned} x &= L_1x_1 + L_2x_2 + L_3x_3 + L_4x_4, \\ y &= L_1y_1 + L_2y_2 + L_3y_3 + L_4y_4, \\ z &= L_1z_1 + L_2z_2 + L_3z_3 + L_4z_4. \end{aligned} \tag{B.16}$$

By solving the above equation the following expressions are derived for the linear

elements:

$$L_1 = \frac{\begin{vmatrix} 1 & 1 & 1 & 1 \\ x & x_2 & x_3 & x_4 \\ y & y_2 & y_3 & y_4 \\ z & z_2 & z_3 & z_4 \end{vmatrix}}{\begin{vmatrix} 1 & 1 & 1 & 1 \\ x_1 & x_2 & x_3 & x_4 \\ y_1 & y_2 & y_3 & y_4 \\ z_1 & z_2 & z_3 & z_4 \end{vmatrix}} \tag{B.17}$$

$$L_2 = \frac{\begin{vmatrix} 1 & 1 & 1 & 1 \\ x_1 & x & x_3 & x_4 \\ y_1 & y & y_3 & y_4 \\ z_1 & z & z_3 & z_4 \end{vmatrix}}{\begin{vmatrix} 1 & 1 & 1 & 1 \\ x_1 & x_2 & x_3 & x_4 \\ y_1 & y_2 & y_3 & y_4 \\ z_1 & z_2 & z_3 & z_4 \end{vmatrix}} \tag{B.18}$$

$$L_3 = \frac{\begin{vmatrix} 1 & 1 & 1 & 1 \\ x_1 & x_2 & x & x_4 \\ y_1 & y_2 & y & y_4 \\ z_1 & z_2 & z & z_4 \end{vmatrix}}{\begin{vmatrix} 1 & 1 & 1 & 1 \\ x_1 & x_2 & x_3 & x_4 \\ y_1 & y_2 & y_3 & y_4 \\ z_1 & z_2 & z_3 & z_4 \end{vmatrix}} \tag{B.19}$$

$$L_4 = \frac{\begin{vmatrix} 1 & 1 & 1 & 1 \\ x_1 & x_2 & x_3 & x \\ y_1 & y_2 & y_3 & y \\ z_1 & z_2 & z_3 & z \end{vmatrix}}{\begin{vmatrix} 1 & 1 & 1 & 1 \\ x_1 & x_2 & x_3 & x_4 \\ y_1 & y_2 & y_3 & y_4 \\ z_1 & z_2 & z_3 & z_4 \end{vmatrix}} \tag{B.20}$$

$L_i,\ i = 1, \cdots, 4$, which describes a barycentric or local coordinate system, are the ratios of the volumes of the sub-tetrahedron comprising the point $\mathbf{r}$ and three of nodes of the tetrahedron to the volume of the whole tetrahedron. Substituting the coordinates of the vertices in to the above expressions leads to the following property for the barycentric elements:

$$L_i|_{node=j} \begin{cases} 1, & i = j, \\ 0, & i \neq j. \end{cases} \tag{B.21}$$

Equation B.14 relates three component of the Cartesian coordinate system to three components of the barycentric coordinate system:

$$\begin{aligned} x &= x_4 + L_1(x_1 - x_4) + L_2(x_2 - x_4) + L_3(x_3 - x_4) \\ y &= y_4 + L_1(y_1 - y_4) + L_2(y_2 - y_4) + L_3(y_3 - y_4) \\ z &= z_4 + L_1(z_1 - z_4) + L_2(z_2 - z_4) + L_3(z_3 - z_4), \end{aligned} \tag{B.22}$$

which can be modified to the following form:

$$\mathbf{r} = \mathbf{r}_4 + \mathbf{J}\ \gamma, \tag{B.23}$$

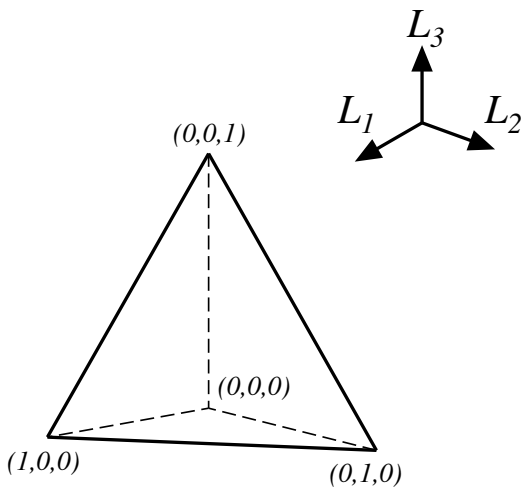

Figure B.1: A simplex tetrahedral element in the barycentric coordinate system.

where $\mathbf{r} = (x, y, z)^T$, $\mathbf{r}_4 = (x_4, y_4, z_4)^T$, and $\gamma = (L_1, L_2, L_3)^T$ (T is the transpose sign). Here the parameter $|\mathbf{J}|$ is the transformation coefficient (Jacobian) and given by the following matrix,

$$\mathbf{J} = \begin{bmatrix} x_1 - x_4 & x_2 - x_4 & x_3 - x_4 \\ y_1 - y_4 & y_2 - y_4 & y_3 - y_4 \\ z_1 - z_4 & z_2 - z_4 & z_3 - z_4 \end{bmatrix}. \tag{B.24}$$

Through performing this transformation the arbitrary shaped tetrahedral element in the Cartesian coordinate system alters to a simplex tetrahedron in the Barycentric (normalized or local) coordinate system shown in Figure B.1. It is seen from equation B.21 that the linear elements posses similar properties as the scalar basis functions. For the tetrahedron shown in Figure B.1 the basis functions in the barycentric

system are given by the following expressions:

$$\begin{aligned} N_1 &= L_1 \\ N_2 &= L_2 \\ N_3 &= L_3 \\ N_4 &= 1 - L_1 - L_2 - L_3. \end{aligned} \tag{B.25}$$

Using the above set of equations the integral shown in equation B.12 is transformed into the normalized coordinate system:

$$\int_{\Omega} N_k(x,y,z) N_l(x,y,z)\ dx\ dy\ dz = \int_{\Omega'} N_k(L_1,L_2,L_3) N_l(L_1,L_2,L_3)\ |\mathbf{J}|\ dL_1\ dL_2\ dL_3, \tag{B.26}$$

where

$$0 \le L_1 \le 1\ ;\ 0 \le L_2 \le 1\ ;\ 0 \le L_3 \le 1, \tag{B.27}$$

and $\Omega^{'}$ is the tetrahedral domain in the normalized system. Considering the bounds of the integral the transformed integral in equation B.26 is solved,

$$G_{kl} = |\mathbf{J}| \int_0^1 \int_0^{1-L_1} \int_0^{1-L_1-L_2} N_k\ N_l\ dL_3\ dL_2\ dL_1 \tag{B.28}$$

For a situation where $k = l$ the integral changes as follows,

$$G_{ll} = |\mathbf{J}| \int_0^1 \int_0^{1-L_1} \int_0^{1-L_1-L_2} L_1^2\ dL_3\ dL_2\ dL_1 = |\mathbf{J}| \int_0^1 \int_0^{1-L_1} L_1^2(1-L_1-L_2)\ dL_2\ dL_1$$

$$= |\mathbf{J}| \int_0^1 \left(L_1^2 L_2 - L_1^3 L_2 - \frac{1}{2} L_2^2 L_1^2 \right) |_0^{1-L_1}\ dL_1 = |\mathbf{J}| \int_0^1 \left(\frac{1}{2} L_1^2 - L_1^3 - \frac{1}{2} L_1^4 \right) dL_1$$

$$= |\mathbf{J}| \left(\frac{1}{6} L_1^3 - \frac{1}{4} L_1^4 + \frac{1}{10} L_1^5\right) |_0^1 = |\mathbf{J}|\ \frac{1}{60}.$$

Therefore,

$$G_{ll} = \frac{|\mathbf{J}|}{60}. \tag{B.29}$$

For the situation where $k \neq l$, solving the integral in equation B.28 gives

$$G_{kl} = \frac{|\mathbf{J}|}{120}. \tag{B.30}$$

Using equations B.29 and B.30 the following closed from is presented for equation B.11:

$$D_{ij} = \frac{\ell_i \ell_j}{(6V^e)^2} \left[F_{i2j2}\ G_{i1j1} - F_{i2j1}\ G_{i1j2} - F_{i1j2}\ G_{i2j1} + F_{i1j1}\ G_{i2j2} \right], \tag{B.31}$$

where $F_{ij} = a_i a_j + b_i b_j + c_i c_j$.

The third term formulized here is the interaction between a vector basis function and the gradient of a nodal basis function which first appeared in equation 3.24. For the particular edge i and node k the integral would be

$$\int_\Omega \sigma \mathbf{N}_j \cdot \nabla N_l \ d\Omega. \tag{B.32}$$

Using equations B.3 and B.6 in the above integral gives,

$$\int_\Omega \sigma \mathbf{N}_j \cdot \nabla N_l \ d\Omega = \ell_j \int_\Omega (N_{j1} \nabla N_{j2} - N_{j2} \nabla N_{j1}) \cdot \sigma \frac{1}{6V^e} (b_k \mathbf{x} + c_k \mathbf{y} + d_k \mathbf{z}) \ d\Omega, \tag{B.33}$$

which can be reorganized as

$$\begin{aligned} \int_\Omega \sigma \mathbf{N}_j \cdot \nabla N_l \ d\Omega = (\frac{1}{6V^e})^2 \ell_j \sigma \ [\ & (b_{j2} b_k + c_{j2} c_k + d_{j2} d_k) \int_\Omega N_{i1}(x,y,z) \ dxdydz \\ & - (b_{i1} b_k + c_{i1} c_k + d_{i1} d_k) \int_\Omega N_{i2}(x,y,z) \ dxdydz \ ]. \end{aligned} \tag{B.34}$$

The normalized coordinate system is again used to calculate the new integrals ap-

pearing in the above equation:

$$\int_{\Omega} N_i \; dxdydz = \int_{\Gamma} N_i(L_1, L_2, L_3)|\mathbf{J}| \; dL_1 \; dL_2 \; dL_3. \tag{B.35}$$

Supposing $i = 2$, the N_2 function will then be L_2 and the above equation is written as follows,

$$\begin{aligned} \int_{\Gamma} N_2(L_1, L_2, L_3)|\mathbf{J}| \; dL_1 \; dL_2 \; dL_3 &= \int_0^1 \int_0^{1-L_1} \int_0^{1-L_1-L_2} L_2 \; |\mathbf{J}| \; dL_3 \; dL_1 \; dL_2 \\ = \int_0^1 \int_0^{1-L_1} L_2(1 - L_1 - L_2) \; |\mathbf{J}| \; dL_1 dL_2 &= \int_0^1 (L_2 L_1 - L_2^2 L_1 - \frac{1}{2} L_2 L_1^2)|_0^{1-L_2} \; |\mathbf{J}| \; dL_2 \\ &= |\mathbf{J}|(\frac{1}{4} {L_2}^2 - \frac{1}{3} {L_2}^3 + \frac{1}{8} {L_2}^4)|_0^1 = \frac{1}{24}|\mathbf{J}|. \end{aligned} \tag{B.36}$$

Therefore,

$$\int_{\Omega} N_i \; dxdydz = \frac{1}{24}|\mathbf{J}| \tag{B.37}$$

By substituting equation B.37 into equation B.34 the following form for the integral in equation B.32 is derived:

$$\int_{\Omega} \sigma \mathbf{N}_j \cdot \nabla N_l \; d\Omega = (\frac{1}{6V^e})^2 \ell_j \sigma \frac{1}{24}|\mathbf{J}| \; [(b_{j2}b_k + c_{j2}c_k + d_{j2}d_k) - (b_{i1}b_k + c_{i1}c_k + d_{i1}d_k)]. \tag{B.38}$$

The forth inner product integral that is seen in the discretized form of the equation of conservation of charge (equation 3.25) is the interaction between the nodal element basis functions,

$$\int_{\Omega} \nabla N_l \cdot (\sigma \nabla N_k) \; d\Omega. \tag{B.39}$$

Again by using equation B.6 this integral can be written as,

$$\int_{\Omega} \nabla N_l \cdot (\sigma \nabla N_k)\ d\Omega = (\frac{1}{6V^e})^2 \int_{\Omega} \sigma(b_l \mathbf{x} + c_l \mathbf{y} + d_l \mathbf{z}) \cdot (b_k \mathbf{x} + c_k \mathbf{y} + d_k \mathbf{z})\ d\Omega. \quad \text{(B.40)}$$

After performing a simple dot-product the following equation is derived,

$$\int_{\Omega} \nabla N_l \cdot (\sigma \nabla N_k)\ d\Omega = (\frac{1}{6V^e})^2 \sigma(b_l b_k + c_l c_k + d_l d_k). \quad \text{(B.41)}$$

B.1.2 Elements of the source term

The first source term considered here calculates the dot-product of a vector basis function with the magnetization vector due to a vertical magnetic source point. According to equation 2.32 in Chapter 2 the following form is given for the source term S_1:

$$S_1 = \int_{\Omega} \mathbf{M} \cdot \nabla \times \mathbf{N}_i\ d\Omega, \quad \text{(B.42)}$$

where $\mathbf{M} = m\ \delta(x - x_0)\delta(y - y_0)\delta(z - z_0)\mathbf{z}$ and $\mathbf{N}_i$ is the edge-element for the edge i (see equations B.2 and B.4). Using these expressions in the above equation gives,

$$\begin{aligned} S_1 &= \frac{2\ell_i}{(6V)^2} \int_{\Omega} m\delta(x - x_0)\delta(y - y_0)\delta(z - z_0)\mathbf{z} \cdot (b_{i1}c_{i2} - c_{i1}b_{i2})\mathbf{z}\ d\Omega \\ &= m\frac{2\ell_i}{(6V)^2}(b_{i1}c_{i2} - c_{i1}b_{i2}) \int_{\Omega} \delta(x - x_0)\delta(y - y_0)\delta(z - z_0)\ d\Omega. \end{aligned} \quad \text{(B.43)}$$

The delta integral in the above equation reduces to unity and the following expression is given for the source term S_1,

$$S_1 = m\frac{2\ell_i}{(6V)^2}(b_{i1}c_{i2} - c_{i1}b_{i2}). \quad \text{(B.44)}$$

The second type of source term seen in equation 2.36 deals with the interaction of a

current segment of a wire with the vector basis functions:

$$S_2 = \int_\Omega \mathbf{N}_i \cdot \mathbf{J}_e^s \, d\Omega \tag{B.45}$$

Considering that the x-directed current segment is bounded inside a particular tetrahedron the following equations is formed:

$$S = \frac{I}{(6V^e)^2} \int_\Omega (N_x\mathbf{x}+N_y\mathbf{y}+N_z\mathbf{z})\cdot(\mathcal{H}(x_{i+1})-\mathcal{H}(x_i))\ \delta(y-y_0)\delta(z-z_0)\ \mathbf{x}\ d\Omega, \tag{B.46}$$

where N_x, N_y and N_z are the components of the vector basis functions given in equation B.7. Because the current line is in the x-direction only the parameter N_x contributes in the above integral which leads to the following expression

$$\begin{aligned} S_2 = \frac{I}{(6V^e)^2} \int_\Omega & [(a_{i1}b_{i2} - a_{i2}b_{i1}) + y(c_{i1}b_{i2} - c_{i2}b_{i1}) + z(d_{i1}b_{i2} - d_{i2}b_{i1})] \\ & [(\mathcal{H}(x_{i+1}) - \mathcal{H}(x_i))\ \delta(y - y_0)\delta(z - z_0)]\ dx\ dy\ dz. \end{aligned} \tag{B.47}$$

After calculating the above integral the following equation is derived

$$S_2 = \frac{I\Delta x}{(6V^e)^2}\ \ (a_{i1}b_{i2} - a_{i2}b_{i1}) + y_0(c_{i1}b_{i2} - c_{i2}b_{i1}) + z_0(d_{i1}b_{i2} - d_{i2}b_{i1}), \tag{B.48}$$

where the parameter Δx is the length of the current segment in the considered tetrahedral cell.

The third type of source term existing in equation 3.26 involves the interaction of the divergence of the current segment with the scalar basis functions:

$$S_3 = \int_\Omega N_l \nabla \cdot \mathbf{J}_e^s \, d\Omega. \tag{B.49}$$

Considering an x-directed wire the above equation is firstly changed to

$$S_3 = \int_\Omega \nabla N_l \cdot \mathbf{J}_e^s \, d\Omega, \tag{B.50}$$

and using the current density expressed, for example, by equation 2.37 gives:

$$S_3 = \frac{1}{6V^e} I \int_\Omega (b_l \mathbf{x} + c_l \mathbf{y} + d_l \mathbf{z}) \cdot (\mathcal{H}(x_{i+1}) - \mathcal{H}(x_i)) \; \delta(y - y_0) \delta(z - z_0) \; \mathbf{x} \; dx \; dy \; dz. \tag{B.51}$$

By calculating the above integral the following equation for this source term is obtained

$$S_3 = \int_\Omega N_l \nabla \cdot \mathbf{J}_e^s \, d\Omega = \frac{I}{6V^e} \; b_l \; \Delta x_l. \tag{B.52}$$

B.2 Expansion of $\nabla \times \nabla \times \mathbf{A}$ using edge-elements

Imposing the Coulomb gauge condition on equation 3.6 requires splitting the first term, $\nabla \times \nabla \times \mathbf{A}$, on the left into $\nabla(\nabla \cdot \mathbf{A}) - \nabla^2 \mathbf{A}$:

$$\nabla(\nabla \cdot \mathbf{A}) - \nabla^2 \mathbf{A} + i\omega\mu_0\sigma\mathbf{A} + \mu_0\sigma\nabla\phi = \mu_0 \mathbf{J}^s - \frac{i}{\omega} \nabla \times \mathbf{J}_\mathbf{m}^\mathbf{s}. \tag{B.53}$$

If the Coulomb gauge condition ($\nabla \cdot \mathbf{A} = 0$) is considered, the first term on the left of the above equation, $\nabla(\nabla \cdot \mathbf{A})$, will cancel to zero. Therefore the equation B.53 (e.g. for an electric type of source) will change to,

$$-\nabla^2 \mathbf{A} + i\omega\mu_0\sigma\mathbf{A} + \mu_0\sigma\nabla\phi = \mu_0 \mathbf{J}^s. \tag{B.54}$$

If equation B.54 is to be discretized using edge-element basis functions in the Galerkin method (see in Chapter 3), the first term on the left, $-\nabla^2 \mathbf{A}$, produces the following

integral:

$$-\int_{\Omega} \mathbf{N}_i \cdot \nabla^2 \mathbf{N}_j d\Omega, \tag{B.55}$$

where $\mathbf{N}_i$ and $\mathbf{N}_j$ are vector basis functions for edges i and j respectively. Using three scalar components for the vector laplacian and three components of the vector basis functions alters the above equation to:

$$-\int_{\Omega} (N_i^x \mathbf{x} + N_i^y \mathbf{y} + N_i^z \mathbf{z}) \cdot (\nabla N_j^x \mathbf{x} + \nabla^2 N_j^y \mathbf{y} + \nabla^2 N_j^z \mathbf{z})\ d\Omega, \tag{B.56}$$

which eventually gives:

$$-\int_{\Omega} (N_i^x \nabla^2 N_j^x + N_i^y \nabla^2 N_j^y + N_i^z \nabla^2 N_j^z)\ d\Omega, \tag{B.57}$$

where

$$\begin{aligned}
\nabla^2 N_j^x &= \frac{\partial^2}{\partial x^2} N_j^x + \frac{\partial^2}{\partial y^2} N_j^x + \frac{\partial^2}{\partial z^2} N_j^x, \\
\nabla^2 N_j^y &= \frac{\partial^2}{\partial x^2} N_j^y + \frac{\partial^2}{\partial y^2} N_j^y + \frac{\partial^2}{\partial z^2} N_j^y, \\
\nabla^2 N_j^z &= \frac{\partial^2}{\partial x^2} N_j^z + \frac{\partial^2}{\partial y^2} N_j^z + \frac{\partial^2}{\partial z^2} N_j^z,
\end{aligned} \tag{B.58}$$

are three scalar components of the vector laplacian $\nabla^2 \mathbf{N}_j$ and

$$\begin{aligned}
N_i^x &= \ell_i (\frac{1}{6V^e})^2 (a_{i1} b_{i2} - a_{i2} b_{i1}) + y(c_{i1} b_{i2} - c_{i2} b_{i1}) + z(d_{i1} b_{i2} - d_{i2} b_{i1}), \\
N_i^y &= \ell_i (\frac{1}{6V^e})^2 (a_{i1} c_{i2} - a_{i2} c_{i1}) + x(b_{i1} c_{i2} - b_{i2} c_{i1}) + z(d_{i1} c_{i2} - d_{i2} c_{i1}), \\
N_i^z &= \ell_i (\frac{1}{6V^e})^2 (a_{i1} d_{i2} - a_{i2} d_{i1}) + x(b_{i1} d_{i2} - b_{i2} d_{i1}) + y(c_{i1} d_{i2} - c_{i2} d_{i1}),
\end{aligned} \tag{B.59}$$

are three components of the vector basis function $\mathbf{N}_i$ with the appropraite expansion coefficients a, b, c and d for the end-point nodes $i1$ and $i2$ related to the edge i. Parameters ℓ_i and V^e are the length of edge i and the volume of cell e respectively.

By substituting equations B.58 and B.59 into equation B.57 and using the integration by parts I obtained,

$$-\int_{\Omega}\mathbf{N}_i\cdot\nabla^2\mathbf{N}_j d\Omega = -\int_{\Omega}(\frac{\partial N_i^x}{\partial x}\frac{\partial N_j^x}{\partial x}+\frac{\partial N_i^x}{\partial y}\frac{\partial N_j^x}{\partial y}+\frac{\partial N_i^x}{\partial z}\frac{\partial N_j^x}{\partial z}+ \frac{\partial N_i^y}{\partial x}\frac{\partial N_j^y}{\partial x}+\frac{\partial N_i^y}{\partial y}\frac{\partial N_j^y}{\partial y}+\frac{\partial N_i^y}{\partial z}\frac{\partial N_j^y}{\partial z}+\frac{\partial N_i^z}{\partial x}\frac{\partial N_j^z}{\partial x}+\frac{\partial N_i^z}{\partial y}\frac{\partial N_j^z}{\partial y}+\frac{\partial N_i^z}{\partial z}\frac{\partial N_j^z}{\partial z})\,d\Omega + \mathbf{D}^x+\mathbf{D}^y+\mathbf{D}^z, \tag{B.60}$$

where $\mathbf{D}^x$, $\mathbf{D}^y$, and $\mathbf{D}^z$ are some surface integral terms (for similar expressions see Jin, 2002) that are zero under the Dirichlet conditions and also for the basis functions used here. Using the expressions listed in equation B.59 for equation B.60 produces a zero integral, therefore

$$-\int_{\Omega}\mathbf{N}_i\cdot\nabla^2\mathbf{N}_j d\Omega = 0. \tag{B.61}$$

Appendix C

C.1 Quality unstructured mesh generation

Generating suitable meshes for three-dimensional finite-element modeling of EM problems requires more than just tetrahedralization of the computational domain. In particular, in order to guarantee the convergence of the method and also obtaining accurate results, for example for the both electric and magnetic fields, all tetrahedra or triangles are required to be of suitable shapes and sizes. The mesh generator TetGen (Si, 2007) used in this thesis meshes the computational domain into Delaunay tetrahedral elements. Considering a set of vertices, for a Delaunay mesh no vertex lies inside the circumcircle (in 2D) or circumsphere (in 3D) of any triangle or tetrahedra. By definition, a circumcircle (circumsphere) is a circle (sphere) that passes through all vertices of a triangle (tetrahedron). A 2D Delaunay triangulation is illustrated in Figure C.1. It can be seen here that all three vertices (abc and aed for triangles in pink and beige colors respectively) are located on the area of the corresponding circumcircles. Delaunay meshes in particular maximize the minimum angle, and also minimize the maximum circumradius (Shewchuk, 1998). For accuracy in the FE solutions, quality measures need to be applied to both the shape and size of each tetraherdral element in the mesh. Imposing bounds on the aspect ratio of each

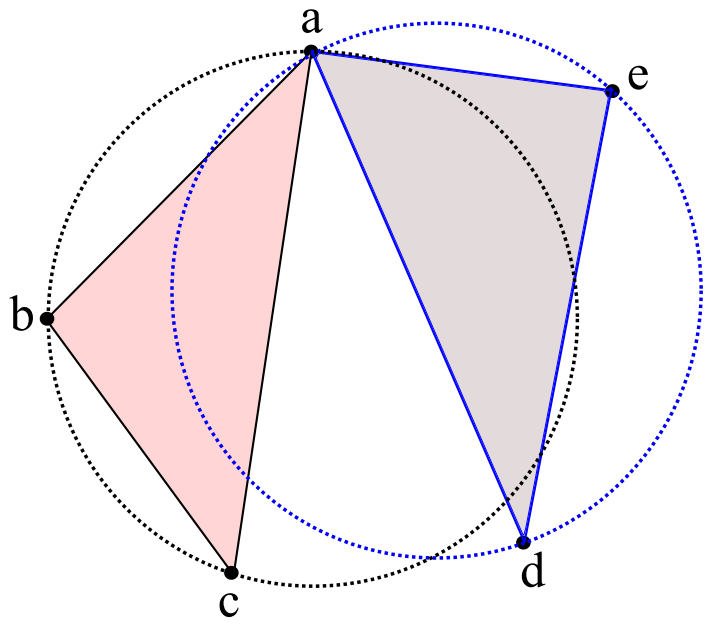

Figure C.1: Delaunay triangulations for vertices abc and ade. The circumcircles are indicated in dotted circles: black for the abc triangle and blue for the ade triangle.

tetrahedron in the mesh is the first quality measure that needs to be considered. For each element the aspect ratio is given by the ratio of the maximum side length to minumum altitude. For a well-shaped triangle or tetrahedron this value would be as small as possible. TetGen however uses the similar radius-edge ratio as a quality measure for the shape of cells (Miller et al., 1995; Shewchuk, 1998). The redius-edge ratio (circumradius-to-shortest edge ratio) is defined as the ratio of the circumsphere to the length of the shortest edge of the tetrahedral element. Figures C.2 to C.7 show the generated meshes for a range of radius-edge ratios (Figures C.2 to C.4 for the xy cross-sections and Figures C.5 to C.7 for the corresponding xz cross-sections). Each of these meshes are used to model the data from a magnetic dipole source located on the surface of a half-space model of 0.01 S/m. Here a frequency of 300 Hz is used. The dimension of the whole mesh is 25 km $\times$ 25 km $\times$ 25 km. The mesh is refined about the source at the origin and around the observation locations in the x-axis. For these three meshes mentioned above the problem is iteratively solved with a dimension of

100 for the Krylov subspace and for 8000 iterations.

Figure C.8 shows the residual norm of the iterative solver for the three meshes used. It can be seen here that the decrease in the residual norm of GMRES is very slow for the model meshed using cells with a radius-edge ratio bound of 2 (see line in black in Figure C.8). Here, by using radius-edge ratio bounds of 1.414 and 1.2 the quality of the mesh has increased and as a result the convergence rate is improved. (see the corresponding lines in red and blue in Figure C.8). For these solutions Figures C.9 and C.10 show the calculated eletric and magnetic fields respectively. As anticipated here, the fields obtained for the mesh that includes cells with radius-edge ratio bounds of 2 (shown in circles in Figures C.9 and C.10) are significantly noisy and different from their corresponding anlytic responses. For meshes of higher qualities the numerical electric and magnetic responses are becoming closer to their corresponding analytic solutions (see red and blue circles in Figures C.9 and C.10). However, the reduction in the residual norms for the runs due to these meshes are not adequate such that both the electric and magnetic fields do not nicely match the analytic answers (particularly at distances far from the source). Hence, in order to obtain more accurate numerical results for these iterative solutions the quality of the mesh needs to be increased. Choosing smaller bounds for the radius-edge ratio produces meshes with relatively higher numbers of elements (e.g., 1258046 cells for a radius-edge ratio of 1.12). The problem of unncessarily high number of cells can be counteracted by imposing bounds on the dihedral angles, i.e., angles between tetrahedral facets, in the mesh. In particular, by imposing bounds on radius-edge ratios and dihedral angles at the same time, TetGen generates meshes of high qualities which also have reasonable number of elements. The default for the dihedral angle is 5 degrees and can be increased as large as 18 degrees. Here in order to have a trade-off between the number of elements and the accuracy of the solution I introduced a radius-edge ratio of 1.414 along with

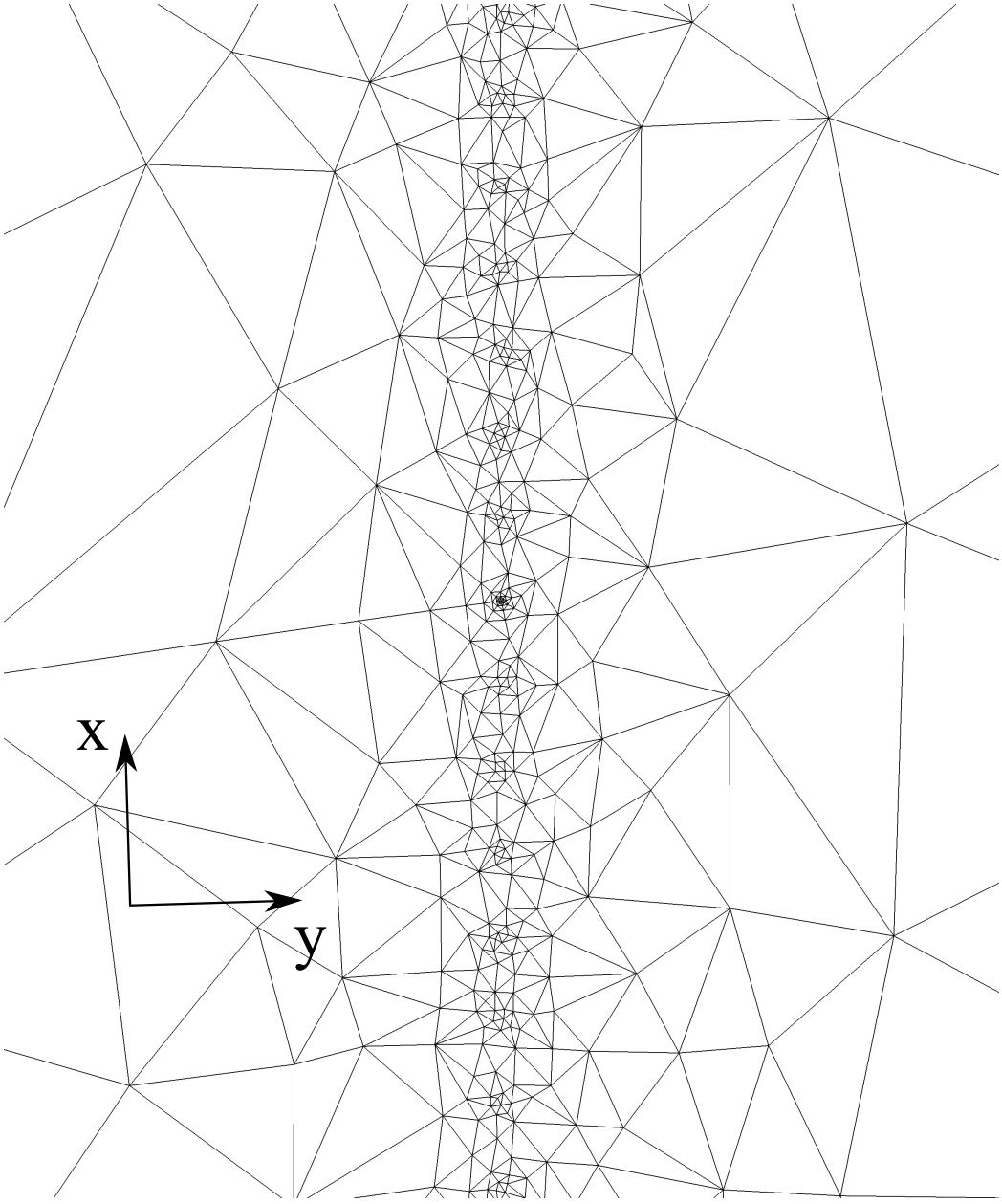

Figure C.2: An enlarged xy view of the central part of the mesh on the Earth surface for a radius-edge ratio of 2. The number of elements, nodes and edges are 41338, 7002, and 48572 respectively.

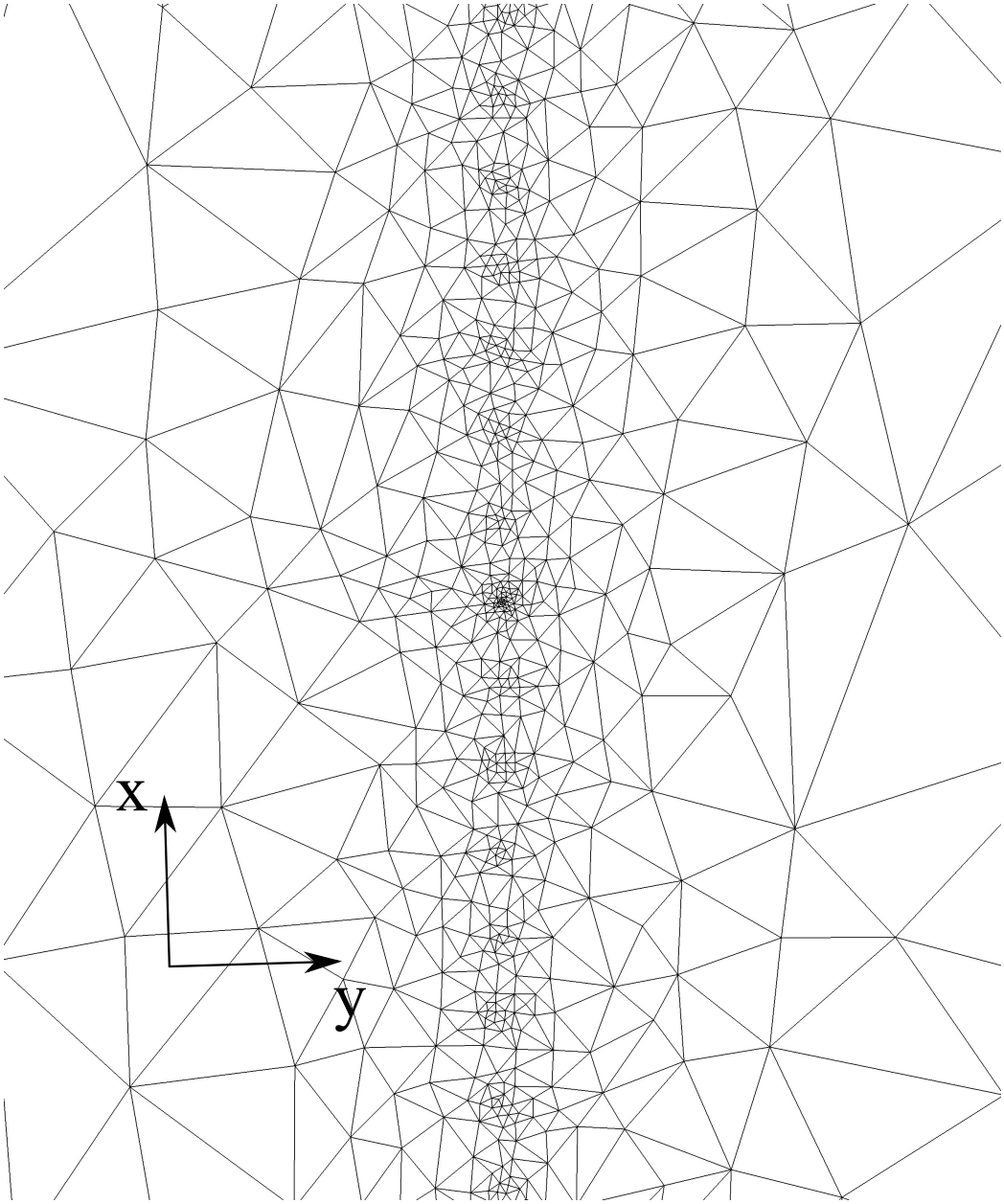

Figure C.3: An enlarged xy view of the central part of the mesh on the Earth surface for a radius-edge ratio of 1.414. The number of elements, nodes and edges are 91849, 15055 and 107162 respectively.

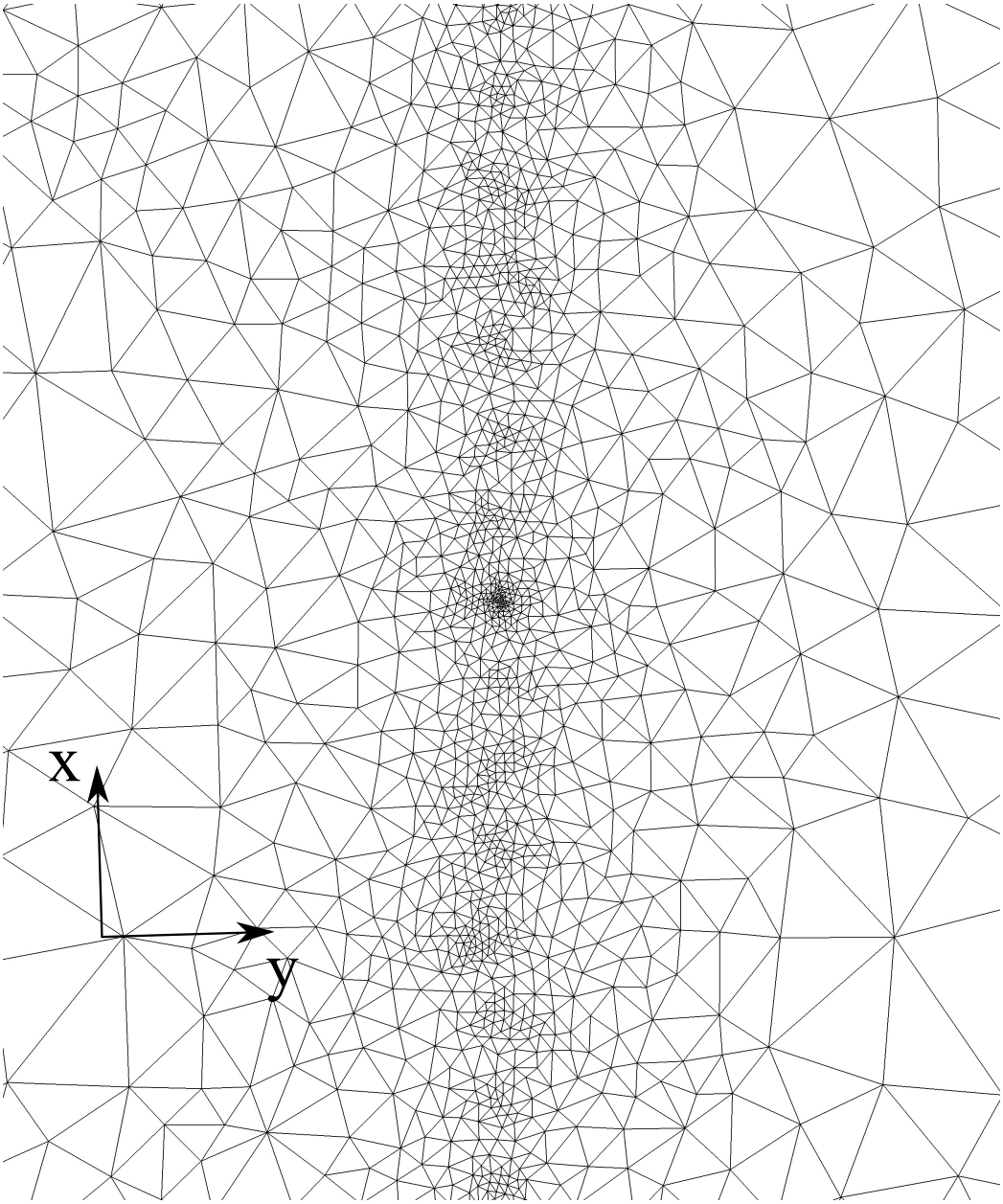

Figure C.4: An enlarged xy view of the central part of the mesh on the Earth surface for a radius-edge ratio of 1.2. The number of elements, edges and nodes are 237423, 38246, and 276002 respectively.

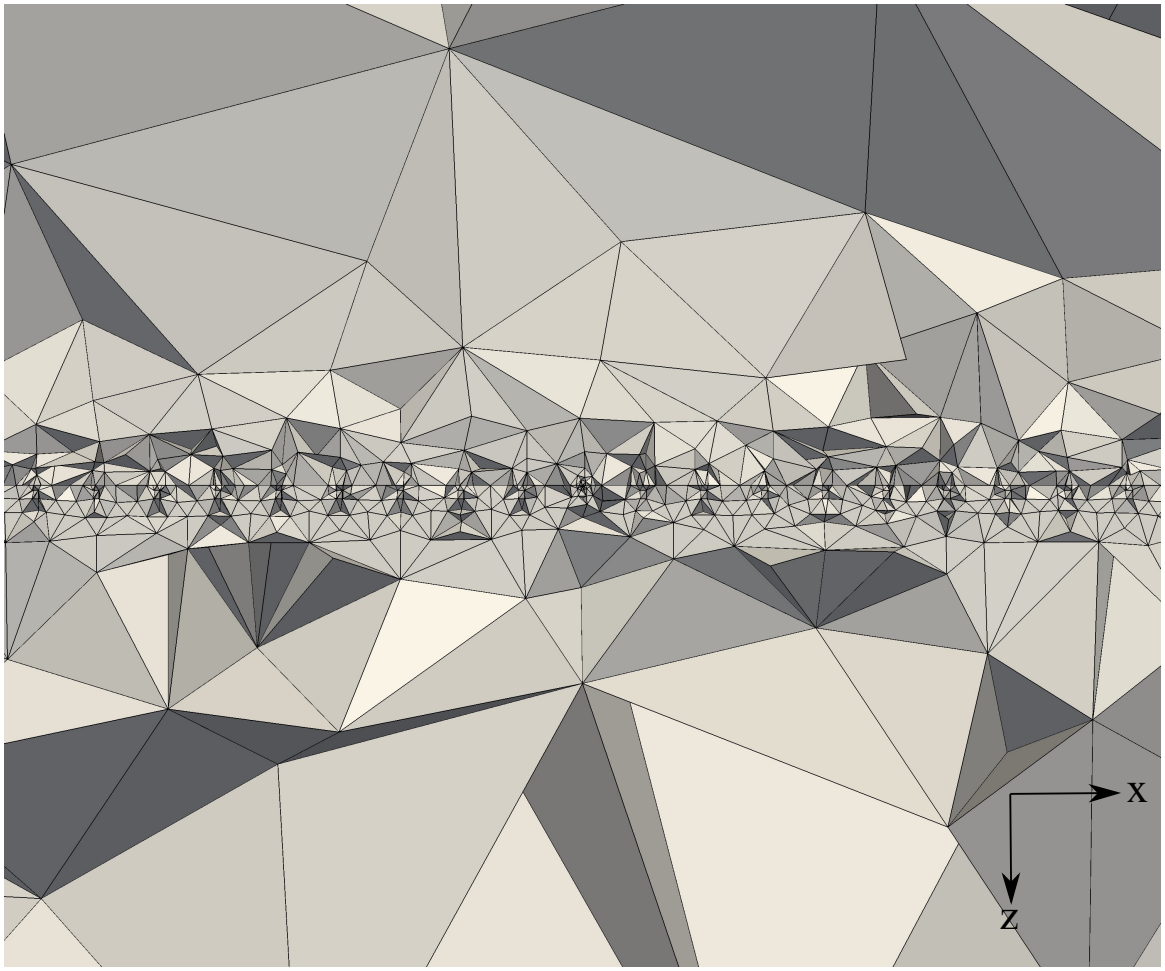

Figure C.5: An enlarged xz view of the central part of the mesh on the Earth surface for a radius-edge ratio of 2.

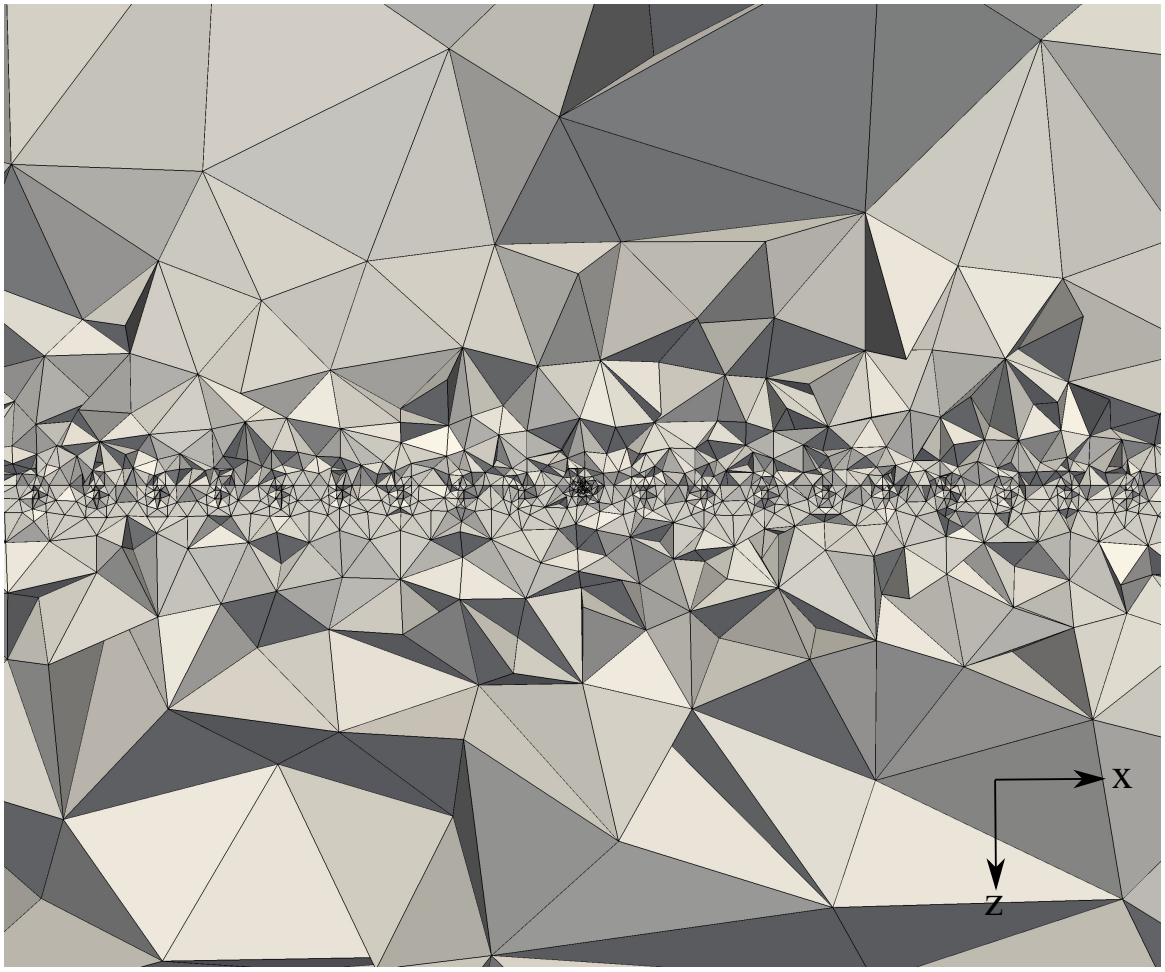

Figure C.6: An enlarged xz view of the central part of the mesh on the Earth surface for a radius-edge ratio of 1.414.

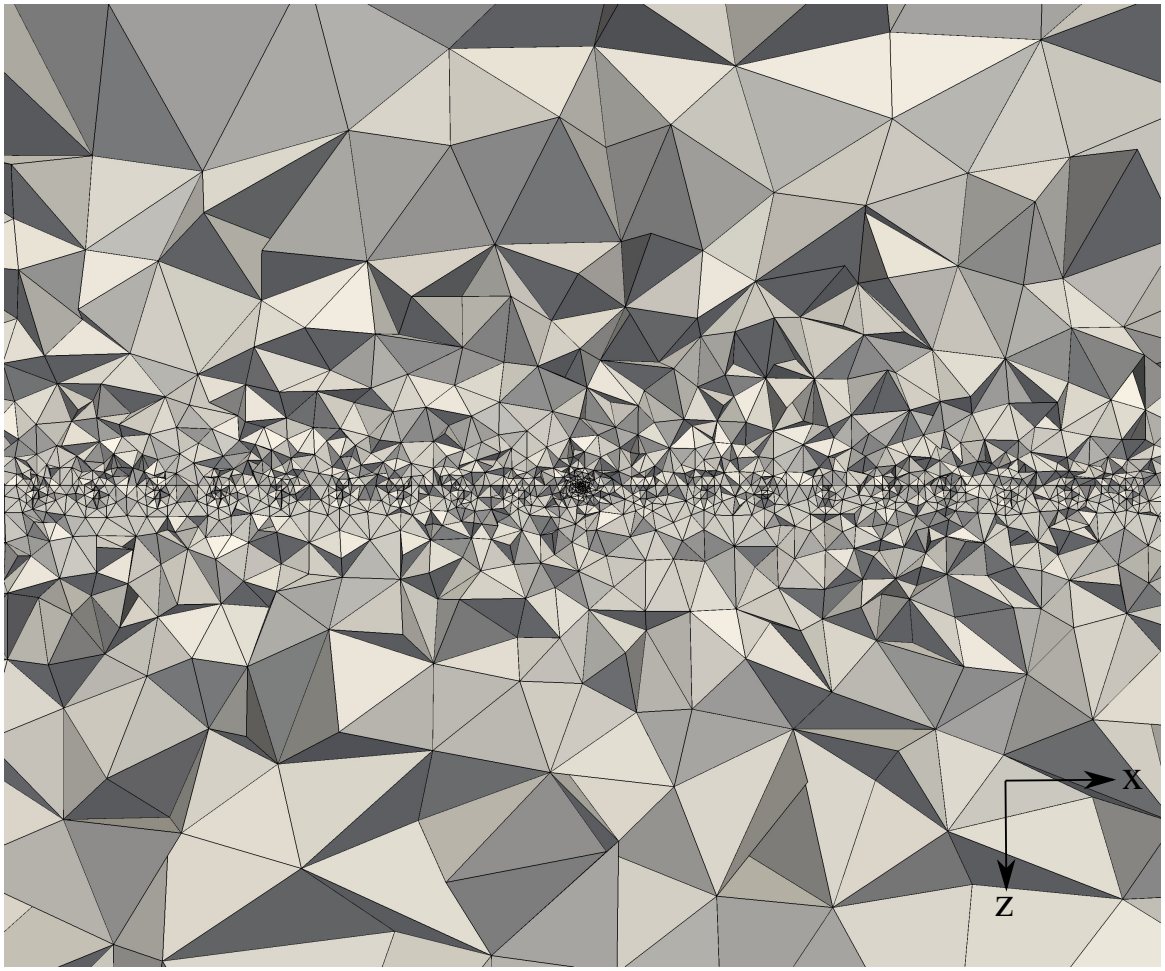

Figure C.7: An enlarged xz view of the central part of the mesh on the Earth surface for a radius-edge ratio of 1.2.

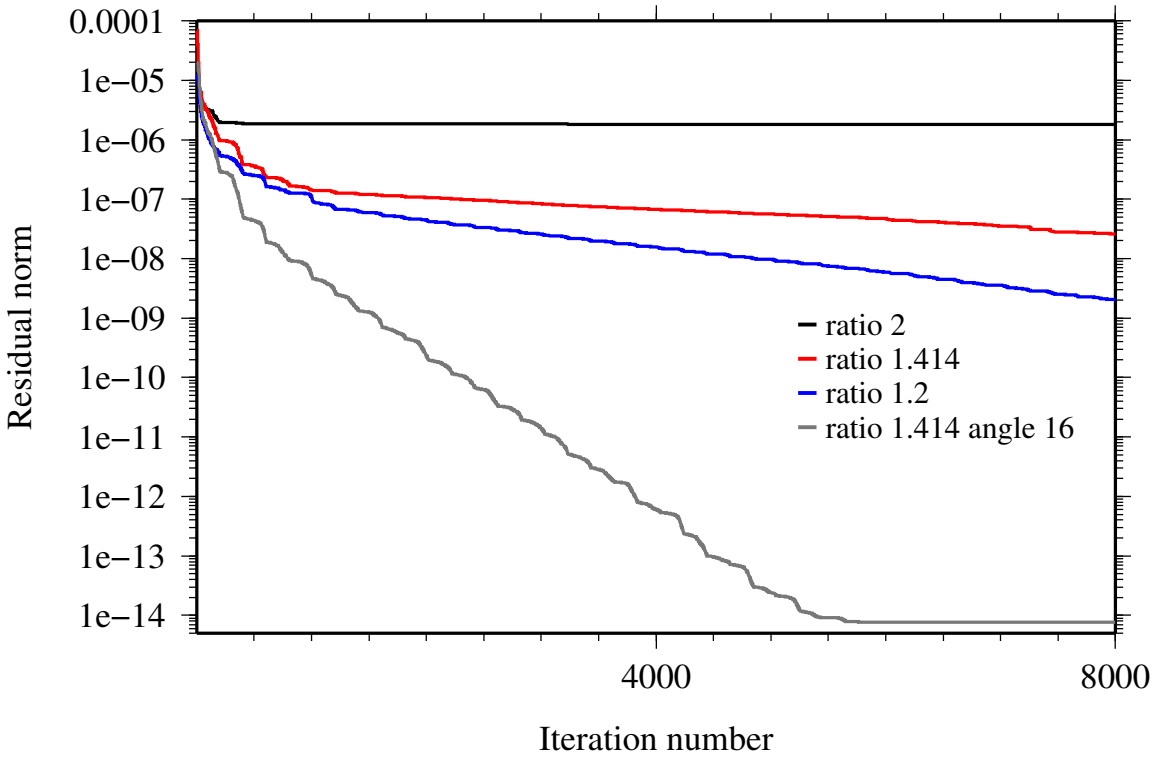

Figure C.8: The convergence curves for the $\mathbf{A} - \phi$ solutions for frequency of 300 Hz for four meshes of different qualities used for the half-space model of 0.01 S/m. Data are the residual norms provided by the GMRES solver.

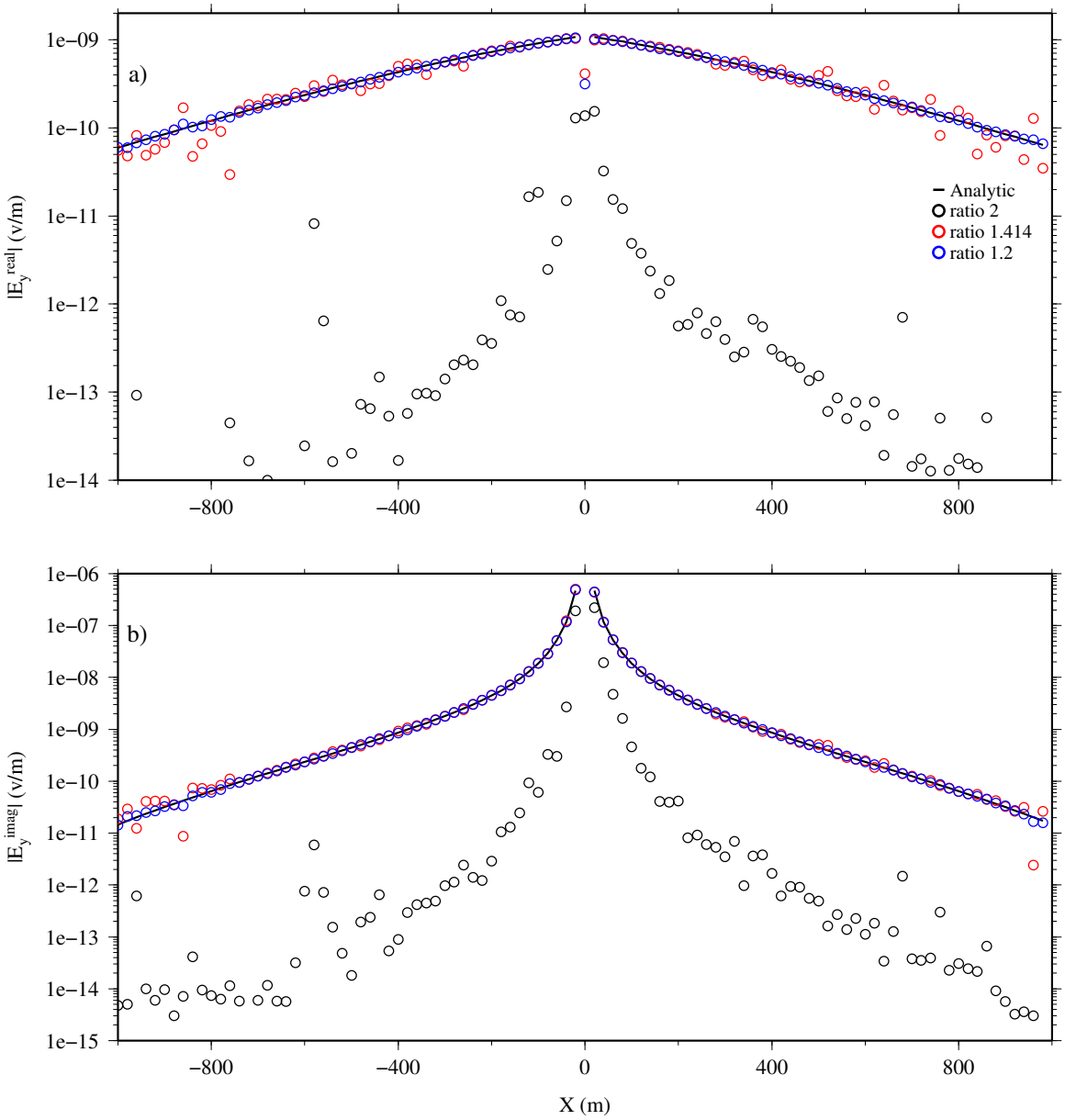

Figure C.9: The real and imaginary parts of the y-component of the electric field for a frequency of 300 Hz for the half-space model of 0.01 S/m. Circles in black, red, and blue are data from meshes with radius-edge ratios of 2, 1.414, and 1.2 respectively for tethradedral cells.

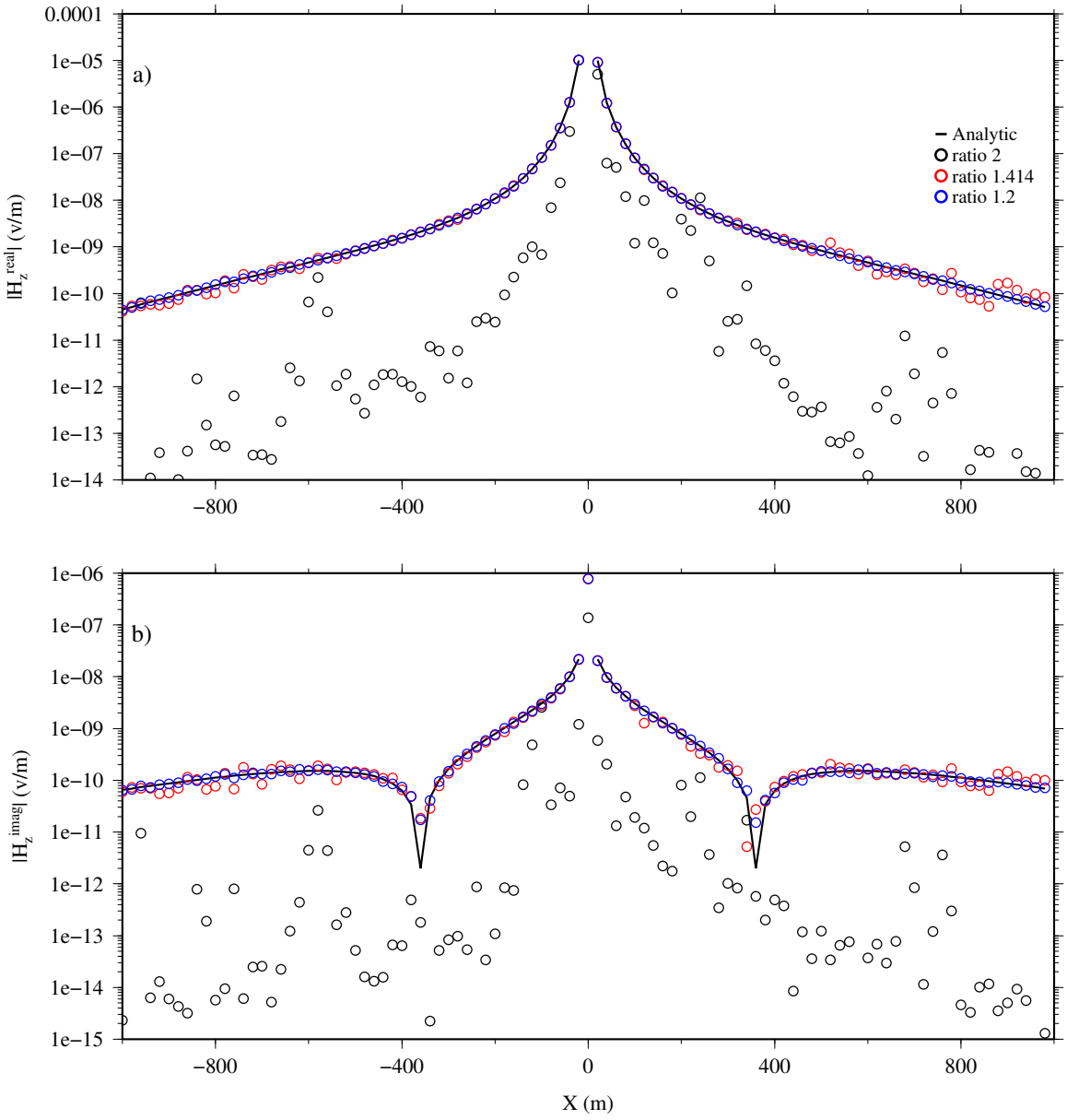

Figure C.10: The real and imaginary parts of the z-component of the magnetic field for a frequency of 300 Hz for the half-space model of 0.01 S/m. Circles in black, red, and blue are data from meshes with radius-edge ratios of 2, 1.414, and 1.2 respectively for tetrahedral cells.

a dihedral angle bound of 16 degrees as mesh quality inputs for TetGen. Figures C.11 and C.12 show the resulting tetrahedral mesh. The mesh consists of 217301 cells, 35691 nodes, and 253397 edges. The convergence of the solution for the half-space model run using this mesh is also shown in Figure C.8 (see solid gray lines therein). Figures C.13 and C.14 show the electric and magnetic fields (for the same data range shown in Figures C.9 and C.10) respectively. It can be seen for this run that for the relatively faster convergence compared to those meshes with no quality enforcement on dihedral angles (see Figure C.8) more accurate electric and magnetic fields are obtained.

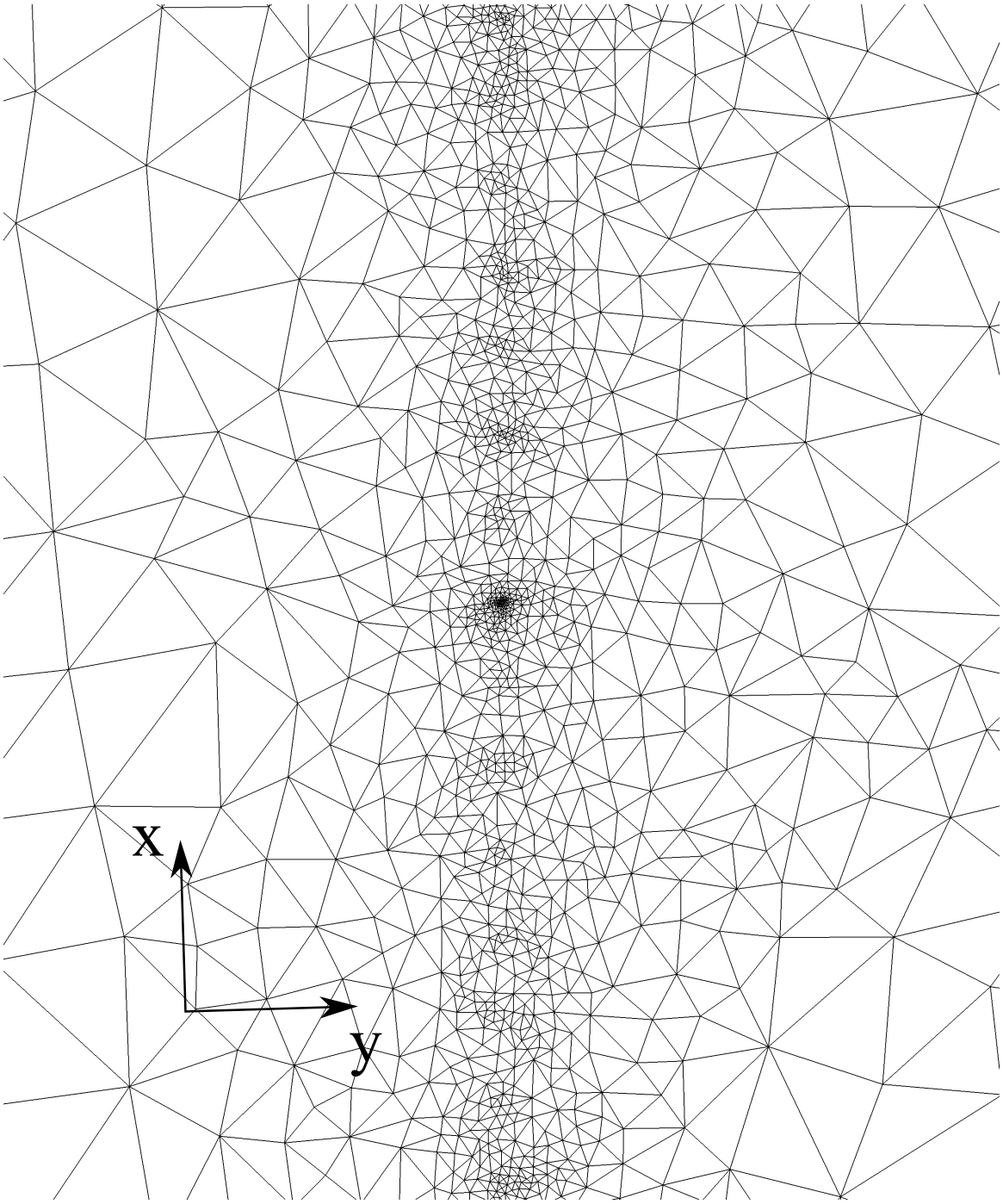

Figure C.11: An enlarged xy view of the central part of the mesh on the Earth surface for a radius-edge ratio of 1.414 and a dihedral angle of 16 degrees.

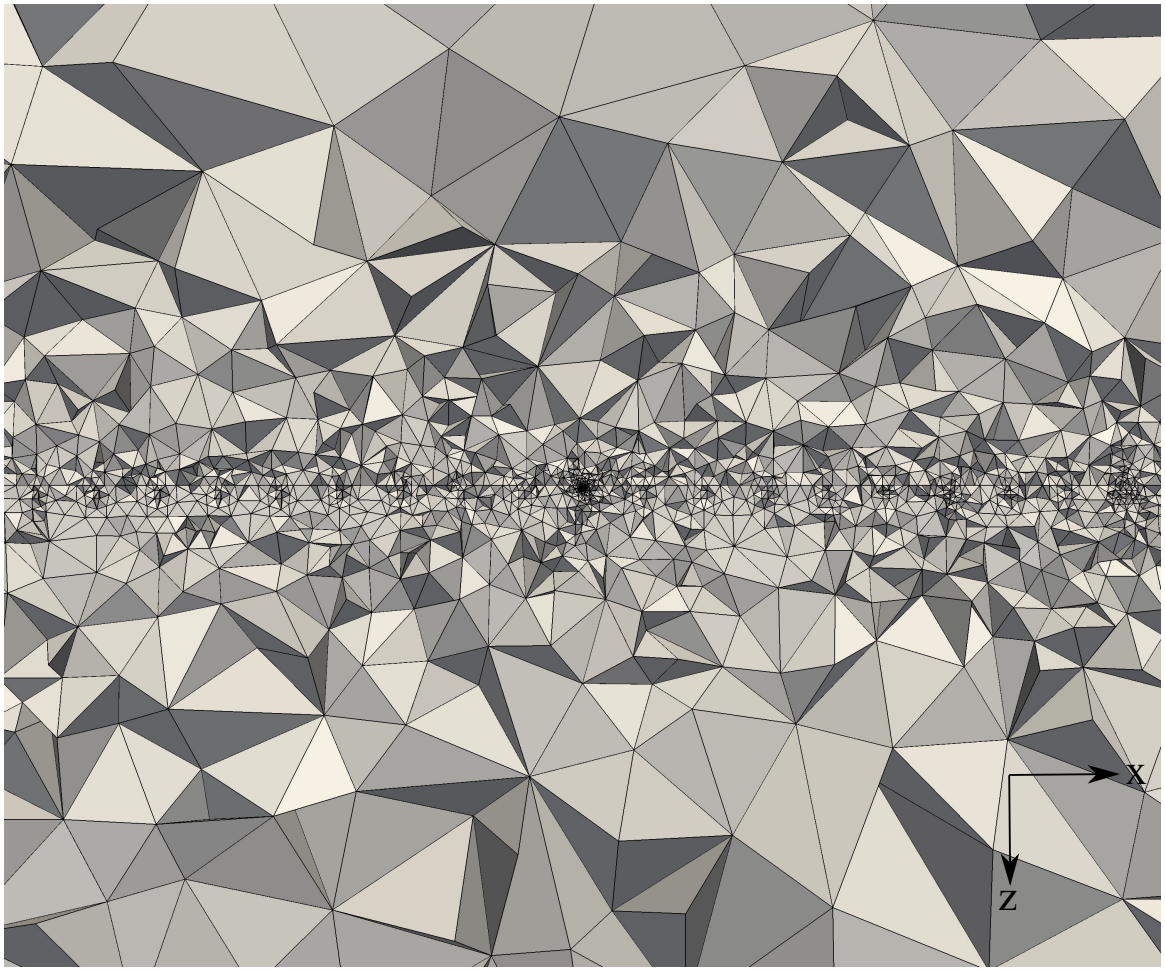

Figure C.12: An enlarged xz view of the central part of the mesh on the Earth surface for a radius-edge ratio of 1.414 and a dihedral angle of 16 degrees.

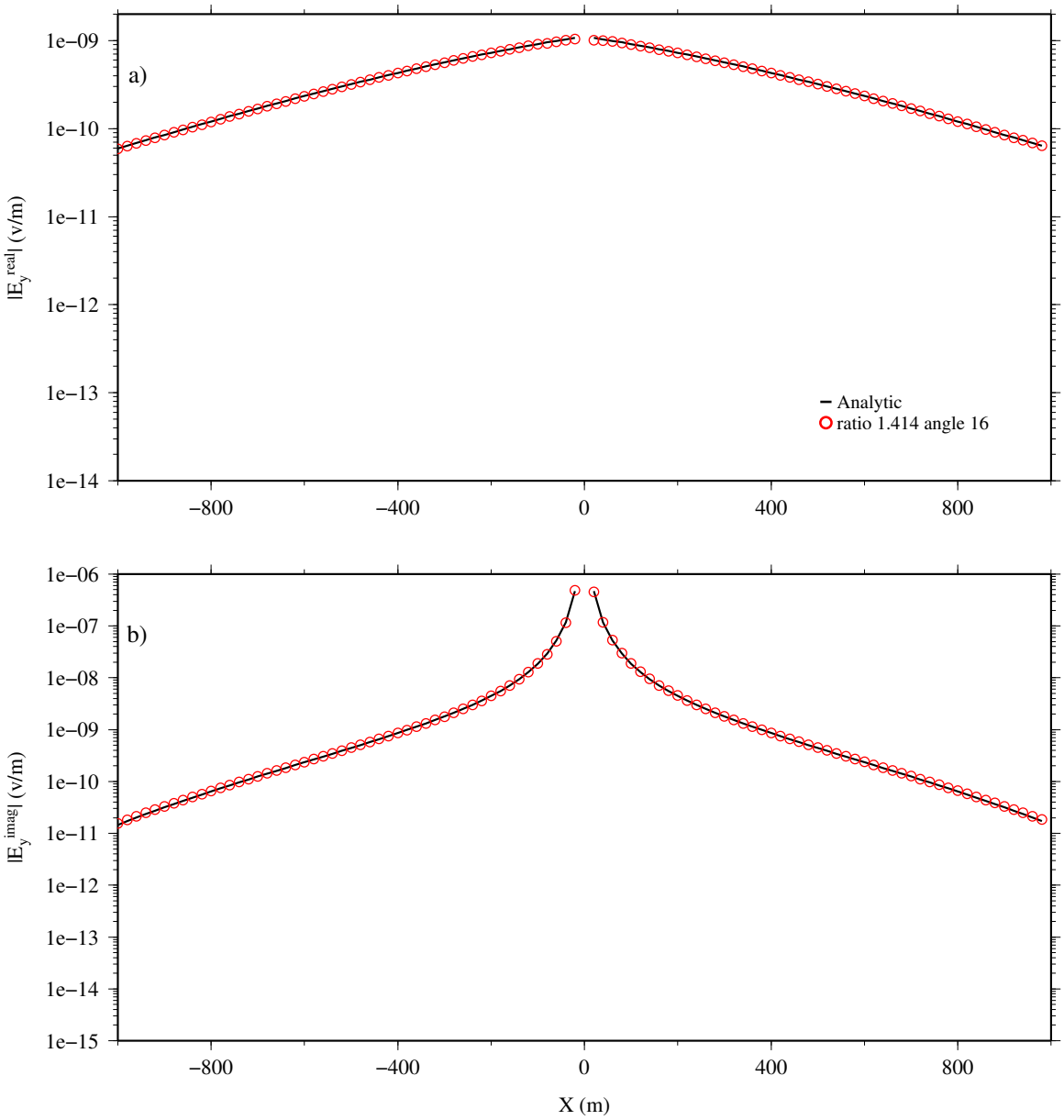

Figure C.13: The real and imaginary parts of the y-component of the electric field for a frequency of 300 Hz for the half-space model of 0.01 S/m. Circles are data from the mesh with radius-edge ratio of 1.414 and a minimum dihedral angle of 16 degrees for tetrahedral cells.

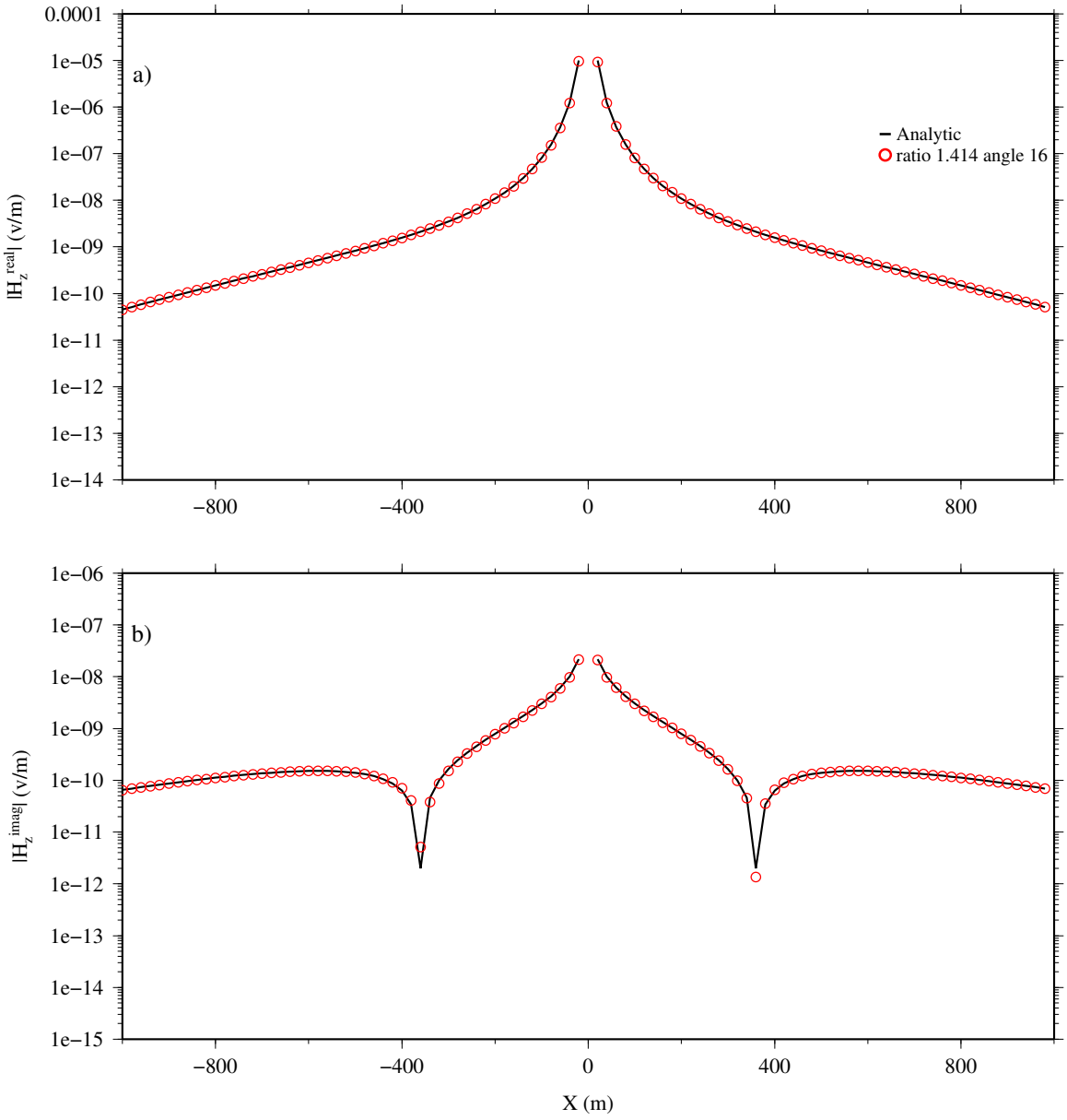

Figure C.14: The real and imaginary parts of the z-component of the magnetic field for a frequency of 300 Hz for the half-space model of 0.01 S/m. Circles are data from the mesh with radius-edge ratio of 1.414 and a minimum dihedral angle of 16 degrees for tetrahedral cells.

Bibliography

Amestoy, P. R., I. S. Duff, J. Koster, and J. Y. L'Excellent, 2001, A fully asynchronous multifrontal solver using distributed dynamic scheduling: SIAM Journal of Matrix Analysis and Applications, **23**, 15–41.

Amestoy, P. R., A. Guermouche, , J. Y. L'Excellent, and S. Pralet, 2006, Hybrid scheduling for the parallel solution of linear systems: Parallel Computing, **32**, 136–156.

Aruliah, D. A., U. M. Ascher, E. Haber, and D. Oldenburg, 2001, A method for the forward modelling of 3D electromagnetic quasi-static problems: Mathematical Models and Methods in Applied Sciences, **11**, 1–21.

Axelsson, O., and A. Kucherov, 2000, Real valued iterative methods for solving complex symmetric linear systems: Numerical Linear Algebra With Applications, **7**, 197–218.

Axelsson, O., M. Neytcheva, and B. Ahmad, 2013, A comparison of iterative methods to solve complex valued linear algenraic systems: Numerical Algorithms, Springer US.

Badea, B., M. Everett, G. Newman, and O. Biro, 2001, Finite element analysis of controlled-source electromagnetic induction using coulomb-gauged potentials: Geophysics, **66**, 786–799.

Biro, O., 1999, Edge element formulations of eddy current problems: Computer Meth-

ods in Applied Mechanics and Engineering, **169**, 391–405.

Börner, R.-U., G. O. Ernst, and K. Spitzer, 2008, Fast 3-D simulation of transient electromagnetic fields by model reduction in the frequency domain using krylov subspace projection: Geophysical Journal International, **173**, 766–780.

Ciarlet, P. G., 1978, The Finite Element Method for Elliptic Problems: Studies In Mathematics and Its Applications, North-Holland, New York.

Coggon, J. H., 1971, Electromagnetic and Electrical Modeling by the Finite Element Method: Geophysics, **36**, 132–155.

Constable, S., and C. Weiss, 2006, Mapping thin resistors and hydrocarbons with marine EM methods: Insights from 1D modeling: Geophysics, **71**, G43–G51.

Dey, A., and H. F. Morrison, 1979, Resistivity Modelling for Arbitrary Shaped Three-Dimensional Structures: Geophysics, **44**, 753–780.

Dohr, G., 1981, Applied Geophysics, Introduction to Geophysical Prospecting: Halsted Press.

Du, Q., D. Wang, and L. Zhu, 2009, On mesh geometry and stiffness matrix conditioning for general finite element spaces: SIAM Journal of Numerical Analysis, **47**, 1421–1444.

Dyczij-Edlinger, R., G. Peng, and J. Lee, 1998, A Fast Vector-Potential Method Using Tangentially Continuous Vector Finite Elements: IEEE Transactions on Microwave Theory and Techniques, **46**, 863–868.

Everett, M. E., and A. Schultz, 1996, Geomagnetic induction in a heterogenous sphere: Azimuthally symmetric test computations and the response of an undulating 660-km discontinuity: JOURNAL OF GEOPHYSICAL RESEARCH, **101**, 2765–2783.

Farquharson, C. G., K. Duckworth, and D. W. Oldenburg, 2006, Comparsion of integral equation and physical scale modeling of the electromagnetic response of models with large conductivity contrasts: Geophysics, **71**, G169–G177.

Farquharson, C. G., and M. Miensopust, 2011, Three-dimensional finite-element modelling of magnetotelluric data with a divergence correction: Journal of Applied Geophysics, **75**, 699–710.

Farquharson, C. G., and D. W. Oldenburg, 2002, An integral equation solution to the geophysical electromagnetic forward-modelling problems: *in* M. S. Zhdanov and P. E. Wannamaker, eds., Three-Dimensional Electromagnetics: Elsevier, Inc., 3–19.

Franke, A., R.-U. Börner, and K. Spitzer, 2007, 3D finite element simulation of magnetotelluric fields using unstructured grids: 4^{th} International Symposium on Three-Dimensional Electromagnetics, Germany, Expanded Abstracts, 15–18.

Franke-Börner, A., R.-U. Börner, and K. Spitzer, 2012, On the efficient formulation of the MT boundary value problem for 3D finite-element simulation: 21^{th} International Workshop on Electromagnetic Induction in the Earth, Australia, Expanded Abstracts.

Frischknecht, F. C., V. F. Labson, B. R. Spies, and W. L. Anderson, 1991, Profiling methods using small sources: *in* M. N. Nabighian, eds., Electromagnetic methods in applied geophysics: Society of Exploration Geophysicists,2, 105–270.

Fujiwara, K., T. Nakata, and H. Ohashi, 1996, Improvement of Convergence Characteristic of ICCG Method for the $\mathbf{A} - \phi$ Method Using Edge Elements: IEEE Transactions on Magnetics, **32**, 804–807.

Grant, F. S., and G. F. West, 1965, Interpretation Theory in Applied Geophysics: McGraw-Hill Book Company.

Grayver, A., and R. Streich, 2012, Comparison of iterative and direct solvers for 3D CSEM modeling: 82nd Annual International Meeting, SEG, Expanded Abstracts, 1–6.

Griffiths, D. J., 1999, Introduction to Electrodynamics: 3rd Ed., Prentice Hall.

Haber, E., U. M. Ascher, D. M. Aruliah, and D. Oldenburg, 2000, Fast Simulation of

3D Electromagnetic Problems Using Potentials: Journal of Computational Physics, **163**, 150–171.

Hanneson, J. E., and F. West, 1984, The horizontal loop electromagnetic response of a thin plate in a conductive earth: Part II-Computational results and examples: Geophysics, **49**, 421–432.

Hohmann, G. W., 1975, Three-dimensional induced polarization and electromagnetic modeling: Geophysics, **40**, 309–324.

———, 1987, Numerical modeling for electromagnetic methods of geophysics: *in* M. N. Nabighian, eds., Electromagnetic methods in applied geophysics: Society of Exploration Geophysicists,1, 313–363.

Jin, J. M., 2002, The finite element method in electromagnetics: 2nd ed., John Wiley and Sons, New York.

Jiracek, J. R., 1990, Near-surface and topographic distortions in electromagnetic induction: Survery in Geophysics, **11**, 163–203.

Jones, F. W., and L. J. Pascoe, 1972, The Perturbation of Alternating Geomagnetic Fields by Three-Dimensional Conductivity Inhomogeneities: Geophys. J. R. astr. Soc., **27**, 479–485.

Lajoie, J. J., and G. F. West, 1976, The Electromagnetic Response of a Conductive Inhomogeneity in a Layered Earth: Geophysics, **41**, 1133–1156.

Lamontage, Y., and G. F. West, 1971, EM response of a rectangular thin plate: Geophysics, **36**, 1204–1222.

Lelièvre, P., A. Carter-McAuslan, C. Farquharson, and C. Hurich, 2012, Unified geophysical and geological 3D earth models: The Leading Edge, **31**, 322–328.

Li, Y., and D. W. Oldenburg, 1991, Aspects of Charge Accumulation in d.c. Resistivity Experiments: Geophysical Prospecting, **39**, 803–826.

Li, Y., D. W. Oldenburg, and R. Shekhtman, 1999, DCIP3D: A Program Library

for Forward Modelling and Inversion of DC Resistivity and Induced Polarization Data over 3D Structures: in Report of the INDI Consortium, University of British Columbia.

Liu, C., Z. Ren, J. Tang, and Y. Yan, 2008, Three-dimensional magnetotellurics using edge-based finite element usnstructured meshes: Applied Geophysics, **5**, 170–180.

Livelybrooks, D., 1993, Program 3Dfeem: a multidimensional electromagnetic finite element model: Geophysical Journal International, **114**, 443–458.

Menvielle, M., 1988, Effects of crustal conductivity heterogenities on the electromagnetic field: Survery in Geophysics, **9**, 319–348.

Miensopust, M., B. Siemon, R.-U. Börner, and S. Ansari, 2013, Multi-dimensional forward modeling of frequency-domain helicopter-borne electromagnetic data: American Geophysical Union, Fall Meeting 2013, Abstract NO. NS23A-1584.

Miller, G. L., D. Talmor, S.-H. Teng, N. Walkington, and H. Wang, 1995, A Delaunay Based Numerical Method for Three Dimensions: Generation, Formulation, and Partition: Proceeding of 27th Annual ACM Symposium on the Theory of Computing, 683–692.

Mitsuhata, Y., and T. Uchida, 2004, 3D magnetotelluric modeling using the T-Ω method: Geophysics, **69**, 108–119.

Monk, P., 2003, Finite Element Methods for Maxwell's Equations: Oxford University Press Inc., New York.

Nam, M. J., H. J. Kim, Y. Song, T. J. Lee, J.-S. Son, and J. H. Suh, 2007, 3D magnetotelluric modelling including surface topography: Geophysical Prospecting, **55**, 277–287.

Nédéléc, J.-C., 1980, Mixed finite element in R^3: Numerische Mathematik, **35**, 315–341.

Newman, G. A., and D. L. Alumbaugh, 1995, Frequency-Domain Modeling of Air-

borne Electromagnetic Responses Using Staggered Finite Differences: Geophysical Prospecting, **43**, 1021–1042.

Palacky, G. J., and G. F. West, 1991, Airborne electromagnetic methods: *in* M. N. Nabighian, eds., Electromagnetic methods in applied geophysics: Society of Exploration Geophysicists,2, 811–879.

Pridmore, D. F., G. W. Hohmann, S. H. Ward, and W. R. Sill, 1981, An investigation of finite-element modeling for electrical and electromagnetic data in three dimensions: Geophysics, **46**, 1009–1024.

Puzyrev, V., J. Koldan, J. de la Puente, G. Houzeaux, M. Vázquez, and J. M. Cela, 2013, A parallel finite-element method for three-dimensional controlled-source electromagnetic forward modelling: Geophysical Journal International, **193**, 678–693.

Raiche, A. P., 1974, An Integral Equation Approach to Three-Dimensional Modelling: Geophys. J. R. astr. Soc., **36**, 363–376.

Saad, Y., 1990, Sparskit: A basic tool kit for sparse matrix calculations, Report RIACS-90-20: Research Institute for Advanced Computer Science, NASA, AMES Research Center.

———, 2003, Iterative methods for sparse linear systems: Society for industrial and Applied Mathematics.

Sadiku, M., 2001, Numerical Techniques in Electromagnetics: 2nd Ed., CRC Press LLC.

Schwarzbach, C., 2009, Stablility of Finite Element Solutions to Maxwell's Equations in Frequency Domain: PhD thesis, Technische Universität Bergakademie Freiberg.

Schwarzbach, C., R.-U. Börner, and K. Spitzer, 2011, Three-dimensional adaptive higher order finite element simulation for geo-electromagnetics — a marine CSEM example: Geophysical Journal International, **178**, 63–74.

Schwarzbach, C., R. Streich, R.-U. Börner, and K. Spitzer, 2010, Low frequency

stable numerical solution of Maxwell's equations: IAGA WG 1.2 20th Workshop on Electromagnetic Induction in the Earth, Giza, Egypt.

Shewchuk, J. R., 1998, Tetrahedral Mesh Generation by Delaunay Refinement: Proceedings of the Fourteenth Annual Symposium on Computational Geometry, 86–95.

Si, H., 2007, TetGen: A quality tetrahedral mesh generator and three-dimensional delaunay triangulator: Available at http://tetgen.berlios.de, accessed 1 January 2014.

Silvester, P. P., and R. L. Ferrari, 1983, Finite elements for electrical engineers: Cambridge University Press.

Smith, J. T., 1996a, Conservative Modeling of 3-D Electromagnetic Fields, Part I, Properties and Error Analysis: Geophysics, **61**, 1038–1318.

———, 1996b, Conservative Modeling of 3-D Electromagnetic Fields, Part II, Biconjugate Gradient Solution and an Accelerator: Geophysics, **61**, 1319–1324.

Sommerfeld, A., 1949, Partial Differential Equations in Physics: Academic Press, Inc.

Stalanker, J., 2004, A finite element approach to the 3D CSEM modeling problem and applications to the study of the effect of target interaction and topography: PhD thesis, Texas A & M University.

Subbaro, V., 2011, Numerical Methods in Electromagnetic Fields: Alpha Science International Ltd., Oxford, U.K.

Sugeng, F., 1998, Modelling the 3D TDEM responses using the 3D full-domain finite-element method based on the hexahedral edge-element technique: Exploration Geophysics, **29**, 615–619.

Telford, W. M., L. P. Geldart, , and R. E. Sheriff, 1990, Applied geophysics: Cambridge University Press.

Um, E. S., J. M. Harris, and D. L. Alumbaugh, 2010, 3D time-domain simulation of electromagnetic diffusion phenomena: A finite-element electric-field approach:

Geophysics, **75**, F115–F126.

Vallée, M. A., R. S. Smith, and P. Keating, 2011, Metalliferous mining geophysics - state of the art after a decade in the new millennium: Geophysics, **76**, W31–W50.

Wang, T., and G. W. Hohmann, 1993, A Finite-Difference Time-Domain Solution for Three-Dimensional Electromagnetic Modeling: Geophysics, **58**, 797–809.

Ward, S. H., and G. W. Hohmann, 1988, Electromagnetic Theory for Geophysical Applications: *in* M. N. Nabighian, eds., Electromagnetic Methods in Applied Geophysics: Society of Exploration Geophysicists,1, 131–311.

Weidelt, P., 1975, Electromagnetic induction in three-dimensional structures: Journal of Geophysics, **41**, 85–109.

Weiss, C., 2013, Project APhiD: A Lorenz-gauged $\mathbf{A}-\phi$ decomposition for parallelized computation of ultra-broadband electromagnetic induction in a fully heterogeneous Earth: Computers and Geosciences, **58**, 40–52.

Weiss, C., and S. Constable, 2006, Mapping thin resistors and hydrocarbons with marine EM methods: Modeling and analysis in 3D: Geophysics, **71**, G321–G332.

West, G. F., and J. C. Macnae, 1991, Physics of the electromagnetic induction exploration method: *in* M. N. Nabighian, eds., Electromagnetic Methods in Applied Geophysics, Volume 2: Society of Exploration Geophysicists, 5–45.

Whitney, H., 1957, Geometric Integration Theory: Princeton University Press.

Xu, S., 2001, The Boundary Element Method in Geophysics, in Geophysical Monograph Series, number 9: Society of Exploration Geophysicists.

Yee, K. S., 1966, Numerical solution of initial boundary value problems involving Maxwell's equations in isotropic media: IEEE Transactions on Antennas and propagation, **14**, 302–309.

Zonge, L. K., and J. L. Hughes, 1987, Controlled-source audio frequency magnetotellurics: *in* M. N. Nabighian, eds., Electromagnetic Methods in Applied Geophysics,

Volume 2: Society of Exploration Geophysicists, 713–809.